AFIT/DS/ENP/95J-02

ELECTRICAL CHARACTERIZATION
OF GaSb-BASED SEMICONDUCTORS
FOR 2–4 μm DIODE LASER APPLICATIONS

DISSERTATION

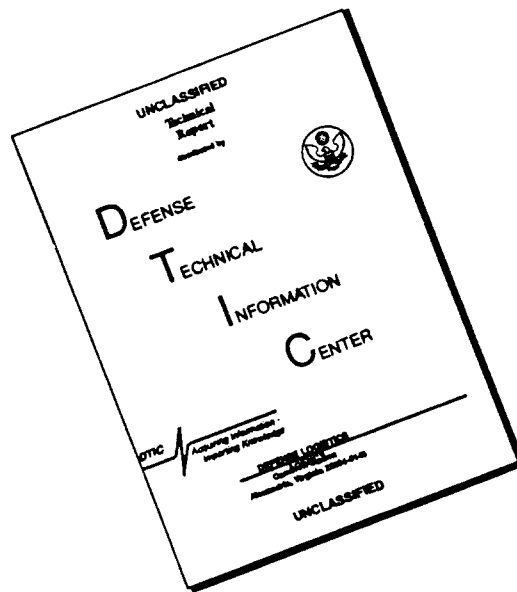Daniel K. Johnstone, Major, USAF

June 1996

DTIC QUALITY INSPECTED 3

19960718 110

DISCLAIMER NOTICE

THIS DOCUMENT IS BEST
QUALITY AVAILABLE. THE COPY
FURNISHED TO DTIC CONTAINED
A SIGNIFICANT NUMBER OF
PAGES WHICH DO NOT
REPRODUCE LEGIBLY.

ELECTRICAL CHARACTERIZATION OF GaSb-BASED

SEMICONDUCTORS FOR 2–4 µm DIODE LASER APPLICATIONS

DISSERTATION

Presented to the Faculty of the Graduate School of Engineering

of the Air Force Institute of Technology

Air University

In Partial Fulfillment of the

Requirements for

the Degree of Doctor of Philosophy

Daniel K. Johnstone, B.S., M.S.

Major, USAF

June 1996

ELECTRICAL CHARACTERIZATION OF GaSb-BASED
SEMICONDUCTORS FOR 2-4 μm DIODE LASER APPLICATIONS

Daniel K. Johnstone, B.S., M.S.
Major, USAF

Approved:

_____   5/13/96

YUNG KEE YEO
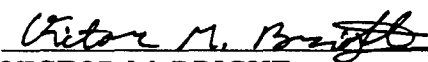Chairman, Advisory Committee

_____   5/13/96

ROBERT L. HENGEHOLD
Member, Advisory Committee

_____   5/13/96

PAUL H. OSDIEK
Member, Advisory Committee

_____   5/13/96
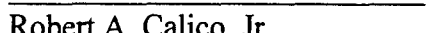
VICTOR M. BRIGHT
Member, Advisory Committee

_____   13 May 1996

PETER J. TORVIK
Dean's Representative

Accepted:

_____

Robert A. Calico, Jr.
Dean, Graduate School of Engineering

Preface

This work was a result of an opportunity presented by Dr. George Turner of Lincoln Lab to improve on the quality and understanding of GaSb-based diode lasers. He took time to sort through samples, and grew samples specifically for this work. His work was sponsored by Nick Pchelkin from Phillips Lab. I am also grateful to Professor Yung Kee Yeo who, as my advisor, spent many patient hours with me developing ideas and polishing written work. It was always a challenge to meet his high standards. It was exciting to experience the dynamics of working with Jim Scofield whose knowledge seemed complementary to my own, providing an excellent sounding board to dig into new twists of characterization or interpretation of results. Dr. Dave Elsaesser deserves thanks for introducing me to DLTS, and for talking me into entering AFIT's doctoral program.

The people at the Solid State Electronics Directorate at Wright Labs generously provided clean room facilities to fabricate the diodes, including Si_3N_4 deposition and RIE from Paul Cassidy and packaging from Larry Calahan. The staff at AFIT, particularly Greg Smith, Belinda Johnson, and Diana Jordan, were instrumental in making sure that all of the equipment was purchased and working when it was needed.

I owe many thanks and many hours of kite flying, bicycling, story reading, wagon rides, crossword puzzles, and just hanging around to my children, Aaron, Daniel, Zachary, Courtney, and my wife, Kathy. They made an art form of feigning interest in the exciting results of the day, and boosted my morale when I encountered difficulties.

<div align="right">Daniel K. Johnstone</div>

Table of Contents

List of Figures

List of Tables

Abstract

Deep level transient spectroscopy (DLTS) was used to characterize the band offsets and deep levels in GaSb-based materials that are used in 2–4 μm laser diode structures. Capacitance-voltage (C-V) profiling, current-voltage-temperature (I-V-T) measurements, and variable temperature Hall measurements were also made in support of the DLTS measurements. Important deep level traps found in $Al_xGa_{1-x}As_ySb_{1-y}$ (x=0, 0.5, 0.6, 1.0) barrier/cladding material grown by MBE are a Ga_{Sb} double acceptor trap and a DX center. Significant progress has been made in establishing the model for the DX center in this material. The reduction in trap energy of the DX center with electric field was less than expected for a center that is neutral after trapping two electrons. This suggests that the DX center is charged -1q after trapping two electrons, rather than neutral. Two group V species in three sites involved in the DX center should result in four unique DX trap energies. However, only one DX trap emission energy was found at 282 meV below the conduction band, suggesting that preference is given to one configuration over the others, possibly influenced by the high concentration of Ga_{Sb}. This DX trap was also used to demonstrate a new, efficient method of measuring capture barriers using the change in capacitance transient amplitude as a function of temperature. A capture barrier of 137 meV was measured for the 282 meV DX trap using the new method, with an excellent fit to the model for capture by multiphonon emission. In the narrow gap $Ga_{0.85}In_{0.15}As_{0.12}Sb_{0.88}$ used in the well, one minority trap level 320 meV below the conduction band, and six hole trap levels 24, 76, 108, 122, 224, and 276 meV above the valence band were found using DLTS measurements. The two low energy hole trap

levels (24 and 76 meV) are attributed to a Ga_{Sb} double acceptor. It is believed that the minority trap level at 320 meV and the hole trap level at 276 meV originate from the same trap. Furthermore, this trap could be the most efficient non-radiative recombination center in this material, greatly reducing laser efficiency. DLTS measurements on quantum well samples show an increase in emission energy from the well with increasing reverse bias measurement conditions, as opposed to a decrease in emission energy with increasing electric field exhibited by some natural deep levels. This can be explained by the inaccuracy of using Boltzmann's approximation rather than Fermi-Dirac statistics at lower reverse bias where the quasi-Fermi level is close to the confined state energy. Extrapolating a series of quantum well emission energies to a point where Boltzmann's approximation is valid results in a valence band offset of 0.52 eV between $Ga_{0.81}In_{0.19}AsSb$ and $Al_{0.9}Ga_{0.1}AsSb$ lattice matched to GaSb. This is significantly different from the value of 0.38 eV calculated from the difference in average valence band energy interpolated from the binary constituents using bowing parameters. Using a value for the band offset that is extrapolated from a series of measured energies is more accurate than a method that is presently used requiring an iterative calculation of the position of the Fermi level prior to emission, which is subject to stray capacitance and inaccuracy in diode area.

ELECTRICAL CHARACTERIZATION OF GaSb-BASED SEMICONDUCTORS FOR 2–4 μm DIODE LASER APPLICATIONS

I. INTRODUCTION

Semiconductors lattice-matched to GaSb are becoming increasingly important for diode laser applications as the understanding of the growth and processing becomes more mature (Turner *et al.*, 1994:1266–1268; Polyakov *et al.*, 1992:1316–1319; Chiu, Zyskind, and Tsang, 1987:57–61; Luquet *et al.*, 1986:3581–3591). $Ga_xIn_{1-x}As_ySb_{1-y}$ lattice matched to GaSb covers the 2-4 μm wavelength range when used with $Al_xGa_{1-x}As_ySb_{1-y}$ as a barrier material (Milnes and Polyakov, 1993:803–818). Increasing the indium mole fraction in $Ga_xIn_{1-x}As_ySb_{1-y}$ decreases the bandgap of the material, covering the mid-infrared wavelengths. $Al_xGa_{1-x}As_ySb_{1-y}$ material with higher aluminum mole fraction is useful for barrier layers since the bandgap increases with increasing aluminum content, resulting in better carrier confinement. Also, the decrease in index of refraction with increasing aluminum content in $Al_xGa_{1-x}As_ySb_{1-y}$ offsets a decrease in index of refraction with increasing indium content in the narrower gap $Ga_xIn_{1-x}As_ySb_{1-y}$ active region of 2-4 μm lasers. Thus, higher Al mole fraction in the cladding material allows

better photon confinement. Recently, the number of investigations of this material system has been increasing due to its application toward laser diodes for the next generation of low loss fluoride optical fibers (Pascal-Delannoy *et al.*, 1992:409–414). Other applications include laser radar operating at wavelengths of minimum atmospheric attenuation, remote sensing of atmospheric gases, and molecular spectroscopy (Eglash *et al.*, 1991:669–678; Le *et al.*, 1994:152–154).

Some issues involved in the development of the materials and devices are:

• effectiveness of the buffer layer,

• availability of both conductivity types for barrier and well materials,

• solubility limits and background impurity concentrations,

• mismatch between well and barrier lattices, and resulting critical thickness,

• heterojunction band offsets as a function of composition,

• bulk defects and interface state defects, and their influence on device operation.

An important piece of information for crystal growers and device designers is the characteristics of deep levels as traps or non-radiative recombination centers. The deep level defects will have varying effects depending on their locations, concentrations, and activation energies. The presence of deep levels in the active or interface region of a laser diode results in loss of efficiency or complete loss of lasing action because of non-radiative recombination via the deep levels (McAfee, Lang, and Tsang, 1982:520–522). Also, deep levels present in the cladding or barrier layer result in efficiency loss by carrier recombination via the deep levels or a delay in lasing from trapping effects (Uji, Suzuki, and Kamejima, 1980:655–657). Another important piece of information is the conduction

band and valence band offsets that determine energy levels in a well. Therefore, most of the effort here concentrates on using deep level transient spectroscopy (DLTS) to characterize the band offsets and deep levels in GaSb-based materials that are used in 2–4 μm laser diode structures. Capacitance-voltage (C-V) profiling, current-voltage-temperature (I-V-T) measurements, and variable temperature Hall measurements were also made in support of the DLTS measurements.

II. BACKGROUND

Semiconductors for Wavelengths Greater than 2μm

Interest in narrow gap semiconductors has been increasing steadily over the past 30 years, since demonstration of the first GaAs p-n junction laser (Nathan *et al.*, 1963:62). The investigations varied from materials that exhibit a direct transition at the Γ minimum (InAs and InSb) to those that exhibit a direct transition at the Brillouin zone edge in the [111] direction (chalcogenides). In these narrow gap materials the first InAs p-n junction diode was made operating at 3.1 μm (Melngailis, 1963:176), and the first InSb diode lasers were made operating at 5.3 μm (Phelan *et al.*, 1963:143; Guillaume and Lavallard, 1963:148), each in 1963. In the following year, the first PbTe and PbSe p-n junction laser diodes were made operating at much longer wavelengths (Butler *et al.*, 1964:75).

Outside of optical devices, the applicability of narrow gap materials is not as extensive as GaAs- or InP-based devices. But extremely high mobilities make them attractive for field effect transistors (FETs). Optical fiber communications requirements may provide the same boost in progress to semiconductors operating at 4-4.5 μm as was received by AlGaAs/GaAs and InP/InGaAsP double heterostructure lasers. The optical fiber loss in this wavelength range can be as low as 10^{-2}–10^{-5} dB/km for fluoride fibers. This is at least two orders of magnitude lower than conventional silica fibers (Pinnow *et al.*, 1978:28). The drawbacks that have caused narrow gap semiconductors to lag behind their 0.8–1.6 μm counterparts include excessive loss mechanisms such as tunneling

current, Auger recombination, and free-carrier absorption (Horikoshi, 1985:93–151). Each of these tend to degrade device performance by raising the threshold current and lowering the maximum operating temperature limit for laser operation.

The expected emission wavelength ranges for several III-V quaternary semiconductors are shown in Figure II-1. The wavelengths correspond to the direct energy gap at room temperature. The heavy lines denote the compositions lattice matched to stable binary substrates of GaAs, InP, GaSb or InAs, as indicated. Cross-hatched areas correspond to the miscibility gaps where the epitaxial layer segregates into more than one phase. From this figure, it can be seen that many quaternary materials have band gaps corresponding to emission wavelengths exceeding 2 μm. However, only AlInAsSb, GaInAsSb, and InAsPSb lattice-matched to GaSb or InAs substrates are stable. $Ga_xIn_{1-x}As_ySb_{1-y}$ can be lattice-matched to GaSb for compositions with $y \approx 0.91x$. One peculiar aspect of $Ga_xIn_{1-x}As_ySb_{1-y}$ is that the refractive index becomes smaller as the band gap becomes smaller. This is the opposite behavior from most other semiconductors that are used in optical devices. In order to use the $Ga_xIn_{1-x}As_ySb_{1-y}$ composition corresponding to longer wavelengths, $Al_xGa_{1-x}As_ySb_{1-y}$ lattice-matched to GaSb must be used as both an optical and carrier confining layer. As the composition of active region tends toward InAs, the cladding material composition required for optical confinement tends toward AlSb. High aluminum content $Al_xGa_{1-x}As_ySb_{1-y}$ has a lower refractive index than GaSb or GaSb-enriched $Ga_xIn_{1-x}As_ySb_{1-y}$ allowing efficient photon confinement to the active region.
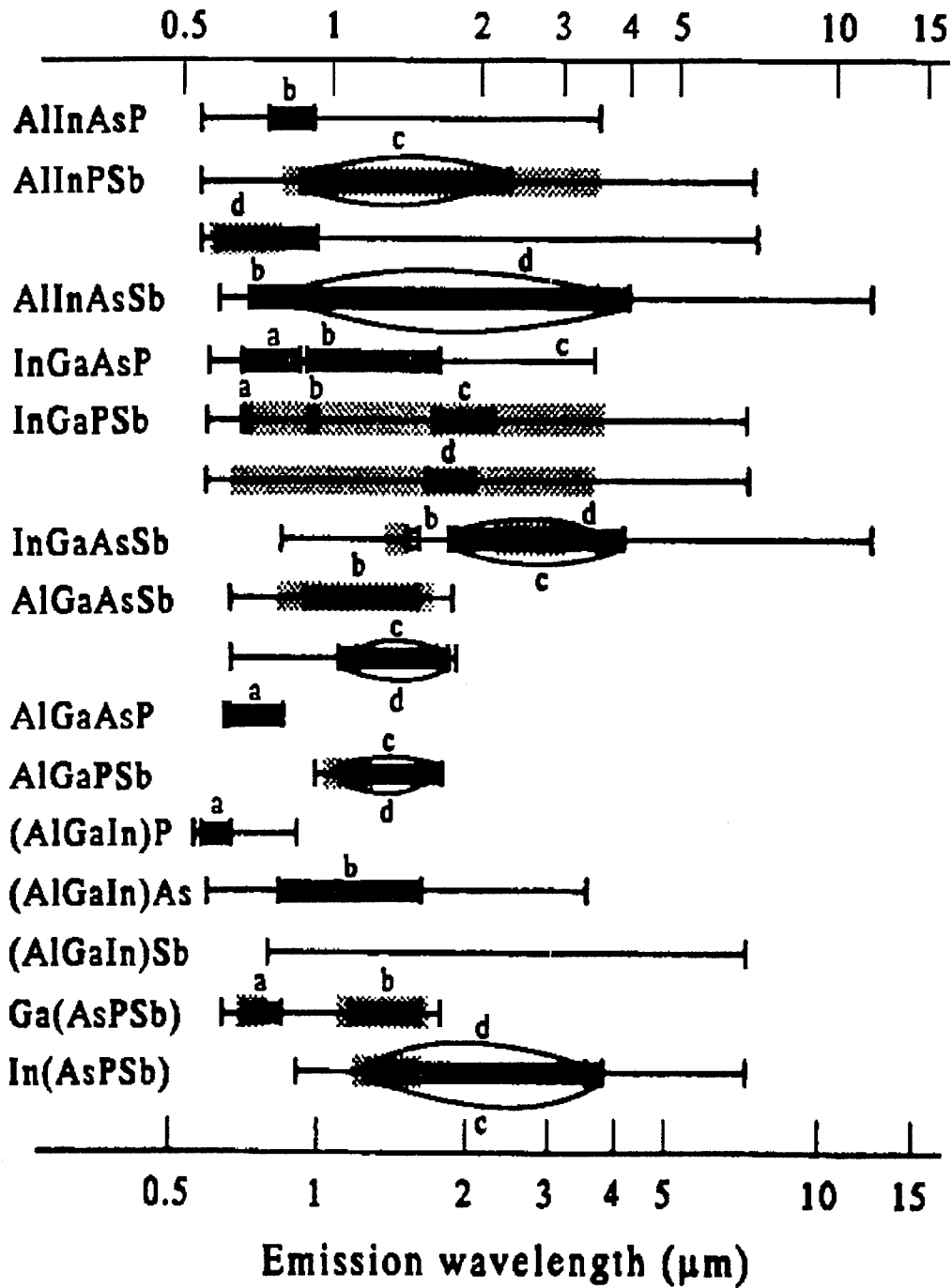
Figure II-1. Expected emission wavelengths for various III-V quaternaries at 300K. The lettering denotes lattice matching to (a) GaAs, (b) InP, (c) GaSb, (d) InAs.

GaSb-Based Systems

GaSb has a band gap of 0.72 eV at room temperature and a cubic lattice constant of 6.095 Å. Layers grown epitaxially on GaSb must have a close lattice match to GaSb, otherwise poor interface quality will degrade device performance. Another important property is the band offset. Figure II-2 shows energy gap line-ups between InSb, GaSb, AlSb and InAs. The energy gap line-ups show that InAs is a broken gap heterojunction on GaSb, as is the lattice matching ternary $InAs_{0.9}Sb_{0.1}$. Most of the band gap difference
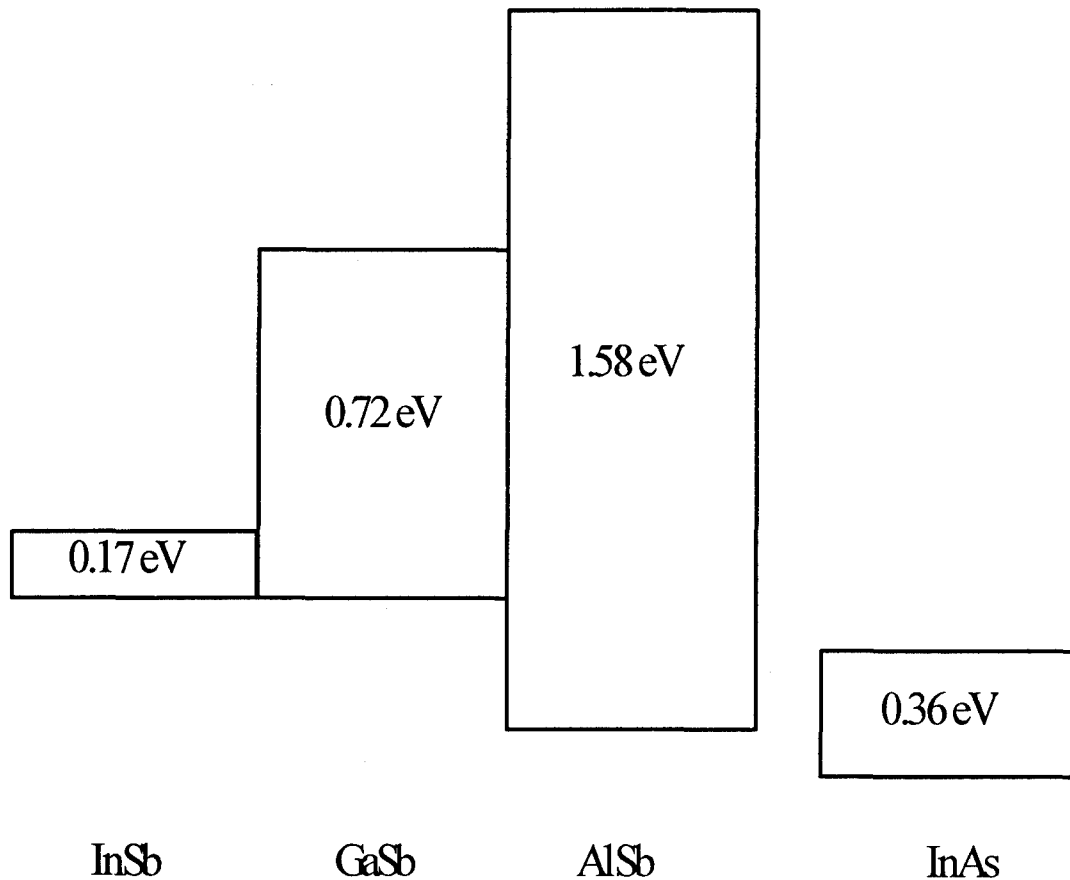
Figure II-2. Approximate energy gap line-ups for InSb, GaSb, AlSb, and InAs.

between the other materials is taken up by the conduction band. None of these binary compounds are lattice-matched to each other. They must be combined as ternary or quaternary compounds to have a lattice match to these binary compounds unless the layer is thin enough to accommodate the strain without relaxation.

Figure II-3 is a compositional diagram of the band gaps and wavelengths versus lattice constant for compound semiconductors. As already stated, the index of refraction decreases for compositions away from GaSb, so that double heterojunction structures with increasing indium content $Ga_xIn_{1-x}As_ySb_{1-y}$ must be confined with cladding layers of increasing aluminum content $Al_xGa_{1-x}As_ySb_{1-y}$. The composition versus band gap and lattice constant can be used along with index of refraction measurements, such as those given in Figure II-4 for AlGaAsSb, to design double heterojunction (DH) or quantum well (QW) laser structures (Alibert *et al.*, 1991:3206–3211).

The band structure versus wave-vector k for GaSb (Milnes and Polyakov, 1993:803–818), InAs (DeAlvarez *et al.*, 1973:337–345), and AlSb (Milnes and Polyakov, 1993:803–818) are given in Figure II-5, Figure II-6, and Figure II-7, respectively. These show that the conduction band minimum and the valence band maximum are at the same momentum space direction in GaSb and InAs, and are thus direct materials. However, AlSb has an indirect band gap requiring phonon interaction to accommodate the change in momentum for a transition from the conduction band minimum to the valence band maximum. Figure II-8 shows the variation of band gap and conduction band minimum in the AlSb/GaSb ternary system as a function of Al mole fraction in $Al_xGa_{1-x}As_ySb_{1-y}$, where

$$y = \frac{0.0396x}{0.4426 + 0.0318x}$$

(Adachi, 1987:4872). This shows the small difference of only 0.085 eV between the Γ band and the indirect minimum L band for GaSb at the left where x=0, crossing over to indirect material at a composition of x=0.24.
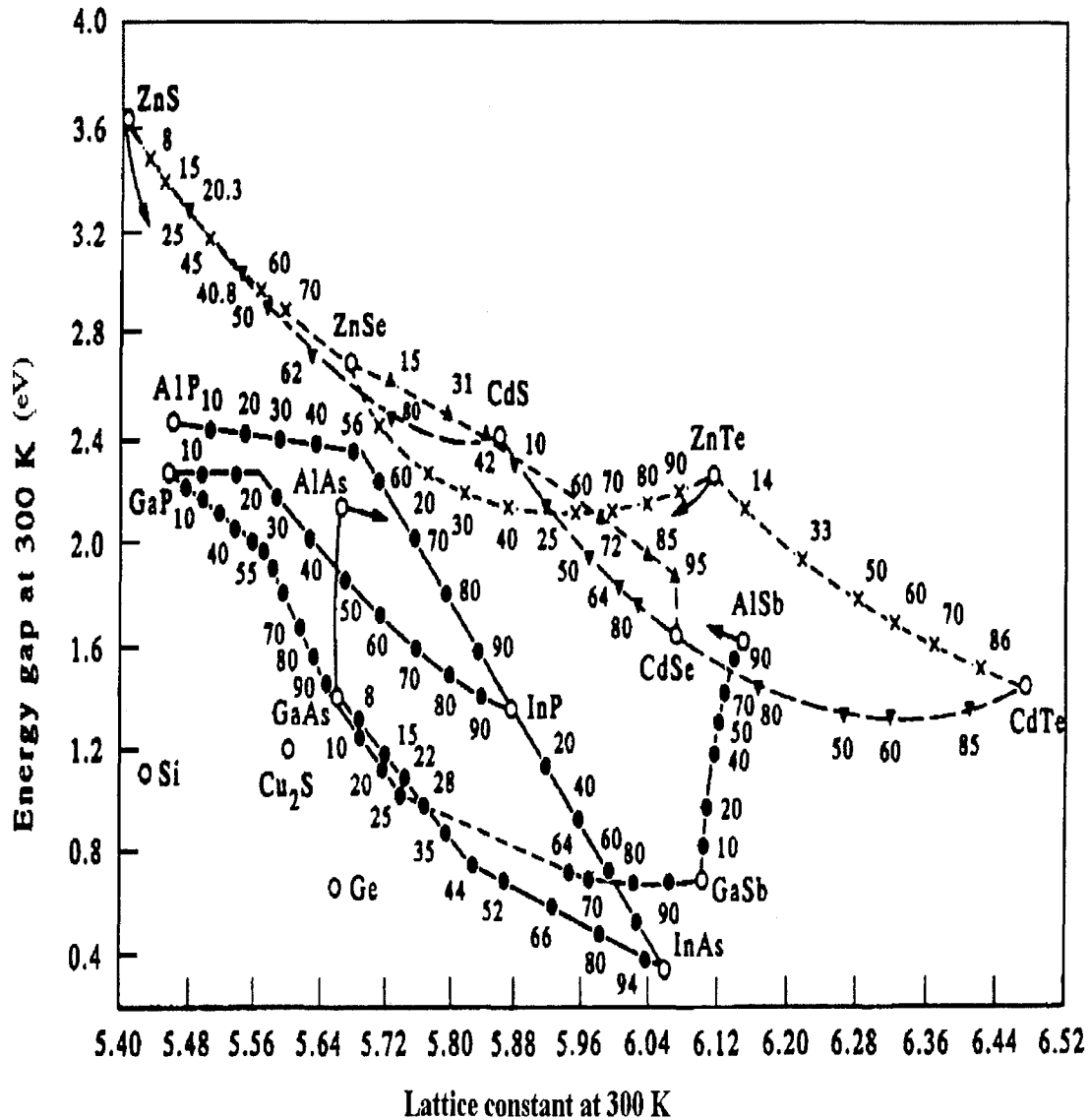
Figure II-3. Energy gap (300 K) vs. lattice constant for compound semiconductors.
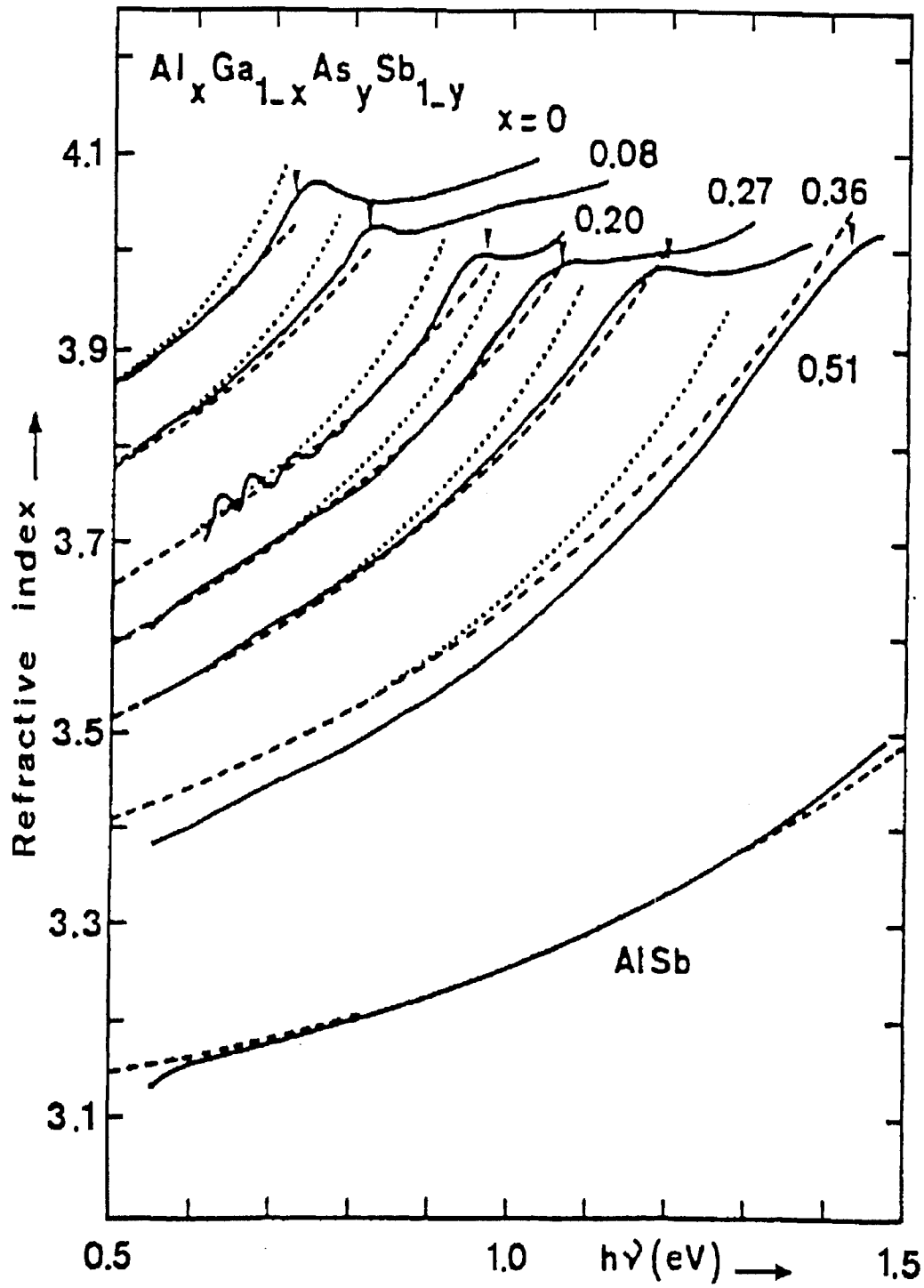
Figure II-4. Measured refractive indices at 300 K vs. photon energy for AlSb and $Al_xGa_{1-x}As_ySb_{1-y}$ layers lattice-matched to GaSb (y~0.085x). Dashed and dotted lines are calculated.

Band structure of GaSb
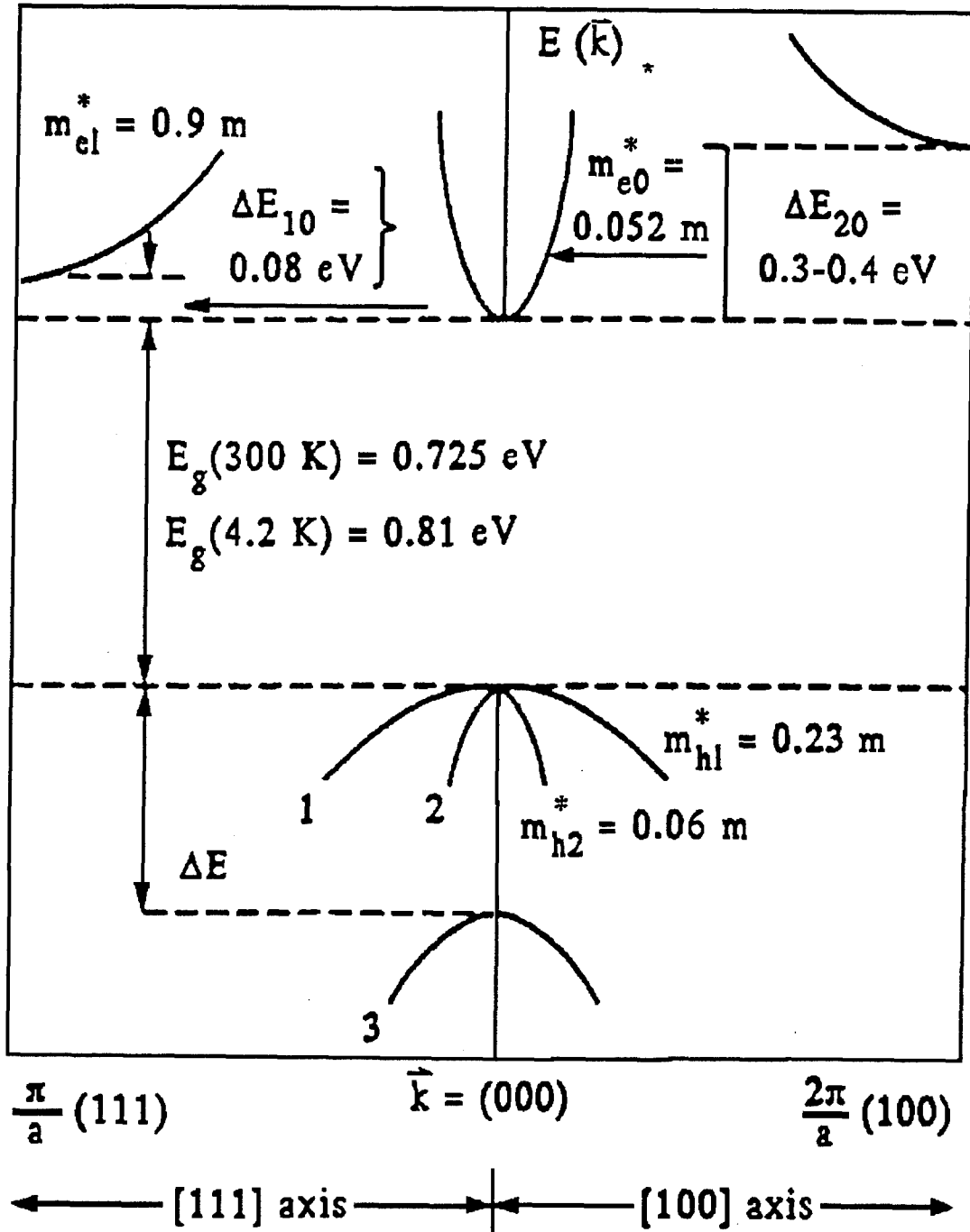
Figure II-5. E vs. k energy band diagram of GaSb at 300 K.
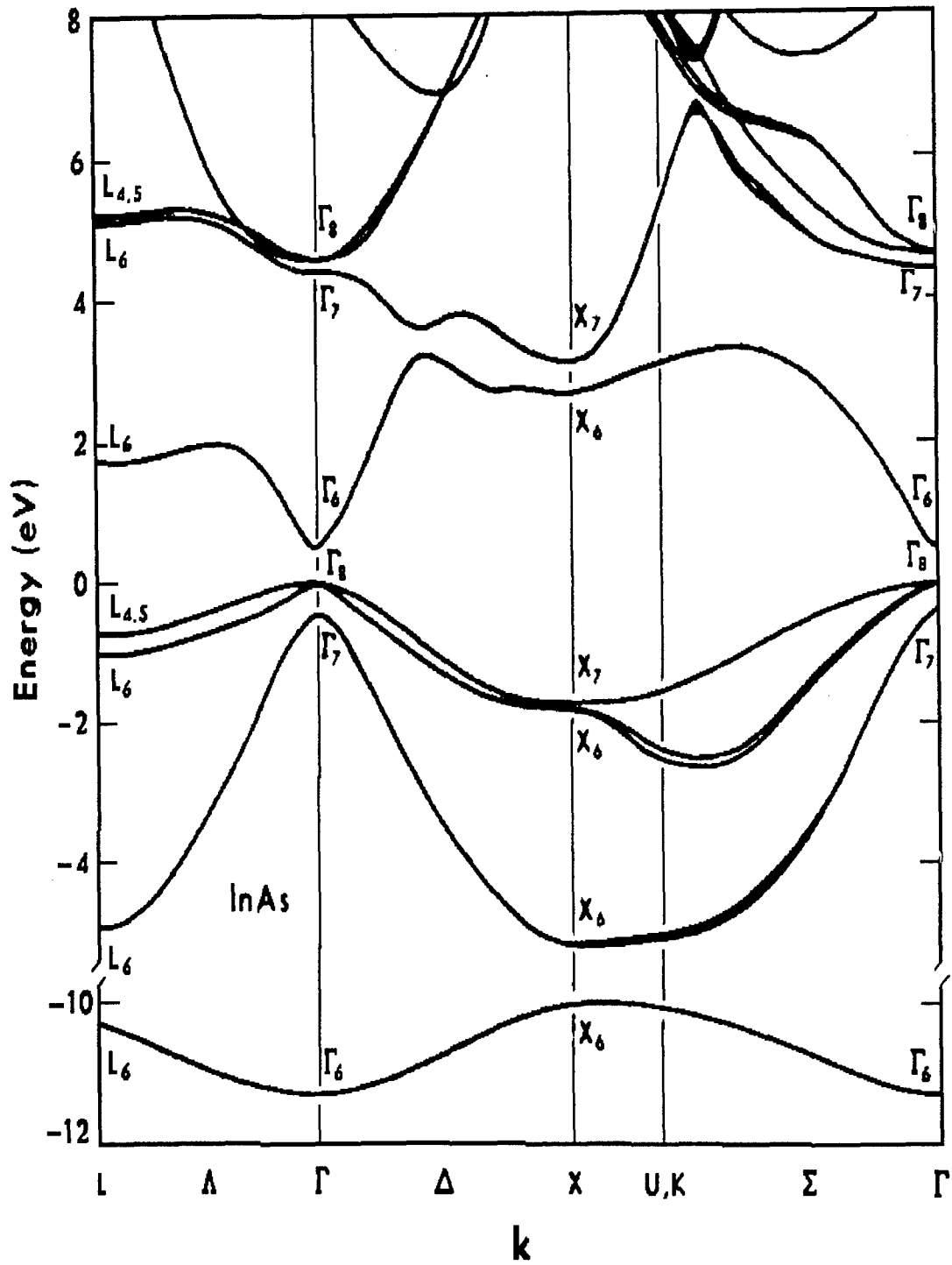
Figure II-6. E vs. k energy band structure of InAs.
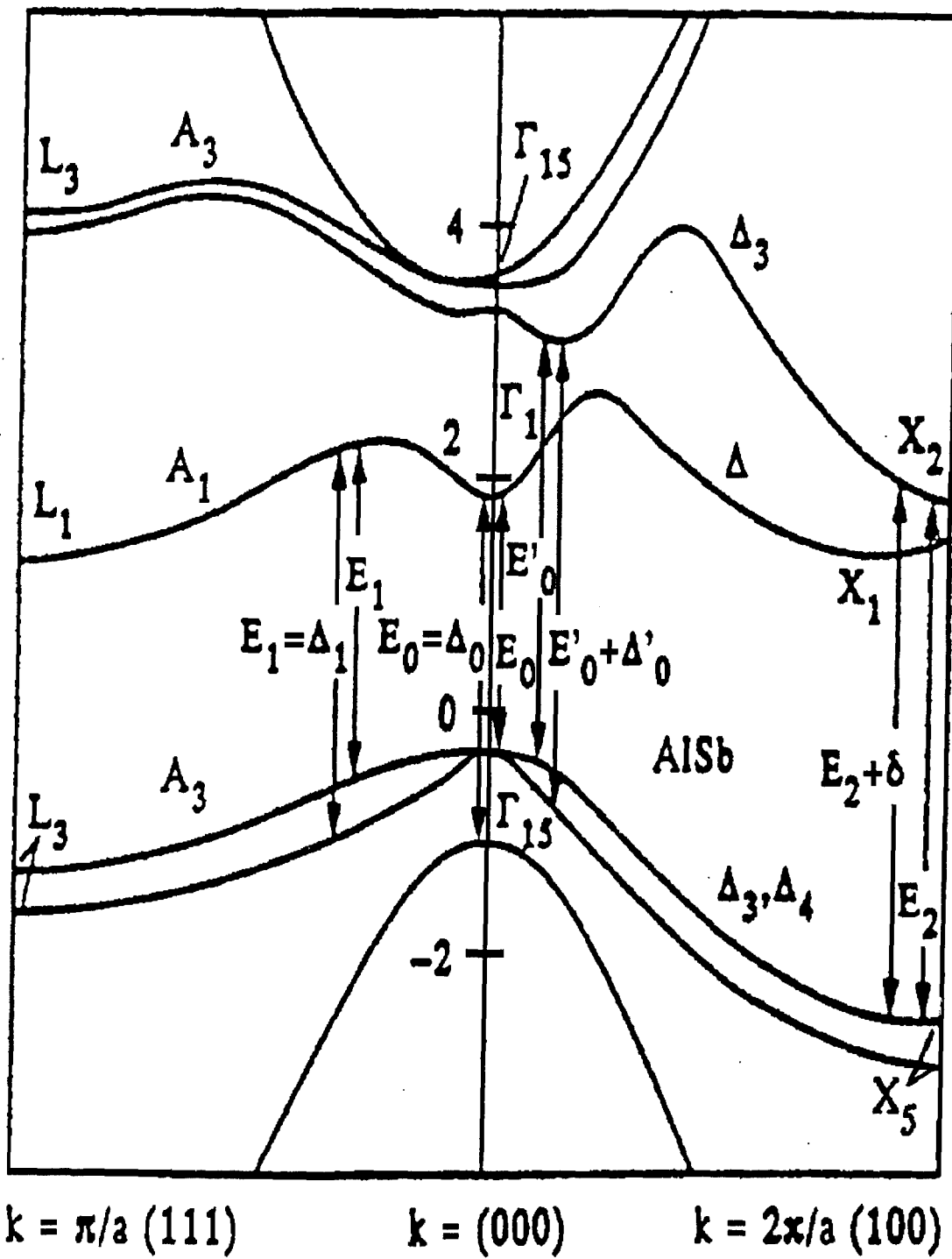
Figure II-7. E vs. k energy band diagram of AlSb.
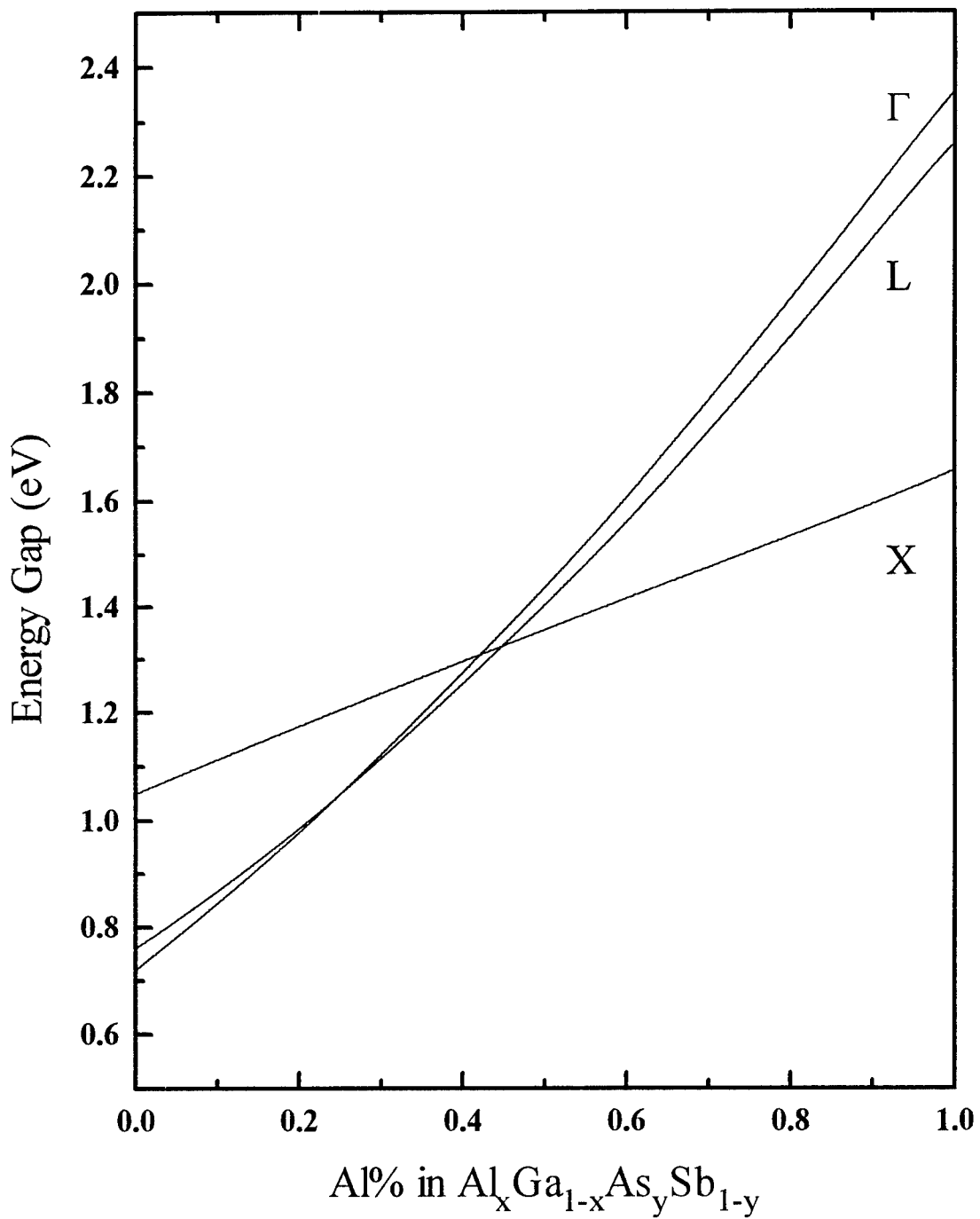
Figure II-8. Variation of X, L and Γ band minima as a function of Al content of $Al_xGa_{1-x}As_ySb_{1-y}$.

Laser-Diode Characteristics

Laser-diodes using quantum-well heterostructures have the advantage that recombination proceeds from a block of electrons all in a nearly fixed energy with a similar block of holes also at a nearly fixed energy. In either p-n homojunctions or wide wells, referred to as double heterojunctions, the recombining carriers are distributed in energy over parabolically varying densities of states. The density of states are small at the band edges, so that substantial recombination of higher energy electrons and holes can occur, broadening the luminescent line width. The arrangement of density of states also favors quantum well systems to reach equilibrium faster after carriers are injected. Carriers injected in a sample at high energy scatter downward in energy (thermalize) to ultimately a lesser density of states at a rate dependent on the final density of states. The constant density of states regions of a quasi-two dimensional quantum-well system has a distinct advantage over the decreasing density of states encountered in a bulk semiconductor. Carrier thermalization from the higher energies of the cladding layer to the energy of the well proceeds more efficiently since the rate depends on the final density of states.

Carriers will diffuse to the narrow gap material, then recombine radiatively if the narrow gap material is wide enough for carrier thermalization to occur in the active region. Electrons injected into a well scatter and lose energy primarily by emitting longitudinal optical (LO) phonons (Holonyak *et al.*, 1979:502–505). The scattering rate determines the minimum thickness of the well. Figure II-9 shows the calculated energy distributions of electrons reaching the far side of a well for GaAs/AlGaAs. The cross-hatched curve is the distribution of carrier energy of the photogenerated electrons in the

barriers. Curve (a) shows that the energy distribution of electrons injected into a well 200 Å wide is much closer to the bottom of the well than the energy distribution of electrons injected into wells of the other thicknesses listed. When the electron distribution peaks near the L indirect minima, the luminescence is quenched (Dupuis *et al.*, 1978:531-533).

The efficiency of the thermalization of carriers from the cladding layer to the active region can be measured by determining an effective capture cross section for the well. This can be done by looking at the DLTS response as a function of filling pulse width (Jiao and Anderson, 1993:271–276). At very short filling pulses, only a fraction of the quantum states in the well will be filled, and the DLTS response will be much smaller. At some point, the response will saturate. The capture rate of electrons into the well, r_{cn}, is proportional to the electron concentration in the barrier, n_B, and to the empty states in the well, n_w,

$$r_{cn} = \langle v_{th} \rangle X n_B \, n_w \, ,$$

where $\langle v_{th} \rangle$ is the average thermal velocity of electrons, and X (cm^2) is a capture cross section related to the scattering rate of the carriers into the well.

At equilibrium, the well fills until the diffusion potential prevents further filling. The carrier density in the well is determined by integrating the product of the density of states and the distribution function over the allowed energy. The density of states in two dimensions is given by

$$g = \frac{m^*}{\pi \hbar^2} \, ,$$
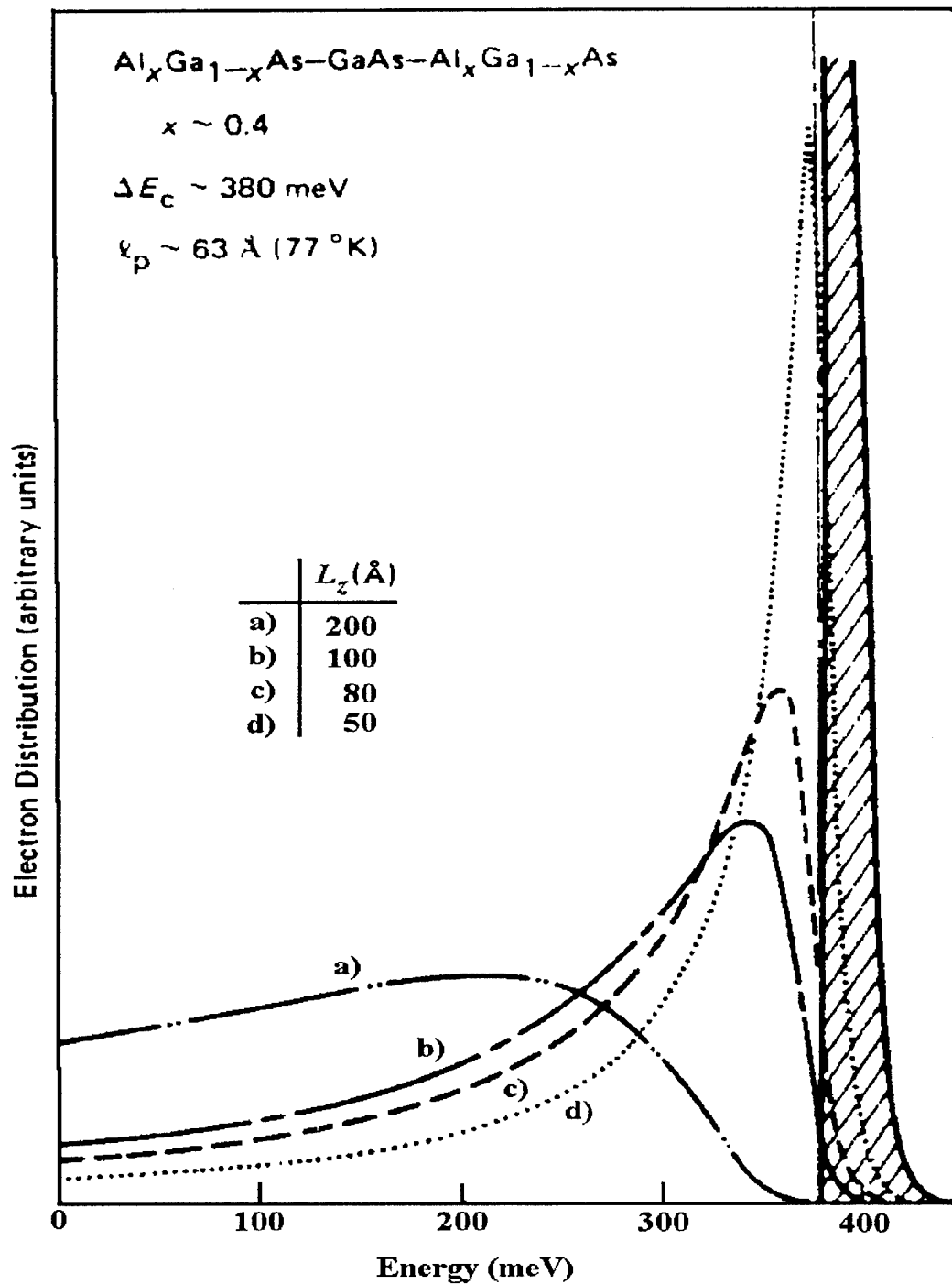
Figure II-9. Calculated energy distributions of electrons diffusing a distance L_z and scattering into a GaAs quantum well between two $Al_xGa_{1-x}As$ (x=0.4) barriers. The curves are normalized. The cross-hatched curve represents the initial distribution of the photogenerated electrons in the confining layers.

so that each discrete energy, E_i, that is determined as an eigenstate of the square well potential with k-vector perpendicular to the plane of the well, increases the number of states by g. States with energies other than E_i are available for confined carriers that have a component of their k-vector parallel to the plane of the well. The carriers are distributed among the states according to Fermi-Dirac statistics. The integral then becomes

$$n_w = \int_0^\infty \frac{m^*}{\pi\hbar^2} \frac{1}{1 + \exp\left(\dfrac{E - E_f}{kT}\right)} dE$$

with the solution

$$n_w = \frac{m^* kT}{\pi\hbar^2} \sum_i \left\{ \ln\left[1 + \exp\left(\frac{E_i - E_f}{kT}\right) \right] - \frac{E_i - E_f}{kT} \right\} .$$

This function is plotted for two confined states at the bottom of a well in Figure II-10. The temperature used was 150 K and the effective mass was 0.03m*. At higher temperature there is a smaller difference between the maximum and minimum concentrations, and an increase in the occupation of higher energy states. This shows that, for deep enough wells, measurable emission from states other than the ground state can take place. However, the condition must be met that the states higher in the well must be sufficiently filled at a temperature low enough to observe the emission.

<u>Problems and Limitations</u>

The main problems with low band gap materials are considered to be loss of carriers by free-carrier absorption, and Auger recombination. A laser can operate as long as the lifetime of non-radiative recombination processes aren't shorter than the stimulated
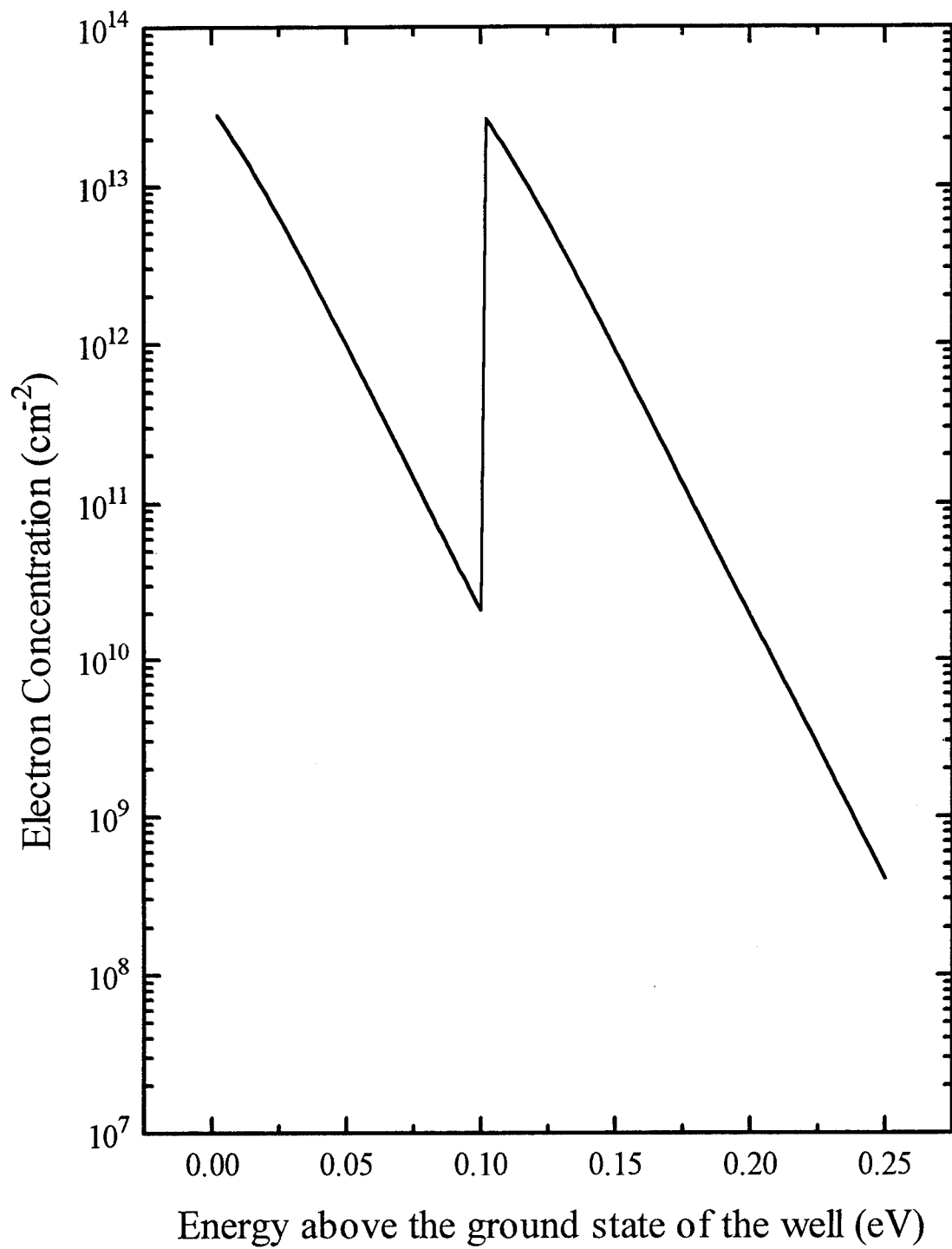
Figure II-10. The product of the density of states in two dimensions and the distribution function for an arbitrary effective mass of 0.03m*, a temperature of 150 K, and a first excited state 10 meV above the ground state.

radiative recombination lifetime. Deep levels can also present non-radiative paths that limit the carrier lifetime.

Of the nonradiative processes, band-to-band Auger transitions have the greatest temperature dependence. The high temperature limit may therefore be established by Auger effects, and aggravated by junction heating. The temperature dependence for Auger limited lifetime can be seen in the equation for the electron-hole (e-h) pair lifetime,

$$\tau_A \propto \left(\frac{E_g}{kT}\right)^{\frac{3}{2}} \exp\left[\frac{(1+2M)}{(1+M)}\frac{E_g}{kT}\right],$$

where M is the ratio of the electron to hole effective mass. $M=m_e/m_h$ if $m_e<m_h$, and τ_A is dominated by electron-electron collision, and $M=m_h/m_e$ if $m_h<m_e$, and τ_A is dominated by hole-hole collision (Beattie and Landsberg, 1958:16). The dependence on the gap of the material also shows that the narrow gap material should be particularly susceptible to Auger processes. Since the Auger recombination rate is also sensitive to the carrier concentration, determining the rate of photon loss by Auger recombination as a function of carrier concentration is not definitive without a study of the emission kinetics, because radiative recombination may also obey the same statistics.

Some of the band-to-band Auger processes in direct-gap semiconductors are shown in Figure II-11. Other Auger processes can involve conduction band to light hole band, or conduction band to split-off band transitions, rather than the band to band transitions denoted in the figure. The first two letters refer to the initial and final states of one particle, and the second two letters refer to the second particle taking place in the Auger process. C refers to the conduction band, H refers to the heavy hole band,
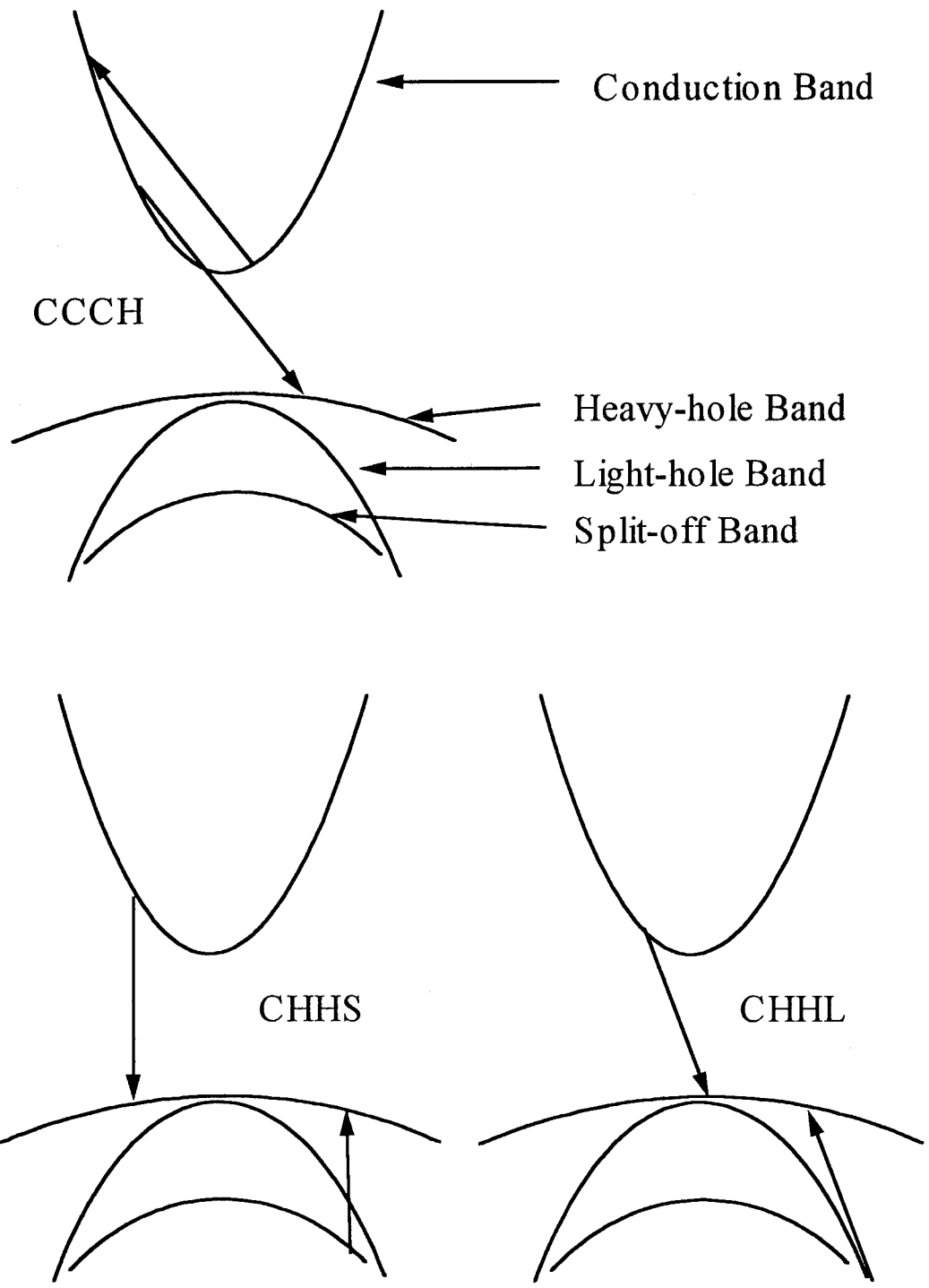
Figure II-11. Band-to-band Auger processes in direct band-gap material. The four letters that identify each process, taken in pairs, indicate the initial and final band for the two particles taking place in the Auger process.

L refers to the light hole band, and *S* refers to the split-off band. This figure shows that a number of processes can be involved in Auger carrier recombination. Low gap materials such as InAs, with the split-off band separated from the valence band maximum by an energy approximately equal to the band gap, are particularly susceptible to Auger processes involving the split-off band. For example the CHHS process involving a conduction band to heavy hole transition, and a heavy hole to split-off transition. By using the band-structure parameters such as the energy gap at zero doping, heavy-hole mass, light-hole mass, dielectric constant, spin-orbit coupling, and conduction-band mass, the band-to-band Auger rates can be related to a nonradiative e-h pair lifetime τ_A by the relation $R = N/\tau_A$ where N is the injected carrier density and R is the total Auger rate. Equations for R are given for each of the processes in Figure II-11 by Nelson and Dutta (Nelson and Dutta, 1985:16–25). The effect of Auger processes on the threshold current of a diode laser is reflected by T_o in the temperature sensitivity of J_{th}, as given by $J_{th} = J_o exp(T/T_o)$.

Another loss mechanism is by free-carrier absorption, where the photon energy is lost by creating a hot electron. The absorption within the band takes place with the assistance of phonons or scattering from ionized impurities. The scattering source can be determined by the exponent of the wavelength λ in absorption experiments. For example, scattering by acoustic phonons leads to an absorption increasing as $\lambda^{1.5}$, optical phonons as $\lambda^{2.5}$, and scattering by ionized impurities as λ^3 or $\lambda^{3.5}$. The actual scattering will be a weighted average of the three processes, with the dominant mode depending on the

impurity concentration. A rough expression for the free-carrier absorption coefficient, assuming a wavelength exponent of two, is

$$\alpha_f = \frac{Nq^2\lambda^2}{m^* 8\pi^2 nc^3 \tau},$$

where N is the carrier concentration, q is the charge of an electron, m^* is the effective mass, n is the index of refraction, and τ is the relaxation time (Pankove, 1971:74–76).

In addition to free-carrier absorption and Auger recombination carrier loss mechanisms, the non-radiative recombination rate through deep levels is also very important and needs to be determined. The first half of this work concentrates on characterization of the deep levels in order to determine the non-radiative recombination rates.

<u>Deep Level Effects</u>

Interest in the deep levels is primarily for their effects on device degradation by providing efficient nonradiative recombination centers, and reducing the effective carrier concentration. Recombination via a deep level can be either radiative or non-radiative, but will most likely be non-radiative if the defect has strong coupling to the lattice. The efficiency of a recombination center can be seen from equation [II-1] for the occupancy factor of a level available for recombination,

$$f = 1 / \left[1 + \left(\frac{N_c}{g_n} \right) \exp\left(\frac{-E_A}{kT} \right) \right] \qquad [\text{ II-1}]$$

where N_c is the density of states (in the conduction band in this case), g_n is the degeneracy factor, k is Boltzmann's constant, T is the temperature, and E_A is the activation energy of the trap. Recombination is a two step process. First the deep level must capture a carrier

from one band, then the deep level must capture a carrier of the opposite charge from the opposite band. These two processes can take place at different rates. The rate limiting step for recombination is then limited by the larger of the two energies between the level in the gap, and either band edge. Deep levels toward the middle of the gap will result in comparable capture rates from either band, and therefore are the most efficient recombination centers. For example, midgap levels in GaP (E_g=1.9 eV) located at ~1.1 eV from the band edge can dominate the behavior at very low concentrations, possibly even at $10^{12} - 10^{14}$ cm^{-3} (Willardson and Beer, 1983). This can be shown more directly by Shockley-Read-Hall statistics. The lifetime τ of excess charge carriers in a semiconductor with a single impurity level is given by

$$\tau = \frac{c_p\left(p_0 + p_1\right) + c_n\left(n_0 + n_1\right)}{c_n c_p N_T\left(n_0 + p_0\right)},$$

where n refers to conduction band electrons and p refers to valence band holes, c_n and c_p are the capture rates, n_0 and p_0 are the free-carrier concentrations at thermal equilibrium, and n_1 and p_1 are the free-carrier concentrations for the case in which the Fermi level is at the same energy as the trap (E_f=E_T). N_T is the concentration of deep levels. For a p^+–n junction, the equation for lifetime reduces to

$$\tau = \frac{n_1}{N_T c_p n_0}.$$

Since n_1 is a function of the energy position of the impurity level relative to the Fermi level, the free-carrier lifetime changes exponentially with E_T.

The significance of deep level energy position on the free-carrier lifetime can be shown by the ratio of lifetimes due to two different trap energies

$$\frac{\tau(1)}{\tau(2)} = \frac{c_p(2)N_T(2)}{c_p(1)N_T(1)} \exp\left(\frac{E_T(1) - E_T(2)}{kT}\right),$$

where $\tau(1)$ and $\tau(2)$ are the free-carrier lifetimes due to trap levels (1) and (2), respectively. $N_T(1)$ and $N_T(2)$ are the total trap concentrations of trap levels (1) and (2), respectively. For the same values of capture rates and $E_T(1) > E_T(2)$, the ratio is much larger than unity as long as $n_i(1)N_T(2) \gg n_i(2)N_T(1)$, where $n_i(1)$ and $n_i(2)$ are as defined above. For example, at room temperature a trap energy level difference of 0.4 eV, or at 77 K a difference of only 0.1 eV is enough for the lifetime of excess charge carriers to be determined by the trap that is closer to midgap even if its concentration is six orders of magnitude smaller than the concentration of the shallower trap level (Grimmeiss, 1977:341–376).

The deep level trapping center effects may be manifest in a change in switching times in devices such as photoconductors, and nonradiative recombination processes which can affect the efficiency of light-emitting diodes and lasers. In a study of AlGaAs/GaAs double-heterostructure lasers, a marked correlation has been found between the concentration increase of a hole trap and the threshold current increase in degraded lasers (Uji *et al.*, 1980:655–657). The trap responsible for the threshold current increase was found to be 0.24 eV from the valence band in the *n*-AlGaAs passive layer and led to slow long-term degradation of the device.

Current Laser Diode Progress

Several researchers have made use of the GaSb-based alloy system to design laser devices operating within the wavelength range of 0.8–2.3 µm which includes atmospheric transmission windows, and the useful optical fiber wavelengths of 1.3–1.55 µm. A brief survey of recent state of the art achievements is described below with benchmarks such as the threshold current densities for lasing. The values obtained are comparable to what is available for GaInAsP/InP lasers: ~1 kA/cm^2 operating at 1.3 µm.

Oscillation at 2.07 µm was achieved by optical pumping for a $Ga_{0.85}In_{0.15}As_{0.13}Sb_{0.87}$ active layer with $Al_{0.4}Ga_{0.6}As_{0.035}Sb_{0.965}$ confining layers grown by molecular beam epitaxy (MBE) on GaSb (van der Ziel et al., 1986:4087). Initial success was achieved with diode structures grown by liquid phase epitaxy (LPE) allowing injected current. Operation at 2.2 µm at room temperature for structures grown by LPE started with a requirement of a threshold current of about 8 kA/cm^2. Improvements were made by using an active layer of $Ga_{0.84}In_{0.16}As_{0.15}Sb_{0.85}$ and confining layers of $Al_{0.34}Ga_{0.66}As_{0.04}Sb_{0.96}$, cutting the 290 K threshold current densities to 3.5 kA/cm^2 (Caneau et al., 1986:992). In the following year, the same group, using the same material composition, obtained a threshold current of 1.7 kA/cm^2. Continuous wave (CW) operation of LPE lasers with higher Al content confining layers was demonstrated at room temperature by Bochkarev et al. (Bochkarev et al., 1988:1362). The MBE method was used to grow $Ga_{0.84}In_{0.16}As_{0.14}Sb_{0.86}/Al_{0.5}Ga_{0.5}As_{0.04}Sb_{0.96}$ lasers of 0.4 µm thick active layer, operating with a threshold current density of 1.7 kA/cm^2 and differential quantum efficiencies of 18% per facet (Eglash et al., 1991:669). Further work by these same

researchers has demonstrated high-performance GaSb-based diode lasers with threshold current densities of only 260 A/cm^2 and CW output power of 190 mW/facet using quantum well structures. It was found that high aluminum content cladding layers were required for the degree of electrical and optical confinements needed.

Many of the techniques used in GaAs lasers to improve performance have not yet been investigated in the GaInAsSb injection laser. For example, quantum well laser structures had not been used extensively, and graded index confining layers, which could improve the line width and efficiency, had not been used (Baranov, 1991:2360).

III. EXPERIMENT

The quantum well has become a primary engineering tool for state of the art semiconductor optoelectronic devices. Fundamental to the design are the band offsets, which have not been systematically determined for this GaSb-based system. The band offsets have been determined for a few semiconductor pairs by various techniques such as DLTS, C-V, admittance, I-V-T, optical absorption, and photoluminescence. The number of analyses of heterostructures by DLTS has been steadily increasing over the last ten years since the adaptation of DLTS from analyzing bulk defects to analyzing single quantum wells.

The goal here is to determine the parameters in the $Ga_xIn_{1-x}As_ySb_{1-y}/Ga_xAl_{1-x}As_ySb_{1-y}/GaSb$ system to allow quantum well design for tailored electrical and optical device characteristics. DLTS is the primary method used to determine band offsets in this work. Variable temperature Hall measurements, C-V profiling, and I-V-T measurements are also made in support of the DLTS measurements. There can be several sources of signal other than the well for the capacitance transients that are measured. They are the interface states at the heterojunction, bulk (uniformly distributed) levels from native defects or impurities in the well and confining layers, and mismatch induced defects extending away from the interface. Ideally, each of these should be physically isolated and identified.

Bulk Defects

In order to separate the well signal from any signal from the ordinary deep levels or interface states located at the heterojunction, DLTS on the individual material will need to be accomplished. The defects in the bulk cladding and barrier materials are characterized in heterojunction structures where the depletion region can be swept through the heterojunction. The traps in the well material are characterized in a structure grown with a thick layer of the well material. The objectives are to identify signals that may show up when the DLTS spectra from a QW are measured, and identify non-radiative recombination centers in the well and traps in the barrier.

Theoretical Aspects of Deep Level Energies and Capture Cross Sections

The energy levels of deep levels can be determined for simple defects such as a single vacancy using the tight binding method. A general method of applying the tight binding method uses the Green's function method, which can in principle give exact results for a given defect perturbation potential (Lannoo, 1981:68–112). A brief description of the method will be given here, and then some general observations of trends based on calculations using this method. More elaborate calculations focus on many-electron effects.

In the tight-binding approximation, the wave function is expanded using a basis formed by the free-atom eigenstates. This is also known as the linear combination of atomic orbitals (LCAO) method. The solution of Schrödinger's equation can be expressed in terms of the matrix elements of the Hamiltonian

$$H_{i\alpha,j\beta} = \left\langle \chi_{i\alpha} | H | \chi_{j\beta} \right\rangle,$$

where $\chi_{i\alpha}$ is the αth state of atom i. The atomic orbitals of different atoms are not orthogonal in general. Calculation of the overlap integrals by finding the roots of

$$\det \left| H_{i\alpha,j\beta} - \varepsilon S_{i\alpha,j\beta} \right| = 0$$

is difficult because it converges slowly. The tight-binding approximation is to neglect all overlap integrals. In practice, it has mainly been used to reproduce some known experimental properties by adjusting the Hamiltonian matrix elements and then use the Hamiltonian to predict other physical properties.

Hjalmarson used a Koster-Slater model in an orthogonalized-tight-binding function basis to predict which elements of the periodic table are likely to form substitutional A_1-symmetric traps with energy levels deep in the band gap of covalently bonded semiconductors (Hjalmarson, 1980:810–813). Koster-Slater is the model generally used for substitutional impurities. From their calculations, they determined a conceptual framework for understanding the major chemical trends in deep-trap energies. They found that substitutional deep trap energies are asymptotic to the dangling-bond energies, so that no traps exist deeper than the dangling-bond energy. Since the dangling-bond energy is a property of the host lattice, the deep-trap wave function is predominantly host-like rather than impurity-like. This explains why impurities whose atomic energies differ by ~10 eV may produce trap energies differing by only a fraction of an electron volt. Another property of deep levels is that they couple to distant energy bands as the composition changes, not following the nearest band edges as shallow impurity levels do. Another

general trend is that bonding-antibonding splitting associates a filled, electrically inactive level in the valence band with every deep electron trap within the band gap. The electronic structure of the deep level is determined by its orthogonality to the lower level. A diagram of the model is given in Figure III-1 showing the calculated perturbations for a nitrogen impurity in a GaP lattice: the deep trap in the gap, and the state in the valence band. The dangling bond energies associated with Ga and P in GaP are shown on the far left next to the conduction and valence band energies of the crystal (ε_{Ga} and ε_P respectively). Similarly, the dangling bond energies associated with Ga and N in GaN are shown on the far right (ε_{Ga} and ε_N respectively). Then the two energy levels of nitrogen in GaP are shown. One is the hyperdeep trap level within the valence band of GaP and the other is shown with a binding energy less than the dangling bond energy of gallium.

In addition to the energy of the trap, another parameter that characterizes a deep level is the capture cross section. This refers to the distance from a trap at which a free carrier will be captured, if it approaches within the radius of the cross section. It can be roughly approximated by the point where the Coulomb attraction is equal to the thermal energy, kT, or

$$\frac{e^2}{r\varepsilon} = kT,$$

where e is the charge of the electron, r is the radius of the capture cross section, and ε is the dielectric constant. For AlAsSb with a dielectric constant of ~10, the corresponding capture cross section would be 10^{-12} cm^2 at room temperature. Actual capture cross sections for various materials range from 10^{-11} to 10^{-22} cm^2, showing that different
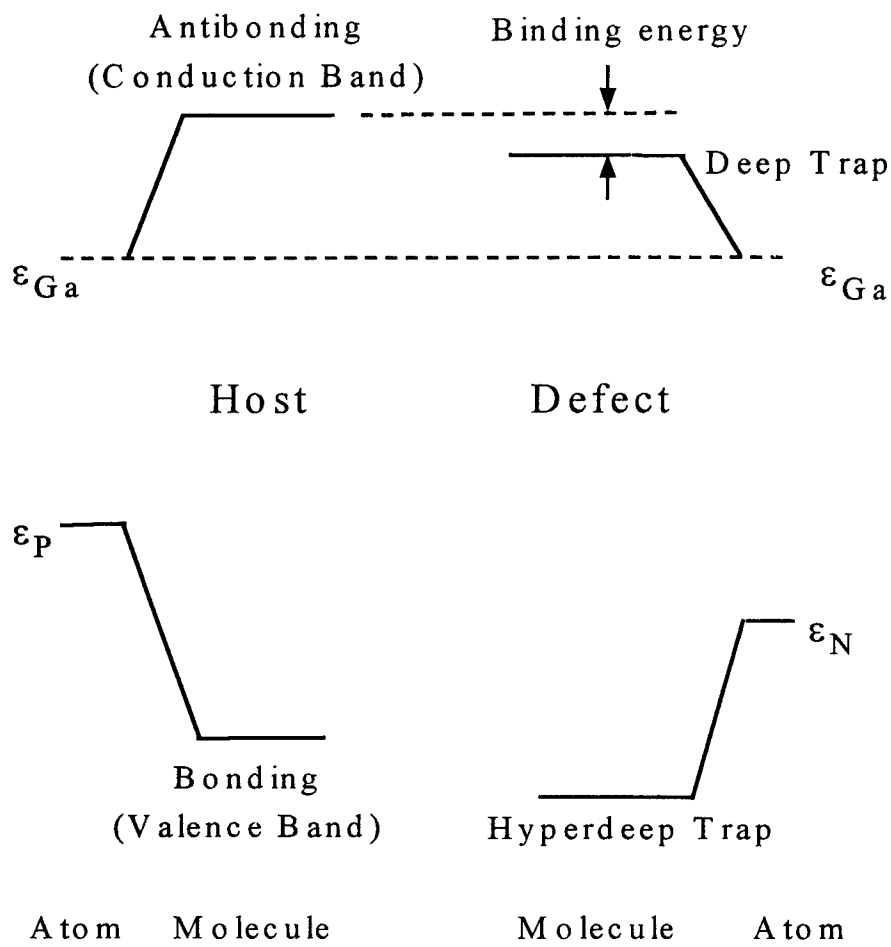
Figure III-1. Two-state model, schematically showing the atomic energy levels of Ga, P, and N, and the corresponding bonding and antibonding levels.

mechanisms other than this simple picture affect the capture process. The reason for such a wide range of capture cross sections is that the defect can take on a potential that deviates from a pure Coulombic potential. Two capture processes will be discussed later in this section in more detail. The importance of the capture cross section is its influence on the free carrier lifetime in devices, approximated by

$$\tau = \frac{1}{\langle v \rangle \sigma N_T},$$

where $\langle v \rangle$ is the average thermal velocity, σ is the capture cross section, and N_T is the trap concentration.

The wide range of capture cross sections and trapping center concentrations result in a wide range of recombination rates. A more complete relationship between the recombination rate U, and the trap characteristics is given by

$$U = \frac{\sigma_p \sigma_n v_{th} \left(pn - n_i^2 \right) N_T}{\sigma_n \left[n + n_i \exp\left(\frac{E_T - E_i}{kT} \right) \right] + \sigma_p \left[p + n_i \exp\left(-\frac{E_T - E_i}{kT} \right) \right]},$$

showing the dependence on the trap depth, E_T, and the capture cross section for trapping from the conduction band, σ_n, and the valence band, σ_p. E_i is the intrinsic Fermi energy, k is Boltzmann's constant, T is the temperature, p is the density of holes, n is the density of electrons, and n_i is the intrinsic carrier concentration. The two exponential terms in the denominator show that the most effective recombination centers are near mid-gap.

What is not shown in the equation is the explicit temperature dependence of the capture cross sections. The manner in which the trapping energy is dissipated is reflected in the magnitude and temperature dependence of the capture cross section. The energy can be dissipated as phonons or through a lattice relaxation, the energy can be transferred to another charge carrier, or a photon can be given off. Terminology used in describing the mechanisms are multi-phonon emission, Auger, and cascade capture. Of course, combinations of each mechanism can also take place.

A graphical description of a trap is given by the configuration-coordinate diagram shown in Figure III-2. This is a plot of the elastic lattice and electronic energy versus real space position. E_e is the emission energy, E_c is the capture barrier, E_{oe} is the optical excitation energy and E_{oc} is the energy for radiative capture. U_c is the energy of an electron in the conduction band, U_T in the defect potential well, and U_v in the valence band. The curvature of each potential curve depends on the bond strengths and masses of surrounding atoms. The potential well for the lattice is given by

$$U\left(Q\right) = E_i(Q) + \tfrac{1}{2}M\omega^2 Q^2,$$

where Q is the lattice displacement position, E_i is the electron energy of the ith state, M is the atomic mass of a lattice atom or the reduced mass of lattice atoms in compound semiconductors, and ω is the vibrational frequency. A lattice relaxation can be shown experimentally by an energy difference in optical emission and absorption measurements, or by thermally stimulated transition measurements. When a lattice relaxation is required for capture, the binding energy of the deep level is increased by the product of $\hbar\omega$ and the Huang-Rhys factor S, which is related to the number of phonons involved in a transition. In optical emission transitions, the increase is known as a Franck-Condon shift. The magnitude of the relaxation that takes place when the trap is full can determine what transitions are possible. It is instructive to look at the result of various lattice relaxations. If the lattice relaxation is large enough to shift the defect potential energy curve U_T farther to the right so that the intersection Q_c with the conduction band curve is to the right of $Q=0$, then the optical emission transition E_{oc} can't take place at all. Conversely, very small lattice relaxations such that the minima of curves U_c and U_T coincide allow capture only by

optical means, resulting in very small capture cross sections. If capture can take place into the minimum of curve U_T via excited electronic states represented by the set of horizontal lines on curve U_T, the capture can be described as a cascade process.
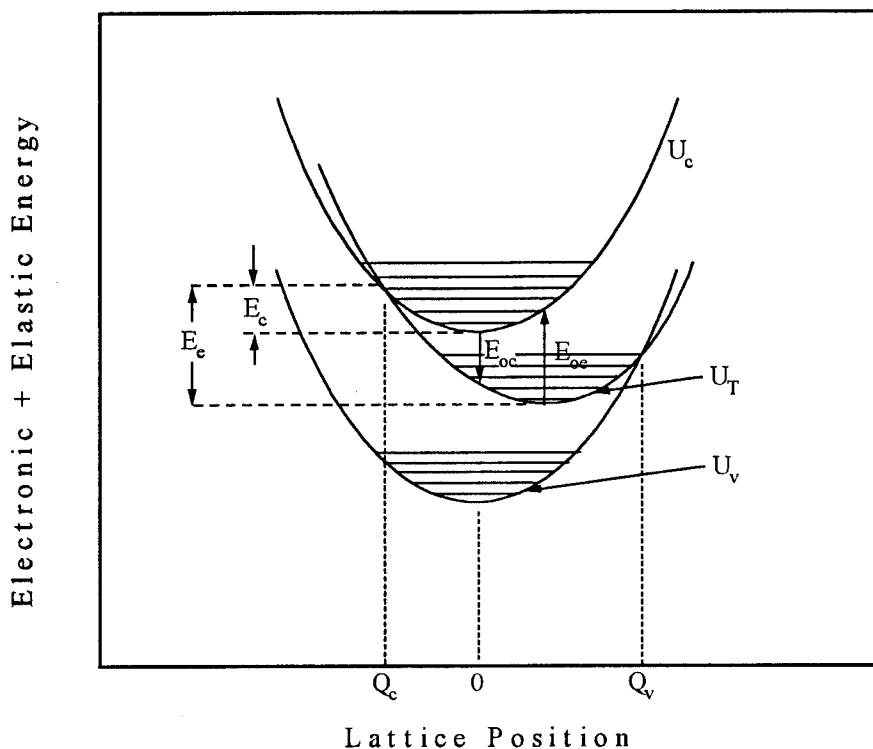
Figure III-2. Configuration coordinate diagram for the electronic and vibrational energy levels for a defect that requires a lattice relaxation for capture of a charge.

The configuration coordinate diagram is used to describe one of the more commonly reported temperature dependent capture cross sections. Capture that dissipates the excess energy by multi-phonon emission (MPE) was proposed by Henry and Lang (Henry and Lang, 1977:989). As an example, they work through the capture of an

electron by a neutral impurity. The spherical potential well is described by a radius b equal to the nearest-neighbor distance, and potential depth V_o. The Hamiltonian of the system has three terms:

$$H = H_E + H_{EL} + H_L$$

$$H = \left[\frac{p^2}{2m^*} + V(r)\right] + BQV(r) + \left[\frac{P^2}{2M} + \frac{1}{2}M\omega^2 Q^2\right],$$

where H_E is the electronic Hamiltonian with $Q=0$, H_{EL} describes the change in the potential well depth by a lattice displacement Q, and H_L is the Hamiltonian of a harmonic oscillator vibrating about $Q=0$. The eigenfunctions of H_E for a free electron state at the bottom of the conduction band, a trapped electron, and a free electron state at the top of the valence band are given by $|c\rangle = \varphi_c(\vec{r})$, $|t\rangle = \varphi_t(\vec{r})$, and $|v\rangle = \varphi_v(\vec{r})$. The electronic energies of the states $i = c, v, t$ are given by

$$E_i(Q) = \langle i|\frac{p^2}{2m^*} + V(r) + BQV(r)|i\rangle.$$

For a free electron state, the energy is independent of Q so that the matrix elements involving overlap of the conduction band or valence band states with the lattice displacement Q are negligible. However, the matrix element involving the lattice vibration and the eigenfunction of the trapped electron may be large.

Capture by multi-phonon emission implies that the defect is strongly coupled to the lattice. The thermal activation of the capture process is given by

$$\sigma = \sigma_\infty \exp\left(\frac{-E_c}{kT}\right).$$

The energy E_c is the height of the capture barrier, σ_∞ is the capture cross section at high temperature. The availability of phonons increases with increasing temperature, making this a predominant capture mechanism at higher temperatures.

The capture cross section can be determined by dividing the average value of the transition probability by the flux J, which is equal to the thermal velocity divided by the total volume, $\langle v \rangle / \Omega$. The transition probability, P_k, is obtained from the matrix elements of the non-adiabatic Hamiltonian operator, H^{NA} (Borgoin and Lannoo, 1983:188–193).

$$P_k = \frac{2\pi}{\hbar} A v_m \left| \left\langle \psi_{ek} \chi_{km} \left| H^{NA} \right| \psi_{ed} \chi_{dn} \right\rangle \right|^2 \delta\left[(p+m-n)\hbar\omega \right]$$

$A v_m$ is the thermal average over the vibrational quantum number in the initial state. ψ_{ek} is the electron wavefunction in the conduction band, ψ_{ed} in the defect potential, and χ_{km} and χ_{dn} are the harmonic oscillator wave functions in the conduction band and the defect potential, respectively. k and d are the electron quantum numbers, n and m are integers representing the vibrational quantum number, and p is the number of phonons of frequency ω that are involved in the transition. There can be a number of different phonon frequencies taking place in the transition, so an average value needs to be taken over the range of phonon energies:

$$\overline{P}_k = \frac{2\pi}{\hbar} A v_m \left| \left\langle \psi_{ek} \chi_{km} \left| H^{NA} \right| \psi_{ed} \chi_{d,n+p} \right\rangle \right|^2 .$$

If the electronic wave function term can be separated from the harmonic oscillator wave function term, assuming that the electronic matrix element is independent of Q, then the average transition probability is

$$\overline{P}_k = \frac{2\pi}{\hbar} \left| \left\langle \psi_{ek} \left| H^{NA} \right| \psi_{ed} \right\rangle \right|^2 W_p.$$

Here W_p is the overlap of harmonic oscillator wavefunctions.

There are predictions for the temperature dependence of the capture cross section based on high and low temperature approximations for W_p. The low temperature range is defined by the condition that

$$\frac{S^2}{p} \overline{n}(\overline{n}+1) \ll 1,$$

with

$$\overline{n} = \left[\exp\left(\frac{\hbar\omega}{kT}\right) - 1 \right]^{-1}.$$

If $\overline{n}$ is smaller than one, then the inequality is satisfied for

$$\frac{\hbar\omega}{kT} \gg \ln\left|1 + \frac{S^2}{p}\right|.$$

Again, p is the total number of phonons between the trapped and free electron ground state energy levels, and S is the number of phonons emitted following optical emission, required to get to the ground state of the trapped electron potential. If the trap potential crosses the band potential at the minimum energy of the band potential, then this represents the case where $S=p$, which is the maximum that S can be. If $S^2/p \sim 1$, then $T \ll 600$ K is the low temperature regime. If $S \sim 1$, that is, for an optical transition with very little lattice relaxation, then T must be $\ll 3000$ K. This predicts that the low temperature limit would be valid for all traps measured by DLTS, although this is not always found to be the case experimentally.

In the low temperature limit, the capture cross section is given by

$$\sigma = \sigma_0 (\bar{n}+1)^p \frac{S^p}{p!} \exp\left[-2S\left(\bar{n}+\tfrac{1}{2}\right)\right] ,$$

with

$$\sigma_0 = \frac{2\pi}{\hbar\omega} \frac{\Omega}{\langle v \rangle} \left| \langle \psi_{ek} | H^{NA} | \psi_{ed} \rangle \right|^2 .$$

The high temperature region is reached if $p \gg 1$ and

$$\frac{4S}{p}\left[\bar{n}(\bar{n}+1)\right]^{\frac{1}{2}} \gg 1,$$

or

$$\frac{\hbar\omega}{kT} \ll \ln\left(1+\frac{4S}{p}\right) .$$

For a trap depth of 0.4 eV and a phonon energy of 40 meV, p would be equal to 10. S increases for large lattice relaxation. In this case the capture cross section is given by

$$\sigma \approx \sigma_0 \sqrt{\frac{\hbar\omega}{4\pi kTS}} \exp\left[-\frac{(p-S)^2 \hbar\omega}{4kTS}\right] .$$

For parabolic approximations for $E_k(Q)$ and $E_d(Q)$, the exponent

$$-\frac{(p-S)^2 \hbar\omega}{4S}$$

is equal to the capture barrier, E_c. In contrast, the exponent in the low temperature case is independent of T.

In spite of the low temperature regime being in the range of T<<600 K, capture barriers associated with the high temperature regime are observed in a wide variety of

materials for several deep levels. The source of the capture barrier may also introduce some complications. A capture barrier that is present as a result of screening of the empty trap by conduction electrons will also depend on carrier concentration and biasing conditions. Screening by adjacent core electrons may be expected to behave much differently.

Another mechanism that has a temperature dependence is cascade capture (Lax, 1960:1502–1523; Borgoin and Lannoo, 1983:185–188). Here, shallow excited states of a trap with a Coulombic potential act as intermediate states for capture into a deeper level of the trap center. As the temperature increases, the distribution of carriers in the excited states of the trap center shifts higher towards the band, making fewer carriers available for capture into deeper levels. This results in a decreasing capture cross section with increasing temperature, opposite to the behavior from capture by multi-phonon emission, so that this mechanism is observed only at low temperature.

The trapping occurs when a carrier within the capture cross section of a trap loses energy by emitting a phonon as shown in Figure III-3. If E_0 is defined as an electron energy before the collision, then the electron energy after the collision is $(E_0 - \hbar\omega)$. If the minimum energy of a free carrier is defined as zero, and the energy after a collision is negative, then the carrier is trapped. The number of trapped carriers will be proportional to the flux times the probability of capture within a sphere of radius r_0. Only states with a binding energy greater than kT will be able to trap carriers. Lowering the temperature permits initial trapping into states of larger orbit. The probability of capture is the same as the probability of a collision, which is the distance across the sphere divided by the mean
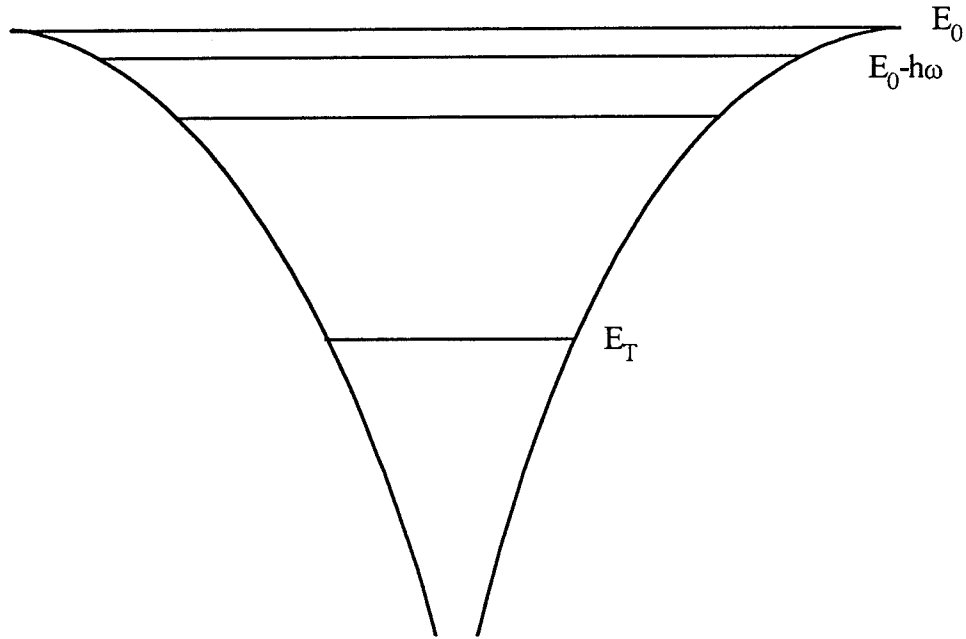
Figure III-3. Coulombic trap potential showing the trap energy E_T, the excited state energies, and the free electron energy E_0. Initial capture takes place into the excited state with binding energy $\hbar\omega$.

free path, $l(E_0, U)$, which is a function of the binding energy U. The cross section is then given by

$$\sigma\left(E_0, U\right) = \frac{4}{3}\frac{\pi r_0^3}{l\left(E_0, U\right)} \ .$$

In one case, if the mean free path is greater than the average distance across the sphere, $4r_0/3$, then at most one collision will occur within the sphere. Conversely, if the mean free path is much less than the average distance across the sphere, the trapping is said to be diffusion limited. In the study of recombination in gases, these two cases are modeled by the Thomson theory and the Langevin theory, respectively. The Langevin

recombination rate can be converted into a cross section on the order of 10^{-9} cm^2. This is considerably larger than any observed cross sections. Therefore, the mean free path must be typically larger than the average distance across the sphere.

Depending on the shape of the defect potential, the energy levels can be approximated by a continuum, allowing integration over all of the possible transitions. The capture cross section to a final state with binding energy U is determined by integrating over all U as

$$(E_0) = \int \sigma'(E_0, U) P(U) dU,$$

where $P(U)$ is the probability that the carrier reaches potential U before being emitted. The mean free path for collisions between carriers and acoustical or optical phonons is required to predict the capture cross section, which may be obtained from the temperature dependence of the mobility, through Hall effect measurements. What is desired at this point is the temperature behavior of cascade capture.

$P(U)$ is close to one when the binding energy is large ($U > 4\ kT$), corresponding to larger orbits, when compared to the average kinetic energy of incident carriers, kT. Then the largest trapping orbits will have states with energy $E_0 + U \sim 5\ kT$ required for emission. The corresponding radius of the sphere will then be

$$r_0 \approx \frac{1}{5kT\varepsilon}.$$

This results in an estimate of the capture cross section of

$$\sigma \approx \frac{4}{3} \frac{\pi}{(5kT\varepsilon)^3} \frac{1}{l}.$$

Coupling to acoustic phonons gives an overall temperature dependence of T^{-4}, which is close to some experimental observations. At ~5 K the radius is on the order of 10^4 Å, but drops off rapidly with temperature.

The magnitude and temperature dependence of the capture cross sections, whether capture occurs by cascade capture, multi-phonon emission, or some other mechanism, are related to the potential shape of the defect. A Coulombic center will have excited states available for intermediate transitions, and cascade capture may occur. However, deviations from that potential shape to one that changes more quickly, approaching a Dirac delta function, will reduce the number of excited states and put them at a larger energy difference from the ground state. The different potential cases are presented by the following picture of attractive, neutral, and repulsive centers.
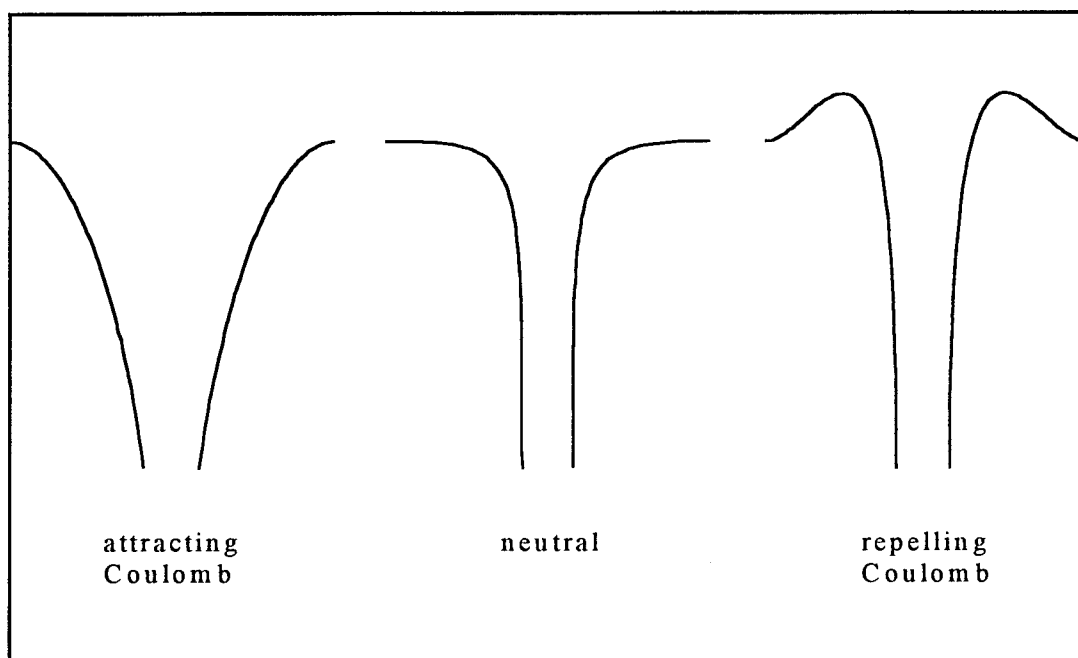
Figure III-4. Possible potential forms for variously charged defects.

A majority carrier trap that is charged when it is filled will be attractive to minority carriers and act as a non-radiative recombination center depending on the size of the emission rate for majority carrier emission, compared to the minority carrier capture rate. A survey of measured capture cross sections of traps of known charges by Lax indicates that the capture cross section for capture into different charge states can be divided loosely into different ranges (Lax 1960:1504). A repulsive center can have a capture cross section in the range from 10^{-24} to 10^{-21} cm^2. Attractively charged centers with Coulomb potential profiles tend to have very large capture cross sections in the range of 10^{-15} to 10^{-12} cm^2. Doubly or triply charged traps can have even larger cross sections. Neutral trap capture cross section ranges have been found to lie in the 10^{-17} to 10^{-15} cm^2 range with relatively little temperature dependence.

DLTS Technique for Bulk Defects

Deep levels are characterized generally as those states deeper in the band gap than shallow hydrogenic states. Impurities with small ionization energies have wave functions that are diffuse, and their binding energies are reduced by the square of the dielectric constant of the host. The larger ionization energy of deep levels means that they are more localized in direct space, and therefore delocalized in k-space, requiring more Fourier components to describe the smaller orbit. The larger number of k values allows coupling to a wider variety of phonons, resulting in a tendency for deep levels to be non-radiative centers. For this reason, luminescence measurements are not particularly good methods for study of deep levels.

Deep levels are characterized here in much the same way as originally developed by Lang, but with significant differences in the way data is collected and analyzed (Lang, 1974:3023–3032). The objectives of both methods are to determine the trap energy for each trap from the emission rate, e_i, as a function of temperature based on the equation for the emission rate.

A structure with a voltage-variable depletion width is required for deep level transient spectroscopy. Traps are initially filled by applying a forward bias to the diode that reduces the depletion width, bringing the Fermi level above the trap energy. Then a reverse bias is applied, bringing the Fermi level below the trap energy, so that emission of the trapped carriers can be measured. The change in concentration of filled traps in the depletion region is measured as a change in capacitance. Carriers trapped in the depletion region are released with an emission rate given by

$$e_n = A_n \exp\left(\frac{-\Delta E}{kT}\right),$$

where A_n is a property of the particular defect, and ΔE is the depth of the trap from the band to which it emits. The principle of detailed balance can be used to determine A_n. At equilibrium, the capture and emission rates are equal, as expressed by

$$e_n\, p = c_n(1 - p),$$

where p is the probability that the state is occupied. The capture rate of electrons in this equation is given by

$$c_n = \sigma_n \langle v_T \rangle n,$$

where σ_n is the capture cross section, $<v_T>$ is the carrier thermal velocity, and n is the free carrier concentration given by

$$n = N_c \exp\left(\frac{-(E_c - E_f)}{kT}\right).$$

Here, N_c is the effective density of states in the conduction band, and is given by

$$N_c = 2M_c \left(\frac{2\pi m^* kT}{h^2}\right)^{3/2},$$

where M_c is the number of equivalent conduction band minima, m^* is the effective mass, and h is Planck's constant. Combining these expressions gives the equation for the emission rate with an explicit form for the prefactor as

$$e_n = \frac{\sigma_n \langle v_n \rangle N_c}{g} \exp\left(\frac{-E_T}{kT}\right), \qquad\qquad [\text{III-1}]$$

including g as the degeneracy factor.

DLTS is a form of capacitance transient analysis that provides a convenient way to present the evolution of the emission rate with temperature, that is, the rate window plot. The original method proceeds by recording the difference in capacitance, ΔC, at two times during a capacitance transient. The two sampling times establish a rate window, which can be used to determine an emission rate. ΔC, measured using boxcar integrators, is given by

$$\Delta C = C_\infty \left(\exp(-e_n t_1) - \exp(-e_n t_2)\right).$$

C_∞ is the steady state capacitance of the junction, and t_1 and t_2 are the selected sample times. This signal is then plotted over a range of temperatures, with a maximum signal at a temperature where the emission rate is defined by

$$e_n = \frac{\ln\left(\frac{t_2}{t_1}\right)}{t_2 - t_1}.$$

A peak in the plot of ΔC versus temperature can then be used to obtain the emission rate at the temperature of the peak. Setting the boxcar integrators to measure ΔC at another two points during the transients and repeating the temperature scan results in an emission rate at another temperature. One temperature cycle is then required for each pair of points, T and e. From several temperature scans, pairs of e_n and T can be obtained and plotted in a standard Arrhenius plot of $ln(e_n/T^2)$ versus $1/kT$ based on equation [III-1]. The T^2 factor removes the temperature dependence of the density of states ($T^{3/2}$), and the temperature dependence of the thermal velocity ($T^{1/2}$), in the exponential prefactor. The slope of the Arrhenius plot is the activation energy of the defect level. The intercept with the vertical axis can be used to determine the capture cross section. If $\Delta C \ll C$, the magnitude of ΔC is also related to the trap concentration by

$$N_T \cong 2(N_D - N_A)\frac{\Delta C}{C}.$$
[III-2]

The direction of the transient, positive or negative, distinguishes between majority carrier and minority carrier traps. When a majority carrier trap is filled, it reduces the carrier concentration, thereby increasing the depletion width. Since capacitance is inversely proportional to the depletion width, immediately after filling the traps and establishing a measurement bias, the capacitance of a junction containing a majority carrier trap will start out smaller than the steady state capacitance, and increase as the traps empty. A minority carrier trap will have the opposite effect.

In the experiments for characterizing deep traps in this work, a method is used that is more efficient than the rate-window method. Rate-window methods include any method that derives the trap characteristics from spectral (rate-window plot) peaks. The basic experimental setup that was used here is shown in Figure III-5. Two major differences between the current method and the rate-window method comes from the use of more recent technology. One is the use of a data acquisition board to record the entire capacitance transient, and the second improvement uses modulating functions to fit the recorded transients. Rather than making several temperature sweeps, one for each emission rate at a temperature for the Arrhenius plot, the entire transient is recorded at stable temperatures. Then the temperature is stepped through a range of interest. Next, the transients are fit using modulating functions and least square errors. This method of exponential transient fitting has the capability of separating several overlapping emission signals. This is a significant improvement from a rate-window plot analysis which may be unable to extract characteristics from two traps with similar characteristics, indicated by a broadened peak, whereas fitting by modulating functions can separate the two trap characteristics. Finally, the emission rates at each temperature are used to determine the trap characteristics from an Arrhenius plot.

Specifically, a DLTS scan is performed for each sample over the entire temperature region from 15-475 K. The equipment is computer controlled, so that averaging several capacitance transients at each temperature can be made and thus limited smoothing takes place efficiently for an improved signal-to-noise ratio. The sensitivity of the capacitance measurements is $\sim 5 \times 10^{-5}$ relative to the shallow carrier concentration. For
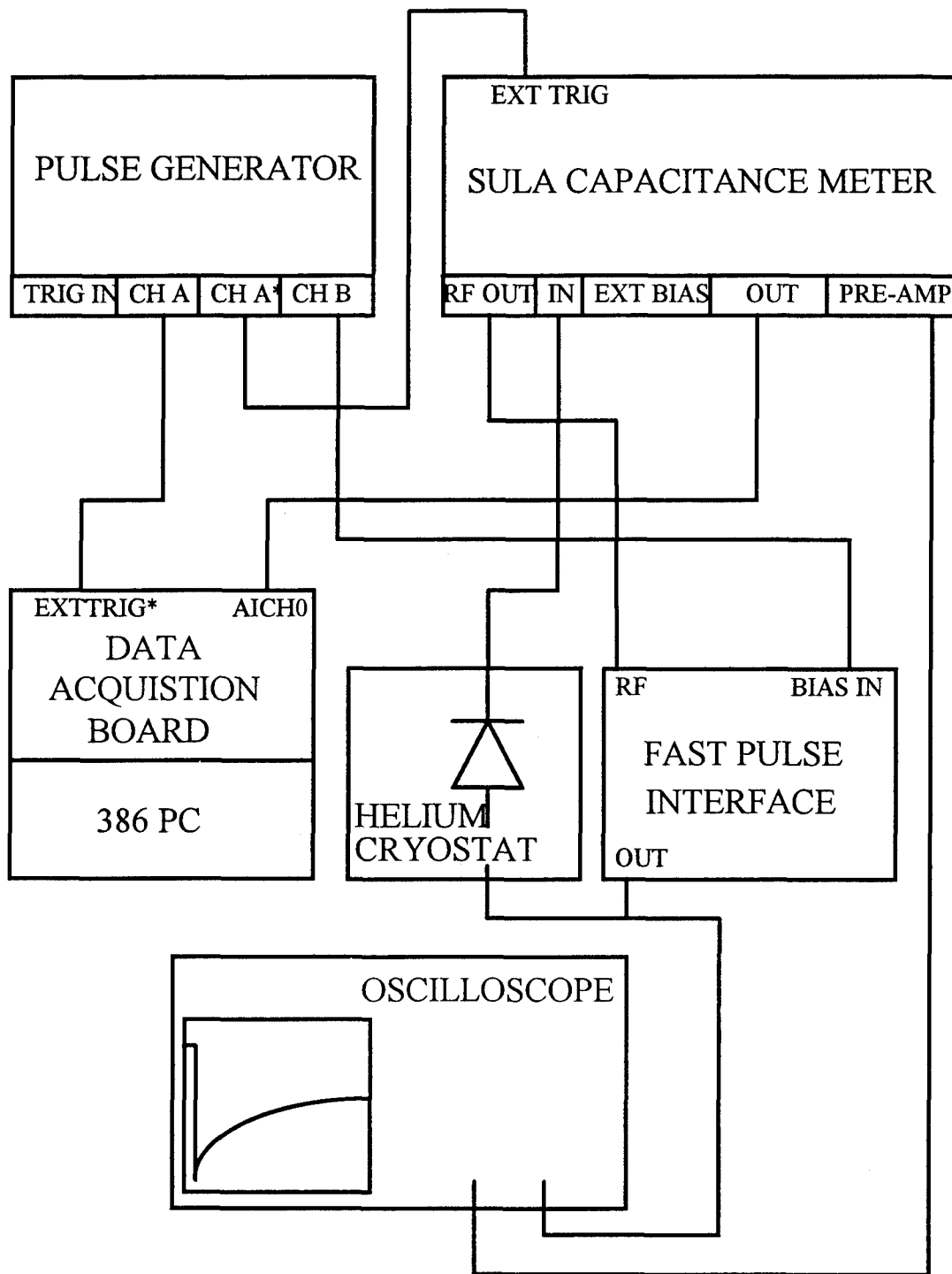
Figure III-5. DLTS equipment.

example, if the doping level is 10^{16} cm^{-3}, then defect concentrations of 5×10^{11} cm^{-3} or greater would be detected.

The capacitance is measured by a SULA capacitance meter with a minimum conversion time of 10 μsec, with data acquisition performed by a high resolution 16-bit National Instruments board. Representative conditions are to record ~500 points, averaged over ~1000 transients at each temperature, stepping the temperature every 2-5 K. Once the transients are acquired, they are fit for as many as three exponential components at each temperature, using modulating functions and least squares analysis (Kirchner *et al.*, 1981:6462–6470). The analysis fits the capacitance as a function of time, *t*, given by

$$C(t)^2 = \sum_{i=0} A_i \exp(-e_i t),$$ [III-3]

where A_i is the squared amplitude of the transient due to the ith energy level at a given temperature. A_0 is the steady state value of capacitance squared with $e_0=0$. The transients are fit for one, two, and three exponential components. Then the emission rates are taken from the fit with the smallest least squares error and used to form the Arrhenius plot. The activation energy of the trap is obtained from the slope of the Arrhenius plot, and the capture cross section is obtained from the vertical intercept. The trap concentration is determined from the amplitude of each transient. The method of recording and fitting the entire transient used here has been shown to be more accurate than rate-window methods (Doolittle and Rohatgi, 1994:4570–4575).

Another benefit of recording the entire transient is the ease with which capture barriers can be measured. Comparison of deep level properties between different

investigators or different experiments have shown a wide variation in values. Part of the problem is the various mechanisms involved in carrier capture. Typical analysis assumes that the capture cross section is not dependent on temperature. Several models of capture have been proposed, however, some are temperature dependent as described in the first sub-section of this chapter. More thorough investigation of the capture cross sections of traps will contribute to the understanding of each of the models. The next part of this section illustrates an efficient method of characterizing the capture of carriers via multi-phonon emission, followed by descriptions of other variations from the original DLTS equipment that have been implemented and used in this study.

The initial method used for DLTS, as incorporated by the rate window concept, uses only a small portion of the capacitance transient. Typical reported characteristics are the trap energy, the capture cross section, and the trap concentration. As data acquisition has become faster and available as an add-in board for a personal computer, the method of recording and analyzing the entire transient rather than just two points is gradually replacing the earlier method. Measurement of the capture barrier is now routinely possible as a by-product of recording the entire transient capacitance versus time and temperature in a DLTS analysis using a single temperature scan. This should allow capture barriers to be reported more frequently, and add the capture mechanisms to the deep level characteristics that are usually reported, providing more accurate numbers for predicting carrier lifetimes used in device design and operation.

The method proposed here applies to measurement of caputre barriers due to multi-phonon emission. Among the models of capture, three of the more prominent

capture processes are cascade capture, capture by multi-phonon emission, and capture associated with Auger recombination. The first two were discussed at length earlier in this chapter in the section on the theoretical aspects of deep levels, and are summarized here for convenience. Lax proposed the model of capture of a carrier when it cascades through closely spaced, highly extended states (Lax, 1960:1502–1523). The carrier loses energy by emitting a phonon between each extended state. The process of cascade capture has a negative temperature dependence as an exponent of temperature, T^x. A deeper Coulombic level would have lower levels spaced too far apart energetically to allow transitions accompanied by the loss of only one phonon. In this case, simultaneous emission of multiple phonons has been shown to take place by Henry and Lang (Henry and Lang, 1977:989). As opposed to cascade capture, multi-phonon emission has a cross section that increases exponentially with increasing temperature, with a characteristic activation energy. The energy loss is realized by either a relaxation or a distortion of the lattice.

In a DLTS experiment, a filling pulse that saturates the trap is required in order to obtain an accurate trap activation energy and capture cross section from the Arrhenius plot. If saturating conditions are achieved, then the trap depth, E_T, and the capture cross section, σ, are obtained from the slope and intercept of a plot of the emission rate versus 1/kT, respectively, as given by equation [III-1]. Alternatively, the capture barrier can easily be measured by using a narrower, non-saturating filling pulse, and then recording the transients. The barrier for capture by multi-phonon emission will be evident from the change in the amplitude of the capacitance transient as the temperature increases.

The rate of change of filled traps is given by

$$\frac{dN_r^0}{dt} = c_f N_T^+ - e N_T^0,$$

where N_T^0 is the concentration of filled traps, N_T^+ is the concentration of empty traps, assuming a donor trap, and e is the emission rate given in equation [III-1]. c_f is the capture rate during the filling cycle given by

$$c_f = \sigma_\infty n_s v_{th} e^{-\frac{E_b}{kT}} \qquad \text{[III-4]}$$

Here, σ_∞ is the high temperature limit of the capture cross section, n_s is the shallow carrier concentration, and E_b is the capture barrier energy. The total trap concentration is the sum of the filled and empty traps:

$$N_T = N_T^0 + N_T^+.$$

From the solution of the differential equation, the concentration of filled traps at the end of a filling pulse of width t_f is given by

$$N_T^0 = N_T \frac{c}{c+e}\left(1 - e^{-(e+c)t_f}\right) \qquad \text{[III-5]}$$

Comparing the equations for e and c, the capture rate will be much greater than the emission rate unless the capture barrier is about the same height as the emission barrier. Therefore, making the approximation that $e \ll c$ and inserting the explicit form for the capture rate from equation [III-4], equation [III-5] for the concentration of filled traps can be simplified to

$$N_T^0 = N_T\left[1 - \exp\left(-t_f \sigma_\infty v_{th} n_s e^{-\frac{E_b}{kT}}\right)\right]. \qquad \text{[III-6]}$$

In practice, to measure the capture barrier the temperature is set for maximum response from the trap. Then the pulse width is reduced until there is a reduction in capacitance transient amplitude, but wide enough so that the transient amplitude is well above the noise level. Next, the transients are recorded at temperature steps covering the temperature range where the trap responds. Equation [III-6] shows that as the temperature increases, the concentration of filled traps increases until the exponential term goes to zero and the trap is saturated. The change in concentration of filled traps is reflected in the amplitude of the capacitance transient

$$C(t,T) = \left(\frac{q\varepsilon\left(n_s - N_T^0(t,T)\right)}{2(V + \varphi)} \right)^{\frac{1}{2}}, \qquad [\text{ III-7}]$$

where n_s is the ionized donor concentration, V is the applied bias, and φ is the built-in potential. The capacitance transient fitting routine uses equation [III-3] which is slightly different from equation [III-7]. The first two terms are given here for simplicity.

$$C(t,T)^2 = A_0^2 + A_1^2 e^{\frac{-t}{\tau}},$$

By comparing this equation with equation [III-7], one can obtain A_0 as the steady state capacitance,

$$A_0^2 = \frac{q\varepsilon n_s}{2(V + \varphi)}$$

and A_1 as the amplitude of the capacitance transient

$$A_1^2 = \frac{-q\varepsilon N_T(1 - e^{-c_f t_f})}{2(V + \varphi)}.$$

It is convenient to record the amplitude as

$$\frac{A_1^2}{A_0^2} = \frac{-N_T(1-e^{-c_f t_f})}{n_s}.$$

The ionized shallow impurity concentration changes slowly in the temperature range where the deep levels respond, so that using n_s in the denominator rather than N_T introduces a change of scale but does not affect the measured capture barrier energy.

From the fitting of the capacitance transients, the trap concentration versus temperature are fit according to equation [III-6] to obtain the capture barrier energy. This method is similar to other methods of measuring the capture barrier but doesn't require the complexities of repeated temperature scans or elaborate pulse shaping (Criado et al., 1988:660–661; Palma et al., 1993:2605–2612).

Other variations from the original DLTS method that are important in this analysis include constant capacitance DLTS (CC-DLTS) and double-pulse DLTS (DDLTS) modes. DLTS uses capacitance transients measured at constant bias to determine trap properties according to equation [III-7]. If $n_s \gg N_T$, then an expansion in powers of N_T^0 / n_s results in an exponential signal given by

$$C(t) = \left(\frac{\varepsilon q n_s}{2(V+\varphi)} \left(1 - \frac{1}{2} \frac{N_T^0}{n_s} \exp(-e_i t) \right) \right)^{\frac{1}{2}}.$$

This truncated power series expansion is valid if the ratio of trap concentration to shallow carrier concentration is less than 10%, in which case constant voltage DLTS can be used. Otherwise, for a large trap concentration, the depletion width will become narrow as the emission of trapped carriers progresses. The change in depletion width introduces a time dependent reduction in the number of traps that can emit, making the transient non-

exponential. In this case, a feedback circuit is used to change the bias on the diode to hold the capacitance at a constant value in the CC-DLTS mode (Goto *et al.*, 1973:150; DeJule *et al.*, 1985:639–641). The signal is now the feedback bias, rather than the capacitance, which is exponential regardless of the trap concentration. The voltage transient is given by

$$V(t) = \left\{ \frac{\varepsilon q}{2C^2} \left(n_s + N_T^0 (1 - \exp(-e_i t)) \right) \right\} - \varphi.$$

Another measurement mode, double-pulse DLTS (DDLTS), has two purposes. DDLTS can be used to profile the deep levels, or determine the electric field dependence of the trap energy. In multi-layer structures, if identification of the layer responsible for the emission is ambiguous with standard DLTS, DDLTS can be used to reduce overlapping signals from the adjacent layer. A spatial observation window is defined by two filling pulse biases and a measurement bias as given in Figure III-6. W_D is the shallow carrier depletion width at the measurement bias. The first filling pulse, V_{p1}, results in emission from traps between X_{p1}, which is the deep level depletion at V_{p1}, and X_D, which is the deep level depletion at the measurement bias. The second filling pulse, V_{p2}, results in emission from traps between X_{p2} and X_D. The emission signal obtained from subtracting the capacitance transient due to filling pulse V_{p2} from the capacitance transient due to filling pulse V_{p1} is therefore only from traps between X_{p2} and X_{p1}. A profile of the deep levels is obtained by stepping through a series of spatial observation windows.

One scheme that is used to determine the electric field dependence of the emission energy is to establish two filling pulses that define a narrow region for emission as

described in the previous paragraph, and additionally vary the measurement bias. Varying

the measurement bias changes the field present in the spatial observation window. The

trap characteristics can then be determined as a function of electric field. A donor or

acceptor trap, both of which are neutral when they are filled, can be identified by a

reduction in trap energy with increasing electric field. The electric field has the effect of
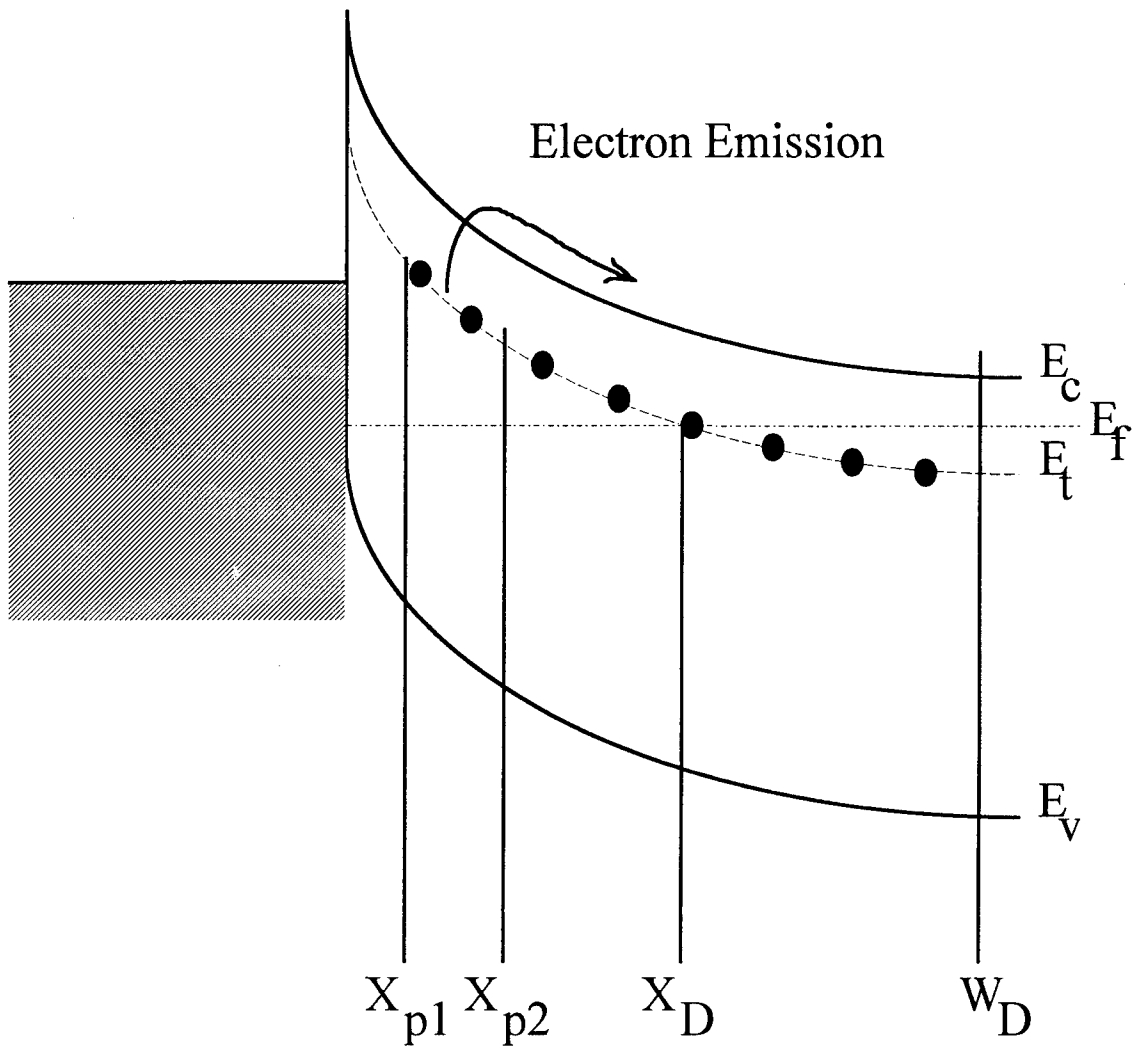
Figure III-6. Band bending diagram for a Schottky diode defining an emission window for spatially resolved deep level measurements. The layer between X_{p1} and X_{p2} is the emission window.

increasing the dipole charge separation, reducing the thermal energy required for ionization. This is known as the Poole-Frenkel effect (Vincent, Chantre, and Bois, 1979:5484–5487; Hartke, 1968:4871–4873). The electric field effect for traps that are charged when filled will therefore be different than for traps that are neutral when filled.

Figure III-7 shows the effect of the barrier lowering on a single trap in the depletion region of a diode. The total electric field from both the defect potential and the applied bias is given by

$$U_{PF}(x) = \frac{-\eta q^2}{\varepsilon x} - qFx,$$

where η is the charge after emission, q is the electronic charge, ε is the dielectric constant, x is the distance from the defect, and F is the electric field intensity (Buchwald and Johnson, 1988:958–961). The reduction in emission energy by the electric field can be determined from this equation by taking the derivative with respect to x and setting it equal to zero. The position where the slope of the defect potential is zero is the minimum potential barrier. The Poole-Frenkel barrier lowering is then determined by substituting this distance for x. The result is

$$\Delta U_{PF} = 2q \left(\frac{\eta q F}{\varepsilon} \right)^{1/2}.$$

The effect on the emission rate is a direct reduction of the emission energy as shown by

$$e = e_0 \exp\left(\frac{\Delta U_{PF}}{kT} \right)$$

$$= \langle v_{th} \rangle \sigma N_c \exp\left(\frac{-E_T + \Delta U_{PF}}{kT} \right),$$
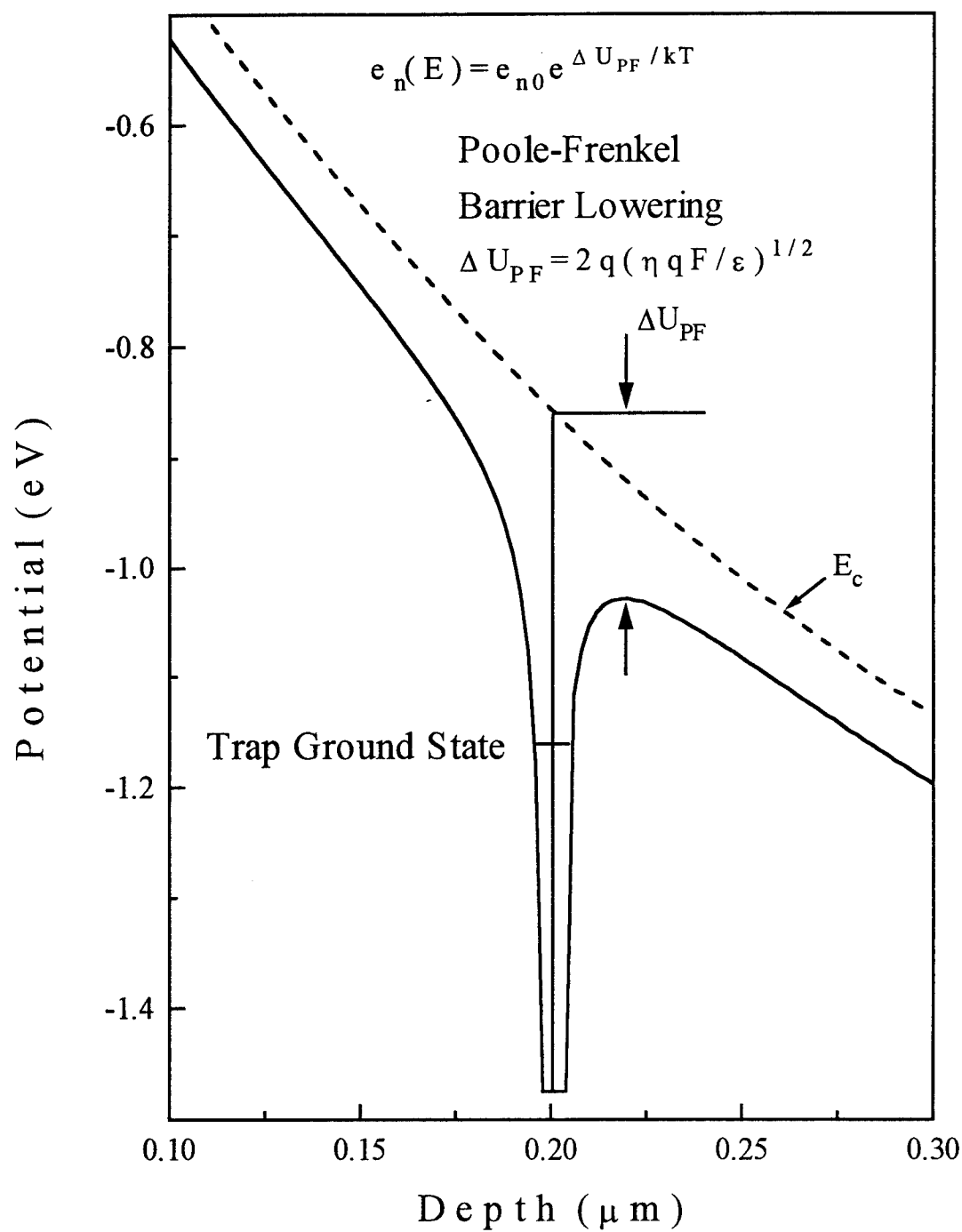
Figure III-7. Potential energy of an electron bound to a positive point charge located in the depletion region of a diode. ΔU_{PF} is the amount that the emission barrier is lowered by the applied electric field.

where e_0 is the zero field emission rate. Measurement of the emission rate as a function of electric field, using DDLTS to establish the electric field in an emission window, can then be used to determine the charge state of the defect.

In addition to the differences in technique and capabilities from the basic DLTS just mentioned, C-V profiling has essential information for DLTS on multi-layer structures. Deep levels in the barrier/cladding material were characterized using a structure with two types of materials in the depletion region. For these multi-layer structures where there is a *p-n* junction and an adjacent heterojunction made from two materials of different bandgaps, the applied voltage can increase the depletion width in both junctions for some bias range. The capacitance of both junctions can be dependent on the applied bias. For some bias ranges, the trap filling pulse used in DLTS can fill traps in all three materials, the p-type material, the n-type material, and the semiconductor with the different bandgap. The C-V profile can be used in conjunction with DLTS to identify a layer responsible for the measured emission by pairing the filling pulse and measurement biases with their respective depletion widths. C-V and DLTS measurements of a compound junction are therefore different from measurements made on a single junction. More detail on C-V profiling through a heterojunction, and an example of the use of C-V measurements to distinguish which layer a trap emission is coming from will be given in the first section of Chapter IV on deep levels in the barrier material.

Reported Deep Levels

Most of the reports on deep levels in $Al_xGa_{1-x}As_ySb_{1-y}$ so far have concentrated on the DX centers. The DX center is characterized by a temperature dependent electron capture cross section associated with persistent photoconductivity. Within the first studies performed, there is some disagreement on the presence of the DX center in GaSb. Poole *et al.* reported on deep levels in MBE grown GaSb that are similar to the DX center in AlGaAs (Poole *et al.*, 1990:1645–1647). Very little difference was seen in the measured DX center energy for different dopants. These DX centers are also seen in Te doped LPE $Al_xGa_{1-x}Sb$ on GaSb (Zhu *et al.*, 1988:1897–1901). However, Zhu *et al.* reports the presence of a deep donor only for x>0.4. Zhu *et al.* also measured the trap characteristics for various compositions of $Al_xGa_{1-x}As_ySb_{1-y}$ and found that the energy changed from 0.39 eV for x=0.3 to two levels at 0.49 and 0.51 eV for x=0.72 (Zhu *et al.*, 1987:127–130). The trap energy only loosely follows the conduction band edge as the composition changes, as does the DX center in $Al_xGa_{1-x}As$. Table III-1 summarizes the properties of the traps found in GaSb from several groups. Some of the values for the concentrations are given as fractions of the shallow carrier concentration, n_s. Similarly, Table III-2 summarizes the properties of the traps found in $Al_xGa_{1-x}As_ySb_{1-y}$.

The DX center is therefore seen as one of the major areas where improvements in $Al_xGa_{1-x}As_ySb_{1-y}$ material characteristics can be made. Another problem that has been most noted in GaSb is the presence of the Ga antisite defect, Ga_{Sb}. In fact, the Ga_{Sb} antisite defect makes GaSb *p*-type as-grown. However, there has not been any reports yet on the Ga_{Sb} antisite defect characteristics as measured by DLTS.

Information on the deep levels present in the $In_xGa_{1-x}As_ySb_{1-y}$ material that used in the quantum well lattice-matched to GaSb is even more limited. All of the measurements so far have been on InAs (x=1). Salman *et al.* used a metal insulator semiconductor (MIS) structure to look at the traps in InAs (Salman, Korshunov and Vertoprakhov, 1990:509–514). They found electron traps at 60 meV and 160–200 meV below the conduction band. The capture cross sections were $5x10^{-14}$ and $1x10^{-14}$ cm^2, and trap concentrations were $2x10^{14}$ and $\sim10^{16}cm^{-3}$, respectively. These were suspected to be intrinsic defects. Other measurements showed electron traps 110 and 150 meV below the conduction band (Fomin, Lebedev, and Annenko, 1984:734; Loskutova *et al.*, 1985:36).

Table III-1. Reported deep levels in GaSb.

Energy (eV)	cross section σ (cm^2)	capture barrier (eV)	concentration (cm^{-3})	type	growth method	ref
0.25	3×10^{-14}	present	$1 \times n_s$	electron	CZ	1
0.25	1.3×10^{-15}	none		electron	MBE	2
0.33	1.3×10^{-15}		5×10^{14}	hole	MBE	2
0.25	2.3×10^{-19}		10^{14}	hole	MBE	3
0.3-0.35				hole	MBE	3
0.63	7.1×10^{-20}		10^{15}	hole	MBE	3
0.33, 0.7				hole		4
0.280	6×10^{-18}	0.200	$1 \times n_s$	electron	S-doped MBE	5
0.315	2×10^{-20}	0.195	$0.045 \times n_s$	electron	Se-doped MBE	5
0.310	3×10^{-20}	0.190	$0.015 \times n_s$	electron	Te-doped MBE	5

[1] (Hubik et al., 1993:19–22)
[2] (Polyakov et al., 1992:337–343)
[3] (Kuramochi et al., 1993:2664–2666)
[4] (Shen et al., 1993:8313–8318)
[5] (Poole, Lee, and Cleverly, 1990:1645–1647)

Table III-2. Reported deep levels in $Al_xGa_{1-x}Sb$.

Al %	Energy (eV)	cross section σ (cm^2)	capture barrier (eV)	concentration (cm^{-3})	type	comment	ref
0.5	0.145				hole	GaSb or AlSb	6
0.5	0.38-0.41	5x10^{-14}	0.285	2.5x10^{17}	donor	Hall E_d=0.125	7
0.3	0.39	4.1x10^{-13}			electron	Te-doped	8
0.4	0.43	2.1x10^{-11}	0.32		electron	Te-doped	8
0.49	0.48	1.3x10^{-11}	0.35		electron	Te-doped	8
0.61	0.49	1.2x10^{-12}			electron	Te-doped	8
0.72	0.49	2.9x10^{-13}			electron	Te-doped	8
0.72	0.51	5.1x10^{-13}			electron	Te-doped	8
0.1	0.24				electron	Se-doped	8
0.1	0.37				electron	Se-doped	8
0.3	0.35				electron	Se-doped	8
0.2	0.0068				electron	Hall	8
0.4	0.06				electron	Hall	8
0.5	0.110				electron	Hall	8
1.0	0.26	2.9x10^{-15}	0.16	~2 x n$_s$	electron		9
1.0	0.1				electron	Hall	9
0.4	0.46	1.3x10^{-11}		15 x n$_s$	electron		10

[6] (Ideshita et al., 1992:2549)
[7] (Meyer et al., 1993:475–478)
[8] (Zhu et al., 1987:127–130)
[9] (Nakagawa et al., 1990:1551–1553)
[10] (Takeda et al., 1987:L273–275)

Band Offsets

Theoretical Models

Much of the theoretical work on band offsets was done in support of work on the GaAs/Al$_x$Ga$_{1-x}$As system. One of the simplest cases examined is for the binary system AlAs/GaAs. A comparison between predicted valence band discontinuity for this heterojunction and the most recent measurements is given in Table III-3. The experimental values span the range from 0.45 to 0.55 eV. The experimentally determined values are from Wang and Stern (0.45 eV) using a charge transfer method (Wang and Stern, 1985:1280), and Arnold *et al.* (0.55 eV) who used Kroemer's adaptation of C-V profiling (Arnold *et al.*, 1984:1237). The theoretical models included in the comparison are the self-consistent interface potential (SCIP) model (Pickett, Louie and Cohen, 1978:815), Harrison atomic orbital (HAO) model (Harrison, 1977:1016), Frensley-Kroemer pseudopotential (FKP) (Frensley and Kroemer, 1977:2642), and a model by Tersoff (Tersoff, 1984:4874). Offsets calculated using SCIP and FKP methods are slightly low, while the HAO method gives a value that is off by an order of magnitude. The HAO method is useful for determining the trends in offset behavior for different materials. The best agreement is achieved by the method of Tersoff.

Table III-3. Summary of the theoretical estimates and experimental measurements of the valence band offset at the AlAs-GaAs heterointerface (energy in eV).

	SCIP	HAO	Tersoff	FKP	exp
AlAs/GaAs	0.25	0.04	0.35	0.3	0.45±0.05 0.55±0.05

The theories of band lineup attempt to establish a common energy scale that can be used to compare the bands of two semiconductors. Harrison's theory is based on a linear combination of a single atomic s-state and three atomic p-states of each atom, each of which is taken to be orthogonal to the other. For two atoms per primitive cell, the four orbitals of each atom result in an eight-by-eight matrix. At special wave vectors, the matrix can be diagonalized exactly to determine the eigenvalues. In particular, the energy of the valence band maximum at the Γ-point is given by

$$E_v = \frac{\varepsilon_p^c + \varepsilon_p^a}{2} - \left[\left(\frac{\varepsilon_p^c - \varepsilon_p^a}{2} \right)^2 + V_{xx}^2 \right]$$

where ε_p^c is the p-state energy on the cation and ε_p^a is the p-state energy on the anion. V_{xx} is the interatomic matrix element between atomic p-states on adjacent atoms. More distant atoms are neglected. The offset between valence bands of two semiconductors is the difference in energy at the valence band maximum of each. Harrison's theory assumes that no significant dipole is formed at the interface.

Tersoff's model, however, makes used of the interface induced states in the gap of one or both semiconductors to establish conditions that allow a reasonable prediction of the band lineup. For a given system, there is a unique band alignment that results in zero interface dipole. The dipole arises when the bulk electronic states in one semiconductor overlap with the band gap of the other and tunnel into the latter. The band offset is calculated from the condition at which equal contributions from conduction and valence band states ensures charge neutrality. This condition is equivalently defined by an

effective midgap point where valence and conduction bands contribute equally to the cell-averaged real-space Green's function. The input to the Green's function is the band structure which was determined from a linearized augmented-plane-wave method (APW) in Tersoff's calculations (Ashcroft and Mermin, 1979:200–202). The heterojunction discontinuity is the difference between the effective midgap point of the two semiconductors. It is stated that the calculated band structures are only reliable to within 0.1–0.2 eV in general. Comparison of theory and experiment for six heterojunctions reflect this accuracy. Given that the actual interface properties often depend on the growth conditions, agreement better than 0.1 eV is fortuitous.

The band offset estimates used here are from a scheme by Krijn (Krijn, 1991:27–31). An interpolation scheme is presented for band offsets between binary, ternary, and quaternary heterojunctions based on the average energy of the valence-band starting with the binary constituents. The average valence band energy is determined by a method proposed by van de Walle, which establishes a common reference level chosen to be the average electrostatic potential in a semi-infinite 'model-solid'. The model-solid is built up from a superposition of neutral atoms which are required to mimic the bulk electron density. The common reference then depends on the density of each type of atom and the detailed form of the atomic charge density. The band offset for a heterojunction involving a quaternary material is a series of linear interpolations, first between the binary constituents of two ternary compounds, then between the ternary compounds to arrive at the average valence band energy of the quaternary material. An example of the use of this method will be presented in the section on Band Offset Estimates in Chapter IV.

DLTS Method

The band offset in a heterojunction determines the depth of a potential well. This information can be used to determine the proper width of a well for desired energy levels within the well. DLTS has traditionally been used to characterize the deep levels in bulk material where the defects are assumed to be uniformly distributed. Alternatively, a single quantum well can be put into range of the depletion region of a Schottky or *p-n* diode and act as a trapping center as shown in Figure III-8 (Letartre, Stievenard and Lanoo, 1990:116–119). The well is filled by applying a forward bias that collapses the junction. Then, once a reverse bias is reapplied, carriers trapped in the well are emitted over the barrier according to the thermionic emission energy and Fermi-Dirac statistics. The emission can be recorded as a capacitance transient for analysis and fitting of the parameters such as band offset and concentration of carriers in the energy level of the well. However, the analysis is different from that of a uniformly distributed trap since the well can be thought of as one trap with N places rather than N defects with one place each.

The initial approach was to look at the well as a giant artificial deep level (Martin *et al.*, 1983:4689). Subsequent analysis has shown that the proper treatment of the statistics of carriers in the well reduces a source of error, which is estimated to be about 10%, in the treatment of the well as a giant trap (Letartre, Stievenard and Lanoo, 1990:116–119; Letartre and Stievenard, 1991:1047–1049; Vescan, Apetz, and Lüth, 1993:7427–7430). The analysis is based on a balance between the currents between the well and barrier, J_{WB}, and the barrier and well, J_{BW}. The total current is given by

$$J = J_{WB} - J_{BW} \, ,$$
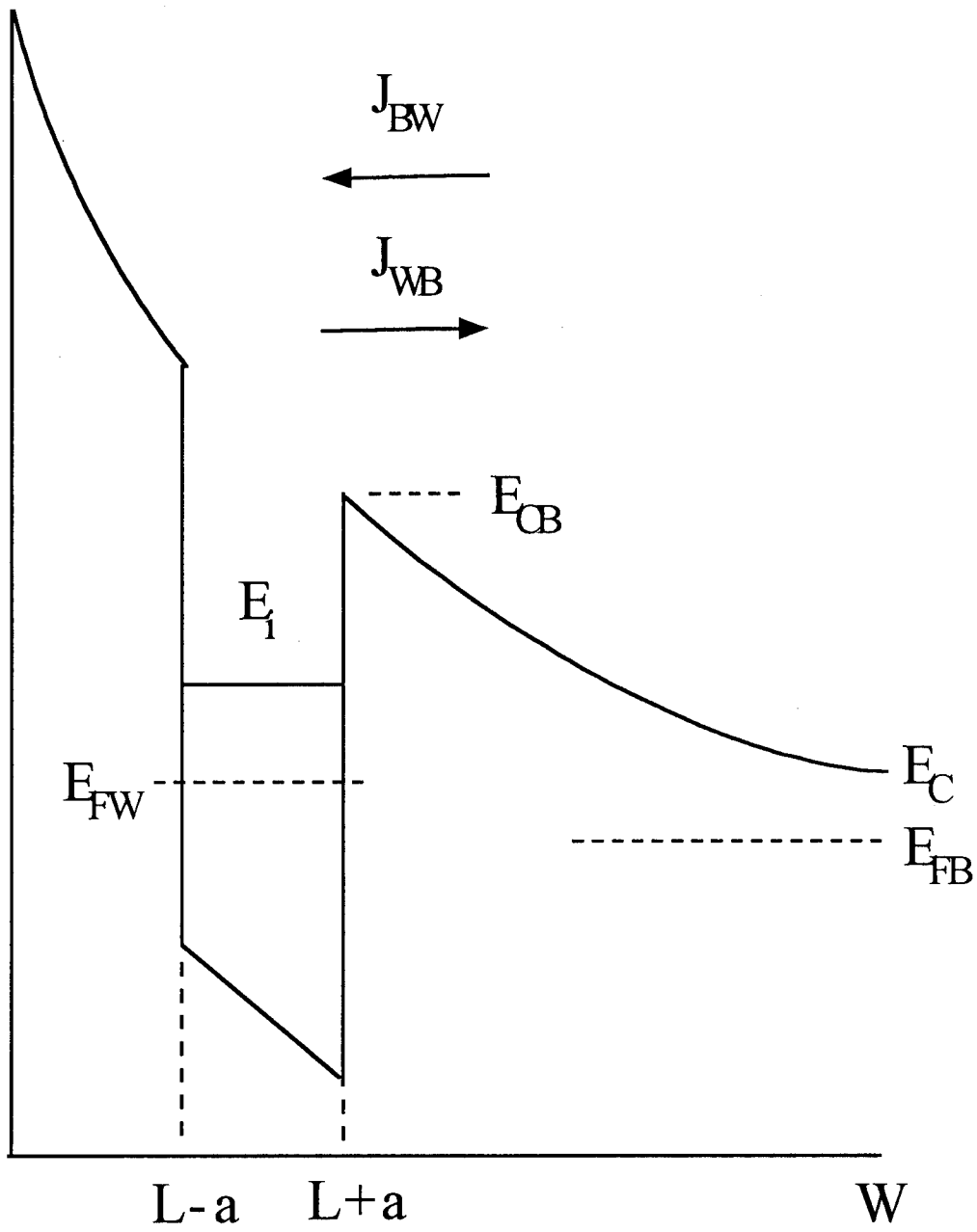
Figure III-8. Conduction band of a well located in the depleted region. The energies can be taken with respect to the conduction band energy of the bulk, E_c.

or

$$J = eN_c v\left(\exp\left(\frac{E_{FB} - E_{CB}}{kT}\right) - \exp\left(\frac{E_{FW} - E_{CB}}{kT}\right)\right),$$

where N_c is the density of states in the conduction band of the barrier, v is the thermal velocity of the electrons in the barrier, E_{FB} is the Fermi level in the bulk material, E_{FW} is the Fermi level in the well, and E_{CB} is the conduction band energy at the edge of the well. The concentration of electrons in the well, n_W, changes at a rate given by

$$\frac{\partial n_w}{\partial t} = \frac{J}{e}.$$

This method uses an iterative calculation starting with the concentration of carrier in the well under filling conditions, i.e. with the Fermi level above the energy level in the well. Integrating Poisson's equation determines the relationship between the applied potential, V, and the depletion width, W,

$$V = -\frac{en_s W^2}{2\varepsilon} + \frac{en_w L}{\varepsilon}, \qquad\qquad\qquad [\text{III-8}]$$

where n_s is the shallow carrier concentration.

The width of the depletion region is calculated using the assumed n_W, followed by calculation of the band bending from the edge of the well farthest from the junction to the depletion region edge, $L+a$, to W using

$$E_{CB} = \frac{(W - (L+a))^2 e^2 n_s}{2\varepsilon},$$

where E_{CB} is measured from the conduction band at the edge of the depletion region. Then the shift of the energy levels, E_i, in the well as a result of the band bending from the

applied bias and the filling of the well can be determined. Assuming the well width is narrow enough to approximate the charge density in the well as constant, n_s-$(n_W/2a)$, and integrating Poisson's equation between $L+a$ and L, we find the energy level E_i:

$$E_i = E_{CB} - \Delta E_C + \frac{e^2 n_s}{\varepsilon}(W - (L+a))a - \frac{e^2}{2\varepsilon}\left(\frac{n_W}{2a} - n_s\right)a^2 + \Delta E_i,$$

where the ΔE_i are the energy levels of the square well potential without applied bias. From this information the concentration of carriers in the well can be calculated using

$$n_W = \frac{m_W^*}{\pi \hbar^2} kT \sum_i \left\{ \log[1 + \exp(u_i)] - u_i \right\},$$

where $u_i = (E_i - E_{FW})/kT$ and m_W^* is the effective mass of an electron in the well. Then it is inserted back into equation [III-8], and iterated until this set of equations converges on the initial concentration of carriers in the well for the applied bias.

The initial concentration in the well is used as a starting point for the emission of carriers from the well when the voltage is switched to the measurement bias, lowering the Fermi level below the energy levels in the well. The occupation of the well will decrease with time according to

$$\frac{dn_W}{dt} = \frac{-m_B^*(kT)^2}{2\pi^2 h^3} \exp\left[\frac{-(E_{CB} - E_{FW}(n_W))}{kT}\right].$$

Here, m_B^* is the effective mass of an electron in the barrier. The solution is of the form

$$n_W = n_W^0 \exp(-e_W t),$$

where n_W^0 is the initial occupation. For emission involving only one level, the emission rate, e_W, is given by

$$e_W = \frac{m_B^*}{m_W^*} \frac{kT}{h} \exp\left(\frac{-(E_{CB} - E_i)}{kT}\right) .$$

E_{CB}-E_i is the barrier for emission of electrons from the well which can be measured by DLTS in the same manner as uniformly distributed traps. The only difference is that the pre-exponential factor of the emission rate is proportional to T rather than T^2. A semilog plot of e_W/T versus $1/kT$ has a slope equal to the thermal emission energy of the confined state, E_{CB}-E_i. At this point the only unknown is the band offset which can then be calculated by adding the calculated energy of the confined state to the thermal emission energy. For emission from the ground state in the well, corresponding to the highest temperature emission, the calculated confined state energy does not change much with band offset. A correction for the band bending in the well can also be made, but it will be small for low a doped well. A similar set of equations apply to emission from the valence band well. The accuracy of this method is reported to be ~10 meV.

C-V Method

A heterojunction with the same doping on either side of the heterojunction is found to give a characteristic depletion and accumulation region in a C-V profile. An iterative technique has been used to obtain the actual carrier profile and the band offset in a heterostructure (Kroemer et al., 1980:295). The surface potential is assumed as a first step, and a guess is made for the electric field at the surface. Then, Poisson's equation is

integrated to the bulk of the semiconductor and the boundary condition of the electric field at the surface is checked. If it does not match the boundary conditions, a new value for the surface field is chosen and the calculation is repeated. The procedure is repeated until the boundary condition in the surface is matched to the desired degree of accuracy.

In a revised method requiring no iteration, integration of Poisson's equation proceeds from the interior towards the surface (Missous and Rhoderick, 1985:233–237). At the interface $n_1=n_{i1}exp(u_1)$ and $n_2=n_{i2}exp(u_2)$, where n_{i1} and n_{i2} are the intrinsic concentrations corresponding to the two sides of the heterojunction. Subscripts *1* and *2* refer to the wide and narrow gap material, respectively, *2* being closer to the Schottky interface, and $u=(E_f-E_i)/kT$ in each material. Here, E_i is the intrinsic Fermi energy in each material. The ratio of the concentration of electrons on either side of the junction depends on the band offset as given by

$$\frac{n_1}{n_2} = \frac{N_{c1}}{N_{c2}} \exp\left(\frac{-\Delta E_c}{kT}\right),$$

[III-9]

where N_{c1} and N_{c2} are the effective densities of states for the conduction bands in the two regions.

The accuracy of using equation [III-9] to determine the band offset relies on how accurately n_1 and n_2 can be determined from measurements. In other words, a C-V profile would have to show a region on either side of the heterojunction with a flat profile.

<u>Previous DLTS Measurements of Band Offsets</u>

Measurement of the band offset between two materials using DLTS has had mixed success in the past. This section presents a review of published papers reporting on the measurements made by DLTS on quantum well structures. Observed behavior that is not typical of uniformly distributed deep levels will be pointed out along with the explanations given in each paper, and some possible alternative explanations.

The DLTS signal for a potential well in the valence band of a structure composed of a SiGe well with Si barriers grown by LPCVD shows a broad peak centered at 80 K (Vescan, Apetz, and Lüth, 1993:7427–7430). This peak is attributed to emission from energy levels in the well. Their simulations, based on calculations of the energy levels with varying well thickness, predicted that the broadening was due to non-uniform well width. The thicknesses of the SiGe wells were desired to be 2 nm. Thickness measurements by cross section transmission electron microscopy showed a continuous and homogeneous layer of ~2 nm thickness having a sharp bottom interface. However, there were also some islands ~300 nm in diameter that were 5-10 nm thick rather than 2 nm thick. The wider wells have deeper eigenstates resulting in higher energy measurements. The signal from the wider well regions would appear at a higher temperature than the signal from the narrow well regions. The combined signal from the various well thicknesses is much broader than the signal from a uniform well thickness.

Another explanation for the breadth of the peak is that states in the well with lower thermionic emission energy are occupied during the filling pulse. Increasing the occupation of higher states in the well would appear as a low temperature signal,

broadening the peak. The well was assumed to have appreciable occupation only in the level closest to the bottom of the well.

A shift in the DLTS peak signal to lower temperatures with increasing electric field was attributed to Poole-Frenkel barrier lowering. The effect in a quantum well structure that is analogous to the Poole-Frenkel effect for bulk traps is the reduction in thermionic emission energy due to the band bending from the center of the well to the edge of the well caused by the electric field. The reduction is on the order of 25 meV, but depends on the distance of the well from the junction. This degree of band bending was assumed to be enough to cause the reduction in the peak signal temperature of ~20 K that was observed after changing the measurement bias from -1 V to -4 V.

Measurements on a GaAs well in $Al_{0.35}Ga_{0.65}As$ showed some odd shifts of the DLTS peak depending on the direction of the temperature scan and filling pulse duration (Jiao and Anderson, 1993:271–276). A normal DLTS signal peak should remain in the same position when scanning the temperature either from high to low, or from low to high, if the emission is exponential (Lang, 1974:3023). However, the peak signal position shifts if the emission is non-exponential. The peak observed in the spectrum of the $GaAs/Al_{0.35}Ga_{0.65}As$ quantum well when the sample was being cooled appeared at a temperature that was 13 K higher than the peak that was observed when the sample was being heated. The scan rate was set at 0.4 K/s compared to an emission time constant much less than 1 sec, so that the time constant would be unreasonably long if one attributes this to a relaxation mechanism. A reasonably linear Arrhenius plot was obtained in spite of the non-exponential emission rate. Jiao *et al.* suggest that as long as the DLTS

scanning is in the same direction among different rate widows, the conventional exponential expression for the emission rate will hold.

A shift in the temperature of the peak was also observed in the same sample when the filling pulse width was changed in steps from 1 μs to 10 ms. The shift in peak position with filling pulse width showed that two mechanisms may be present affecting the capture of carriers. The peak signal temperature initially increased with filling pulse width. Then the peak signal temperature began to decrease with further widening of the filling pulse. The suggested reasons for this behavior were Coulomb repulsion among electrons in the well, charge redistribution during the filling phase, and the Pauli exclusion principle, although the details were not given.

In an interesting report, As et $al.$ examines the capture kinetics of a quantum well of GaAs in $Al_xGa_{1-x}As$ (0.24<x<0.39) (As, Epperlein, and Mooney, 1988:2408–2414). As et $al.$ profiled five traps that were related to the well. The profile exhibits a maximum trap concentration located 88 nm from the Schottky junction. However, the well was located 100 nm from the Schottky junction. Thus, they tentatively attributed the traps to defects at the interface between the AlGaAs barrier that was grown last and the GaAs well. The reasoning behind suspecting that the emissions are from interface defects rather than from the energy levels in the well is that this portion of the top AlGaAs barrier layer was grown under non-optimum conditions. The growth conditions used for the top barrier layer are known to produce defects of energy comparable to the measured energies.

The traps were also profiled several times using a different filling pulse duration for each profile. The profiles showed a peak that shifted toward the surface of the Schottky

diode and away from the well with decreasing filling pulse width. The shift was greater with higher energy trapping levels. It was stated that the presence of confined electrons in the quantum well increases the depletion width. For profile measurements, this would result in a virtual shift to smaller depth values when more electrons are captured in the quantum well when longer filling pulses are used. The shift in the peak of the profiles toward the Schottky junction with increased filling of the well is therefore the opposite of what is expected from the increased filling pulse width.

It was also noted that the amplitude of the response increased logarithmically with filling pulse width. The reason cited in the report for the logarithmic relationship of the DLTS amplitude on the filling pulse duration and the shift of the trap profile is the effect of a capture barrier arising from the band bending in the AlGaAs barrier adjacent to the well.

In an investigation of the $GaAs/Al_xGa_{1-x}As$ system using admittance spectroscopy and DLTS, Ababou et $al.$ were unable to observe any signal from the well. They attributed this to a DX trap in the barrier (Ababou, Guillot, and Regreny, 1992:4134–4138). The barrier material was bulk $Al_{0.43}Ga_{0.57}As$ in one sample and a $Al_{0.46}Ga_{0.54}As$ superlattice in a second sample. A DLTS response from the energy levels in the quantum well was expected at low temperature. However, the high concentration of DX centers in the barrier material prevented measurements below 150 K by depleting the carriers, thereby preventing the well from being filled. The decrease in available carriers was apparent from a large decrease in capacitance below 150 K. A band offset of 0.35 eV

from the Γ-band in the well to the X-band in the barrier was measured using admittance spectroscopy.

Band offset measurements of a GaAs/GaInAs/GaAs QW were made by DLTS using an improved analysis that treats the well as one trap with N place (Letartre, Stievenard and Barbier, 1991:1047–1049), rather than N traps with one place each. The latter approach was taken in previous treatments of the problem, treating the well as a 'giant trap' (Ababou, Guillot, and Regreny, 1992:4134–4138). The new approach improves the accuracy by taking into account the shift of the Fermi level as the concentration of carriers in the well changes during emission. The DLTS measurements made using this method are corroborated by the C-V profiling technique. The measurement of a band offset of 142 meV was reported to have an accuracy of ~10 meV by either method for the GaAs/GaInAs/GaAs QW. The measured spectra was much broader than expected. The broadening in this case was explained by a tunneling of the electrons from the well at a constant rate. At low temperatures, the emission rate is a combination of the tunneling and thermionic emission rates. As the temperature increases, the tunneling rate remains constant, but the thermionic emission rate increases exponentially, gradually making the tunneling component insignificant. Thus, the tunneling component shows up as a signal only at low temperature.

DLTS measurements are also a good method for determining the band offset on a quantum well structure when the layers are strained (Debbar and Bhattacharya, 1987:3845–3847). The expressions used for the emission rate of electrons from a quantum well formed by 150 Å $In_{0.2}Ga_{0.8}As$ in $Al_{0.16}Ga_{0.84}As$ treat the well as a giant trap,

so that the equations are slightly different from those derived by Letartre *et al.* (Letartre, Stievenard and Barbier, 1991:1047–1049). First, the spectra shown in the report were used to compare the signal from a sample with a quantum well to one with the quantum well etched off. The absense of a low temperature peak in the sample with the QW etched off showed that the signal was due to the QW. The peak attributed to the quantum well was on the low temperature side of a uniformly distributed deep level that is commonly observed in $Al_{0.16}Ga_{0.84}As$. The measured band offset for the conduction band was 204 meV. For comparison, the band offset is estimated to be 192 meV from a general rule of thumb that the conduction band offset is 60% of the band gap difference between the two materials. The difference of 12 meV was attributed to lattice mismatch. The sample with a quantum well also had a background trap emission over the entire temperature range of the DLTS spectra, which is typical of interface states. A wider well of the same composition and mismatch produced a larger background signal, indicating that the background response was from interface states. The strained lattice in the vicinity of the wider well is more likely to relax and cause defects at the hetero-interface.

Behavior different from natural deep levels was noted in a study of a $Al_{0.35}Ga_{0.65}As$ barrier and 800 Å thick GaAs well located 0.3 μm from a Schottky barrier (Martin *et al.*, 1983:4689–4691). Trap characteristics were found to depend heavily on the experimental conditions. Increasing the filling pulse width in several steps from 5 μsec to 2 msec gave a steady increase in peak height by a factor of three overall, and increase in the temperature of the peak by ~5 K. It is expected that increasing the filling pulse width would fill states in the well with lower emission energy, with subsequent measurement of lower energy

thermal emissions at lower temperature. This is opposite to the increase in peak response temperature that was observed. Increasing the filling pulse amplitude from 1 V to 2 V had a more pronounced effect. The temperature of the peak response increased 25 K, and the peak height increased fifty times. Changing the measurement bias from 0 V to -1 V reduced the peak height for all filling pulse amplitudes, with the response going to zero for a pulse height less than 2.5 V. The shift of the temperature of the peak signal with filling pulse width and filling pulse magnitude was left unexplained. A large uncertainty in trap characteristics was also reported. For example, a 2 V filling pulse resulted in a trap energy of 0.35 eV, capture cross section of 4×10^{-15} cm^2, and concentration of 4.5×10^{12} cm^{-3}. A 3 V filling pulse increased the emission energy to 0.53 eV, increased the capture cross section to 1.8×10^{-13} cm^2, and increased the effective trap density to 4.5×10^{14} cm^{-3}.

Previous Reports Related to the Dynamics of Carrier Capture by a Quantum Well

An area of importance to quantum well device design and operation is the manner in which carriers are captured by a quantum well, in addition to the confining potential. The issue concerning DLTS measurements is whether or not the carriers trapped in the well reach thermal equilibrium much sooner than the typical DLTS filling pulse duration. Otherwise, emission could be from carriers distributed throughout the energy levels in the well, resulting in a distribution of measured energies. This section presents a summary of reports dealing with the transfer of carriers to and from a potential well, with consideration given to carrier trapping that involves a change in momentum. Representative relaxation rates are also given.

There has been some controversy regarding the contributions to resonant and non-resonant tunneling from the carriers in the discrete states from different symmetry points in a GaAs/AlAs type-I multiple quantum well (Mendes, Calleja, and Wang, 1986:6026; Bonnefoi et al., 1987:344; Tsuchiya and Sakaki, 1987:1503). In this material the minimum conduction band energy of the AlAs barrier is at X, and the minimum conduction band energy of the GaAs well is at Γ. Resonant tunneling does not involve a change in momentum, whereas non-resonant tunneling does. The multiband tight-binding model (Rousseau, Wang, and Schulman, 1989:1341) and the scattering-matrix formalism (Ko and Inkson, 1988:9945) give energy levels in the well bounded by the Γ minimum of the barriers. However, a simplified single-band tight-binding model predicts that the states in the well are bounded by the lowest energy point of the barrier regardless of its symmetry (Schulz and Goncalves da Silva, 1987:8126). Carrier transfer in a multiple-quantum well structure is found experimentally to occur by both non-resonant and resonant tunneling via the X point of the conduction band minimum in the barrier layers. Confined states in adjacent Γ wells are found to be coupled through the X-band minimum of the barrier if the energy of the confined state is near the energy of the barrier minimum (Dutta et al., 1990:1474–1477). An electric field applied to a level that is nearly degenerate with the barrier energy increases the oscillator strength and reduces the coupling to the barrier (Dutta et al., 1992:282–286). The alignment of the energy level at the top of the well, and the electric field applied can therefore have an impact on the capture and emission rates measured by DLTS.

Thermionic emission current and photoluminescence have been used to experimentally determine the energy states in a well (Dutta, Choi, and Newman, 1989:2429–2431). In superlattices composed of 50 periods of 39 Å GaAs well and 75 Å AlAs barrier, the actual thermionic emission current was compared to the theoretical current, assuming emission is to the X-band of the barrier from the carriers confined in the well by either the X or the Γ potentials. The X-band is the minimum energy in the AlAs barrier. The well width was chosen so that the highest Γ potential confined state energy was higher than the highest X potential confined state energy. The temperature dependence of the thermionic current coincided with emission from the level closest to the X-band barrier. Emission occurred from the Γ confined state at 53 meV below the X-band barrier rather than from the X confined state at 154 meV below the X-band barrier. A sample was also designed with a direct gap barrier, keeping the emission energies at 53 and 154 meV, the same as the sample with an indirect gap barrier. From a comparison of the magnitudes of the thermionic emission currents between the two samples, it was determined that the probability of carrier transfer between wells via Γ-X-Γ real-space intervalley transfer is 9.1×10^{-3} times lower than Γ-Γ-Γ coupling, consistent with the multi-band tight-binding model.

The scattering mean free path comes into play in the operation of negative differential resistance devices. In a structure of multiple layers of modulation doped GaAs and $Al_xGa_{1-x}As$, an electric field applied parallel to the potential wells heats the electrons high enough in the conduction band of the GaAs wells to transfer the electrons to the wider gap $Al_xGa_{1-x}As$ by thermionic emission (Hess *et al.*, 1979:469–471). The

Al$_x$Ga$_{1-x}$As has a lower electron mobility resulting in a sudden shift of the transferred carriers to a higher resistivity path, and the negative differential resistance effect is observed. The time needed for the electrons to return to the GaAs after reducing the field is the switching time, t_s, which is given by

$$t_s = 4L_2^2 / \pi^2 D,$$

where L_2 is the thickness of the barrier and D is the diffusion constant in the barrier. The diffusion limited scattering requires that the mean free path for phonon emission is smaller than the thickness of the well, as discussed earlier in this chapter in the section on theoretical aspects of the capture cross section. If the mean free path for phonon emission is longer than the width of the well, the probability of an electron being captured in the well is reduced by L_1/λ_{ph}, where L_1 is the well width, and λ_{ph} is the mean free path for phonon emission from the electron at the top of the well. In this case, using typical values such as $L_1=L_2=400$ Å, $\lambda_{ph} <10^{-4}$ cm, and $D=10$ cm^2/s, the scattering time was estimated to be in the 10 psec range. The magnitude of the scattering time indicates that the relaxation rate of carriers in the well during a DLTS filling pulse should be insignificant compared to a typical filling pulse width of 1 ms.

Subpicosecond time-resolved Raman spectroscopy has been used to observe the dynamics of small wave-vector phonons in (100) GaAs (Kash, Tsang and Hvam, 1985:2151–2154). For the excitation energy of 2.11 eV, each optically excited electron creates a series of about sixteen LO phonon emissions in a cascade when relaxing to the band edge. It was found that the electron-phonon scattering time is about 165 fs. Under higher pump intensity, where the injected carrier concentration exceeds 10^{18} cm^{-3}, it was

found that the strength of the allowed LO-phonon scattering is reduced by screening from the additional electrons. These findings indicate that for QW carrier densities in excess of 10^{12} cm^{-2}, the relaxation rate may be diminished due to screening.

Interface States

The band offset measurements have been found to be very sensitive to interface state density, even in lattice-matched systems such as GaAs/Al$_x$Ga$_{1-x}$As. If positive charges from interface states on one side of a junction are matched by the same number of negative charges on the other side of the junction, the resulting dipole layer will modify the band line-up. The alteration of the band offset is proportional to the concentration of defects and the dipole spacing (Harrison, 1985:1231–1238). If the spacing is on the order of a bond length d, a high density of defects is required to produce any significant shift. In a tetrahedral semiconductor, the (111) plane has $3^{\frac{1}{2}}/(4d^2)$ atoms per square centimeter.

If the fraction of the atoms in the (111) plane with charge q is X, and the spacing d, then the shift due to the dipole is $3^{\frac{1}{2}}\pi X q^2/\varepsilon d$, or $2.78X$ eV for silicon. So, if 1% of the atomic sites at the interface are defects, the shift in band lineup is only on the order of 30 meV. Larger differences between actual and theoretical band offsets may indicate that the interface defects extend more to three dimensions.

Measurements of the band offset between AlAs and GaAs provides an example of the influence of the interface quality on the band offset. The measured band offset is also found to depend on the order of growth. AlAs on GaAs has a valence band offset of 0.15

eV (Waldrop *et al.*, 1981:573), whereas GaAs on AlAs has a valence band offset of 0.40 eV. The band offset was checked by extrapolation of GaAs/$Al_xGa_{1-x}As$ band lineup data for various values of x. The extrapolated band offset for x=1 corresponds to a value of 0.20 eV which is intermediate between the values of 0.15 and 0.40 eV determined by Waldrop *et al.* (Dingle, 1975:21). This points out the need to qualify the band offset measurements with measurement of the interface states. The interface states will also have an effect on the lifetime of carriers in the well, providing a continuum of states for non-radiative recombination.

DLTS Technique for Interface States

Conventional (constant voltage mode) DLTS has been used for evaluating interface traps in MOS (Schulz and Johnson, 1978:481; Yamasaki, Yoshida and Sugano, 1979:113), and metal-semiconductor junctions (Qhang *et al.*, 1987:341). The CC-DLTS mode has been used for evaluating interface states in MOS structures (Schulz and Klausmann, 1979:169) and p-n junctions (Ikossi-Anastasiou *et al.*, 1992:297–299). The analysis of interface states using either DLTS mode differs from the analysis of bulk levels in that the states are spatially localized but continuously distributed in energy, rather than spatially uniform but at a discrete energy.

The experimental procedure involves the application of a filling pulse that brings the Fermi level to the band edge. Then the measurement condition is established by increasing the reverse bias to bring the Fermi level to mid-gap. Immediately after traps at the interface are filled and the measurement condition has been established, the junction is

in a nonequilibrium condition. In the CC-DLTS mode, the relaxation back to equilibrium is monitored by a voltage transient in the same manner as for bulk defects. The voltage transient is generated by a feedback circuit that keeps the capacitance at a constant value. The signal is proportional to the change of charge trapped at the interface, $dV=dQ_{it}/C$, where Q_{it} is the charge per unit area at the interface. For a discrete bulk trap, a peak will appear in the rate window plot when the emission rate is

$$e_n = \frac{\ln\left(\dfrac{t_1}{t_2}\right)}{t_1 - t_2},$$

where t_1 and t_2 are the sampling times, defining the rate window. For interface states distributed in energy across the band gap, a very broad peak appears, rather than a relatively sharp peak from a discrete defect. The broad peak can be converted to an interface state density plot using

$$N_{ss}(E) = \left(\frac{C}{qkT}\right)\Delta V(t_1,t_2)\ln\left(\frac{t_1}{t_2}\right).$$

The temperature scale is converted to an energy scale using

$$\Delta E = kT\ln\left(\sigma_n v_n N_c \frac{t_1 - t_2}{\ln\left(\dfrac{t_1}{t_2}\right)}\right),$$

where σ_n is the electron capture cross section, assumed to be constant, v_T is the mean thermal velocity for electrons, and N_c is the effective density of states in the conduction band. Both the energy resolution and the energy of the interface states that contribute to the DLTS signal increase linearly with temperature. The energy resolution is therefore

greatest at low temperature where the interface state density is expected to vary most rapidly. The lower energy resolution obtained at high temperature provides enhanced sensitivity for detecting the low density of interface states typically found near midgap (Schulz and Klausmann, 1979:169–175).

Besides a broader rate-window peak, interface states can be distinguished from bulk states by comparing the rate-window plots at two different filling pulse heights. Decreasing the filling pulse height avoids filling traps closer to the band edge, resulting in a reduced response at lower temperatures from the lower energy interface states. On the other hand, the spectra for a discrete trap would not change shape.

Strain Induced Defects

Desirable quantum well properties may be obtained by growing the well as a strained layer. For example, the quantum efficiency may be improved by increasing the antimony mole percent in the InAsSb active layer, or the aluminum or arsenic mole percent in the AlGaAsSb confining region. A change in composition may be accompanied by strain from lattice mismatch. The strain may then force nonradiative recombination defect centers to move to the edge of the crystal (Fitzgerald *et al.*, 1988:693–703). However, too much strain could result in lattice relaxation, forming interface dislocation defects. Sources of strain in the quantum well device structure are the substrate/buffer interface, the well/barrier layer interface, and the barrier/cladding layer interface if separate electrical and optical confining layers are used. An approach to determine the critical

thickness experimentally would be to first approximate the critical thickness from the calculated theoretical critical thickness for one of the semiconductors used in an interface. Then grow samples with layers greater than the calculated critical thickness, and samples with layers less than the calculated critical thickness (Huang *et al.*, 1992:633–640). DLTS profile measurements could then be used to determine the extent and concentration of the defects verifying the calculated critical thickness. However, a dislocation in itself cannot be detected by DLTS. Dislocations would most probably occur along planes of lowest density. Dislocations along a family of planes of equivalent density can cause the dislocations to cross and terminate close to the heterointerface. For example, dislocations from a [100] GaAs/GaInAs interface create 60° dislocations confined to 300-400 Å of the interface in the GaAs (Chen, Chu and Cho, 1985:1145).

Critical Thickness Derivation

The balance between forces at a heterointerface are used to determine the film thickness at which misfit dislocations will be formed. The driving force is the misfit strain. The opposing forces are the tension in the misfit dislocation line, and the Peierls stress (Matthews, Mader, and Light, 1970:3800–3804). The force, F_ε, due to the misfit strain is given by

$$F_\varepsilon = \frac{2G\varepsilon bh(1+v)\cos\lambda}{1-v},$$

where b is the Burgers vector of the dislocation, G is the shear modulus, ε is the elastic strain, h is the film thickness, v is Poisson's ratio, and λ is the angle between the slip

direction and that direction in the film plane which is perpendicular to the line of intersection of the slip plane and the specimen surface. The tension, F_l, in the misfit dislocation line is given by

$$F_l = \frac{Gb^2}{4\pi(1-v)}(1 - v\cos^2\theta)\ln\left(\frac{h}{b}\right),$$

where θ is the angle between the misfit dislocation line and its Burgers vector. Finally, the Peierls stress is a friction force on the dislocation, restraining its motion. The force, F_f, from the Peierls stress is given by

$$F_f = \frac{h}{\cos\phi}\frac{vkT}{bD_0}\exp\left(\frac{U}{kT}\right),$$

in which ϕ is the angle between the film surface and the normal to the slip plane, v is the dislocation velocity, and $D_0\exp(-U/kT)$ is the diffusion coefficient of the leading edge of the dislocation. The relation between v and the rate of change of dislocation line density, δ', is given by

$$v = \frac{\delta'}{\rho\, b\cos\lambda},$$

where ρ is the number of dislocation lines per unit area that migrate to generate a misfit dislocation line. Equating forces and substituting for v results in a differential equation with a boundary condition of $\delta=0$ at $t=0$, where δ is the dislocation line density. The solution describes the conversion of elastic strain into plastic strain as a function of time,

$$\delta = \beta(1 - \exp(-\alpha t)),$$

where

$$\alpha = \frac{2Gb^3\rho(1+v)\cos\phi\cos^2\lambda D_0 \exp\left(-\dfrac{U}{kT}\right)}{(1-v)kT},$$

and

$$\beta = f - \left(\frac{b(1-v\cos^2\theta)}{8\pi h(1+v)\cos\lambda}\right)\ln\left(\frac{h}{b}\right),$$

where f is the misfit between the bulk lattice parameters of the two crystals. The elastic strain (ε), fraction of misfit accommodated by dislocation lines (δ), and lattice misfit (f) are related by

$$\varepsilon + \delta = f.$$

These equations predict that if the film thickness, h, is large enough so that

$$h > \left(\frac{b(1-v\cos^2\theta)}{8\pi f(1+v)\cos\lambda}\right)\ln\left(\frac{h}{b}\right),$$

and $\alpha t \gg 1$, the elastic strain relaxes and is converted into misfit dislocations. The elastic strain is then given by

$$\varepsilon = f - \delta = \left(\frac{b(1-v\cos^2\theta)}{8\pi h(1+v)\cos\lambda}\right)\ln\left(\frac{h}{b}\right).$$

Analyses such as this predict that the substrate or buffer material with the lower elastic strain force will be deformed more easily (Fitzgerald *et al.*, 1988:693–700). The model also predicts that dislocations with appropriate Burgers vectors can be expelled away from the interface as the density of dislocations increases at the interface.

IV. RESULTS AND DISCUSSION

Deep Levels in $Al_xGa_{1-x}As_ySb_{1-y}$

There has been some limited characterization of $Al_xGa_{1-x}As_ySb_{1-y}$ used in the barrier and cladding layers of 2-4 μm diode lasers. The deep levels in GaSb (x=1) range from 0.25-0.63 eV for hole traps (Polyakov *et al.*, 1992:337–343; Kuramochi *et al.*, 1993:2664–2666; Shen *et al.*, 1993:8313–8318) and 0.25-0.315 eV for electron traps (Polyakov *et al.*, 1992:337–343; Poole *et al.*, 1990:1645–1647; Hubik *et al.*, 1993). The traps reported in the quaternary $Al_xGa_{1-x}As_ySb_{1-y}$ compounds have so far been limited to investigation of electron traps ranging from 0.38-0.51 eV. All traps have relatively large capture cross sections, some with large capture barriers, and some with trap concentrations as high as the shallow dopant concentration (Ideshita *et al.*, 1992:2549; Takeda *et al.*, 1987:L273–275; Meyer *et al.*, 1993:475–478; Zhu *et al.*, 1987:127–130; Nakagawa *et al.*, 1990:1551–1553).

Deep level transient spectroscopy (DLTS) was used to characterize the defect levels in $Al_xGa_{1-x}As_ySb_{1-y}$ for x=0, 0.5, 0.6, and 1.0 in order to aid in device design predictions and determine areas of potential improvement of laser-device-quality material. Temperature dependent Hall measurements were also used to look at the primary donor characteristics in $Al_{0.9}Ga_{0.1}As_{0.08}Sb_{0.92}$. The information presented here can be used to identify likely non-radiative recombination centers. Particular emphasis is placed on a double acceptor attributed to a Ga antisite defect (Ga_{Sb}), and the DX center trap. The Ga_{Sb} antisite defect has been reported to have ionization energies over a wide range, as

measured previously by photoluminescence, photoconductivity, absorption and Hall effect measurements. The Ga_{Sb} antisite defect is responsible for the background p-type conductivity of $Al_xGa_{1-x}As_ySb_{1-y}$. The DX center has been characterized extensively in AlGaAs but only to a limited extent in $Al_xGa_{1-x}As_ySb_{1-y}$ and other compound semiconductors. The DX center is technologically important because its concentration can be as high as the shallow dopant concentration.

Sample Descriptions

The samples investigated were grown in an Intevac Gen II molecular beam epitaxy system equipped with conventional ion pumps. The undoped $Al_xGa_{1-x}As_ySb_{1-y}$ has a characteristic background p-type conductivity in the low $10^{16} \, cm^{-3}$. The p-type conductivity is caused by the Ga_{Sb} antisite defect. The background doping level in this range is a property inherent to AlGaAsSb grown by various methods. For each $Al_xGa_{1-x}As_ySb_{1-y}$ epitaxial layer, the growth conditions were set such that the lattice constant of the epitaxial layer equaled the lattice constant of the GaSb substrate at room temperature. The y-value of $Al_xGa_{1-x}As_ySb_{1-y}$ for a desired x-value lattice matched to GaSb is

$$y = \frac{0.0396x}{0.4426 + 0.0318x}.$$

Mounting of the GaSb substrates during the MBE growth was done using In alloyed to the back side of the substrate, which also subsequently provided an ohmic

contact for electrical measurements. Mesa etching was used to define the diode area. The samples were packaged in TO-5 cans for DLTS measurements.

DLTS measurements were performed using three types of structures. The first two sample structures have heterojunctions in the lightly doped side as shown in Figure IV-1. The first diode structure is a *p-n* junction of n^+-GaSb/*p*-GaSb. The *p*-type region also includes a heterojunction between the *p*-GaSb and *p*-$Al_{0.6}Ga_{0.4}As_{0.05}Sb_{0.95}$. The *n*-type region has 20 times the carrier concentration of the *p*-type region, so that most of the depletion will take place in the p-type region. This allows characterization of the more lightly doped *p*-type GaSb and the *p*-type $Al_{0.6}Ga_{0.4}As_{0.05}Sb_{0.95}$ at deeper depletion for hole traps and minority carrier electron traps. The *p*-$Al_{0.6}Ga_{0.4}As_{0.05}Sb_{0.95}$ has a p^+-GaSb cap layer to prevent oxidation. Ohmic contact to the p^+-GaSb was made using 200 Å of Au, 50 Å of Zn, and 3000 Å of Au, annealed at 200 °C for 30 seconds.

The second structure consists of a metal/$Al_{0.5}Ga_{0.5}As_{0.04}Sb_{0.96}$-oxide/*p*-$Al_{0.5}Ga_{0.5}As_{0.04}Sb_{0.96}$/*p*-GaSb/$p^+$-GaSb, forming a metal oxide semiconductor (MOS) capacitor. The top layer of AlGaAsSb-oxide is formed by dipping the sample in deionized water at room temperature for 5 min, which oxidizes part of the exposed $Al_{0.5}Ga_{0.5}As_{0.04}Sb_{0.96}$. The oxide thickness is approximately 100 Å. The AlGaAsSb oxide was contacted with 300 Å of Ti and 3000 Å of Au. This sample also includes a heterojunction in the *p*-type region for characterization of *p*-type $Al_{0.5}Ga_{0.5}As_{0.04}Sb_{0.96}$ and *p*-type GaSb at deeper depletion.

p-n Junction/Heterojunction

Au/Zn/Au

450 Å p-GaSb

0.96 μm 8×10^{16} cm^{-3}
p-Al$_{0.6}$Ga$_{0.4}$As$_{0.05}$Sb$_{0.95}$

0.41 μm 2×10^{16} cm^{-3} p-GaSb

4×10^{17} cm^{-3} n$^+$-GaSb Substrate

conductive epoxy

TO-5 Can

MOS/Heterojunction

Ti/Au

AlGaAsSb-Oxide

~1.45 μm 5×10^{16} cm^{-3}
p-Al$_{0.5}$Ga$_{0.5}$As$_{0.04}$Sb$_{0.96}$

0.43 μm 2×10^{16} cm^{-3} GaSb

2×10^{17} cm^{-3} p$^+$-GaSb Substrate

conductive epoxy
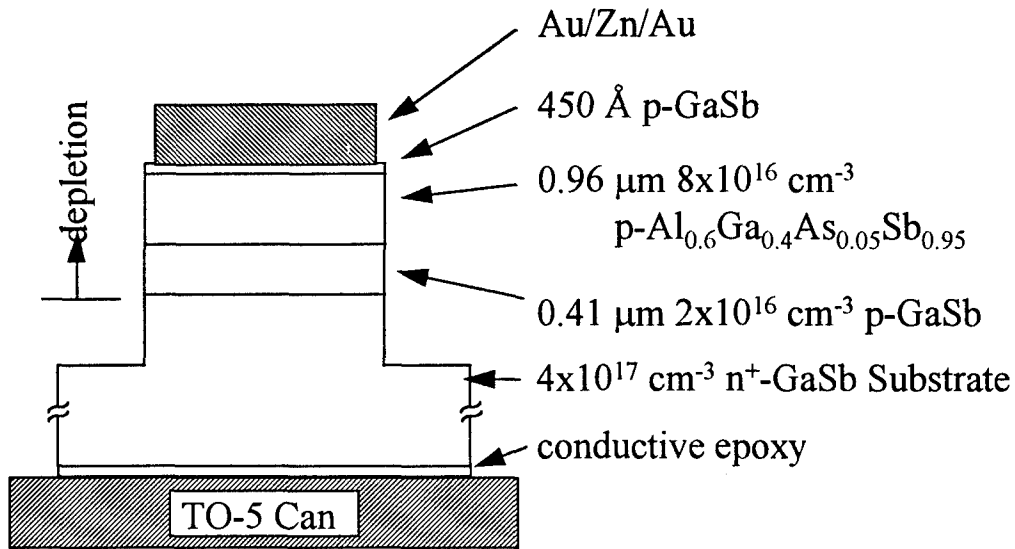
TO-5 Can
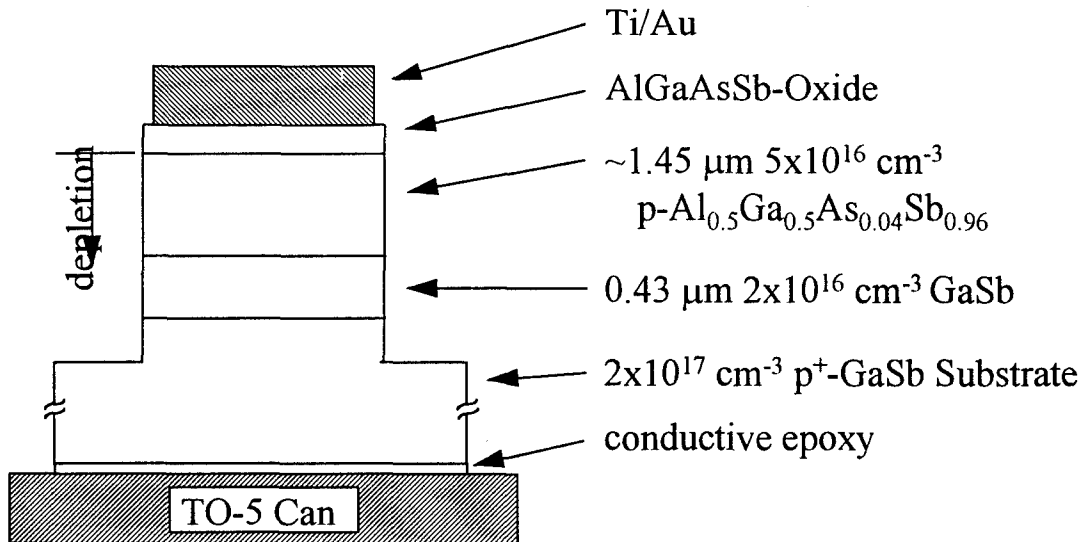
Figure IV-1. p-n junction/heterojunction and MOS/heterojunction sample structures that include a heterojunction in the depletion region. DLTS is used with C-V measurements to characterize the deep levels on either side of the heterojunctions.

The third sample is a *p-n* junction consisting of p-AlAs$_{0.07}$Sb$_{0.93}$/n^+-AlAs$_{0.07}$Sb$_{0.93}$/n^+-GaSb. There is actually a QW located farther from the junction in the p-AlAs$_{0.07}$Sb$_{0.93}$. Emission from the QW was avoided by selecting the biases to include only emission from the p-AlAs$_{0.07}$Sb$_{0.93}$ and the n^+-AlAs$_{0.07}$Sb$_{0.93}$ at the p-n junction. The sample is therefore treated as a simple p-n junction in the bias range that was used. The QW emission will be described in a later section.

DLTS measurements on the p-n junction are straightforward, but measurement of deep levels in the diodes with heterojunctions requires knowledge of the relationship between bias and the region being depleted or filled. The C-V profiles are used to determine appropriate biases needed in DLTS measurements to probe each of the semiconductors that make up the heterojunction.

C-V Measurements of p-Al$_{0.6}$Ga$_{0.4}$As$_{0.05}$Sb$_{0.95}$/p-GaSb/n$^+$-GaSb

A representative plot of bias voltage versus apparent depletion width for the p-Al$_{0.6}$Ga$_{0.4}$As$_{0.05}$Sb$_{0.95}$/p-GaSb/n$^+$-GaSb heterojunction/p-n junction sample measured at various temperatures is given in Figure IV-2. Conventional C-V profiling of a single p-n junction is based on the change in capacitance with bias according to

$$C = \sqrt{\frac{q\varepsilon}{2(V + \varphi_{bi})} \frac{N_a N_d}{N_a + N_d}},$$

where N_a is the ionized acceptor concentration in the p-side, N_d is the ionized donor concentration in the n-side, V is the applied bias, and φ_{bi} is the built-in potential. The
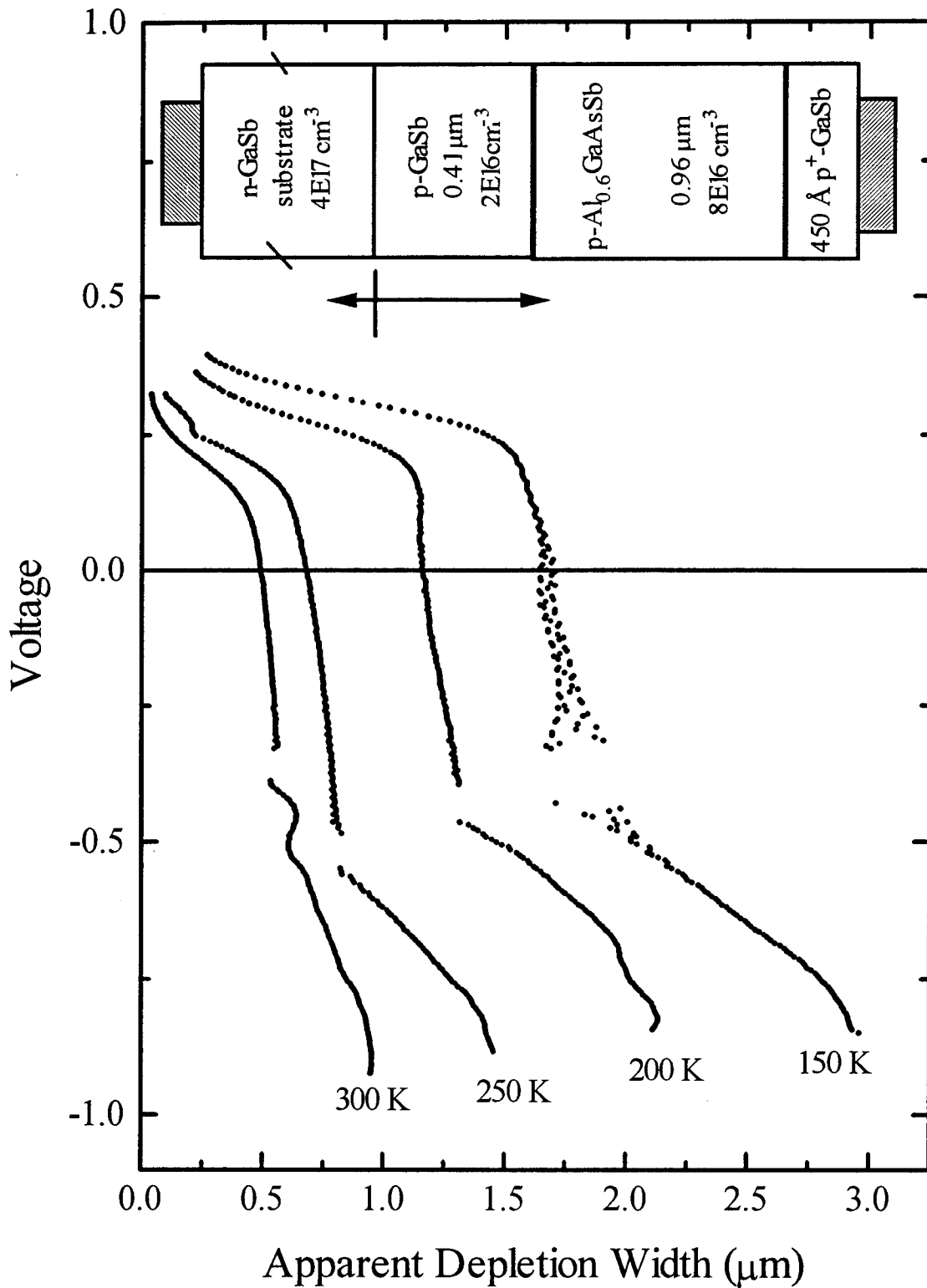
Figure IV-2. Voltage versus apparent depletion width for the *p-n* junction/heterojunction.

The figure contains the following labels:

Diagram labels:
- r-GaSb substrate 4E17 cm^{-3}
- p-GaSb 0.41 µm 2E16 cm^{-3}
- p-Al$_{0.6}$GaAsSb 0.96 µm 8E16 cm^{-3}
- 450 Å p$^+$-GaSb

Axis labels:
- Voltage (vertical axis)
- Apparent Depletion Width (µm) (horizontal axis)

Curve labels: 300 K, 250 K, 200 K, 150 K

capacitance of two junctions is a series combination of the capacitance of both junctions, so that conventional C-V profiling analysis does not apply directly. However, for the purpose of DLTS measurements, an apparent depletion width, W_{app}, can be calculated from the measured capacitance, C_{meas}, using

$$W_{app} = \frac{\varepsilon A}{C_{meas}}.$$

where C_{meas} is the series combination of the homojunction capacitance, C_{hom}, and the heterojunction capacitance, C_{het}, i.e.,

$$C_{meas} = \left(\frac{1}{C_{hom}} + \frac{1}{C_{het}}\right)^{-1}.$$

Similarly, an apparent carrier concentration can be calculated from the differential slope of $1/C^2$ measurements as a function of applied bias voltage according to

$$N_{app} = -\frac{1}{q\varepsilon A^2}\frac{dV}{d\left(\dfrac{1}{C_{meas}^2}\right)}.$$

These are the same equations used for a simple junction except that the measured capacitance, C_{meas}, is the series combination of the homojunction capacitance and the heterojunction capacitance.

The total apparent depletion width can extend into the n- and p-GaSb side of the p-n junction, as well as the p-$Al_{0.6}Ga_{0.4}As_{0.05}Sb_{0.95}$ and p-GaSb sides of the heterojunction. The depletion width of the p-n junction increases from near zero until it meets the heterojunction depletion region as the forward bias voltage decreases, becomes zero, and the reverse bias voltage increases. Then, further depletion will take place beyond the

heterojunction on the p-Al$_{0.6}$Ga$_{0.4}$As$_{0.05}$Sb$_{0.95}$ side as the reverse bias voltage increases. At zero bias, the p-GaSb region is almost depleted for all temperatures. As the reverse bias voltage increases, the apparent depletion width remains about the same until the depletion width extends deeper into the p-Al$_{0.6}$Ga$_{0.4}$As$_{0.05}$Sb$_{0.95}$ layer. Free holes accumulate in the narrow gap material at the barrier presented by the wide gap material, and are depleted from the wide gap material in the region immediately adjacent to the heterojunction. A region of apparently high hole concentration results when the applied bias voltage sweeps through the triangular well created from the band bending at the heterojunction (Kroemer *et al.*, 1980:295–297). The band bending at zero bias is shown in Figure IV-3 for the two samples that include a heterojunction in the depletion region. The arrow points out the location of the triangular notch well. An incremental increase in reverse bias empties some of the free holes from the triangular notch well in the valence band. The high concentration of carriers in the well requires a significantly larger bias change to empty the carriers than the voltage change required to ionize the uniformly distributed bulk impurities. This appears as a nearly vertical variation of voltage versus apparent depletion width shown in Figure IV-2. The position of the heterojunction is characterized by a nearly constant depletion width as the reverse bias voltage changes.

In addition to the vertical section of the bias versus apparent depletion width associated with the heterojunction, there are several other notable features of the C-V measurements. One of the features is a shift in apparent heterojunction position with temperature indicating a carrier freeze-out in the n^+-GaSb adding to the depletion width of the p-side. It would be expected that the semiconductor layer material with the highest
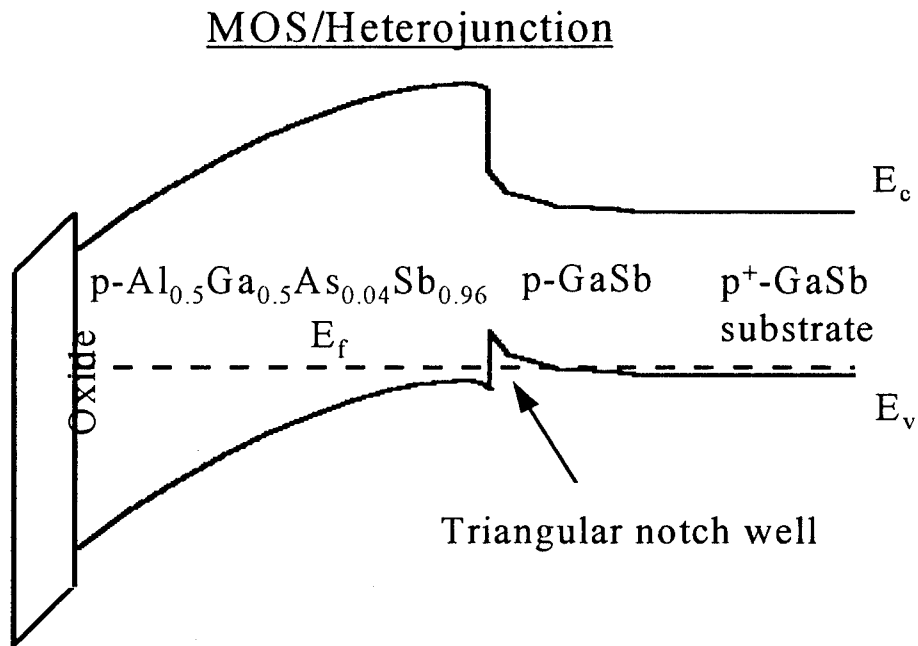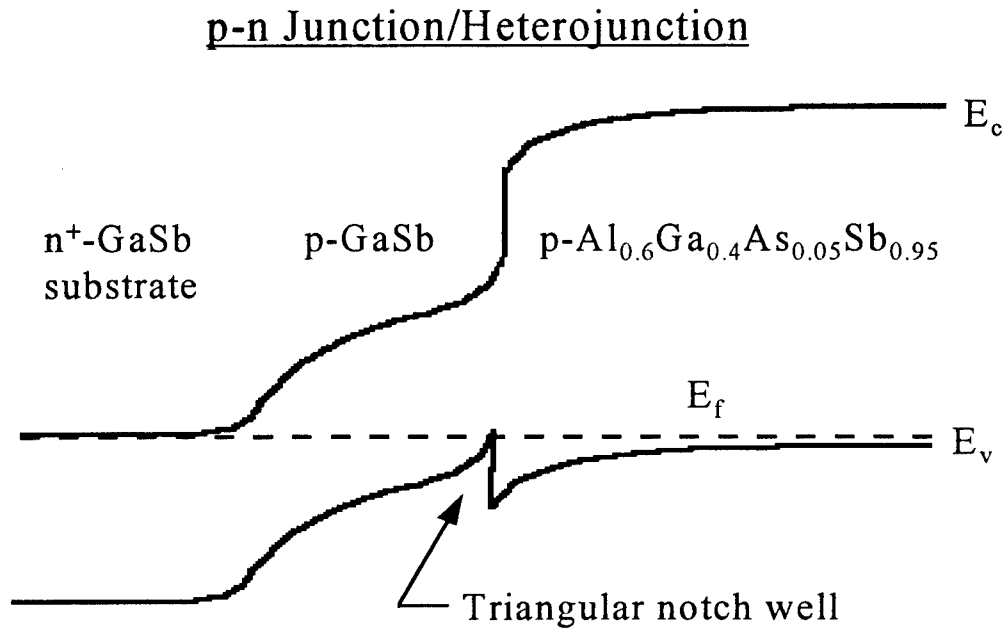
Figure IV-3. Band bending at zero bias for the two samples with heterojunctions in the depletion region.

dopant binding energy would experience carrier freeze-out first as the temperature is reduced. However, it will be shown later that the n^+-GaSb layer loses free carriers to a deep level associated with the shallow dopant even though the $Al_{0.6}Ga_{0.4}As_{0.05}Sb_{0.95}$ layer has a higher shallow dopant binding energy (Ideshita *et al.*, 1992:2549; Nicholas *et al.*, 1987:298–303). The measured apparent shift in the position of the heterojunction is due mainly to the increase in depletion of the heavily doped n^+-side of the n^+-p junction. It should be noted that the measured capacitance across the p-p-n junction, as two capacitors in series, will be smaller than either one of the two individual junctions. As a result, the apparent depletion width shown in Figure IV-2 is larger than the actual value.

Another feature reported occasionally is the discontinuity at the bottom of the vertical section in Figure IV-2 near the heterojunction (Leu and Forrest, 1988:5030–5041; Jeong *et al.*, 1987:792–795; Andre *et al.*, 1986:F6). The points making up the discontinuity were deleted so that the other features could be easily seen. Leu and Forrest attributed the discontinuity either to interface states at the heterojunction, or to confined states in the triangular well at the interface. A sheet of charge from the interface states integrates in Poisson's equation to a delta function. However, a property of interface states is that they have a distribution of energies so that they should respond to the test frequency at a range of biases. The appearance of the discrete discontinuity suggests that it is due to the confined states in the triangular well. C-V measurements of the MOS diode points even more strongly to an assignment of the discontinuity to confined states in the triangular well.

It has been found that in order to accurately model the carrier concentration profile, the interface trap energy density, the capacitance meter measurement frequency, and the measurement temperature need to be taken into account (Leu and Forrest, 1988:5030–5041). Fortunately, the actual concentration profile is not needed for the DLTS measurements since the p-GaSb/p-Al$_{0.6}$Ga$_{0.4}$As$_{0.05}$Sb$_{0.95}$ heterojunction feature shows up prominently as a nearly vertical line in Figure IV-2 throughout the entire temperature range. The voltage versus depletion width is all that is necessary for DLTS measurements on multi-layer structures so that biases corresponding to either side of the heterojunction region, and thus the spatial range of filled traps that are able to emit can be determined. Two bias regimes can be considered. As the depletion width increases from near zero, depletion of the p-n junction and the heterojunction will increase until the p-n depletion region meets the heterojunction depletion region. Then, further depletion will take place only beyond the heterojunction region on the side of the heterojunction opposite to the p-n junction. These two cases can be used to determine the source layer for DLTS emissions.

For example, suppose a trap emission is measured using condition A shown in Figure IV-4. Condition A fills traps in both materials making up the heterojunction. The measurement bias includes depletion of the p-GaSb region between the p-n junction and the heterojunction, and the p-Al$_{0.6}$Ga$_{0.4}$AsSb region beyond the heterojunction. This single measurement of emission A would not allow the source layer to be identified. A second measurement, indicated by condition B and emission B, which probes only the p-Al$_{0.6}$Ga$_{0.4}$AsSb region beyond the heterojunction interface needs to be compared to the

Filling Condition A
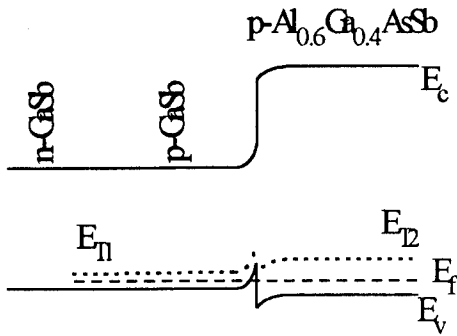
Filling Condition B
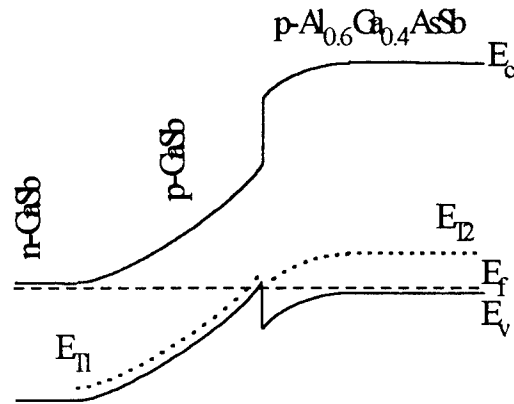
Emission A
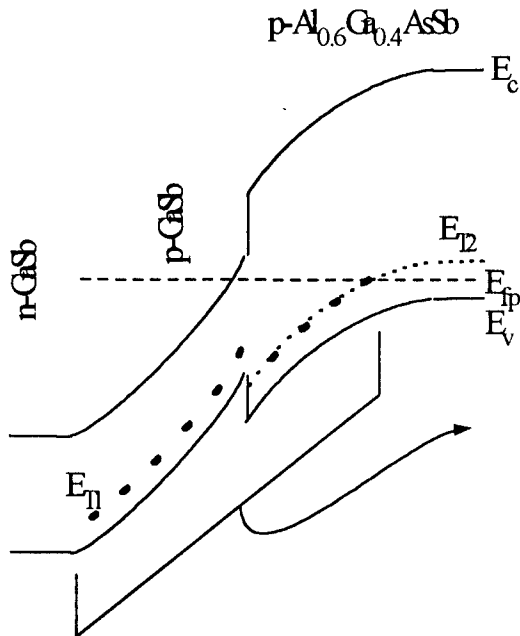
Emission B
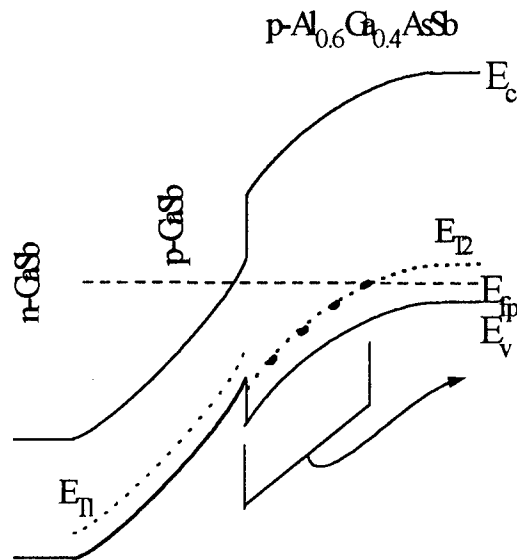
Figure IV-4. Diagram of the trap filling and measurement conditions to determine which of the two heterojunction layers is the source of the deep level emissions. The heavy dots indicate the filled traps that are not in equilibrium immediately after the filling pulse.

first measurement. Condition B fills traps only in the p-$Al_{0.6}Ga_{0.4}AsSb$ material farther

from the p-n junction. A comparison of DLTS signals from each biasing condition can be

used to determine the layer responsible for an emission. If condition A results in a

measured emission, and the emission is absent under condition B, then the trap is found to

be located between the two junctions.

The possibility that the emission is coming from the heavy doped side must also be

kept in mind. The sensitivity of DLTS measurements is limited by the doping density, e.g.,

the sensitivity of the system used here is limited to traps of concentration $\sim 10^4$ times lower

than the shallow dopant density. The measurements should therefore be more sensitive in

the lightly doped side than the heavily doped side since the volume of traps uncovered for

a given voltage change for heavy doping is less than for light doping. Specifically, the

depletion width on the p-GaSb side is about 20 times larger than that on the n-GaSb side

at the p-n junction. Thus, the sensitivity to traps in the material on the n^+ side of the n^+-p

junction should be less than the sensitivity to traps in the lightly doped p side. With the

exception of other considerations, the source of trap emissions should be expected only

from either of the lightly doped isotype heterojunction materials. However, it will be

shown in the next section that the presence of a high concentration of DX traps in the

heavily doped n^+-GaSb side can produce a large signal.

DLTS Measurements of p-$Al_{0.6}Ga_{0.4}As_{0.05}Sb_{0.95}$/$p$-GaSb/$n^+$-GaSb

Figure IV-5 shows the rate-window plot for traps found in the

n^+-GaSb/p-GaSb/p-$Al_{0.6}Ga_{0.4}As_{0.05}Sb_{0.95}$ diode. The signals are positive going for hole

traps, and negative going for electron traps. Three hole traps and three electron traps were observed. Each peak was measured under different bias conditions to optimize the signal from the particular trap. Also, the rate-windows used were different for most of the peaks, but were in the 20-2,000/sec range. The Arrhenius plot for each trap is shown in Figure IV-6.

Traps AH1 and AH2 have trap energy levels of a Ga_{Sb} antisite double acceptor, which have been predicted theoretically, and until now, measured experimentally only by other methods (Nakashima, 1981:1085–1094). The energies reported for Ga_{Sb} in GaSb cover a wide range. The range of energies measured here is a result of the emissions taking place from p-GaSb and p-$Al_{0.6}Ga_{0.4}As_{0.05}Sb_{0.95}$ where the trap energies are expected to be slightly different for each. Level AH1 has energies ranging from 23 to 38 meV, level AH2 from 76 to 102 meV. The lowest energy for AH1 was measured using a filling pulse of 0.5 V and a measurement bias of -0.4 V. According to the C-V profile of Figure IV-2, 0.5 V completely collapses the junction, while the measurement voltage of -0.4 V puts the depletion width into the interface region between the p-GaSb and the p-$Al_{0.6}Ga_{0.4}As_{0.05}Sb_{0.95}$. Therefore, the emission for the peak AH1 displayed in the rate window plot is from the p-GaSb layer. The higher energies for AH1 were measured by shifting the emission window into the p-$Al_{0.6}Ga_{0.4}As_{0.05}Sb_{0.95}$. Trap AH2 was identified as the second Ga_{Sb} antisite level from a similar increase in energy as the emission window shifted into the p-$Al_{0.6}Ga_{0.4}As_{0.05}Sb_{0.95}$. The 76 meV energy emission is from the Ga_{Sb} in GaSb and the 102 meV energy emission is from the Ga_{Sb} in p-$Al_{0.6}Ga_{0.4}As_{0.05}Sb_{0.95}$. Both
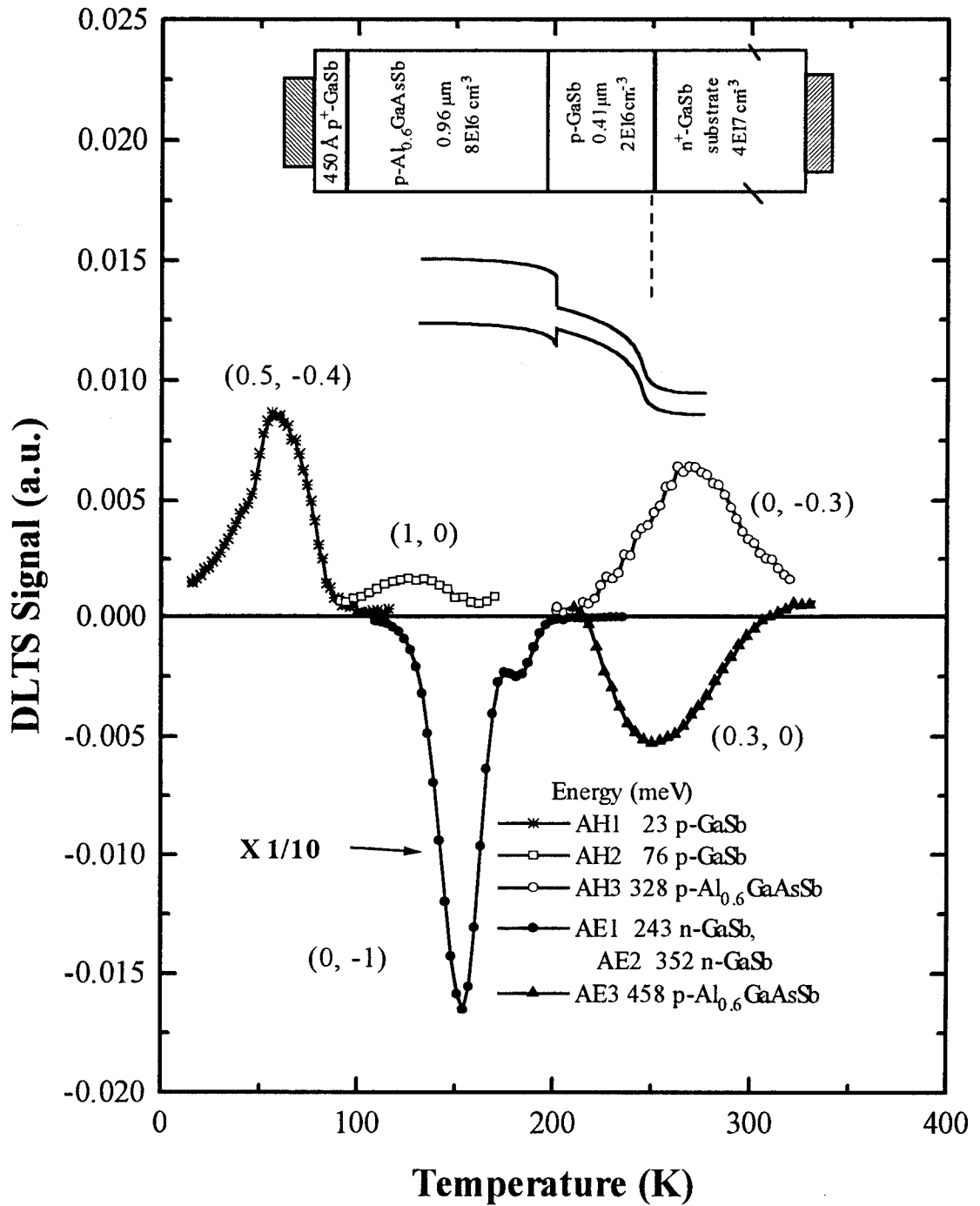
Figure IV-5. DLTS rate-window plot, sample structure, and representative band bending for the p-n junction/heterojunction diode grown by MBE on n^+-GaSb. The first number in parentheses indicates the filling pulse bias and the second number in parentheses indicates the measurement bias.
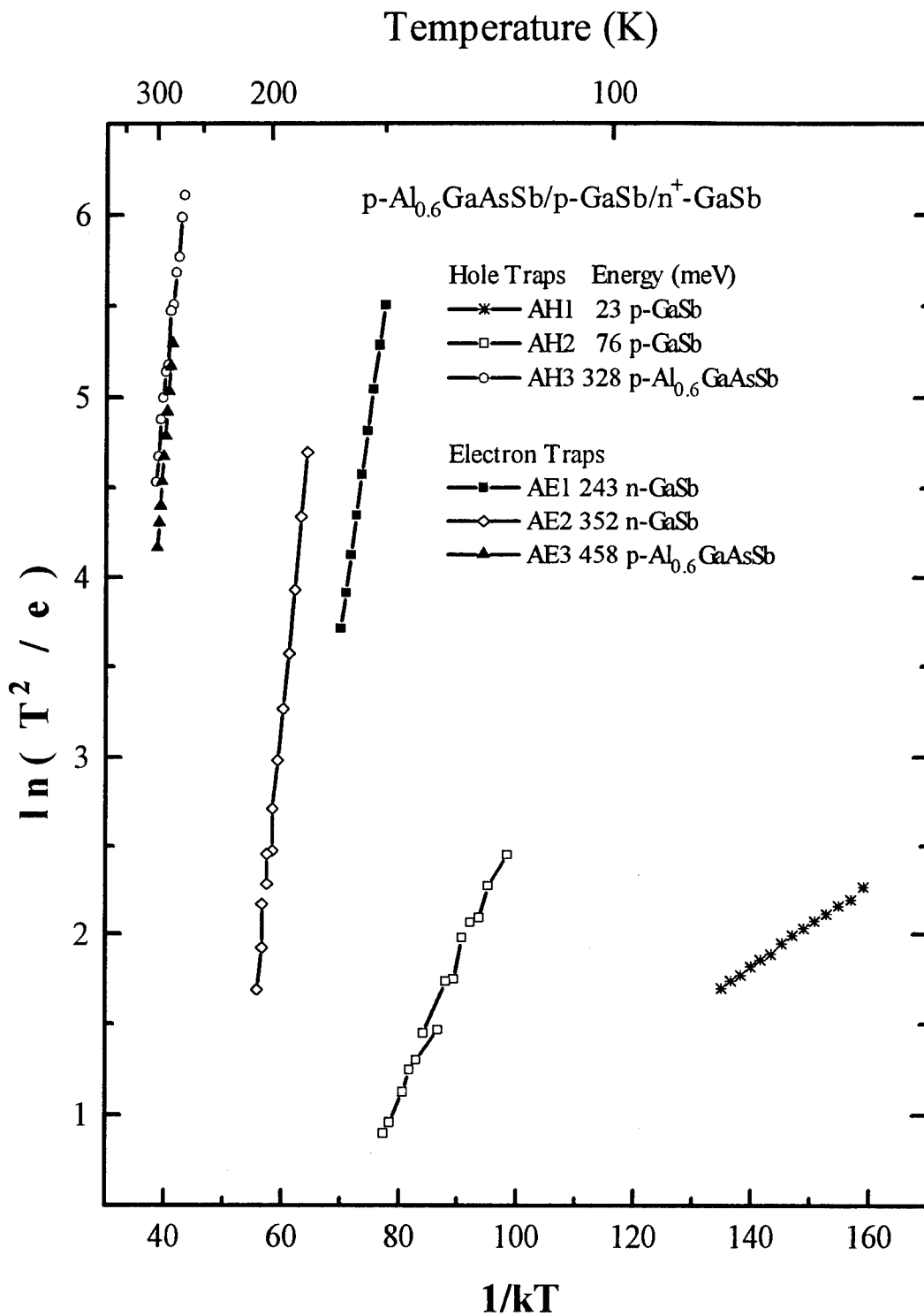
Figure IV-6. Arrhenius plot for the *p-n* junction/heterojunction sample. Each line corresponds to a peak given in the spectrum of Figure IV-5.

energy levels gave indications of the Poole-Frenkel effect, indicating that they are both acceptor traps.

The capture kinetics were different for each of these two traps. The low energy trap showed a decrease in the number of filled traps with increasing temperature, indicating the behavior predicted by cascade capture (Lax, 1960:1502–1523). As discussed in Chapter III, capture into moderately deep levels takes place through intermediate shallow excited states of the trap. The distribution of the trapped carriers shifts to higher energy excited states in the defect potential as the temperature increases, making fewer carriers available for capture into deeper states through the excited states. The higher energy trap showed a capture barrier estimated to be in the range of 40 meV. The presence of a capture barrier corresponds to capture by multi-phonon emission (MPE), although this energy is on the order of only one phonon (Lang and Henry, 1975:1525).

Trap AH3 is the deepest hole trap in this sample, with an energy of 0.328 eV. As can be seen from Figure IV-6, the Arrhenius plot for trap AH3 has some curvature. The energies range from 0.328 eV at low temperature to 0.388 eV at high temperature. An increase in the filling pulse bias past 0 V toward forward bias resulted in current flow and interference by minority carrier trap AE3. Changing the biases from 0.6 V fill and 0 V measure, which would give a response for traps in the p-GaSb, to 0 V fill and -0.6 V measure, which would probe the p-$Al_{0.6}Ga_{0.4}As_{0.05}Sb_{0.95}$, changed the transient from a small minority signal to a larger majority carrier signal. This indicates that the trap is in the p-$Al_{0.6}Ga_{0.4}As_{0.05}Sb_{0.95}$. The peak shown in the rate window plot was obtained with a

filling pulse of 0 V and a measurement bias of -0.3 V to minimize the reverse bias leakage current at the higher temperatures. The microscopic source of AH3 has not been determined.

The main features of Figure IV-5 are the large peaks at 150 K and 180 K from traps AE1 and AE2, respectively. From the C-V profile at 150 K, the biases of 0 V for the filling pulse and -1 V for the measure bias do not restrict the possibilities for emission to any single layer. However, as mentioned before, the spatial shift of the peak from the heterojunction accumulation feature in the C-V profile is a result of significant depletion into the n^+-GaSb. Also, since these large peaks are absent in the MOS diode which does not include n^+-GaSb, it can be concluded that the signal is due to traps in the n^+-GaSb. The difference in doping level of 2×10^{16} cm^{-3} in the p-GaSb compared to 4×10^{17} cm^{-3} from Te doping in the n-GaSb result in a depletion width ratio of 20:1. The measurements should therefore be much more sensitive in the p-side of the junction. However, the defect concentration related to AE1 and AE2 should scale with the dopant concentration if it is related to the Te donor in the n^+-GaSb. AE1 has an activation energy of 243 meV from the conduction band, capture cross section of 4.7×10^{-15} cm^2, and trap concentration equal to the shallow carrier concentration. These characteristics compare well with some of the reported characteristics given for the DX center in GaSb. AE2 appearing on the high temperature side of AE1 has an activation energy 352 meV from the conduction band, and is at the upper end of the energies reported so far for DX center or other traps in GaSb. A small capture barrier of only 51 meV was measured for trap AE1. The capture barrier for AE2 could not be measured due to interference from AE1. A capture

barrier of 190 meV was reported by Poole, *et al.* in Te doped GaSb, but it was suggested that the trap was from S contamination (Poole *et al.*, 1990:1645–1647). Polyakov reported that there was no discernible capture barrier. Reported emission energies for the DX center are 0.28–0.315 eV for GaSb depending on the donor binding energy (Poole *et al.*, 1990:1645–1647; Hubik *et al.*, 1993:19–22), and 0.4–0.5 eV for Al_xGaAs_ySb (Takeda *et al.*, 1987:L273–275; Meyer *et al.*, 1993:475–478; Zhu *et al.*, 1987:127–130). Both AE1 and AE2 are within the energy limits of reported energies in GaSb, and are therefore coming from the n^+-GaSb side of the junction. These two peaks appeared as majority carrier traps, corresponding either to a hole trap in the *p*-side of the junction, or in this case, to an electron trap in the n^+-GaSb. The sign of the peak was later changed to maintain all hole trap signals as positive, and all electron traps as negative. Kuramochi reported a hole trap in GaSb at 0.25 eV, similar in energy to trap AE1 (Kuramochi *et al.*, 1993:2664–2666). However, it is also measured in a *p-n* junction, and may therefore be in the n^+ layer as an electron trap.

The DLTS signal amplitude of trap AE3 decreased with increasing reverse measurement bias. Increasing the reverse bias for measurement shifts the depletion width from including only the *p*-GaSb to including also the p-$Al_{0.6}Ga_{0.4}As_{0.05}Sb_{0.95}$. This suggests that the trap is in the *p*-GaSb. However, increasing the reverse bias for measurement also includes the majority carrier signal from AH3 in the $Al_{0.6}Ga_{0.4}As_{0.05}Sb_{0.95}$ offsetting the minority carrier signal from AE3. This factor accounts for the decrease in amplitude with increasing reverse bias. The filling pulse height was 0.3 V. Higher amplitude filling pulses gave slightly larger capacitance transients, but also

resulted in a sharp spike at the start of the transient due to current overload recovery time of the capacitance meter. The measurement bias was 0 V. The trap energy level of 0.458 eV is close to the levels found in $Al_{0.6}Ga_{0.4}As_{0.05}Sb_{0.95}$ for the DX center. No appreciable capture barrier was measured for level AE3. The concentration was about a hundredth of the shallow carrier concentration. This trap is only tentatively assigned to the p-$Al_{0.6}Ga_{0.4}As_{0.05}Sb_{0.95}$ because the injected minority carrier concentration drops off away from the junction, and there is interference from majority trap AH3.

C-V Measurements of MOS Diode Including a p-$Al_{0.5}Ga_{0.5}As_{0.04}Sb_{0.96}$/$p$-GaSb Heterojunction

The voltage versus apparent depletion width for the MOS sample is shown in Figure IV-7. The nearly vertical region of the plot indicates the position of the heterojunction. However, the depletion width also includes the oxide width along with the bias dependent depletion width of the semiconductors. The shift in position of the vertical line shows that there is a change in carrier concentration in the portion of the p-$Al_{0.5}Ga_{0.5}As_{0.04}Sb_{0.96}$ that was oxidized by exposure to de-ionized water, adding to the total depletion width as the temperature decreases. The oxide layer behaves more like an ideal insulator as the temperature is lowered. The bias required for forward conduction increases from 2 V at room temperature to 13 V at 50 K. The primary use of the C-V measurements in this case is to determine what biases correspond to depletion widths on either side of the heterojunction to support the DLTS measurements.
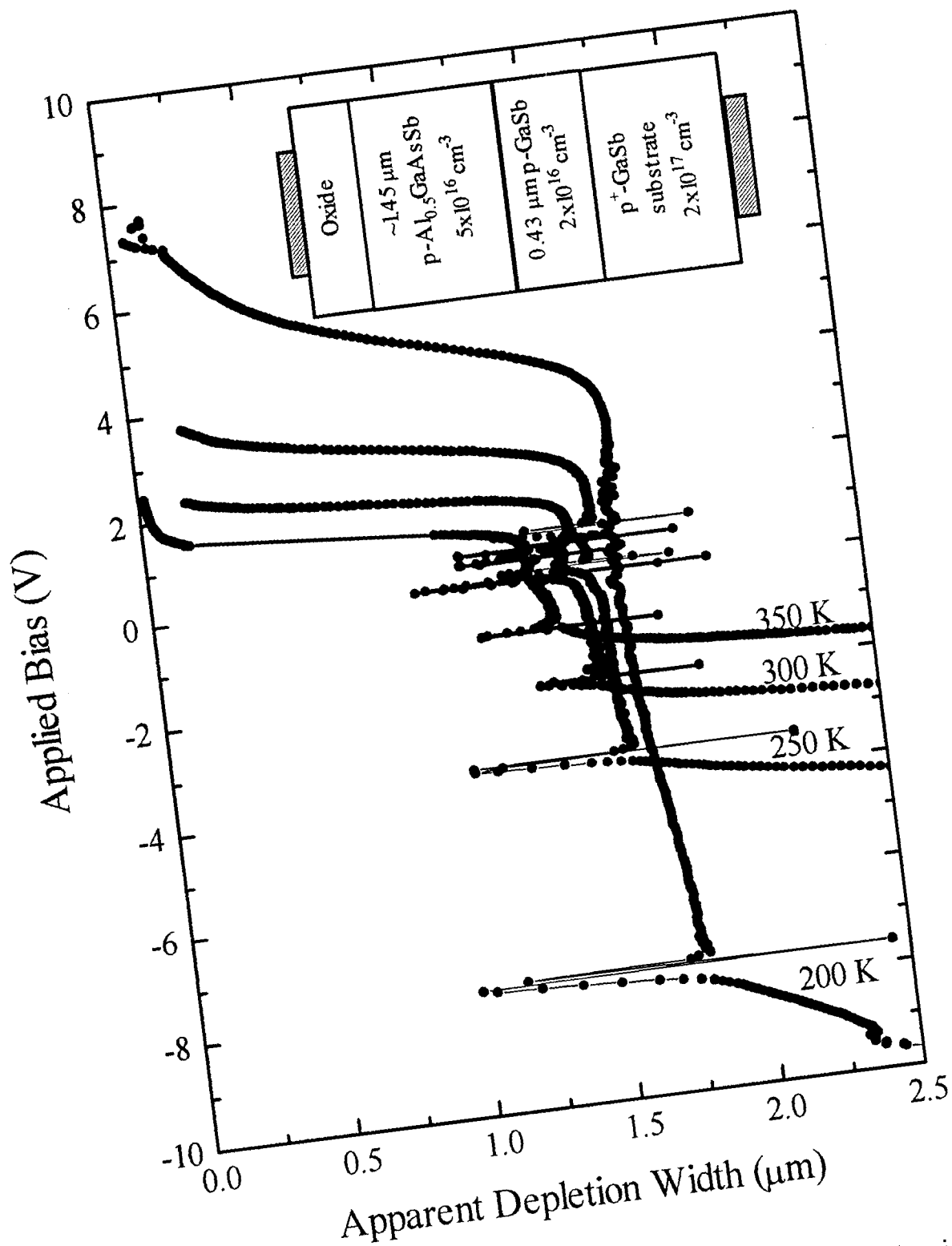
Figure IV-7. Voltage versus apparent depletion width for the AlGaAsSb-oxide/p-$Al_{0.5}Ga_{0.5}As_{0.04}Sb_{0.96}$/p-GaSb MOS capacitor.

A peculiar feature of the MOS C-V measurements is the numerous discontinuities in the vertical section of the plot as opposed to the single discontinuity seen in Figure IV-2 for the *p-n* junction/heterojunction. As mentioned earlier in this chapter in the section on C-V measurements made on the *p-n* junction/heterojunction, it was suggested that the discontinuity is either from interface state defects at the heterojunction or from holes confined in the discrete states in the triangular well at the heterojunction as shown in Figure IV-3 (Leu and Forrest, 1988:5030–5041; Jeong *et al.*, 1987:792–795; Andre *et al.*, 1986:F6). The discrete nature of the discontinuity suggests that it is from the holes confined in the multiple discrete states of the triangular well at the heterojunction rather than interface state defects at the heterojunction. Moreover, the multiple discontinuities seen in the bias versus depletion width in Figure IV-7 strongly supports the former explanation. Each discontinuity results from the Fermi level passing through a confined state of the triangular well.

DLTS Measurements of MOS Diode Including a p-$Al_{0.5}Ga_{0.5}As_{0.04}Sb_{0.96}$/$p$-GaSb Heterojunction

The rate-window plot for the MOS sample is given in Figure IV-8 with features similar to that of the *p-n* junction. It will be shown here that peak BH1 is due to interface states superimposed on two discrete levels. Interface states often display a U-shaped continuous distribution of trap energies throughout the bandgap. The U-shape refers to a high concentration of traps at either band edge, tapering off to a minimum concentration
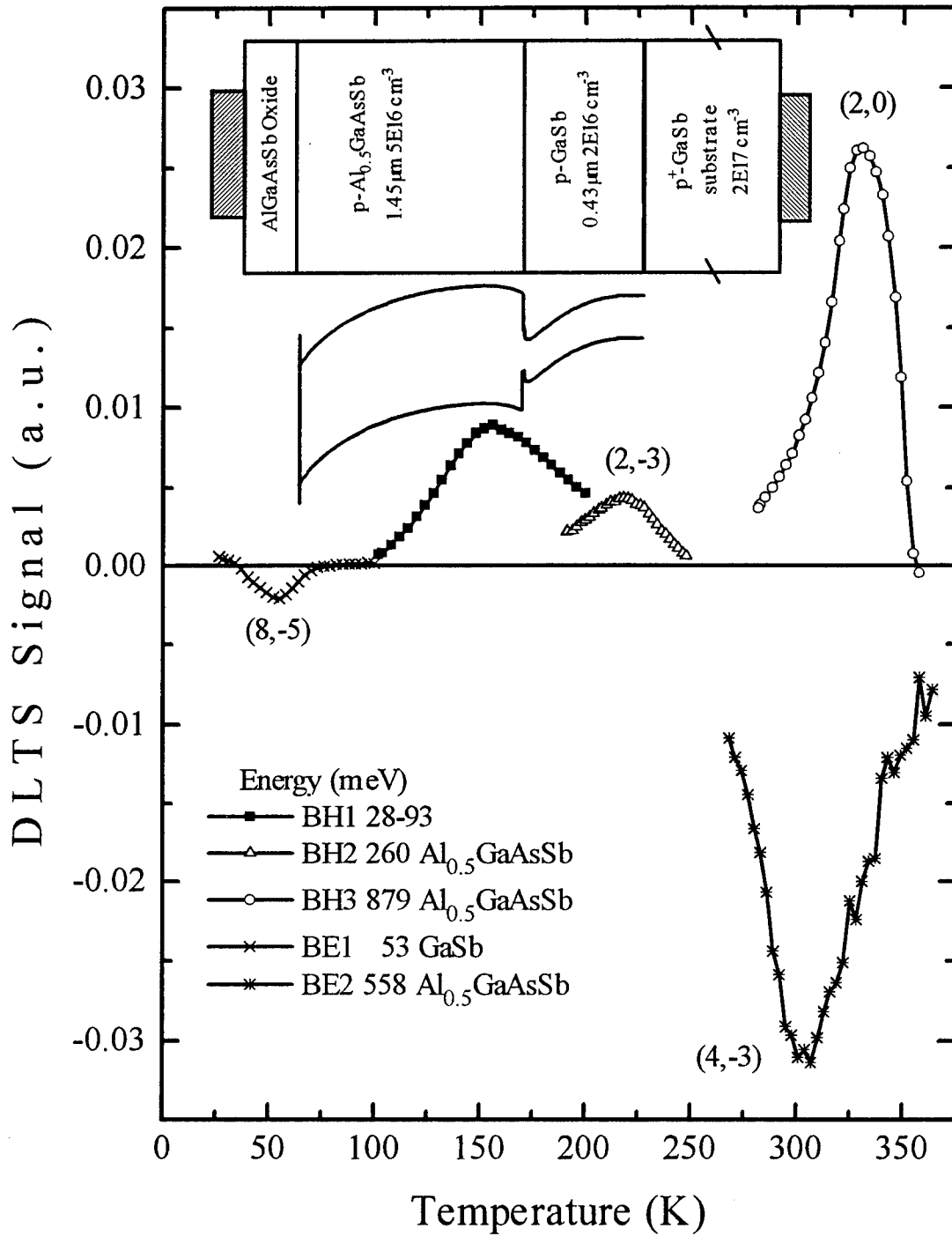
Figure IV-8. DLTS rate-window plot, sample structure, and representative band bending for the MOS capacitor showing the spectrum of defects in unintentionally doped p-type $Al_{0.5}Ga_{0.5}As_{0.04}Sb_{0.96}$ and unintentionally doped p-type GaSb grown by MBE on GaSb. The fill and measure biases are shown in parentheses.

near mid-gap (Hasegawa and Sawada, 1983:119–140). Compared to discrete traps, the shape and position of the spectra of interface states will depend more heavily on the biases during trap filling and measurement. A shift of the filling and measurement biases to slightly larger reverse voltages resulted in a shift of the peak to higher temperatures, as would be expected from probing deeper energy interface states nearer to the middle of the band gap. This shift, the breadth of the peak, and the curvature of the Arrhenius plot in Figure IV-9 all indicate that this peak is due in part to a distribution of energies from interface states at the heterojunction of p-$Al_{0.5}Ga_{0.5}As_{0.04}Sb_{0.96}$/$p$-GaSb. However, two slopes showed up in the Arrhenius plot in Figure IV-9 for several measurements of peak BH1. These ranged in energy from 28 to 32 meV for the lower energy trap, and 67 to 93 meV for the higher energy trap, similar to the Ga_{Sb} antisite defect energies in the n^{+}-p junction/heterojunction sample.

The trap labeled BH2 is identified as an acceptor since it shows an increased emission rate with increasing electric field. This trap was tentatively determined to be in the $Al_{0.5}Ga_{0.5}As_{0.04}Sb_{0.96}$. Changing the filling pulse from 0 V to 2 V, corresponding to increased trap filling in the $Al_{0.5}Ga_{0.5}As_{0.04}Sb_{0.96}$, more than doubled the amplitude of the capacitance transient. However, there was also a small increase in response with increasing reverse measurement bias. This is a result of the non-ideal oxide layer allowing minority carrier injection. Increasing the filling pulse much beyond 2 V resulted in minority carrier injection from the metal contact on the oxide into the p-type heterojunction layers and interference from trap BE2. There was also a capture barrier present for trap BH2 which was indicated by a reduction in transient amplitude by half
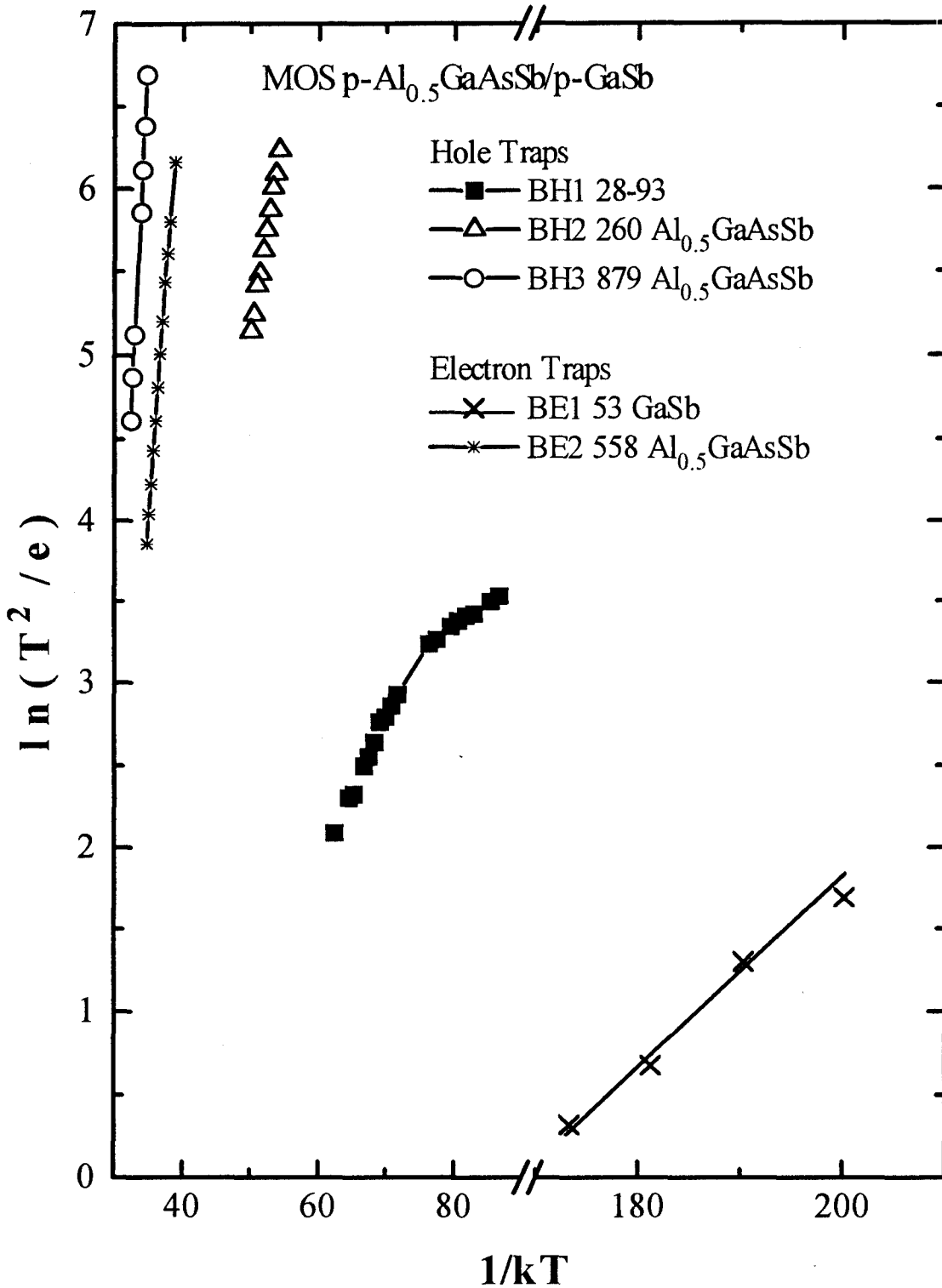
Figure IV-9. Arrhenius plot for the DLTS spectra shown in Figure IV-8 obtained from the MOS capacitor.

when the pulse width was decreased from 10 msec to 0.1 msec. However, the amplitude of the transient was too small to accurately measure the capture barrier.

Trap BH3, in the $Al_{0.5}Ga_{0.5}As_{0.04}Sb_{0.96}$, was measured using a filling pulse of 2 V and measuring the transient at 0 V. The capture rate of the hole trap is significantly larger than that of minority carrier trap BE2. The difference in capture rate was used to eliminate the minority carrier signal. At a temperature of 330 K, the signal could be changed from a negative-going minority transient to a positive-going majority transient by reducing the filling pulse width from 10 msec to 100 μsec. Even so, the rate-window plot shows a depression on the low temperature side of peak BH3 from minority carrier emissions, partially offsetting the trapped hole emissions. Fitting the transients for two exponential components gave evidence of another trap in addition to BH3. The energy of the hole trap on the low temperature side of peak BH3 in the MOS sample is roughly 0.42 eV. This may be the same trap as AH3 at 328 meV found in the p-$Al_{0.6}Ga_{0.4}AsSb$ of the p-n junction/heterojunction.

A minority carrier trap of low concentration was measured at 50 K. Trap BE1 is in the p-GaSb. For an 8 V filling pulse, a change in measurement bias from 0 V to -5 V tripled the transient amplitude. The signal disappears for a measurement bias of +3 V which would probe only the $Al_{0.5}Ga_{0.5}As_{0.04}Sb_{0.96}$ according to the C-V profile. The measurement bias of -5 V is in the nearly vertical section of the plot of voltage versus apparent depth shown in Figure IV-7, where some depletion takes place in both materials of p-$Al_{0.5}Ga_{0.5}As_{0.04}Sb_{0.96}$ and p-GaSb. The energy obtained from the Arrhenius plot is 53

meV for BE1. Since the signal was absent at small depletion and present only at larger depletion, the trap is in the p-GaSb.

Level BE2 at 558 meV was measured in the CC-DLTS mode so that the bias was adjusted by the feedback loop to maintain the capacitance at a constant value. CC-DLTS could only be used in a bias range away from the vertical line region of the voltage versus apparent depletion width curve. Otherwise, the feedback circuit was unstable since the capacitance is not sensitive to bias in this region. The measurement bias was -3 V at 300 K and increased with increasing temperature. A fixed filling pulse of 4 V was used to saturate the minority carriers. The capture cross section was determined to be temperature dependent, and a capture barrier of 0.258 eV was obtained from the change in transient amplitude with temperature. There was also evidence of another trap at slightly higher temperature, but increasing leakage current in the diode prevented accurate measurements. Since this is in unintentionally doped material, the resulting DX-like signal is from residual impurities.

DLTS Measurements of AlAsSb p-n Junction

The rate-window plot for the AlAsSb p-n junction diode is shown in Figure IV-10. The sample consists of unintentionally doped p-AlAs$_{0.07}$Sb$_{0.93}$ with a carrier concentration of 4×10^{16} cm^{-3} and Te-doped n^{+}-AlAs$_{0.07}$Sb$_{0.93}$ with a carrier concentration of 4×10^{17} cm^{-3}. The appearance of only one trap in this material is an indication of the improvement in quality of ternary growth versus quaternary growth. However, the magnitude of the peak also indicates that the one trap is of a very large concentration. The concentration of this
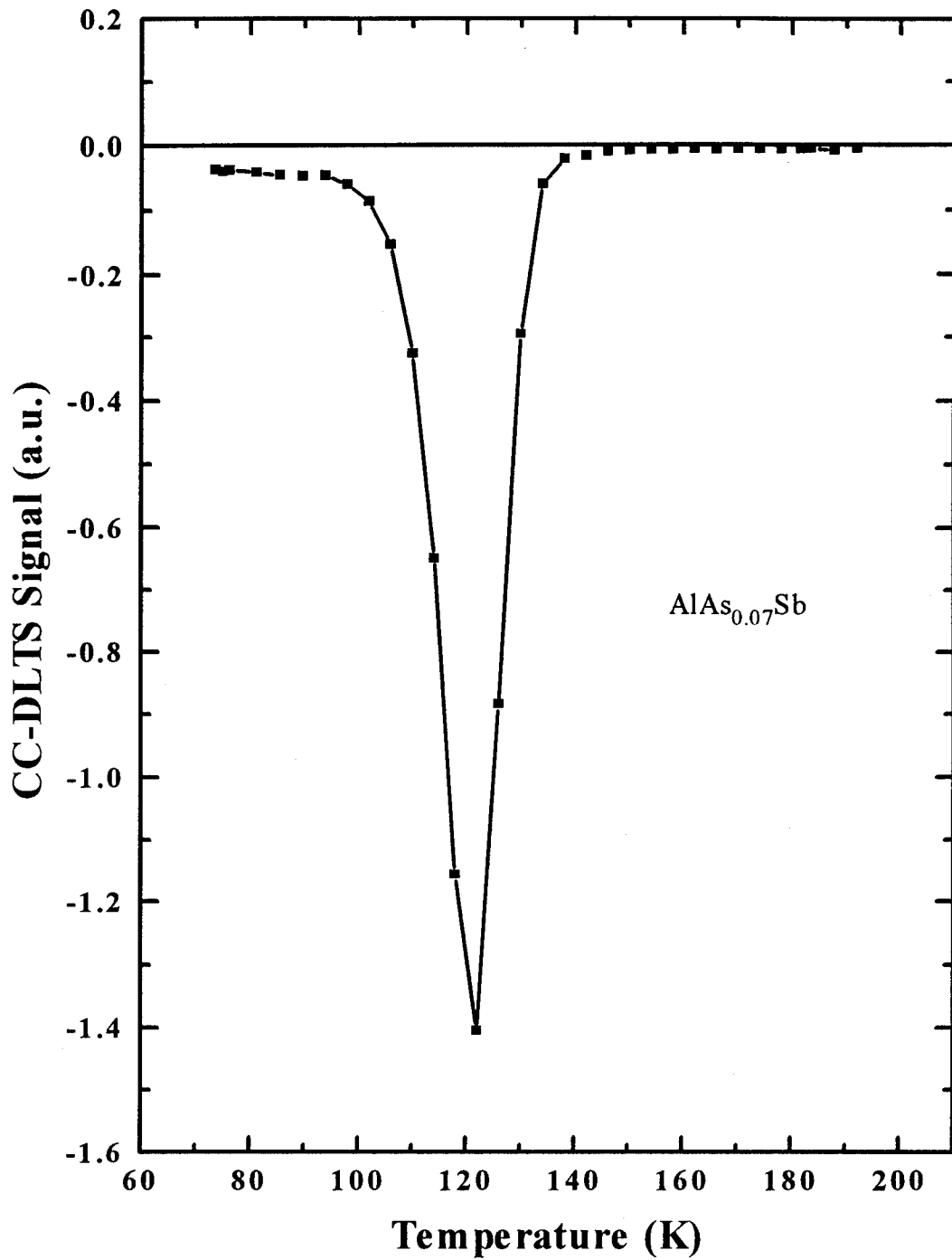
Figure IV-10. CC-DLTS rate-window plot for the AlAsSb sample. The single electron trap has a high concentration and a temperature dependent capture cross section, both of which are characteristics of donor related DX centers.

trap is about the same as the donor concentration of 4×10^{17} cm^{-3}. In this sample the *p*-side is undoped. It is well documented that the Te dopant used in the n^{+}-AlAsSb produces a DX trap. The peak observed here is therefore assigned to the DX center related to the Te dopant in the n^{+}-AlAsSb. Measurement of the DX center showed a well defined emission energy of 282 meV with a capture cross section of 2.1×10^{-12} cm^{2} as shown in Figure IV-11, which was measured over several decades of emission rate.

It is also known that there is a capture barrier associated with the DX trap. The energy of the barrier has not been accurately measured up until now. The low temperature side of the spectrum shown in Figure IV-10 has a low plateau. This is a reflection of the high concentration of this trap, and also indicates the presence of a capture barrier. A non-saturating filling pulse of 10 μsec was used in order to determine the change in amplitude of the transients as the temperature increased. Then the resulting capacitance transient amplitude versus temperature was fit to the solution of the trap-filling rate equation for the capture barrier. The amplitude of the fit of each transient at each temperature was then used to determine the capture barrier of 137 meV. The fit to the model for capture by multi-phonon emission is plotted in a solid curve, and is compared to the data as shown in Figure IV-12. The excellent fit shows that the capture is by multi-phonon emission.

This trap also showed a Poole-Frenkel effect. The measured emission rate versus square root of the applied electric field shown in Figure IV-13 should behave according to the equation:

$$e_n(F) = e_{n0} \exp\left(\frac{\Delta U_{PF}}{kT}\right),$$
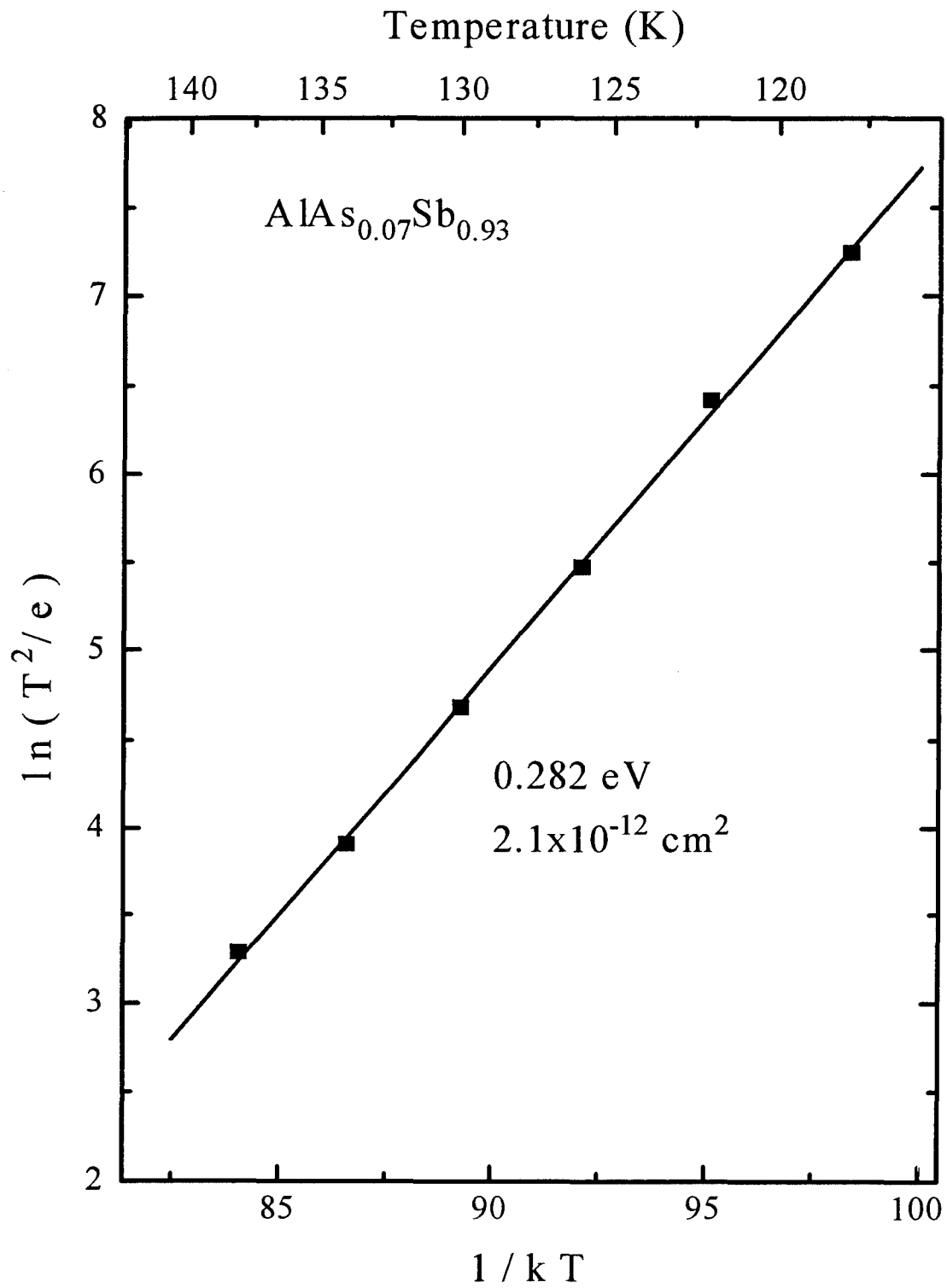
Figure IV-11. Arrhenius plot for the dominant DX trap in the n-AlAsSb of the MBE *p-n* junction sample.
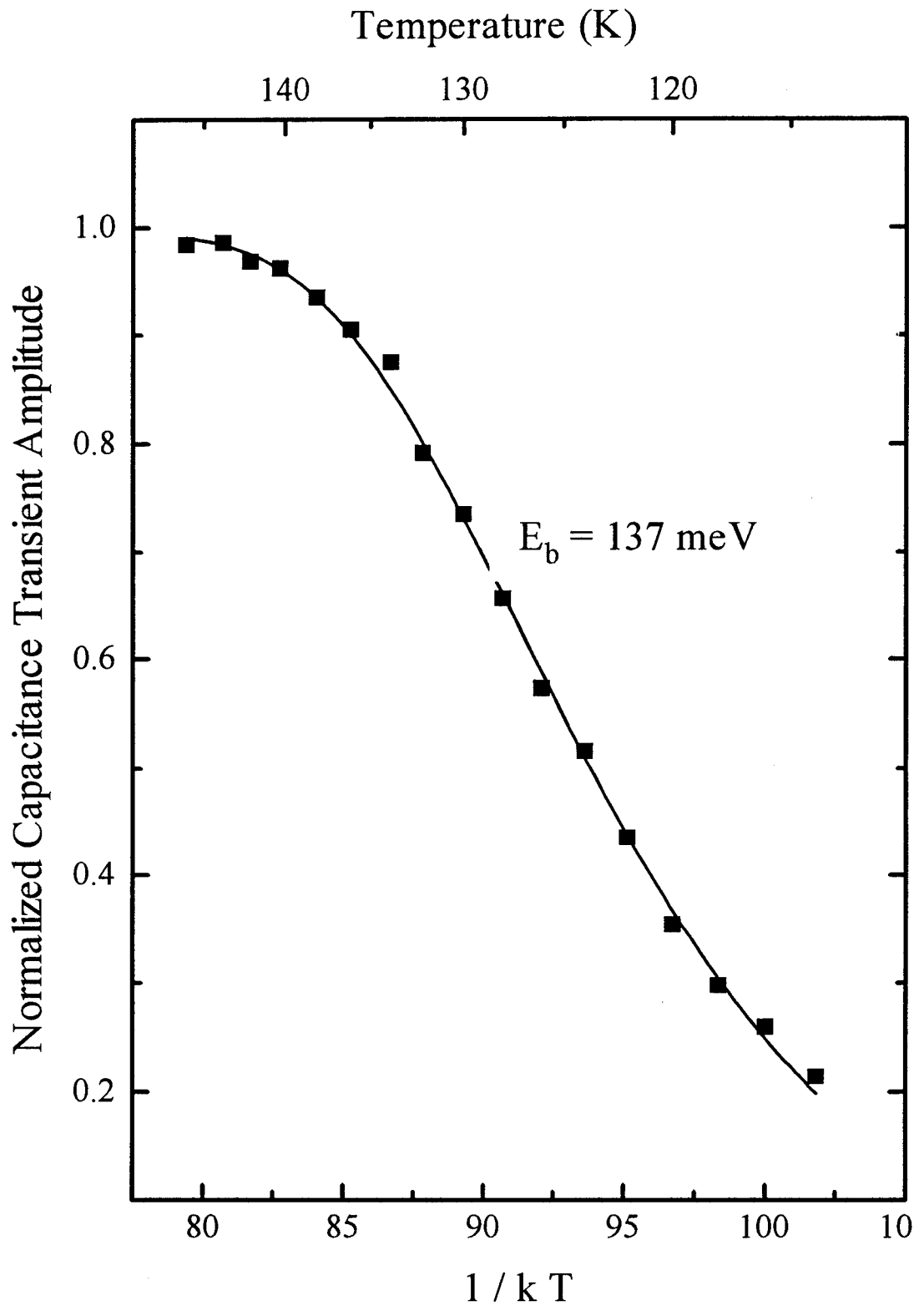
Figure IV-12. Capture barrier for the DX trap in *n*-AlAsSb.
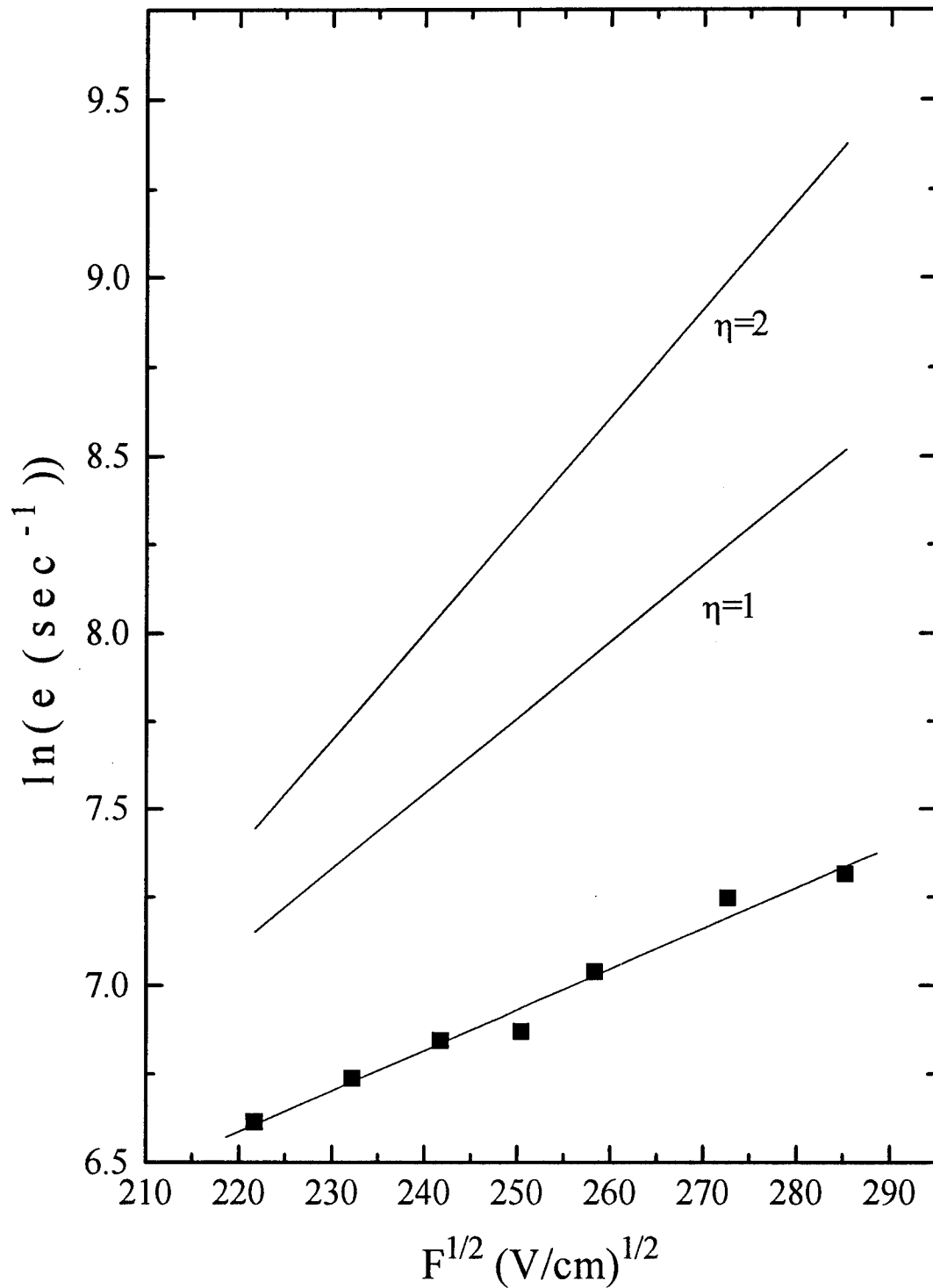
Figure IV-13. Poole-Frenkel effect for the DX trap in n-AlAsSb. The difference between the measured slope and the slope predicted by a one dimensional model for a charge of either η=1 or η=2 is due to the presence of a capture barrier.

where e_{n0} is the zero-field emission rate, and ΔU_{PF} is the barrier lowering by the electric field given by

$$\Delta U_{PF} = q\sqrt{\frac{\eta q F}{\pi \varepsilon}}.$$

Here, F is the electric field, η is the charge on the trap after emission, and ε is the permittivity. The model for the DX center in AlGaAs predicts that the charge after emission is either one or two, either of which would have a much larger slope than what was measured. If the defect has a strictly Coulombic potential, the slope should depend only on the dielectric constant and the charge after emission. The slope of the experimental data plotted in Figure IV-13 is 0.005 $(cm/V)^{1/2}$ which is much lower than the slope of 0.022 $(cm/V)^{1/2}$ predicted for a single donor ($\eta=1$) or 0.031 $(cm/V)^{1/2}$ predicted for a double donor ($\eta=1$) with a permittivity of 9.9 (Alibert *et al.*, 1991:3208–3211). The deviation from the theoretical value is due to the defect potential being altered from a pure Coulombic form by the capture barrier (Buchwald and Johnson, 1988:958–961). The important point is that the field changes the emission rate, and defines the defect as a donor, although it could not be determined what the charge state is after emission.

Hall Measurements of $Al_{0.9}Ga_{0.1}As_{0.08}Sb_{0.92}$

The Hall measurements of $Al_{0.9}Ga_{0.1}As_{0.08}Sb_{0.92}$ were made in order to add information to the DLTS investigation of the charge state of the DX center in Al_xGaAs_ySb. The Hall measurements were performed in a liquid helium cryostat covering

the temperature range from 10-350 K, using Keithley equipment. The magnetic field was 5 kG for all measurements. Photoionization effects were investigated by placing a 2 eV light emitting diode (LED) over the surface of the sample for illumination at low temperature prior to Hall measurements. The epitaxial layer in each sample is 1.07 μm thick grown on semi-insulating GaAs. GaAs was used instead of GaSb since semi-insulating GaSb substrates are not available. The difference in free carrier concentration and mobility of $Al_{0.9}Ga_{0.1}As_{0.08}Sb_{0.92}$ grown with either As_2 or As_4, and the change in free carrier concentration and mobility with illumination are two effects that are characterized in the Hall measurements.

Figure IV-14 shows the measured carrier concentration as a function of inverse temperature for $Al_{0.9}Ga_{0.1}As_{0.08}Sb_{0.92}$. The carrier concentration increases slightly with illumination for both As_2 and As_4. A persistent increase in concentration, or persisted photoconductivity (PPC), after removing the illumination verifies the presence of a capture barrier. The presence of a capture barrier prevents recapture of the photoionized electrons until a high enough temperature is reached. When 150 K is reached, the carrier concentration begins to increase sharply and the data from the illuminated sample merges with that of the non-illuminated sample. At this temperature, the electron mobility with illumination is also the same as the electron mobility without illumination as shown in Figure IV-15. This also corresponds to the temperature in the DLTS measurements of n-$AlAs_{0.07}Sb_{0.93}$ where emission from the DX center takes place. If the measured deep and shallow energies are related to the same center, then the difference in deep level ionization energy and the capture barrier from DLTS should be equal to the binding energy obtained
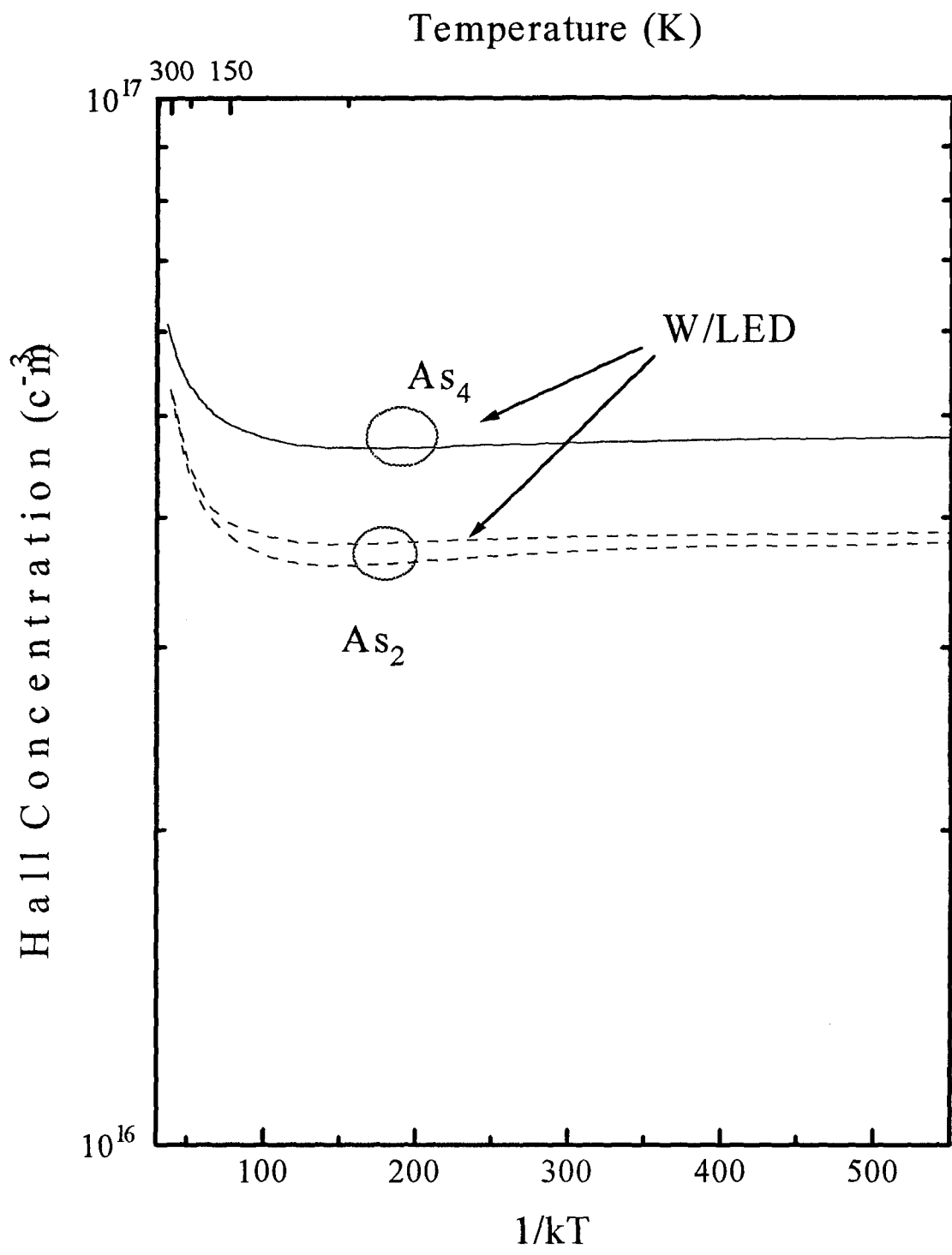
Figure IV-14. Hall carrier concentration versus inverse temperature for Te-doped, *n*-$Al_{0.9}Ga_{0.1}As_{0.08}Sb_{0.92}$ grown with As_2 or with As_4 before and after illumination from a 2 eV LED.
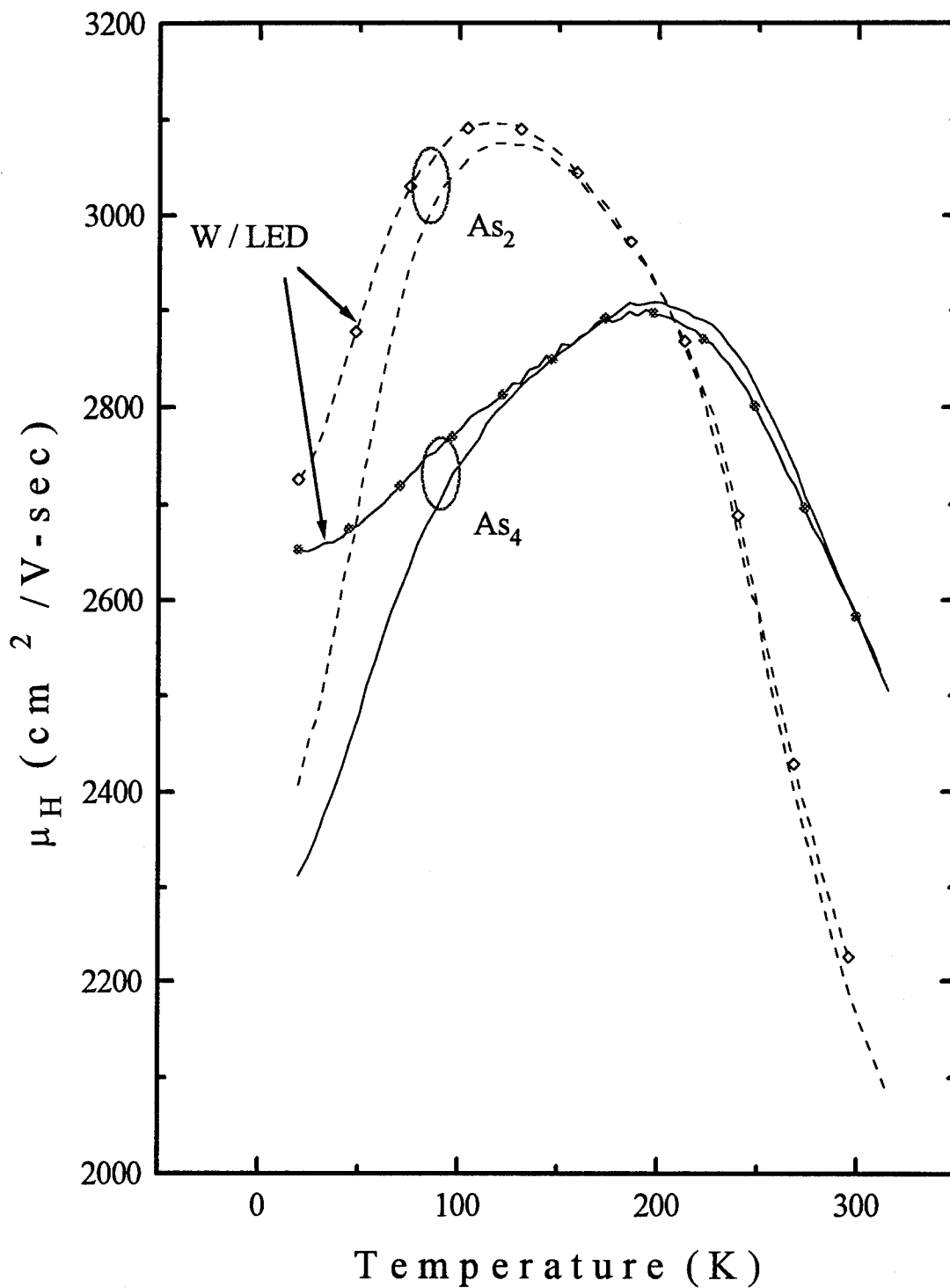
Figure IV-15. Hall mobility versus temperature for n-$Al_{0.9}Ga_{0.1}As_{0.08}Sb_{0.92}$ grown with As_2 and n-$Al_{0.9}Ga_{0.1}As_{0.08}Sb_{0.92}$ grown with As_4 before and after illumination from a 2 eV LED.

from Hall measurements as seen in Figure IV-16. The binding energy (E_d) of 86–114 meV is very close to the difference of 145 meV between the capture (E_c) and emission (E_T) energies measured by DLTS, within the accuracy limits of the DLTS and Hall measurements. It should be pointed out that the DLTS measurements are for an n-$Al_xGa_{1-x}As_ySb_{1-y}$ sample grown lattice-matched to GaSb with x=1.0, while the Hall measurements are made on a sample grown on semi-insulating GaAs with x=0.9. In conjunction with the increase in mobility at low temperature after illumination, the carrier concentration increase shows that there is less scattering from ionized impurities after illumination. This is either because the impurities are now neutral, and/or from increased screening of the impurities.

For approximately the same carrier concentration, the mobility at temperatures less than 200 K is higher for the samples grown with As_2. Plots Figure IV-14 and Figure IV-15 both show that the same persistent photoconductivity (PPC) effect on carrier concentration and mobility at low temperature is present regardless of the arsenic growth species. Comparison of the mobility for the two arsenic species shows different scattering mechanisms at high temperature in the lattice scattering regime. The mobility should change with temperature proportional to T^α, where α depends on the particular scattering mechanism. The sample grown with As_2 has a high temperature exponent of -0.9. This is higher than the -0.75 for scattering by the acoustic phonon deformation potential, and is closer to polar optical mode scattering. On the other hand, the mobility of the sample grown with As_4 has a high temperature exponent of -0.48, matching well to piezoelectric scattering.
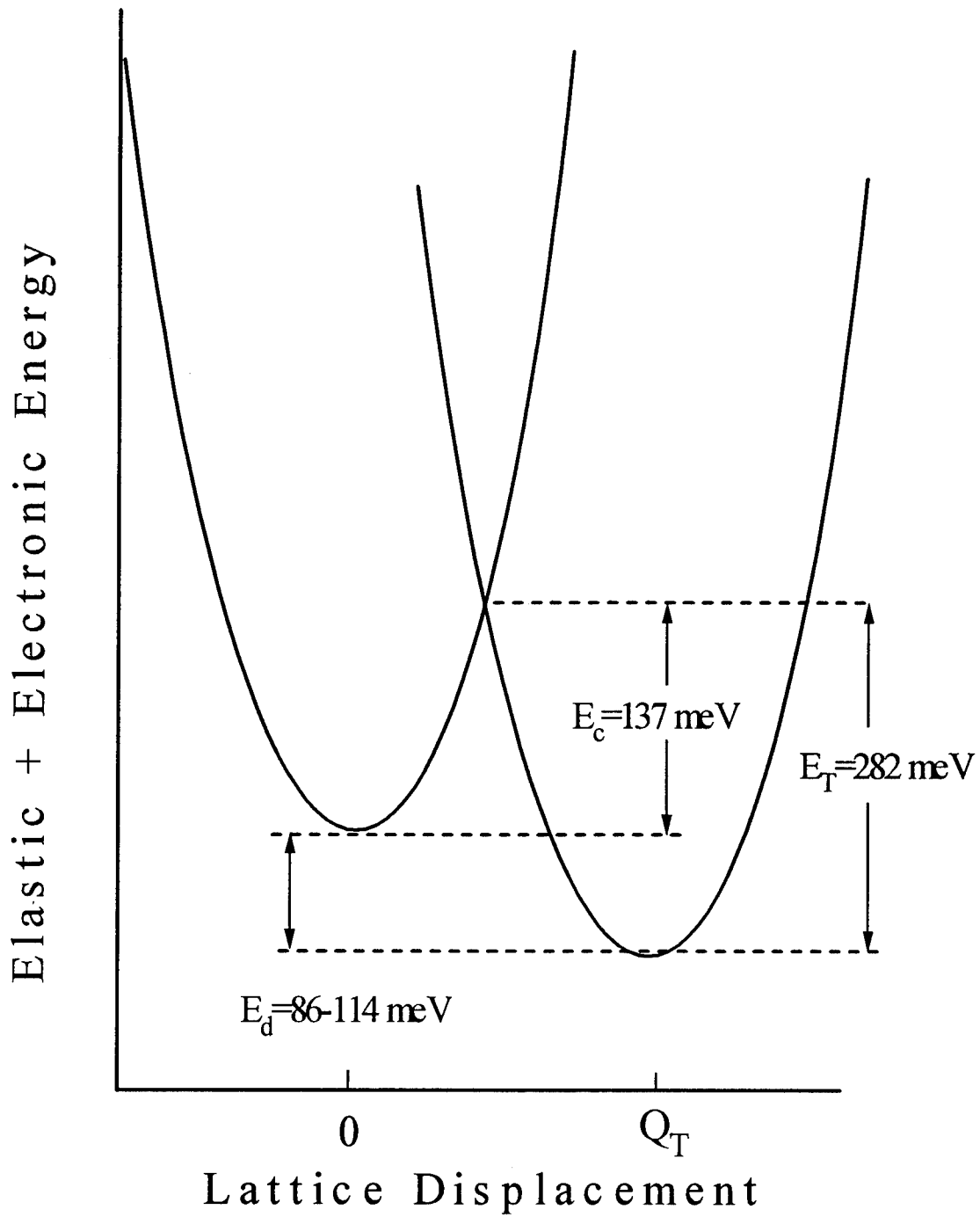
Figure IV-16. Configuration coordinate diagram showing the relationship between the capture barrier, E_c, the binding energy, E_d, and the trap energy, E_T, for the DX center in $AlAs_{0.07}Sb_{0.93}$. Q_T represents the relaxed position after capture.

Discussion

Table IV-1 presents a summary of the traps found in the current GaSb-based materials in each of the characterized structures. The defects that can easily affect free carrier concentration such as the DX traps and the Ga_{Sb} double acceptor traps are the primary focus of this section because of the effects they have on device design and operation, and impact on theoretical modeling of defects.

The levels at 28 and 67 meV in the MOS structure, and the levels at 23 and 76 meV in the *p-n* junction/heterojunction are very similar to the energies of 33 and 80 meV reported for the dominant double acceptor in GaSb, presumably due to the Ga_{Sb} antisite defect (Nakashima, 1981:1085–1094). This trap is of primary interest since it is responsible for the residual *p*-type doping in the mid-10^{16} cm^{-3} for all compositions of undoped Al_xGaAs_ySb. Previous investigations of GaSb by other methods reported a fairly wide range of energies. A table of reported values compiled by Nakashima from several studies of GaSb give the range in energy from 25 to 35 meV for the lower energy level and 60 to 120 meV for the higher energy level. In the same paper, Nakashima reported new measurements by Hall effect, photoconductivity, and photoluminescence. This combination was used to more accurately determine the first and second levels of the doubly ionizable defect, which has energy levels at 33 and 80 meV above the top of the valence band at 4.2 K. While he could conclude from the study that it was related to an Sb vacancy defect, there wasn't enough information to confirm a Ga_{Sb} defect. However, the DLTS measurements reported here offers further evidence of Ga_{Sb} antisite defect. The Ga_{Sb} antisite defect should show double acceptor type behavior due to the difference of

Table IV-1. Deep levels in MBE grown $Al_xGa_{1-x}As_ySb_{1-y}$ (x=0, 0.5, 0.6, 1.0) lattice matched to GaSb.

Run	Label	E_t (meV)	σ_c (cm^2)	Conc. N_T/N_s	Material
_p-n_ junction/ heterojunction					
Hole Traps					
147D1B	AH1	23-38	3.3×10^{-20}	0.06	p-GaSb, $Al_{0.6}GaAsSb$
147C1D	AH2	76-102	1.2×10^{-19}	0.02	p-GaSb, $Al_{0.6}GaAsSb$
147C1F	AH3	328	2.5×10^{-18}	0.04	p-$Al_{0.6}GaAsSb$
Electron Traps					
147B2B	AE1	243	4.7×10^{-15}	1	n-GaSb
147B2D	AE2	352	4.8×10^{-13}	0.26	n-GaSb
147D1E	AE3	458	6.2×10^{-15}	0.022	p-$Al_{0.6}GaAsSb$
MOS capacitor/ heterojunction					
Hole Traps					
A12B	BH1	28-32, 67-93			Interface states, GaSb, $Al_{0.5}GaAsSb$
A3E	BH2	260	2.0×10^{-17}	0.024	$Al_{0.5}GaAsSb$
A12F	BH3	878	2.0×10^{-11}	0.2	$Al_{0.5}GaAsSb$
Electron Traps					
A2A-2	BE1	53	3.7×10^{-17}	0.012	GaSb
A12D-1	BE2	558	4.6×10^{-15}	0.5	$Al_{0.5}GaAsSb$
_p-n_ junction					
Electron Trap					
	CE1	282	3.4×10^{-12}	1	AlAsSb

two valence electrons between gallium and antimony. Each trap energy level does in fact show acceptor type behavior from the field dependence measurements.

Other evidence comes from a prediction of the change in energy with composition of $Al_xGa_{1-x}Sb$. The sp^3s* tight-binding model has been used to calculate the defect energies of intrinsic defects in $Al_xGa_{1-x}Sb$ (Shen *et al.*, 1993:8313–8318; Hjalmarson *et al.*, 1980:810–813; Vogl, Hjalmarson, and Dow, 1983:365; Ren, Dow, and Shen, 1988:10677; Shen, Ren, and Dow, 1992:1089). They found that the most likely defect in this material is a cation-on-anion antisite defect such as Ga_{Sb}. The change in energy of this defect as the $Al_xGa_{1-x}Sb$ composition changes produces *p*-type behavior in GaSb and semi-insulating behavior in AlSb. The calculations predicted a higher ionization energy as the Al mole fraction increases. In fact, the DLTS measurements presented here showed that the higher energy traps were observed when probing the aluminum compounds as described earlier in this chapter.

The total evidence that the traps at 23 and 76 meV exhibit behavior in line with an assignment to the Ga_{Sb} antisite defect is: 1) the increase in energy with aluminum mole fraction measured with DLTS, 2) the good match in energies with theoretically predicted values, 3) acceptor behavior indicated by the Poole-Frenkel effect, and 4) both traps show approximately the same concentration.

Of the hole traps measured, BH3 stands out as having an extraordinarily large capture cross section of 2×10^{-11} cm^2. Capture cross sections of this magnitude have been attributed to capture by an Auger process. Therefore, this trap should have a significant

effect on free carrier concentration in AlGaAsSb, limiting the lifetime of electrons as minority carriers.

All of the previously reported traps measured by DLTS in Al_xGaAs_ySb are for electron traps. A commonly reported trap is the DX center named for its components, which were believed to be the donor and an unknown component. Many of the deep levels associated with the various donors have a capture barrier. In AlGaAs, the model developed for the capture barrier associated with the DX center is a lattice relaxation (Mooney, 1990:R1–R26). The model is different for group IV and group VI donors. The group IV donor shifts toward an interstitial site upon electron capture. Conversely, for a group VI donor, a group III atom adjacent to the donor shifts toward the interstitial site. The sites participating in the relaxation were determined by the number of DLTS peaks in ternary AlGaAs compounds with increasing Al mole fraction. In the first case, the three neighboring atoms for the group IV donor in the interstitial site can be only Ga for GaAs, resulting in only one peak. For AlGaAs, the three neighboring atoms for the group IV donor in the interstitial site can be any combination of three Ga and Al atoms, resulting in four possible peaks corresponding to zero, one, two, or three Al atoms. In the second case, either a Ga or Al would be displaced to the interstitial surrounded by any combination of three Ga and Al atoms for a total of eight possible peaks. The relaxation models for either group IV or VI donors were found to be stable configurations provided that the defect traps two electrons (Chadi and Chang, 1988:873; Chadi and Chang, 1989:10,063). If the DX center in $Al_xGa_{1-x}As_ySb_{1-y}$ has the same behavior, there should be only one peak seen in the n-GaSb. Te (group VI) doped n-AlAsSb should have four

possible distinct traps since the three group V that surround an interstitial aluminum atom site can be occupied by either As or Sb. Similarly there are 32 possible peaks in quaternary compositions of AlGaAsSb. The quaternary materials investigated here for the diodes with heterojunctions in the depletion region are undoped so that only background impurities are responsible for any DX traps present.

Two electron traps were measured in the n-GaSb at 243 and 352 meV, contrary to the single DX trap that is predicted. However, this n-GaSb is the substrate of the p-n junction/heterojunction sample. The n-GaSb substrate was grown by the liquid encapsulated Czochralski method which generally results in a higher impurity incorporation than MBE grown epitaxial layers. The two peaks may therefore be from the Te impurity and an unidentified impurity. Poole et $al.$ compared sulfur related traps (280 meV) with Te (310 meV) and Se (315 meV) related deep levels and found that all had a large lattice relaxation energy of around 200 meV (Poole et $al.$, 1990:1645–1647). This contrasts with other investigations reporting that there was no evidence of a lattice relaxation for Te and Se related traps. Poole suggested that the large relaxation and resultant capture barrier found for Te and Se was a result of S contamination, based on the characteristics of the sulfur doped sample, although only one resolved peak was mentioned. The two peaks reported in this study could be Te and some impurity other than sulfur. Sulfur is ruled out because no significant capture barrier was measured.

The $AlAs_{0.07}Sb_{0.93}$ ternary material showed only one large trap rather than the four predicted traps. In contrast, Mooney observed multiple peaks in the DLTS spectra of $Al_xGa_{1-x}As$ with x=0.04 and 0.08 (Mooney, 1990:R1–R26). For the $Al_xGa_{1-x}As_ySb_{1-y}$

quaternary materials with x=0.5 and 0.6, each showed only one electron trap with DX-like characteristics, BE2 and AE3, respectively. The MOS capacitors which have lower leakage current at high temperature than the *p-n* junctions allowed measurements at slightly higher temperature, and gave evidence of an additional trap at ~350 K. Even so, increasing current prevented an accurate measurement. The appearance of only one or two defect levels in either ternary or quaternary compositions indicates that only one or two defect configurations are significantly favored over all of the other possibilities.

It has been shown previously that for Hall-effect measurements, the change in carrier concentration and mobility after illumination can indicate of the charge state of the DX defect only if the degree of compensation is known (Anand *et al.*, 1993:489–494; Subramanian, Anand, and Arora, 1990:609–612; Leith, Zukotynski, and SpringThorpe, 1992:2517–2519). The charge state of the DX center has been debated since the proposal of the negative U model by Chadi and Chang (Chadi and Chang, 1988:873). In the conventional positive U model, the neutral DX center (DX^0) is formed by the reaction

$$D^+ + e^- \rightarrow DX^0,$$
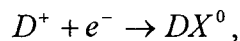
where D^+ represents the donor in its unrelaxed, non-DX state. In the negative U model, the DX center has negative charge (DX^-) and is formed by the net reaction:

$$2D^+ + 2e^- \rightarrow DX^- + D^+$$
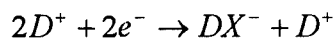
(Leith, Zukotynski, and SpringThorpe, 1992:2517–2519). The ionized impurity concentration that can contribute to scattering for the two models of the DX center is;

$$N_i(DX^0) = N_d^+ + N_A^- = 2N_A^- + n$$

$$N_i(DX^-) = N_d^+ + N_{DX}^- + N_A^- = 2N_A + n_{\max}^{ppc} \quad,$$

where n is the measured free electron concentration, N_A^- is the filled acceptor concentration, N_D^+ is the ionized donor concentration, N_{DX}^- is the filled DX center concentration, and $n_{\max}^{ppc}$ is the maximum free electron concentration under saturated PPC conditions (Subramanian, Anand, and Arora, 1990:609–612). In the case of the DX^0 model, $N_i(DX^0)$ increases after photoexcitation since n increases. The net change in scattering rate will be determined by the competition between the increased scattering due to an increase in N_i, and the increased screening due to an increase in n. For heavy compensation, the screening term dominates, causing the mobility to increase. Otherwise, for low compensation, photoionization increases the number of ionized scattering centers, and thus the mobility decreases. As a result, the DX^0 model predicts an increase in the mobility upon photoionization if the compensation in the sample is high, and a decrease in the mobility if the compensation is low.

In the DX^- model, photoexcitation causes each DX^- center to give rise to two electrons in the conduction band, and converts itself into a positive singly charged donor. Therefore, the scattering impurity concentration is the same before and after illumination. However, with increasing free electron concentration by photoexcitation, the screening also increases and hence the scattering rate decreases. The DX^- model predicts an increase in the mobility upon photoexcitation, regardless of the compensation.

Based on the fact that the Ga_{Sb} antisite defect provides a background p-type doping in the mid 10^{16} cm^{-3}, which is close to the level of tellurium n-type doping, the

$Al_{0.9}Ga_{0.1}As_{0.08}Sb_{0.92}$ samples are heavily compensated. Therefore, unfortunately, both models predict the same behavior for any heavily compensated samples. Thus, the Hall measurements are inconclusive regarding the charge state of the DX center in this case.

Measurement of the Poole-Frenkel effect for the DX center in AlAsSb should have shown a very large reduction in emission energy with increasing electric field if it traps two electrons, and is neutral when filled. The fact that the Poole-Frenkel effect was small, even for a defect that traps only one electron, points toward the DX$^-$ model as being the correct one, although a reduction of the effect by the capture barrier must also be considered.

Summary and Conclusions

This section presented the characteristics of deep level traps found in $Al_xGa_{1-x}As_ySb_{1-y}$ (x=0, 0.5, 0.6, 1.0) grown by MBE. This is the first report of DLTS measurements of a Ga_{Sb} double acceptor trap in $Al_xGa_{1-x}As_ySb_{1-y}$. The energy levels are close to energies calculated theoretically, and energies measured by other methods. Previously reported values cover a wide range of energies. Progress is also made in establishing the model for the DX center in this material. The reduction in energy with electric field was less than expected for a center that is neutral after trapping two electrons, suggesting that the DX center is charged -1q after trapping two electrons. Hall measurements gave results that were inconclusive regarding the charge state, because of heavy compensation. The degree of compensation of the donor by Ga_{Sb} may also be the reason that more peaks related to the donor impurities aren't seen. It is suggested that the

high concentration of Ga_{Sb} antisite defects affect where donors are situated, giving preference to one configuration over the many other possible configurations. Once growth conditions are achieved that reduce the concentration of antisite defects, more peaks may appear with other energies which correspond to different configurations of atoms around the donor related defect.

Deep Levels in $Ga_{0.8}In_{0.2}As_{0.12}Sb_{0.88}$

Sample Structure

DLTS was also used to characterize the deep traps in $Ga_{0.8}In_{0.2}As_{0.12}Sb_{0.88}$ which is used for the active region of 2 μm diode lasers. The sample was grown by MBE, and is lattice-matched to GaSb. The y-value of $Ga_xIn_{1-x}As_ySb_{1-y}$ for a desired x-value lattice matched to GaSb at room temperature is

$$y = \frac{0.91(1-x)}{(1+0.05x)}.$$

The $Ga_{0.8}In_{0.2}As_{0.12}Sb_{0.88}$ diode was grown with unintentional background p-type doping of 1×10^{16} cm^{-3}. 460 Å of Si_3N_4 was deposited by plasma enhanced chemical vapor deposition for a metal-insulator-semiconductor (MIS) structure. A thin insulating layer is desired so that the MIS diode capacitance is determined primarily by the semiconductor depletion capacitance rather than the insulator capacitance. A mesa etch using H_3PO_4, H_2O_2, H_2O, and L-tartaric acid with a ratio of 1ml:1ml:250ml:0.4g was used to define the diode area of 0.0025 cm^2. Ohmic contact to the back side of the sample was made using

the indium left there from bonding the wafer to the wafer holder during epitaxy. The top

ohmic contact was formed by 300 Å of Ti, 600 Å of Pt, and 3,000 Å of Au. It was then

packaged in a TO-5 can with thermally and electrically conductive epoxy. Then the top

ohmic contact was bonded with 0.7 mil Au wire for DLTS measurements.

DLTS Measurements of $Ga_{0.8}In_{0.2}As_{0.12}Sb_{0.88}$

The DLTS spectra for the unintentionally doped p-$Ga_{0.8}In_{0.2}As_{0.12}Sb_{0.88}$ measured

using the MIS capacitor structure is shown in Figure IV-17. The positive going peaks are

for hole emission to the valence band. The negative going peak, in this case, is for hole

emission to the conduction band in the n-type inversion layer. From a multi-exponential

fit of the transients, it was found that the low temperature peaks, (a), (b), (c), and (d),

from 50–200 K are a superposition of four hole trap energy levels. The position and

height of peaks (a), (b), and (c) were found to be very sensitive to the trap filling and

measurement biases. Changing the filling and measurement biases from 0 and -2 V, to -1

and -3 V, and then to -2 and -4 V, respectively, shifted the emission window away from

the semiconductor-insulator interface. Shifting the emission window away from the

semiconductor-insulator interface resulted in a shift of peaks to lower temperature, and an

increase in trap concentrations. The peak shift to lower temperature with increasing

electric field indicates that the defects are acceptor traps in a p-type material. The increase

in acceptor trap concentration with distance from the insulator can be a result of a reaction

between the Si_3N_4 and the $Ga_{0.8}In_{0.2}As_{0.12}Sb_{0.88}$. It has been shown for GaAs that Si_3N_4

deposition causes Ga vacancies near the interface (Dhar, Mallik, and Mazamdar,
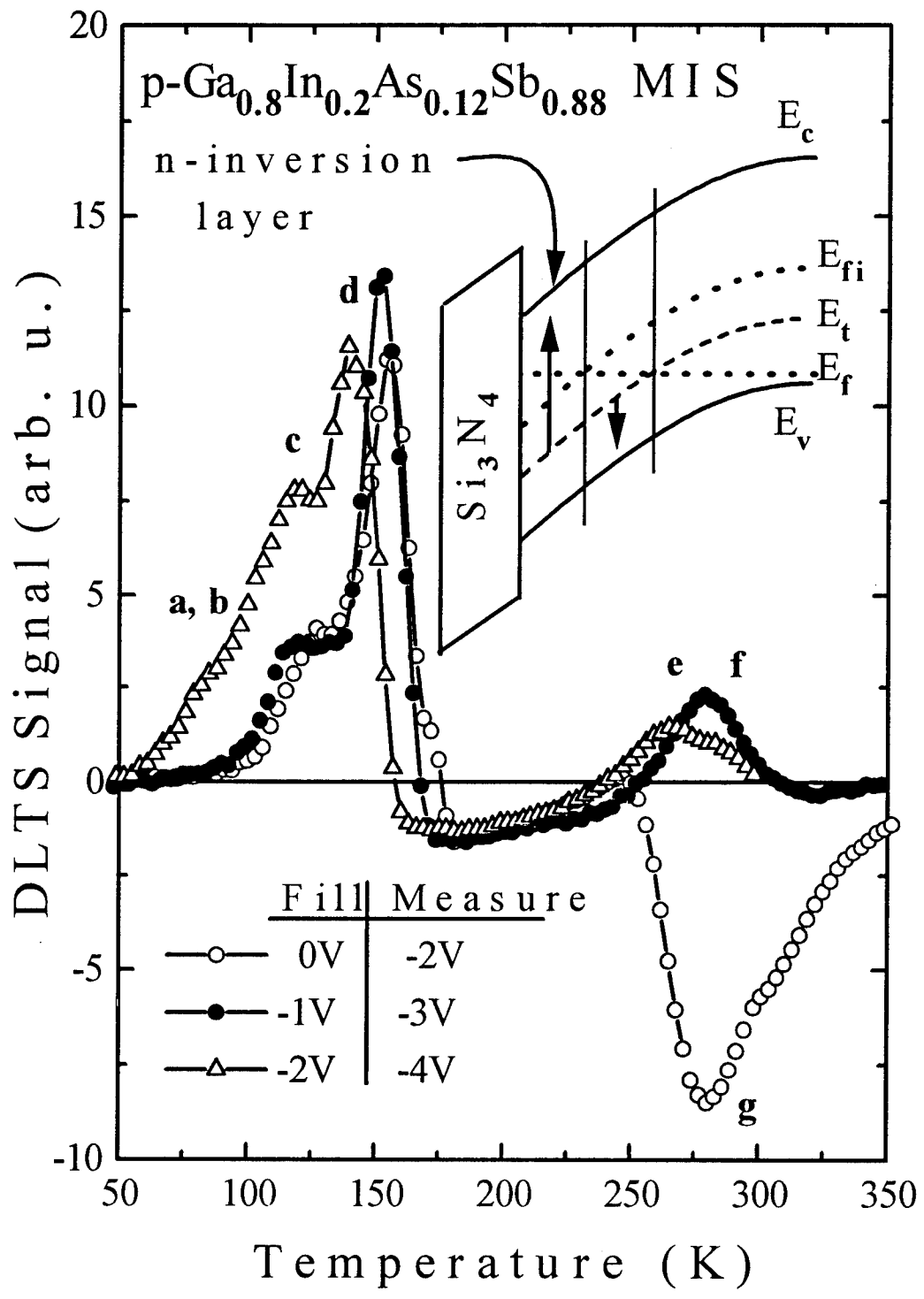
Figure IV-17. DLTS spectra for the traps in MBE-grown p-$Ga_{0.8}In_{0.2}As_{0.12}Sb_{0.88}$.

1994:1531–1535). If a similar phenomenon occurs in $Ga_{0.8}In_{0.2}As_{0.12}Sb_{0.88}$, the Si_3N_4 reduces the Ga or In concentration near the interface. Since $Ga_xIn_{1-x}As_ySb_{1-y}$ grown by various methods has excess Ga, which makes undoped $Ga_xIn_{1-x}As_ySb_{1-y}$ p-type by forming the Ga_{Sb} antisite double acceptor defect (Shen *et al.*, 1993:8313–8318), the reduction of the concentration of Ga near the interface by the Si_3N_4 appears as a higher level of excess Ga away from the interface than that near the insulator. Therefore, the increase in concentration of trap levels (a), (b), and (c) away from the interface suggests that these defects are related to the excess Ga.

The DLTS capacitance transients measured in the temperature range of 20–475 K were digitized and fit using modulating functions to obtain the emission rate as a function of temperature as discussed earlier (Loeb and Cohen, 1965:359). Then, the fit for either one, two, or three exponential components was used to determine the activation energy and capture cross section of the trap by plotting the *ln(T²/e)* vs. *1/k_BT* in a standard DLTS Arrhenius plot (Lang, 1974:3023–3032).

The Arrhenius plot depicted in Figure IV-18 shows one minority carrier trap level at 320 meV below the conduction band, and six majority carrier trap levels at 24, 76, 108, 122, 224, and 276 meV above the valence band. The six hole traps emit to the valence band and one hole trap emits to the conduction band in the *n*-inversion layer. The inversion layer is formed in the $Ga_{0.8}In_{0.2}As_{0.12}Sb_{0.88}$ next to the Si_3N_4 when the Fermi level, E_f, is brought above the intrinsic Fermi level, E_{fi}, as shown in the inset of Figure IV-18. The two low energy traps show an interesting behavior, that is, the 24 meV energy level makes a transition to 73 meV as the temperature increases. This can be explained by
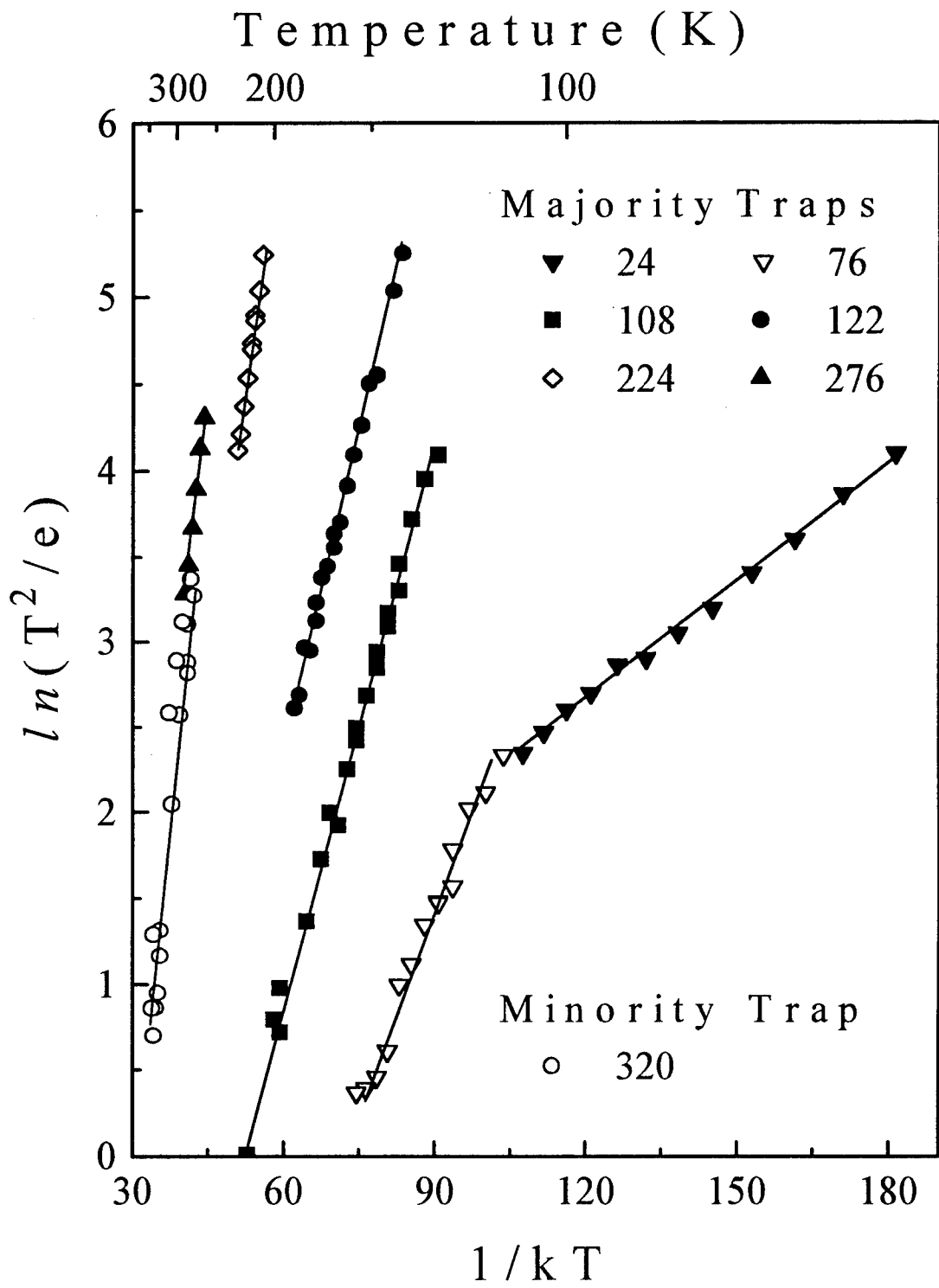
Figure IV-18. The Arrhenius plot for the traps found in p-$Ga_{0.8}In_{0.2}As_{0.12}Sb_{0.88}$.

an emission from a double acceptor defect similar to what was found in the $Al_xGa_{1-x}As_ySb_{1-y}$ for x=0, 0.5, 0.6. At low temperatures, both energy levels are filled, but as the temperature increases, the shallow energy level is emptied. Further increase in temperature is followed by an emission from the deeper energy level to the valence band via the shallow defect level. The deeper energy level does not begin to empty until the shallow defect level is significantly empty. This is shown by the non-crossing behavior of the two lines on the Arrhenius plot. For GaSb, the theoretical predictions and measurements of the double acceptor by other methods have shown that the two energy levels are 33 and 80 meV (Shen *et al.*, 1993:8313–8318; Nakashima, 1981:1085–1094). Therefore, it is believed that trap levels (a) and (b) are due to a III_V antisite defect in $Ga_{0.8}In_{0.2}As_{0.12}Sb_{0.88}$. The origin of traps (c) and (d) are not known at present.

The minority carrier peak (g) shown in Figure IV-17 was obtained using a filling pulse of 0.1 sec at 0 V bias and measurement bias of -2 V. Under these conditions, most of the DLTS minority carrier signal originates from the emission of the trapped holes to the *n*-type inversion layer near the interface as shown in the inset of Figure IV-17. Changing filling and measurement biases to shift the region of filled traps away from the inversion layer decreases the available conduction band states for hole emission, and results in increased competing majority carrier emission. In this case, although the energy levels are difficult to measure accurately due to the spatial dependence of both majority and minority carrier emissions, the energy of the minority carrier signal is estimated to be 320±50 meV. Two energies were also resolved for the majority carrier peak, one (e) at 224 meV, and another (f) at 276 meV. The sum of the minority carrier signal energy (g)

and the deeper majority carrier signal energy (f) is very close to the band gap of 594 meV for $Ga_{0.8}In_{0.2}As_{0.12}Sb_{0.88}$. Therefore, unless there is a significant lattice relaxation during capture to either trap, it is believed that both signals (f) and (g) originate from the same trap center. Since this center is located near midgap, it acts as the most efficient non-radiative recombination center in this material.

Summary

One minority trap level at 320 meV below the conduction band, and six hole trap levels at 24, 76, 108, 122, 224, and 276 meV above the valence band were found in the $Ga_{0.85}In_{0.15}As_{0.12}Sb_{0.88}$ active region material for 2 μm diode lasers, using DLTS measurements. The two low energy levels (24 and 76 meV) are attributed to a Ga_{Sb} double acceptor. It is believed that the minority trap level at 320 meV and the hole trap level at 276 meV originate from the same trap, and it could be the most efficient non-radiative recombination center in this material.

Band Offset Measurements in Quantum Well Samples

Design of the quantum well samples entails estimates of several material parameters from published literature in order to obtain a sample with confined state energies that will result in emissions from the well that are measureable by DLTS. The parameters required to calculate the energy levels in the well are the effective masses of the well and barrier materials, the band gap for each in different reciprocal space directions, and the band offsets. The energy levels in the valence band and conduction band wells will be determined experimentally from the emission rate from the well as it changes with temperature. The end use will be to compare the calculated confined energy values to the measured energies. The measured values can then be used to determine the correct band offsets.

Measurement of thermionic emission processes include transitions that aren't seen with optical characterization. Optical characterization methods consider primarily the confined states that involve direct transitions, so that X and L band potential wells are not a primary concern. However, measurement of thermally stimulated processes such as DLTS need to consider other transitions involving the indirect band minima. Thermionic emission processes depend on absorption of phonons, so that transitions involving a change in momentum are to be expected.

Three conduction band energy minima are represented by the Γ, X, and L symmetry points. A quantum well will therefore have confined states based on the depth of the wells in each of the k-space directions of high symmetry, and on the respective

effective mass. This is contrary to calculating the confined state energies based on the potential difference between the minimum conduction band energy of the well and barrier, regardless of symmetry. A schematic diagram for two symmetry points is shown in Figure IV-19. The band offset at the Γ point is used to calculate the energy levels in the well shown at the left, while the band offset at the X point is used to calculate the energy levels in the well shown at the right. Of course, the two potential wells are physically in the same place. The energies are plotted in reciprocal space for the band diagrams and real space for the potential wells. The band diagram at the top is for the conduction band of the barrier which is an indirect band gap semiconductor since the minimum occurs at the X symmetry point. The lower curve is the band diagram for the conduction band of the well which is a direct band gap material.
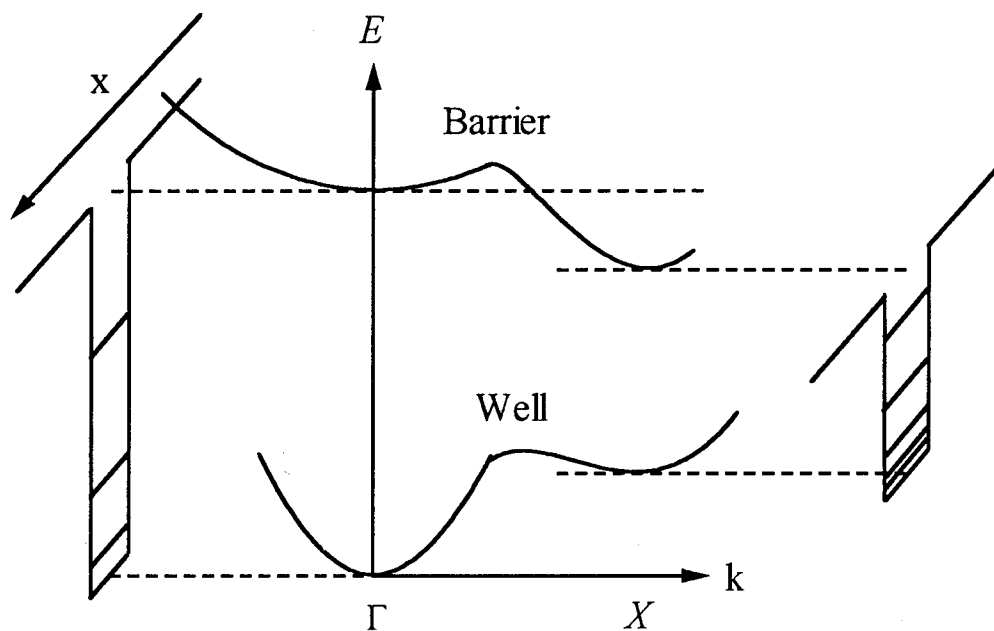
Figure IV-19. Conduction band diagrams for both the barrier (indirect gap) and the well (direct gap) materials. The energy plot shows a real space dimension out of the page for the quantum well diagrams, and reciprocal space dimensions for the band diagrams.

It is important to illustrate the dependence of the magnitude of the confining potential on momentum space. An electron in one of the Γ energy levels in the quantum well will be confined by the Γ potential of the barrier material since its momentum would have to change in order to be reflected by a barrier potential in another k-space direction. If it was reflected by a potential in a different k-space direction, it would have to be travelling in that momentum space direction when it was at the barrier, entailing a change in momentum at the barrier. A change in momentum would require a change in energy. A change in energy of the particle in the well upon reaching the barrier would mean that the original energy level was not a confined state. This contradiction shows that the confining potential is defined by the difference in energy of the band minima of the two materials in the same k-space directions.

A simpler picture exists for the valence band wells. In the valence band, the light hole, heavy hole, and the split-off band minima all occur at $k=0$ for both the well and the barrier. The light and heavy hole bands will be degenerate at $k=0$ if it is unstrained, so that light and heavy holes will have the same offset potentials. The valence band confined states are therefore determined by the difference in hole potential at the valence band minimum in the well and barrier, and the effective masses of the light and heavy holes in the well. Other confined states may be determined by the split-off band effective mass if the split-off band energy of the well is less than the minimum energy for carriers in the barrier.

Sample Structures

The position of the energy levels in the well can be controlled by the width of the well, and the composition of the well and the barrier materials. The sample structures of the three QWs that were characterized are given in Figure IV-20. In the first two samples, the width of the $Ga_xIn_{1-x}As_ySb_{1-y}$ well is 125 Å and 100 Å, respectively. In the third sample, the barrier composition was changed from $AlAs_{0.07}Sb_{0.93}$ to $Al_{0.9}Ga_{0.1}As_{0.07}Sb_{0.93}$. All three of the structures have direct gap $Ga_xIn_{1-x}As_ySb_{1-y}$ wells and indirect gap $Al_xGa_{1-x}As_ySb_{1-y}$ barriers. The valence band and conduction band of the $Ga_xIn_{1-x}As_ySb_{1-y}$ well material is expected to be located within the band gap of the $Al_xGa_{1-x}As_ySb_{1-y}$ barrier material for a type I quantum well arrangement.

Effective Mass

In order to predict the energy levels in a quantum well, the effective mass in $Ga_xIn_{1-x}As_ySb_{1-y}$ needs to be known. There has been some experimental work on the effective mass in $InAs_{1-x}Sb_x$. Also, theoretical models have been revised enough to determine the effective mass fairly accurately. However, most of the measurements and calculations are only for the effective mass at the conduction band minimum. An electron passing from the wide gap barrier material to the narrow gap well may first go into the highest confined energy level available in the same momentum direction that it came from, which is the X band for $Al_xGa_{1-x}As_ySb_{1-y}$ for $x>0.22$. Then, depending on the energy loss rate from electron-phonon scattering, electrons will be transferred to confined states with other k-vectors. Subsequent emission during the DLTS measurement bias phase is from

94-087

50 Å p^+-GaSb
500 Å U.D. p-AlAs$_{0.07}$Sb$_{0.93}$
125 Å U.D. p-Ga$_{0.85}$In$_{0.15}$As$_{0.12}$Sb$_{0.88}$
500 Å U.D. p-AlAs$_{0.07}$Sb$_{0.93}$
6500 Å n^+-AlAs$_{0.07}$Sb$_{0.93}$
3300 Å n^+-GaSb buffer
n^+-GaSb substrate

95-075

500 Å p^+-GaSb
400 Å p^+-AlAs$_{0.07}$Sb$_{0.93}$
5000 Å U.D. p-AlAs$_{0.07}$Sb$_{0.93}$
100 Å U.D. p-Ga$_{0.81}$In$_{0.19}$As$_{0.12}$Sb$_{0.88}$
1000 Å U.D. p-AlAs$_{0.07}$Sb$_{0.93}$
2200 Å n^+-AlAs$_{0.07}$Sb$_{0.93}$
6100 Å n^+-GaSb buffer
n^+-GaSb substrate

95-120

300 Å p^+-GaSb
300 Å p^+-Al$_{0.9}$Ga$_{0.1}$As$_{0.07}$Sb$_{0.93}$
5000 Å U.D. p-Al$_{0.9}$Ga$_{0.1}$As$_{0.07}$Sb$_{0.93}$
100 Å U.D. p-Ga$_{0.81}$In$_{0.19}$As$_{0.12}$Sb$_{0.88}$
1000 Å U.D. p-Al$_{0.9}$Ga$_{0.1}$As$_{0.07}$Sb$_{0.93}$
2200 Å n^+-Al$_{0.9}$Ga$_{0.1}$As$_{0.07}$Sb$_{0.93}$
4000 Å n^+-GaSb buffer
n^+-GaSb substrate

Figure IV-20. Structures of the three quantum well samples that were characterized using current-voltage versus temperature (I-V-T), C-V, and DLTS measurements.

any of the well levels into the conduction band minimum of the barrier with phonon assistance if necessary. The different k-space confined states will impact both the capture process and the emission process, requireng the effective mass in the different k-space directions where there is a local minimum. Effective mass values used to determine the energy levels in the well are taken either from experimental data, if it is available, or from published theoretical calculations.

Rogalski has reported on different group's estimates of effective mass of $InAs_{1-x}Sb_x$ using multi-band k•p calculations, and then compared the calculated values to measurements made by magneto-thermoelectric power, Faraday rotation, and plasma reflectance (Rogalski, 1989:191–231). It was determined that serious discrepancies between calculated and experimentally determined effective mass can be avoided if the multi-band k•p calculations are used rather than a simple Kane model. He came up with the expression for the effective mass (m_e*) of $InAs_{1-x}Sb_x$ as

$$\frac{m_0}{m_e^*} - 1 = \frac{P^2}{3}\left(\frac{2}{E_g} + \frac{1}{E_g + \Delta}\right) - \frac{P'^2}{3}\left(\frac{2}{E(\Gamma_8^c) - E_g} + \frac{1}{E(\Gamma_7^c) - E_g}\right) + C,$$

where m_0 is the free-electron mass, P the matrix element determining the conduction-valence band interaction, P' the matrix element determining the higher Γ_5^c bands contribution. E_g is the band gap, Δ is the spin split-off energy, and $E(\Gamma_n^c)$ is the energy of a higher Γ-point band. C is a constant for the next higher band contribution. This equation has been found to agree well with measured values near the binary composition end points.

However, a more accurate equation over a wider range of compositions and temperatures takes into account the conduction-valence-band mixing which has the effect of transferring valence-band states to the conduction band, thereby increasing the electron effective mass. The equation for $InAs_{1-x}Sb_x$ is given by

$$\frac{1}{m_e^*} = \frac{1}{m_{ce}^*} + \frac{\delta E}{3}\left|\frac{1}{m_{hh}^* E_{gv}} + \frac{1}{m_{lh}^* E_{gv}} + \frac{1}{m_s^*(E_{gv} + \Delta_v)} - \frac{1}{m_{ce}^*}\left(\frac{2}{E_{gv}} + \frac{1}{E_{gv} + \Delta_v}\right)\right|.$$

Here, E_{gv} and Δ_v are values determined from the virtual-crystal approximation, which are given by E_{gv}=0.351-0.176x and Δ_v=0.39+0.42x at 300 K. m_{hh}^*, m_{lh}^* and m_s^* are the effective masses of the heavy-hole, light-hole, and split-off band, respectively, approximated by a linear interpolation of the effective mass of the binary compounds. m_{ce}^* is the effective mass for the conduction band calculated from the Kane model without band mixing. The difference $\delta E = E_{gv} - E_g$ is a reflection of the degree of disorder in the ternary material. The temperature dependence of the band gap of $InAs_{1-x}Sb_x$ used in the effective mass equation is given by

$$E_g(x,T) = 0.411 - \frac{3.4x10^{-4}T^2}{210 + T} - 0.876x + 0.70x^2 + 3.4x10^{-4}xT(1-x).$$

Once the effective mass of the ternary material is determined, the effective mass of the quaternary material is estimated by a linear interpolation of the two ternary materials. The effective mass of $GaAs_{1-x}Sb_x$ is estimated from interpolation of the binary materials because theoretical and experimental data have not been reported. Table IV-2 gives the values used for each of the binary materials. Other necessary effective mass values were

obtained from a handbook on compound semiconductor material constants (Neuberger, 1971).

Table IV-2. Effective mass of binary compounds (Neuberger, 1971).

compound	m_c^* (001)	m_{lh}^*	m_{hh}^*	m_s^*
GaAs	0.07	0.073	0.35	0.17
GaSb	0.033	0.054	0.23	0.17
InAs	0.031	0.055	0.39	0.15
InSb	0.03	0.062	0.26	0.20
AlAs	0.13	0.14	0.44	0.28
AlSb	0.079	0.12	0.29	0.26

<u>Band Gaps</u>

The band gap versus composition can be determined from the band gap of the binary constituents in a similar manner. The accuracy of the estimates is improved by including the bowing parameter, which is a factor that takes into account the deviation from a linear interpolation between the binary components. There is a different bowing

parameter for each parameter of interest. For a ternary material in the form of AB_xC_{1-x}, a parameter $T_{ABC}(x)$ such as the band gap can be estimated from

$$T_{ABC}(x) = xB_{AB} + (1-x)B_{AC} + x(x-1)C_{ABC}$$

where B_{AB} and B_{AC} are the values for the binary alloys, e.g., the band gaps in this case, and C_{ABC} is the bowing parameter. Then the parameter $Q(x,y)$ of a quaternary material in the form of $A_xB_{1-x}C_yD_{1-y}$ can in turn be estimated from

$$Q(x,y) = \frac{x(1-x)[yT_{ABC}(x) + (1-y)T_{ABD}(x)] + y(1-y)[xT_{ACD}(y) + (1-x)T_{BCD}(y)]}{x(1-x) + y(1-y)}.$$

[IV-1]

Table IV-3 lists the band gaps of the binary constituents used to determine the band gaps of the ternary and quaternary compounds. Table IV-4 gives the bowing parameters for each of the band gap symmetry points including the spin split-off band.

The results of the band gap calculations are shown in Figure IV-21 for $Al_xGa_{1-x}As_ySb_{1-y}$, and Figure IV-22 for $Ga_xIn_{1-x}As_ySb_{1-y}$. The value of y in each case is determined from the conditions for lattice matching to GaSb as given previously at the beginning of each section on the deep levels in the barrier and well. The X conduction band minimum is the lowest energy in the $Al_xGa_{1-x}As_ySb_{1-y}$ barrier material for all of the quantum well structures used here. The diagram for the band gap of the $Ga_xIn_{1-x}As_ySb_{1-y}$ active region indicates that it is a direct material over all compositions.

Table IV-3. Band gaps of binary compounds at room temperature (Adachi, 1987:4869–4876).

	$E_g(\Gamma)$	$E_g(X)$	$E_g(L)$
AlAs	2.95	2.16	2.80
AlSb	2.22	1.61	2.21
GaAs	1.42	1.91	1.73
GaSb	0.72	1.05	0.76
InAs	0.36	1.37	1.07
InSb	0.17	1.63	0.93

Table IV-4. Band gap and split-off bowing parameters (Adachi, 1987:4869–4876).

Ternary material	Bowing parameter (eV)			
	C_Γ	C_X	C_L	C_Δ
(Al,Ga)As	0.37	0.245	0.055	0.07
(Ga,In)As	0.6	1.4	0.72	0.20
(Al,Ga)Sb	0.47	0	0.55	0.3
(Ga,In)Sb	0.42	0.33	0.38	0.1
Al(As,Sb)	0	0	0	0
Ga(As,Sb)	1.2	1.09	1.09	0.61
In(As,Sb)	0.58	0.59	0.57	1.2
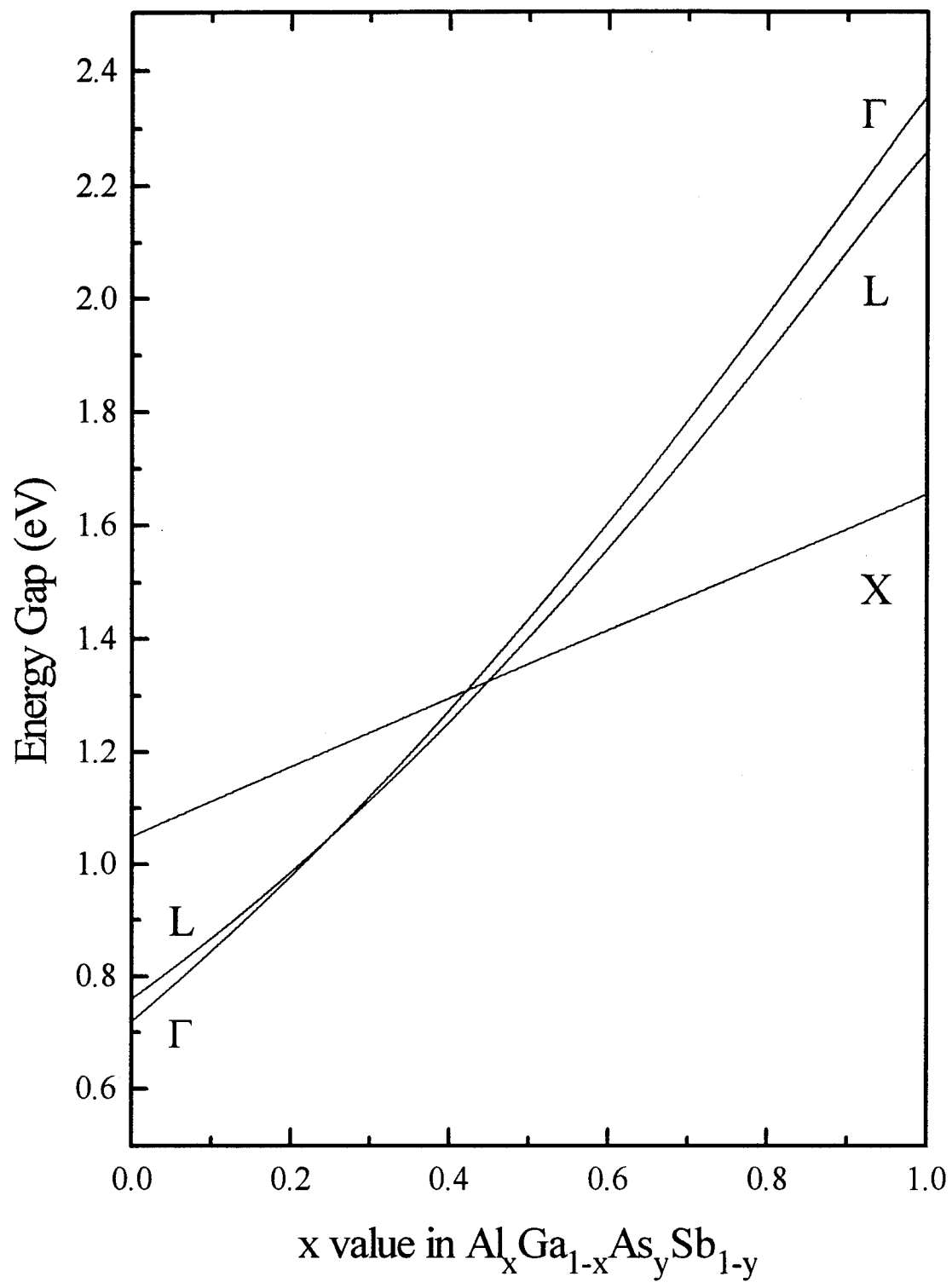
Figure IV-21. Band gap versus composition x for $Al_xGa_{1-x}As_ySb_{1-y}$ used for cladding layers in 2–4 μm diode lasers.
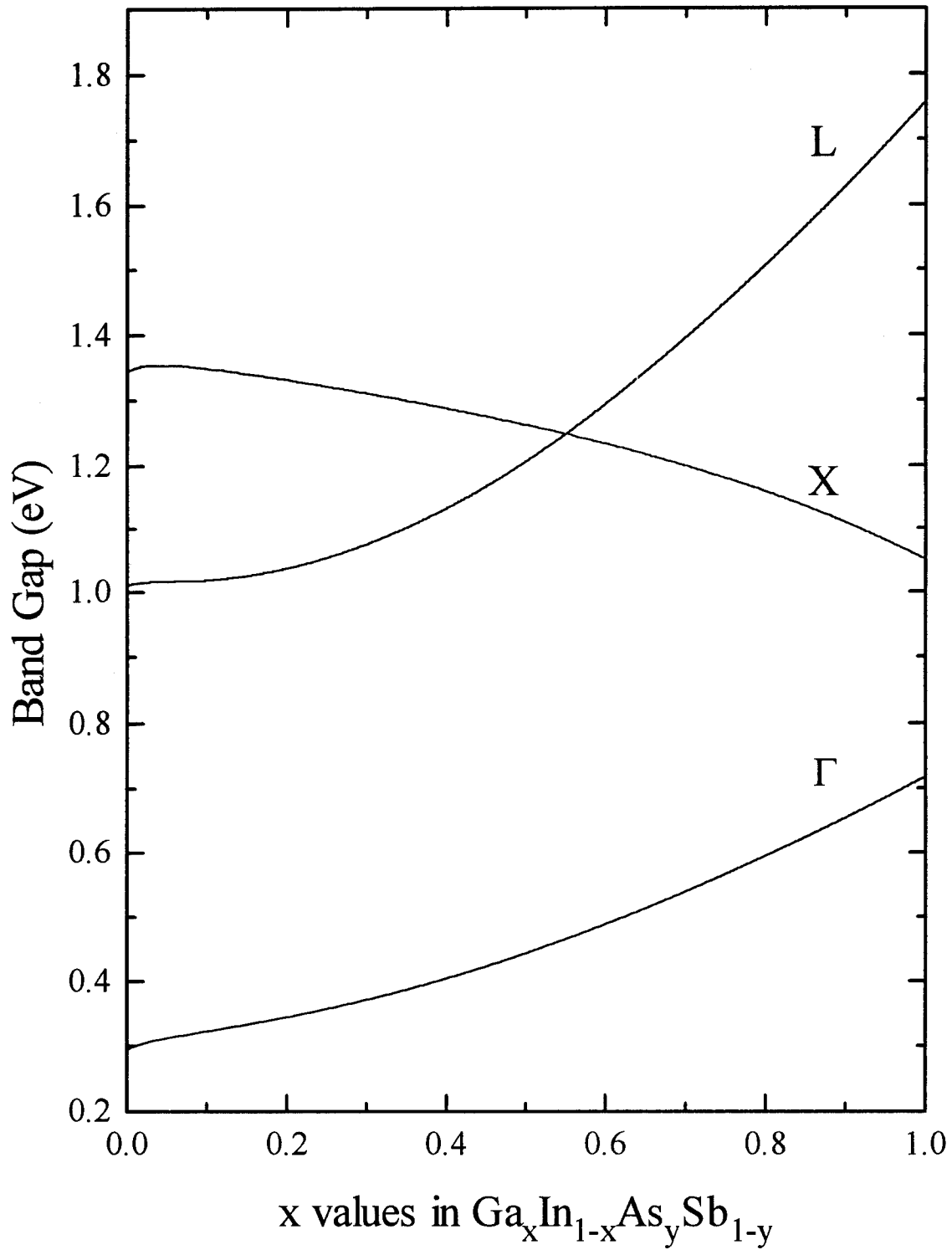
Figure IV-22. Band gap versus composition x for $Ga_xIn_{1-x}As_ySb_{1-y}$ used in the active region of a diode laser for the 2–4 μm wavelength range.

<u>Band Offset Estimates:</u>

The band offsets also need to be estimated in order to predict the energy levels in the quantum well. van de Walle devised a scheme to relate the energy of band minima in different materials. The method is based on a reference level chosen as the average electrostatic potential in a semi-infinite 'model-solid' (van de Walle, 1989:1871). The model-solid is a superposition of neutral atoms that are required to produce the bulk electron density. The reference point is the average valence band energy, $E_{v,av}$. Values for $E_{v,av}$ can be conveniently calculated by a product polynomial from an expansion of the weighted average of each component of equation [IV-1], which is given by

$$E_{v,av}(x,y) = \sum_{i=0}^{2} \sum_{j=0}^{2} C_{ij} x^i y^j$$

The coefficients C_{ij} are reproduced in Table IV-5 (Krijn, 1991:27–31).

Table IV-5. Valence-band average energy ($E_{v,av}$) coefficients C_{ij} (Krijn, 1991:27–31).

	C_{00}	C_{01}	C_{02}	C_{10}	C_{11}	C_{12}	C_{20}	C_{21}	C_{22}
$Al_xGa_{1-x}As_ySb_{1-y}$	-6.250	-0.570	-0.100	-0.421	0.035	-0.188	0.011	0.007	-0.013
$Ga_xIn_{1-x}As_ySb_{1-y}$	-6.090	-0.442	-0.138	-0.075	-0.162	0.036	-0.085	0.034	0.002

Now, using the estimated spin-orbit splitting and average valence band energy, a common reference energy can be used to assign an absolute energy to the valence band of each material. The difference is an estimate of the valence band offset. Then the

conduction band offset can be calculated from the estimated band gaps. The referenced valence band energy, E_v, is given by

$$E_v = E_{v,av} + \frac{\Delta_0}{3}.$$

where Δ_0 is the spin split-off energy. Similarly, the referenced conduction band energy, E_c, is given by

$$E_c = E_{v,av} + \frac{\Delta_0}{3} + E_g.$$

From these calculations, the band offset for a quantum well composed of AlAsSb barrier and $Ga_{0.85}InAsSb$ well is estimated to be 0.3975 eV in the valence band, 1.327 eV for the Γ symmetry point, 0.117 eV for the X symmetry point, and -0.42 eV for the L symmetry point. A negative value at the L point indicates that the L-band minimum of the low gap material (well) is above the L-band minimum of the wide gap material (barrier). The split-off band is separated from the valence band by 0.6797 eV, which is greater than the valence band offset. Thus, neither the L band offset nor the spin split-off effective mass will be a factor in determining the confined state energies. The confined state energies and band offsets will be summarized for each of the samples at the end of the next section. Now the energy of the confined states can be determined using the well thickness, the estimated effective mass at each of the band energy minima, and the estimated band offsets.

Quantum Well Confined Energies

The Schrödinger equation for a finite-well is given by

$$\left(-\frac{\hbar^2}{2m^*(z)}\frac{\partial^2}{\partial z^2}+V(z)\right)X_n(z)=\varepsilon_n X_n(z),$$

where $m^*(z)$ is the effective mass, $V(z)$ is the depth of the well, and ε_n is the confinement energy of the carriers. The boundary conditions at the interfaces are that the wave function, $X_n(z)$, and its derivative weighted by the effective mass on either side of the interface, $[1/m^*(z)][\delta X_n(z)/\delta z]$, are continuous (Bastard, 1981:5693; Bastard, 1982:7594). This equation can be solved graphically or numerically for the energies and wave functions of carriers confined to the potential well. First, an exponentially increasing or decreasing amplitude of the wave function in the barrier, and a standing wave solution in the well are assumed as given by the following equations,

$$
\begin{aligned}
X_n(z) &= A\cos kz, & |z| &< L/2 \\
&= B\exp[-\kappa(z-L/2)], & z &> L/2 \\
&= B\exp[\kappa(z+L/2)], & z &< -L/2 \\
&\textit{or} & & \\
X_n(z) &= A\sin kz, & |z| &< L/2 \\
&= B\exp[-\kappa(z-L/2)], & z &> L/2 \\
&= B\exp[\kappa(z+L/2)], & z &< -L/2
\end{aligned}
$$

The energy inside and outside the well is given by

$$\varepsilon_n=\frac{\hbar^2 k^2}{2m_A^*}-V_0 \quad\text{and}\quad \varepsilon_n=-\frac{\hbar^2\kappa^2}{2m_B^*}\quad\text{for}\quad -V_0<\varepsilon<0\ ,$$

respectively. k is the wave vector inside the well. κ is the wave vector in the barrier. V_0 is the band offset. The even function solutions satisfying the boundary conditions are

$$\cos(kL/2)=B \quad\text{and}\quad (k/m_A^*)\sin(kL/2)=\kappa B/m_B^*,$$

resulting in the condition

$$\tan(kL/2) = \frac{\kappa m_A^*}{k m_B^*}. \qquad\qquad [\text{IV-2}]$$

The odd function solutions satisfying the boundary conditions are

$$-\cot(kL/2) = \frac{\kappa m_A^*}{k m_B^*}. \qquad\qquad [\text{IV-3}]$$

The even and odd function solutions are determined graphically by plotting the left and right sides of equations [IV-2] and [IV-3] as a function of energy. The solutions are obtained where the traces for each function cross. Figure IV-23 shows the energies of the confined states in the Γ and X band potential wells using the band offset and effective masses expected for the first quantum well structure of $AlAs_{0.07}Sb_{0.93}/Ga_{0.85}In_{0.15}As_{0.12}Sb_{0.88}/AlAs_{0.07}Sb_{0.93}$. The other two quantum well structures have similar energy level spacing. The large effective mass in the X-band of the well material results in narrow spacing of the energy levels in the X-band potential well. This presents a quasi-continuum of energy levels since the spacing is on the order of kT at the temperatures where emission is expected to be seen from the deepest levels in the Γ well confined states. This figure points out the possibility that experimental results may include emission from the Γ well to the X-band in the barrier via the X-band in the well. Another case that must be considered when analyzing the experimental results is the possibility of emission from the deepest state in the Γ well via excited states in the Γ well. The valence band well is also similar for each of the three samples. Figure IV-24 shows the energy levels for the valence band well for the first quantum well structure of $AlAs_{0.07}Sb_{0.93}/Ga_{0.85}In_{0.15}As_{0.12}Sb_{0.88}/AlAs_{0.07}Sb_{0.93}$.
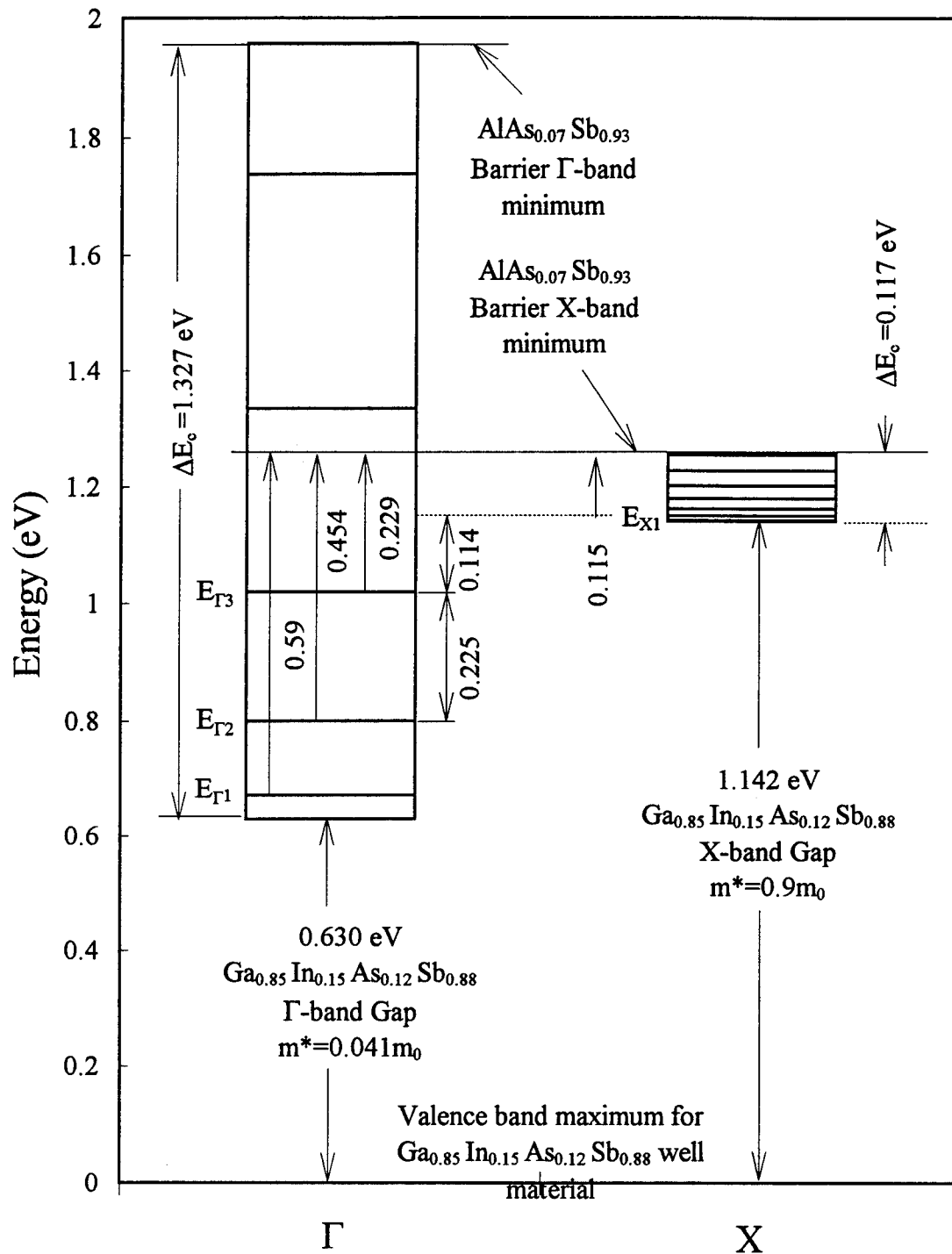
Figure IV-23. Relevant energies in the Γ and X band wells for the first quantum well structure of $AlAs_{0.07}Sb_{0.93}/Ga_{0.85}In_{0.15}As_{0.12}Sb_{0.88}/AlAs_{0.07}Sb_{0.93}$. The two are shown separatly for clarity.
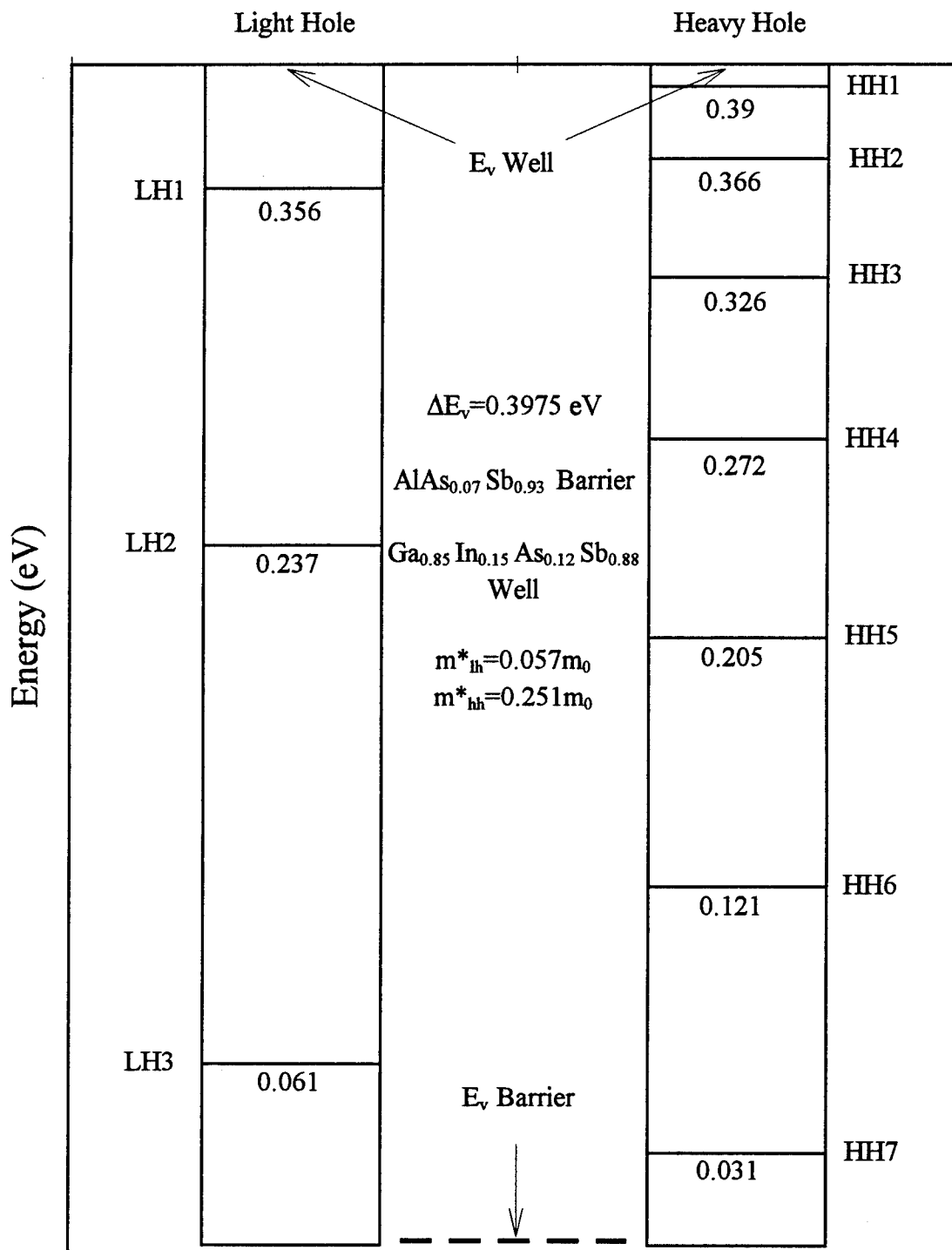
Figure IV-24. Energy levels in the valence band well. The energy values given are for emission to the valence band of the barrier.

Table IV-6 is a summary of the expected discrete energies in the valence band well calculated from the parameters given in the same table. The energies listed are the emission energies to the valence band in the barrier, not the energy from the valence band of the well. The spin split-off band is separated from the valence band maximum by an energy that is greater than the valence band offset, so the energies based on the spin split-off effective mass are not considered. Table IV-7 summarizes the emission energies that are expected for the conduction band wells. The subscripts on the energies indicate the confining potential, either Γ or X, and the value of the excited state, n. The emission energies for the electrons confined by the Γ-band potentials are for emission to the X-band minimum in the barrier.

Table IV-6. Estimated sample parameters and calculated energy levels for the valence band confined states of AlGaAsSb/GaInAsSb/AlGaAsSb quantum wells.

QW Structure No.	1: 94-087	2: 95-075	3: 95-120
ΔE_V (eV)	0.3975	0.428	0.3795
$Ga_xIn_{1-x}As_ySb_{1-y}$	x=0.85, y=0.12	x=0.80, y=0.12	x=0.81, y=0.12
$Al_xGa_{1-x}As_ySb_{1-y}$	x=1.0, y=0.07	x=1.0, y=0.07	x=0.90, y=0.07
well width (Å)	125	100	100
m_{lh}^*	0.057	0.056	0.056
m_{hh}^*	0.251	0.243	0.243
E_{hh1} (eV)	0.390	0.416	0.367
E_{hh2} (eV)	0.366	0.379	0.331
E_{hh3} (eV)	0.326	0.318	0.272
E_{hh4} (eV)	0.272	0.235	0.190
E_{hh5} (eV)	0.205	0.132	0.090
E_{hh6} (eV)	0.121	0.020	
E_{hh7} (eV)	0.031		
E_{lh1} (eV)	0.356	0.385	0.338
E_{lh2} (eV)	0.237	0.262	0.219
E_{lh3} (eV)	0.061	0.078	0.046

Table IV-7. Estimated sample parameters and calculated energy levels for the confined states in the Γ and X band of AlGaAsSb/GaInAsSb/AlGaAsSb quantum wells.

QW Structure No.	1: 94-087	2: 95-075	3: 95-120
$Ga_xIn_{1-x}As_ySb_{1-y}$	x=0.85	x=0.80	x=0.81
$Al_xGa_{1-x}As_ySb_{1-y}$	x=1.0	x=1.0	x=0.90
well width (Å)	125	100	100
$\Delta E_C(\Gamma)$ (eV)	1.327	1.332	1.184
m_{CW}^*	0.0408	0.038	0.0388
m_{CB}^*	0.121	0.121	0.121
$E_{\Gamma 1}$ (eV)	0.59	0.593	0.557
$E_{\Gamma 2}$ (eV)	0.454	0.467	0.382
$E_{\Gamma 3}$ (eV)	0.229	0.251	0.076
$\Delta E_C(X)$ (eV)	0.117	0.071	0.061
m_{CW}^*	0.9	0.704	0.87
m_{CB}^*	0.95	0.95	0.81
E_{X1} (eV)	0.115	0.068	0.057
E_{X2} (eV)	0.108	0.060	0.048
E_{X3} (eV)	0.097	0.047	0.033
E_{X4} (eV)	0.082	0.028	0.013
E_{X5} (eV)	0.063	0.007	
E_{X6} (eV)	0.039		
E_{X7} (eV)	0.014		

I-V Measurements on QW Structures

I-V, C-V, and then DLTS measurements were made on each of the three QW structures described in the previous section. The sample structures are reproduced in Figure IV-25 for convenience. This section is a description of the I-V measurements. I-V curves measured at different temperatures for each of the QW structures can be used to estimate the energy of the primary generation/recombination center, and possibly the band gap of the material used in the well. The I-V-T curves are also useful to establish the bias ranges that can be used in DLTS and C-V measurements over a sample temperature range. A large current flowing at a measurement bias used for DLTS will mask the thermionic emission current from charges trapped at the deep levels or in the QW. The energy measured by reverse I-V-T should correspond to the energy of one of the discrete trap levels measured by DLTS.

In the three quantum well sample structures used for band offset measurements, the etching process had the greatest effect on the current under reverse bias conditions. The effects of different concentrations of phosphoric acid in the etching solution were investigated, as well as the effects of treatment of the surface with ammonium sulfide. Reactive ion etching (RIE) is another etch method used in an attempt to improve the I-V characteristics. A distinguishing characteristic of the different etches is whether the reverse bias current is determined by a generation component or by a surface leakage component from the edge of the mesa etched surface.

94-087

- 50 Å p^+-GaSb
- 500 Å U.D. p-AlAs$_{0.07}$Sb$_{0.93}$
- 125 Å U.D. p-Ga$_{0.85}$In$_{0.15}$As$_{0.12}$Sb$_{0.88}$
- 500 Å U.D. p-AlAs$_{0.07}$Sb$_{0.93}$
- 6500 Å n^+-AlAs$_{0.07}$Sb$_{0.93}$
- 3300 Å n^+-GaSb buffer
- n^+-GaSb substrate

95-075

- 500 Å p^+-GaSb
- 400 Å p^+-AlAs$_{0.07}$Sb$_{0.93}$
- 5000 Å U.D. p-AlAs$_{0.07}$Sb$_{0.93}$
- 100 Å U.D. p-Ga$_{0.81}$In$_{0.19}$As$_{0.12}$Sb$_{0.88}$
- 1000 Å U.D. p-AlAs$_{0.07}$Sb$_{0.93}$
- 2200 Å n^+-AlAs$_{0.07}$Sb$_{0.93}$
- 6100 Å n^+-GaSb buffer
- n^+-GaSb substrate

95-120

- 300 Å p^+-GaSb
- 300 Å p^+-Al$_{0.9}$Ga$_{0.1}$As$_{0.07}$Sb$_{0.93}$
- 5000 Å U.D. p-Al$_{0.9}$Ga$_{0.1}$As$_{0.07}$Sb$_{0.93}$
- 100 Å U.D. p-Ga$_{0.81}$In$_{0.19}$As$_{0.12}$Sb$_{0.88}$
- 1000 Å U.D. p-Al$_{0.9}$Ga$_{0.1}$As$_{0.07}$Sb$_{0.93}$
- 2200 Å n^+-Al$_{0.9}$Ga$_{0.1}$As$_{0.07}$Sb$_{0.93}$
- 4000 Å n^+-GaSb buffer
- n^+-GaSb substrate

Figure IV-25. Structures of the three quantum well samples that were characterized using current-voltage versus temperature (I-V-T), C-V, and DLTS measurements.

Once an etch method that reduces the surface current is found, the reverse bias current is then determined by carrier generation at deep level defects, or intrinsic carrier generation in the low band gap material used in the well. The difference in reverse bias current, controlled by surface current or generation current, can be seen by comparing samples that were prepared with different etches and surface passivation. A generation current is a result of emission of an electron and a hole from states located in the gap. The emission rate depends on the energy from the deep level to either the conduction band or the valence band. If the deep level is farther from one band than the other, then the emission rate to the farther band will be much slower. The slowest emission rate presents a rate limiting step in the sequential generation of an electron and a hole. Surface states present a continuous range of energies in the band gap for conduction. Conversely, current generation from a discrete deep level involves a larger energy. The energy involved in the rate limiting step for current generation at surface states is therefore much less than the energy involved in the rate limiting step at a discrete deep level. Conduction by surface states should therefore be much less temperature dependent than the carrier generation from discrete deep levels or intrinsic carrier generation.

The I-V-T curves for the first sample structure are shown in Figure IV-26. This sample was etched with H_3PO_4, H_2O_2, and H_2O (1 ml:1 ml:10 ml). From the nearly symmetric "V" shape of the curve, it can be said that the rectifying properties of this sample are not very good. It is believed that the poor rectifying properties are due to surface leakage currents. This shows that the reverse biases used in DLTS should be limited to -2 to -1 V. All of the curves are closely spaced showing little dependence on
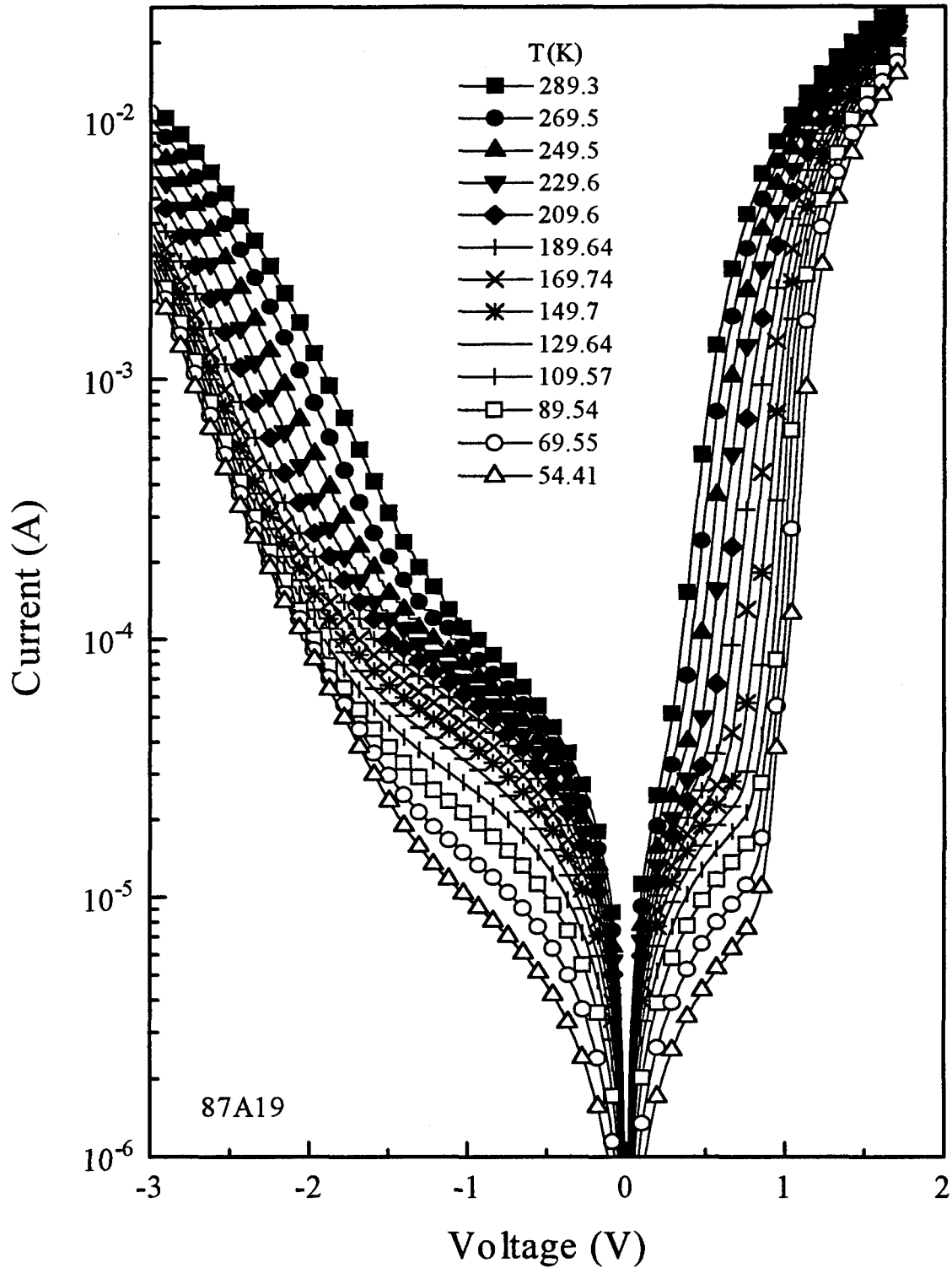
Figure IV-26. Current versus voltage measured at various temperatures for the first quantum well structure of a 125 Å unintentionally doped p-Ga$_{0.85}$In$_{0.15}$As$_{0.12}$Sb$_{0.88}$ well in unintentionally doped p-AlAs$_{0.07}$Sb$_{0.93}$.

temperature. The current changes only by an order of magnitude over a 200 K change in temperature. The kink in the forward bias current at around 0.5 V and 10 μA marks the transition from diffusion dominated to drift dominated current as the forward bias increases. The curve flattens out at higher forward bias due to the resistivity of the material.

A more detailed analysis divides the forward bias current into a diffusion, a recombination, and a tunneling term as given by

$$I = I_{diff} \exp\left(\frac{qV}{A_1 kT}\right) + I_{rec} \exp\left(\frac{qV}{A_2 kT}\right) + I_0 \exp(BV) \ ,$$

where I is the total current at the applied bias V, A_1 and A_2 are ideality factors equal to 1 for the diffusion term and 2 for the recombination term, respectively. The third term is the tunneling current. B is an empirical factor related to tunneling via deep levels (Stirn, 1972:72), or leakage at the perimeter of the junction (Hovel, 1975). The diffusion, I_{diff}, or recombination, I_{rec}, current coefficient can be obtained if a region of the current versus voltage curve can be fit for an ideality factor of 1 or 2. The diffusion current coefficient has a temperature dependence given by

$$I_{diff} \propto T^3 e^{-E_g/kT}.$$

The recombination current coefficient has a temperature dependence given by

$$I_{rec} \propto T^{5/2} e^{-E_g/2kT}.$$

The diffusion or recombination current versus temperature can then be used to determine the energy gap of the material where diffusion or recombination is taking place.

Unfortunately, the ideality factor was not equal to 1 or 2 over a wide enough bias range to get the diffusion or recombination current coefficients for any of the samples. The presence of the quantum well complicates the forward bias characteristics, providing a second set of current components. For example, considering the differences between the band gaps of the well and the barrier, the recombination current should initially be greatest in the well until it saturates. Then, at some higher forward bias, the recombination current in the barrier material should dominate.

Under reverse bias conditions, it is assumed that the current is composed primarily of a generation component or a surface leakage component. Plotting the log of the current at a particular reverse bias versus $1/kT$ should produce a straight line according to

$$I_{rev} = A \exp\left(\frac{-E_a}{kT}\right),$$

if the current mechanism is by generation rather than surface leakage. In this equation, E_a is the activation energy of the generation center, k is Boltzmann's constant, and T is the temperature. The pre-factor A depends on the depletion width and the area of the depletion region. The reverse bias current should increase with the depletion width, which is proportional to $V^{1/2}$, if it is due to generation. The current at -3 V reverse bias was plotted as a function of $1/kT$ on a semi-log plot to get the activation energy of the dominant generation center. For the sample of a 125 Å unintentionally doped p-$Ga_{0.85}In_{0.15}As_{0.12}Sb_{0.88}$ well in unintentionally doped p-$AlAs_{0.07}Sb_{0.93}$ barriers, the measured energy depends on the bias voltage used to measure the current, indicating that the current is not due to a discrete generation center. The low energy of 19 meV obtained with -3 V

reverse bias voltage as shown in Figure IV-27 was varied for different reverse biases. The curvature of the rest of the plot shows a distribution of energies, as would be found for surface states. Thus, the generation center measured with I-V-T is likely to be due to the surface states at the edge of the mesa since there is a range of energies obtained.

A representative I-V curve for the second sample structure is given in Figure IV-28. The second sample structure consists of a 100 Å unintentionally doped p-$Ga_{0.81}In_{0.19}As_{0.12}Sb_{0.88}$ well in unintentionally doped p-$AlAs_{0.07}Sb_{0.93}$ barriers, etched with H_3PO_4, H_2O_2, H_2O, and L-tartaric acid (1 ml:1 ml:350 ml:0.4 g). This etch results in a diode with better rectification and an increased dependence of the current on the temperature. For the sample prepared in this way, the current changes 3-4 orders of magnitude over a 200 K change in temperature. However, the activation energy plot of the reverse I-V-T measurements have much the same behavior as for the first QW sample structure, showing a spread of energies indicating conduction primarily by surface states.

Treatment of the surface with ammonium sulfide (($NH_4)_2S$) has a very dramatic effect, and confirms that the high reverse bias conduction is due mostly to surface states. A separate piece of the 2nd sample structure was dipped in ammonium sulfide after etching the mesas. Figure IV-29 shows the I-V-T measurements for the sample that was dipped in ammonium sulfide for 10 min at room temperature. The treated surface makes the diode current much more temperature dependent, as it would for decreased surface state current and increased generation current. An Arrhenius plot of the current at -4 V is now much more linear, as shown in Figure IV-30. The energy of 127 meV now extends over several decades of current. This energy is very close to an energy of a hole trap located 122 meV
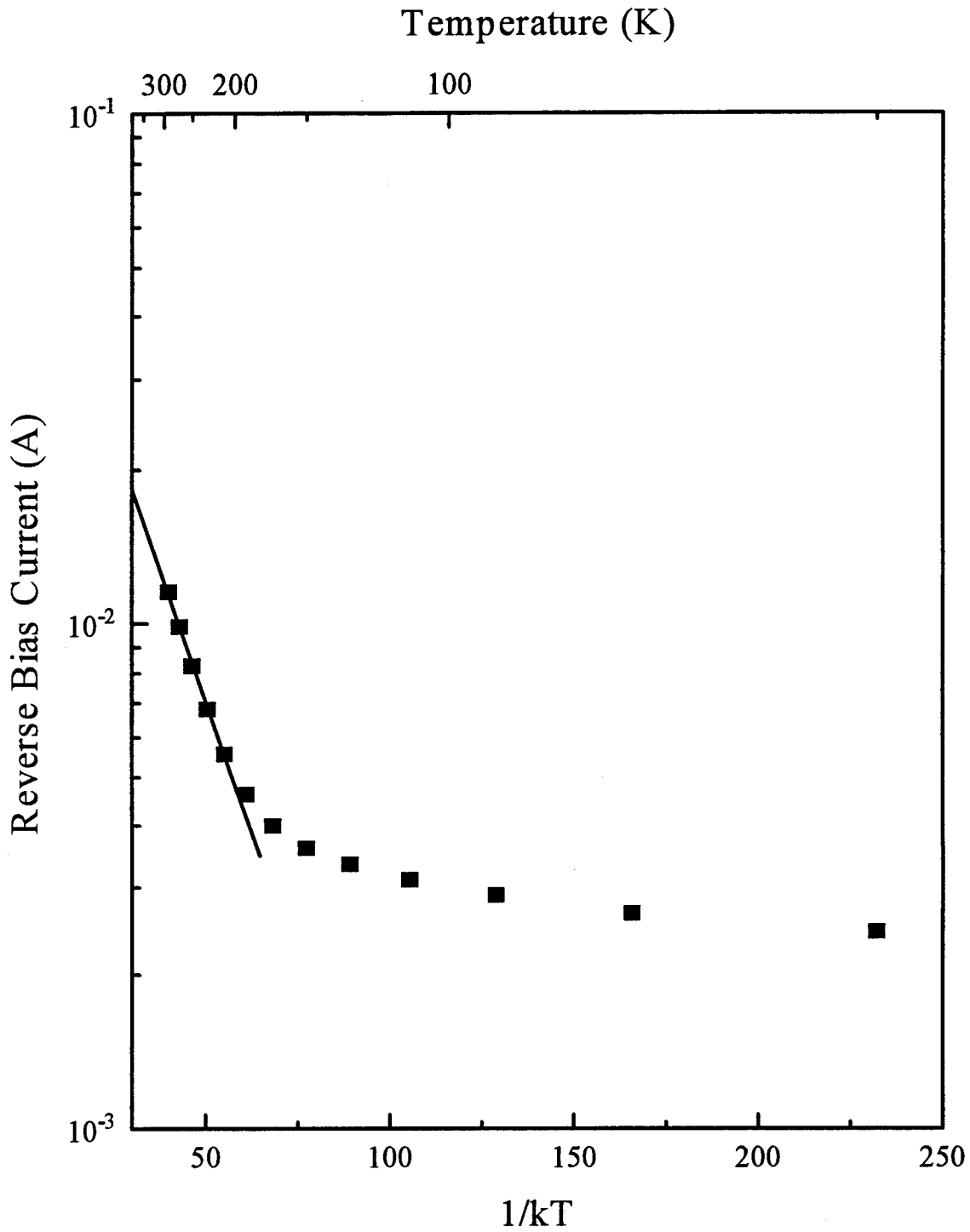
Figure IV-27. The reverse bias current measured at -3 V as a function of 1/kT for the first quantum well structure of a 125 Å unintentionally doped p-$Ga_{0.85}In_{0.15}As_{0.12}Sb_{0.88}$ well in unintentionally doped p-$AlAs_{0.07}Sb_{0.93}$. The points are generated from data in Figure IV-26.
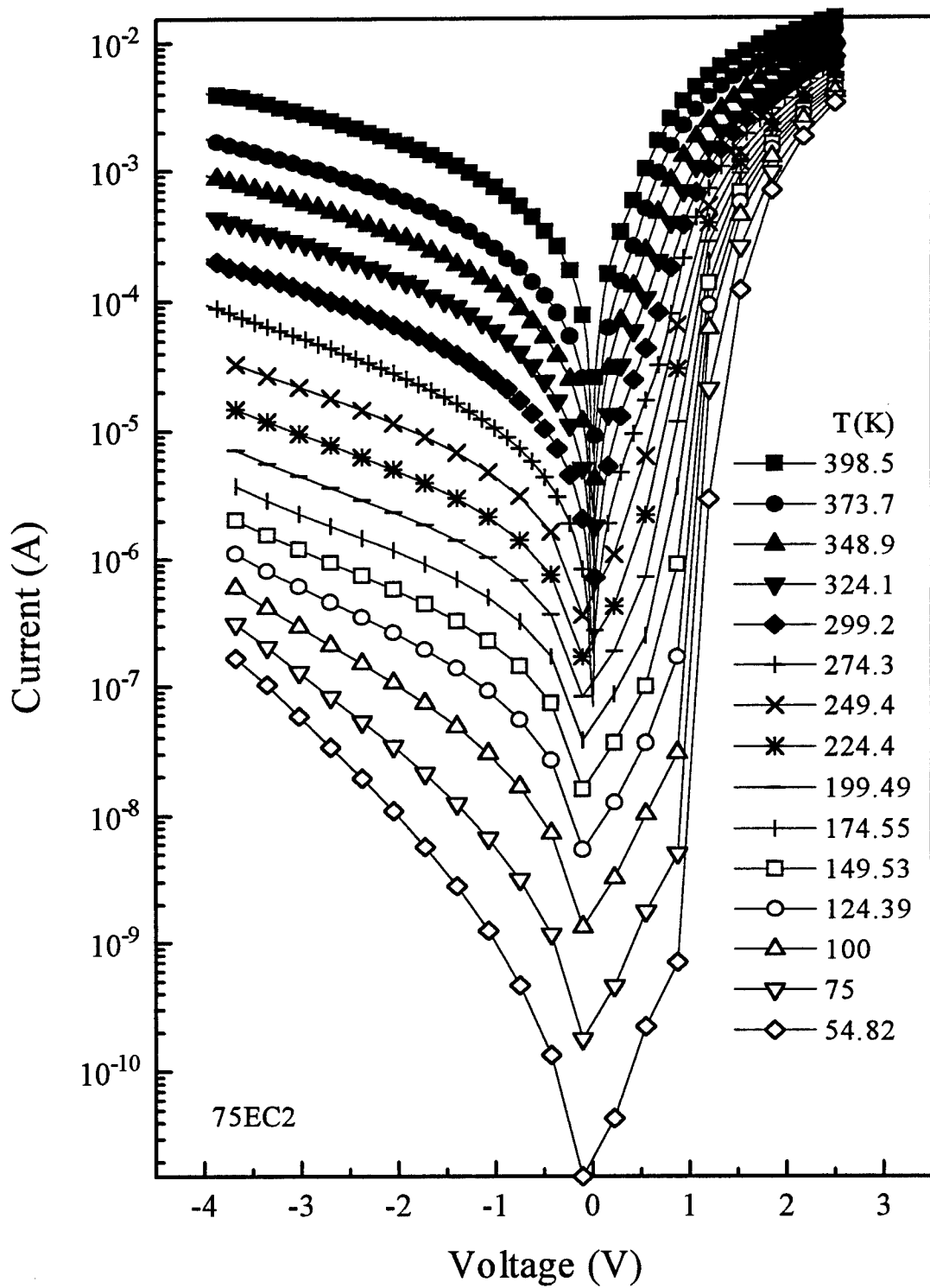
Figure IV-28. I-V-T curves for the second QW structure of a 100 Å unintentionally doped p-$Ga_{0.81}In_{0.19}As_{0.12}Sb_{0.88}$ well in unintentionally doped p-$AlAs_{0.07}Sb_{0.93}$ barriers, etched with dilute phosphoric/L-tartaric acid.
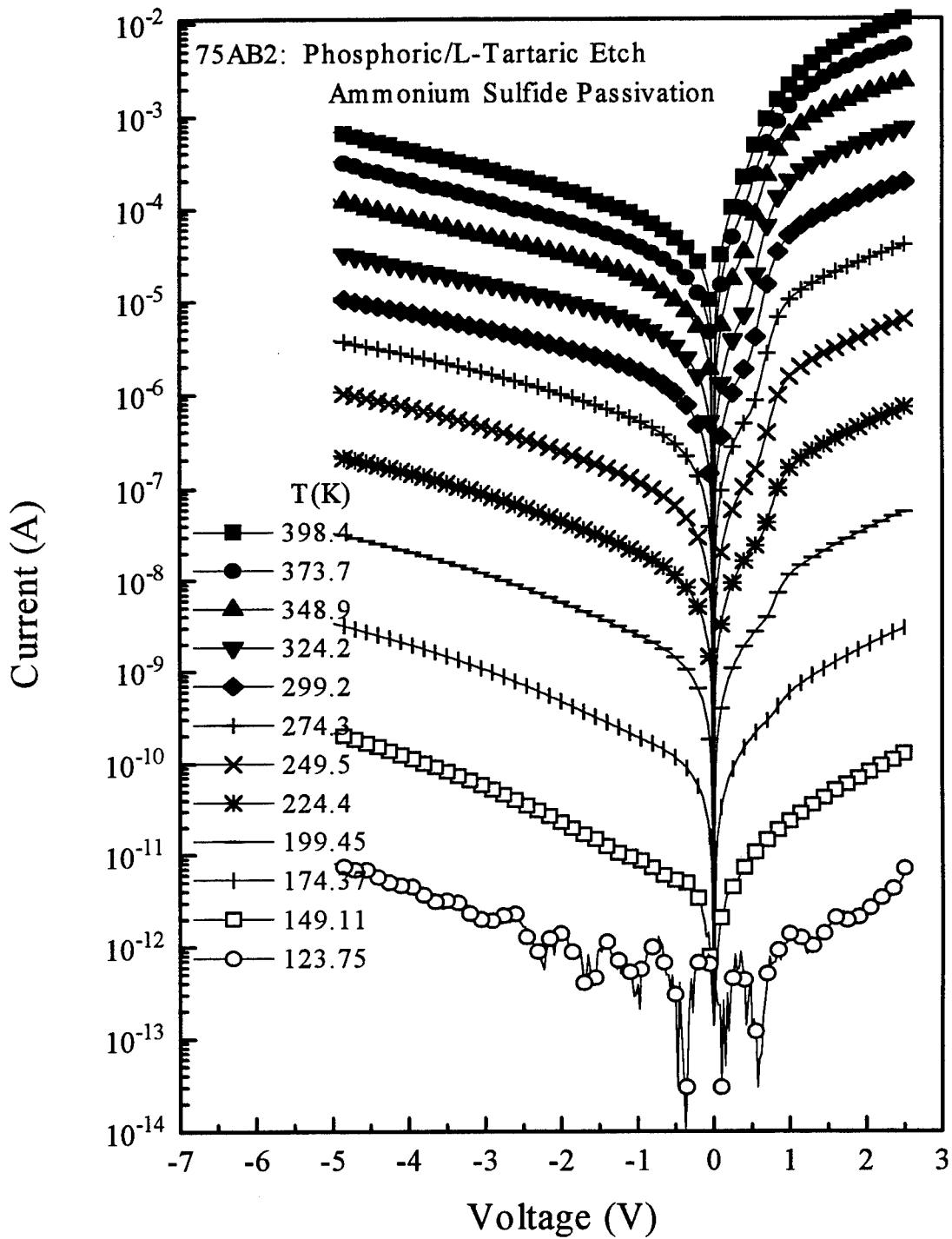
Figure IV-29. I-V-T curves for the second sample structure consisting of a 100 Å unintentionally doped p-$Ga_{0.81}In_{0.19}As_{0.12}Sb_{0.88}$ well in unintentionally doped p-$AlAs_{0.07}Sb_{0.93}$ barriers, etched with dilute phosphoric/L-tartaric acid, and then treated with ammonium sulfide for surface passivation.
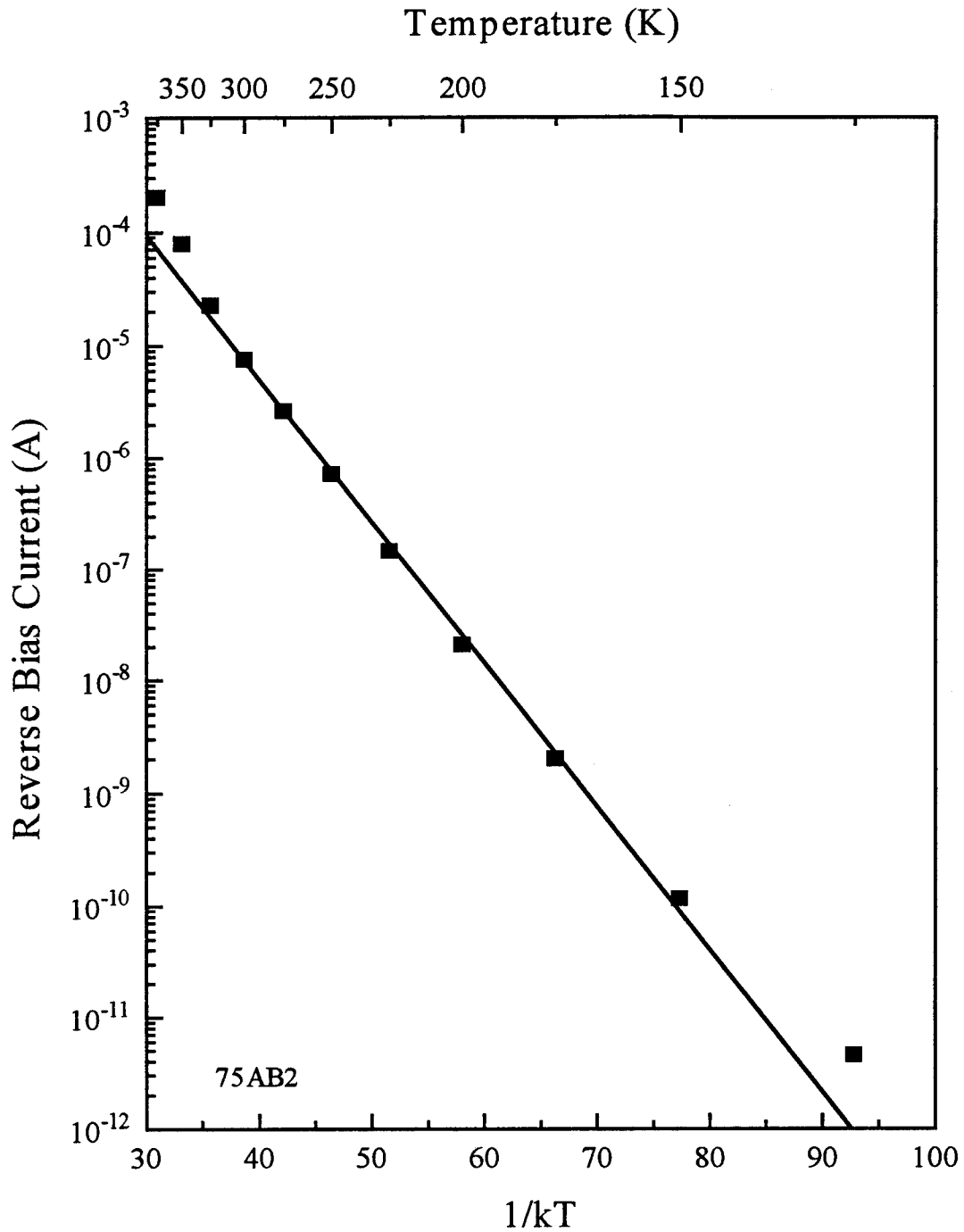
Figure IV-30. Arrhenius plot of the reverse bias current at -4V for the second sample structure, consisting of a 100 Å unintentionally doped p-$Ga_{0.81}In_{0.19}As_{0.12}Sb_{0.88}$ well in unintentionally doped p-$AlAs_{0.07}Sb_{0.93}$ barriers, etched with phosphoric/L-tartaric acid and passivated with ammonium sulfide. The data points are generated from Figure IV-29.

above the valence band as measured by DLTS. The trap characteristics were presented in a previous section. The DLTS measurements were made on bulk $Ga_{0.8}In_{0.2}As_{0.12}Sb_{0.88}$, which is the same material as the narrow-gap well material used in the QW samples. Emission from a generation center in the well material of the quantum well samples would be a multi-step process. First, an electron and hole would be emitted from the deep level to the conduction and valence band of the well material, respectively. Next, emission to the barrier material would require thermionic emission of the electron and hole out of their respective wells. In the QW samples, the depth of the valence band well is estimated to be about 0.4 ± 0.1 eV. The energy levels in the valence band well are separated by much less than 127 meV, so that under steady state conditions, the rate limiting step for generation is the 127 meV energy of the deep level in the well material. In other words, emission from the deep level to the ground state in the valence band well occurs very slowly compared to subsequent emission out of the well. Similarly, the emission rate of an electron is limited by the emission rate from the deep level to the ground state of the conduction band. Otherwise, the 127 meV energy would have to be a generation center in the barrier material. However, the gap of the barrier is ~1.5 eV. A generation center would be located much closer to the mid-gap energy of 0.7-0.8 eV, which strongly reduces the likelihood that this is a generation center in the barrier.

The third sample structure consists of a 100 Å unintentionally doped p-$Ga_{0.81}In_{0.19}As_{0.12}Sb_{0.88}$ well in unintentionally doped p-$Al_{0.9}Ga_{0.1}As_{0.07}Sb_{0.93}$ barriers. The barrier was changed from AlAsSb, used in the first two sample structures, to $Al_{0.9}Ga_{0.1}AsSb$. This change had the immediate effect that the surface of the third sample

structure after etching did not appear as discolored as the first two sample structures after etching. The discoloration is from oxidation of the AlAsSb. Furthermore, the addition of 10% Ga to the barrier material produced a much better etched surface. The difference in etch quality shows up in Figure IV-31 as lower leakage currents. The deep level generation center has an activation energy of 0.14 eV as shown in Figure IV-32. This center also compares well with the trap at 122 meV found by DLTS measurements on $Ga_{0.8}In_{0.2}As_{0.12}Sb_{0.88}$. In addition to the wet etching, RIE was also used to form the mesas on a separate piece of the third QW structure. The reactant gas was BCl_3 (48 standard cubic centimeters per minute (sccm)) in helium (36 sccm). The vacuum was 45 mTorr, and the power was 100 W. The etched surface turned out much flatter, as mentioned in the section on diode fabrication, rather than an arched surface as obtained by wet etching. While the I-V characteristics of RIE etched diodes aren't improved much over that of wet etched diodes, they don't vary as much from diode to diode. The number of good diodes per batch was also improved, increasing the yield from 50-75 % for the wet etching to close to 100% for RIE. A representative I-V-T plot is given in Figure IV-33. RIE seems to have less sensitivity to surface oxides, and doesn't depend as much on composition of the material being etched as the wet etch. A surface oxide, if not completely removed with a pre-etch dip of HCl, H_2O (1:10), and/or NH_4OH, H_2O (1:20), would delay the start of wet etching. Reverse I-V-T measurements at -2 V plotted in Figure IV-34 shows that the dominant generation center in this third sample structure etched with RIE has an energy of 0.14 eV at low temperature, and 0.18 eV at high temperature.
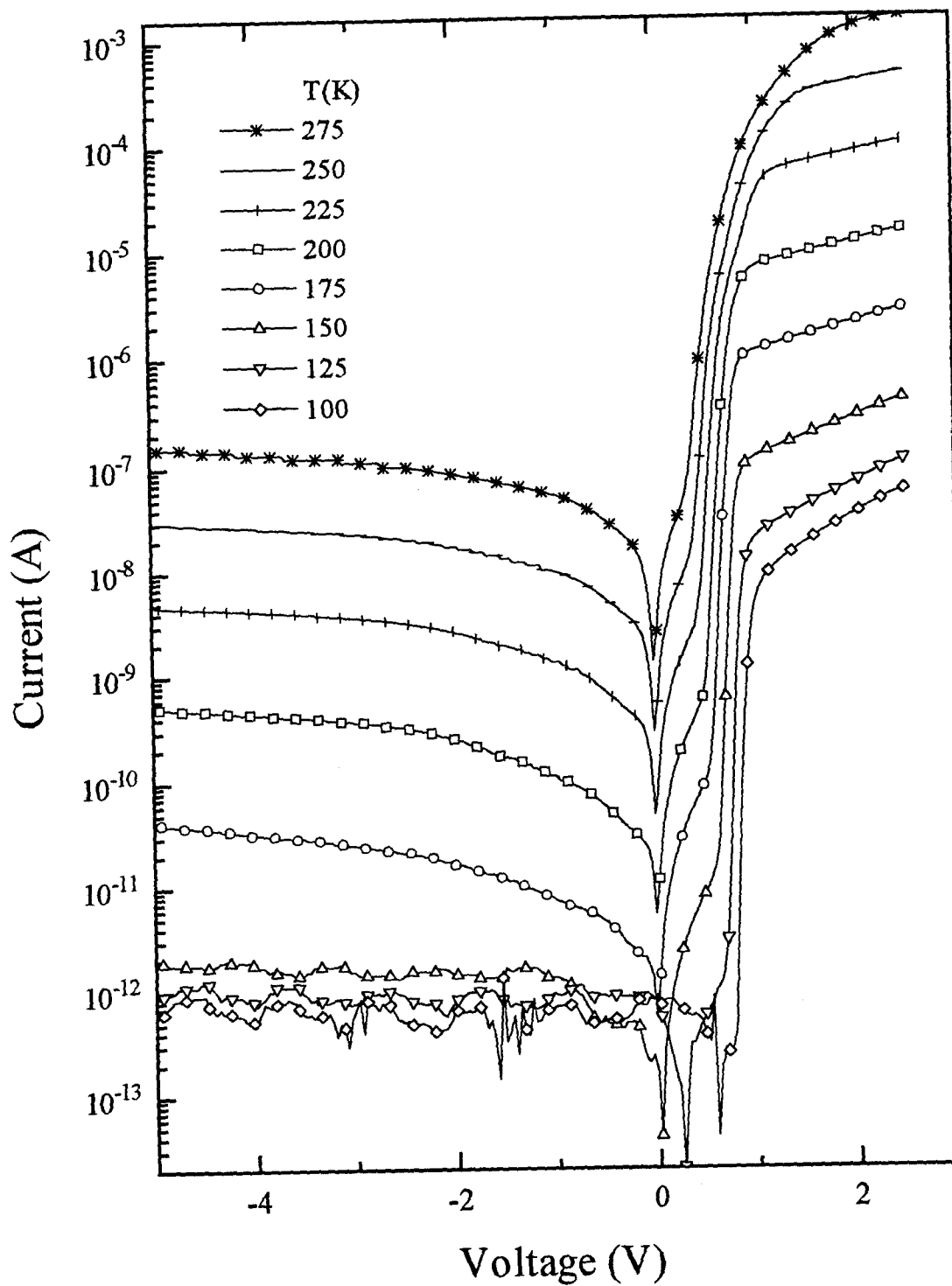
Figure IV-31. I-V-T measurements for the third QW structure consisting of a 100 Å unintentionally doped p-$Ga_{0.81}In_{0.19}As_{0.12}Sb_{0.88}$ well in unintentionally doped p-$Al_{0.9}Ga_{0.1}As_{0.07}Sb_{0.93}$ barriers.
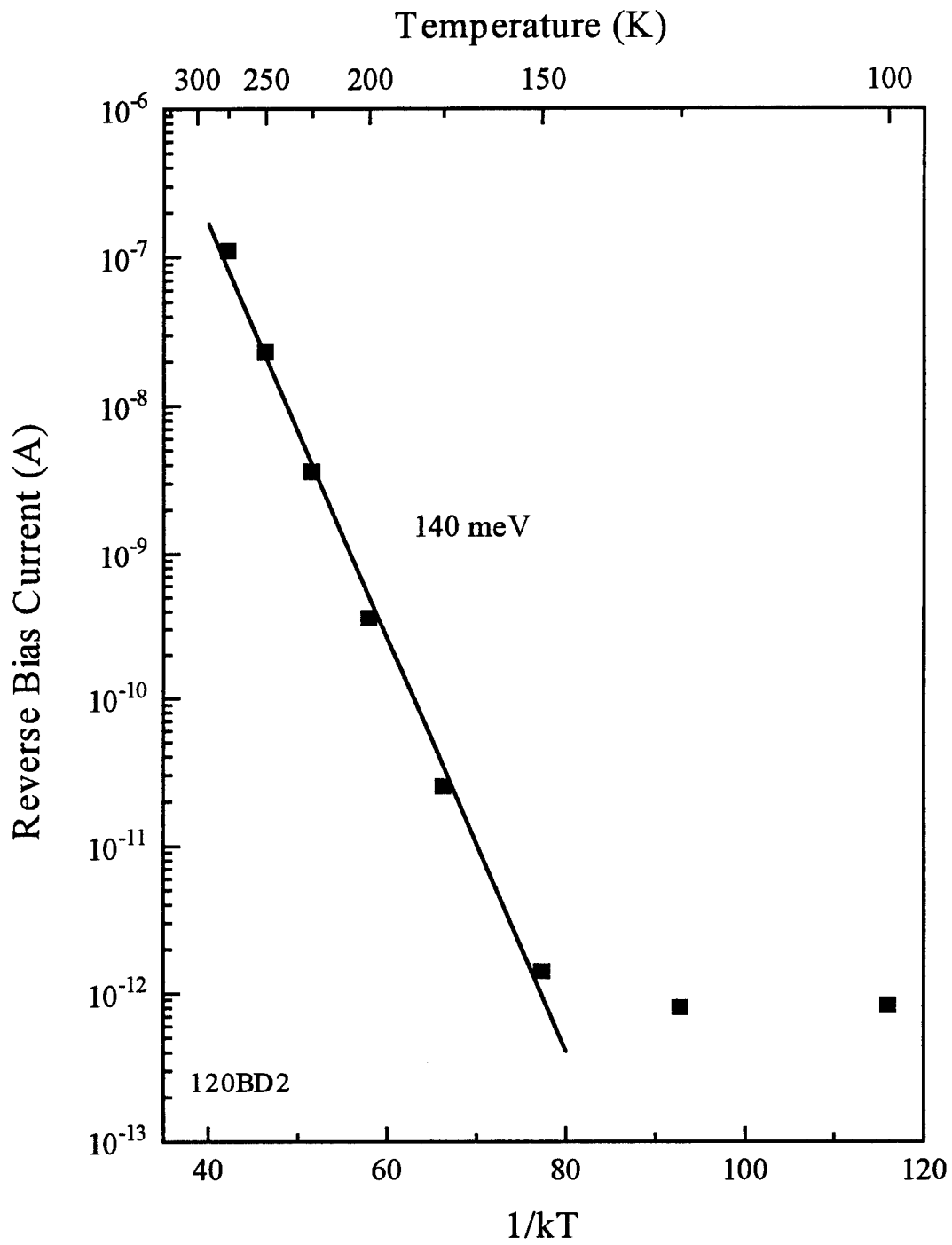
Figure IV-32. Reverse bias current at a measurement bias of -3V versus 1/kT for the third sample structure consisting of a 100 Å unintentionally doped p-$Ga_{0.81}In_{0.19}As_{0.12}Sb_{0.88}$ well in unintentionally doped p-$Al_{0.9}Ga_{0.1}As_{0.07}Sb_{0.93}$ barriers. Data points are generated from Figure IV-31.
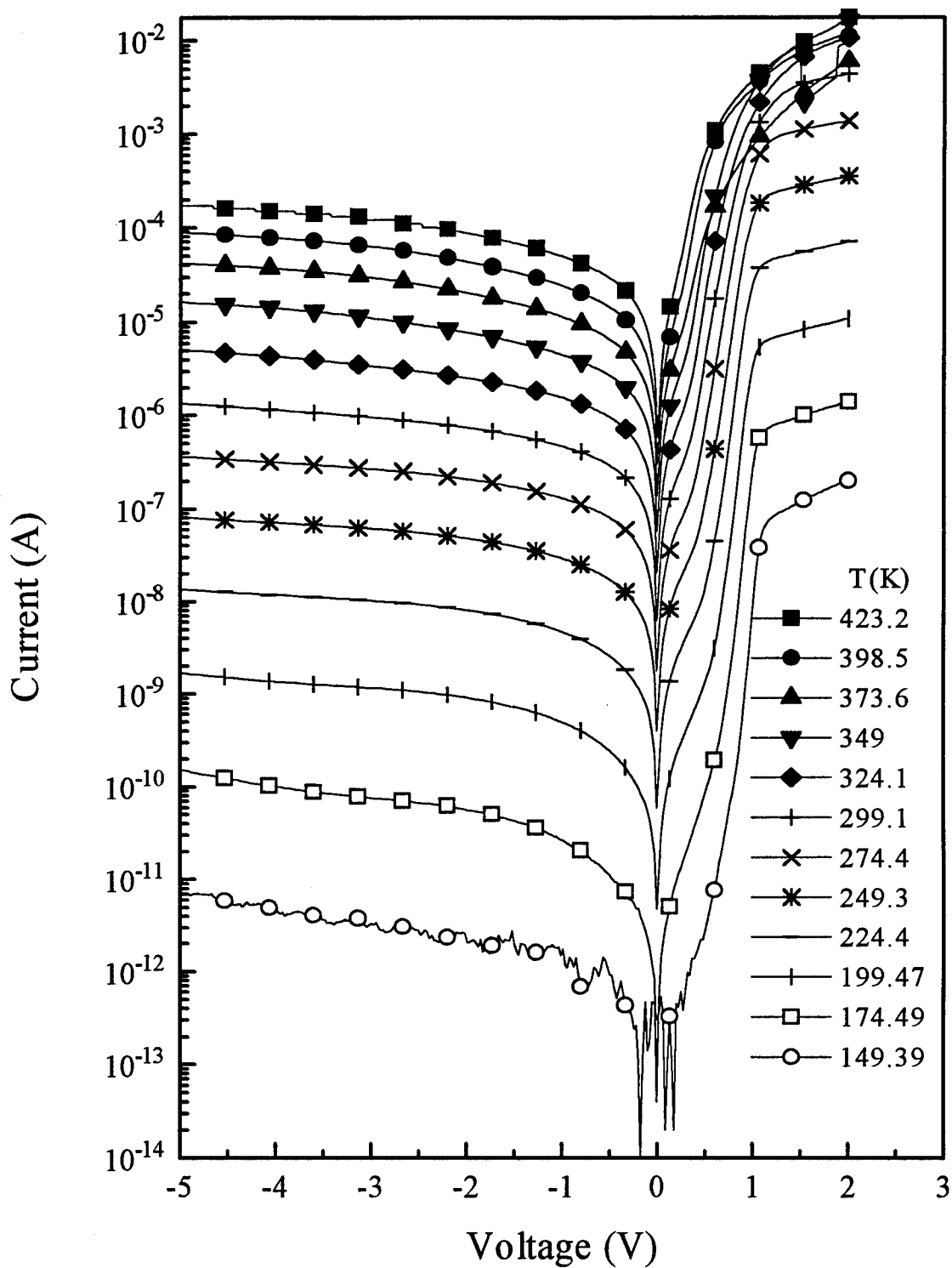
Figure IV-33. I-V-T measurements for the third sample structure, consisting of a 100 Å unintentionally doped p-$Ga_{0.81}In_{0.19}As_{0.12}Sb_{0.88}$ well in unintentionally doped p-$Al_{0.9}Ga_{0.1}As_{0.07}Sb_{0.93}$ barriers. In this case the mesas were etched using BCl_3 RIE.
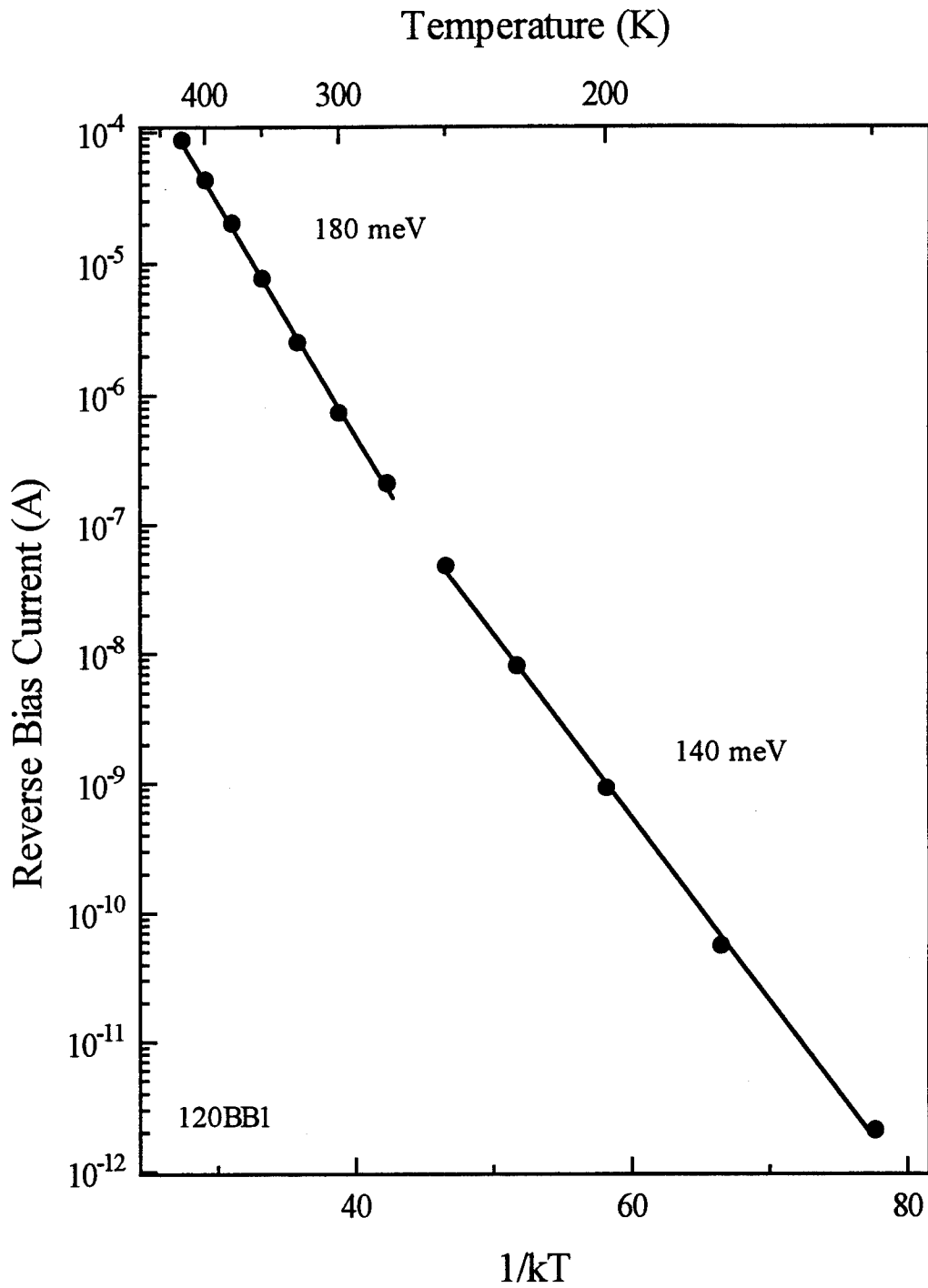
Figure IV-34. Arrhenius plot for the BCl₃ RIE etched quantum well structure, consisting of a 100 Å unintentionally doped p-Ga$_{0.81}$In$_{0.19}$As$_{0.12}$Sb$_{0.88}$ well in unintentionally doped p-Al$_{0.9}$Ga$_{0.1}$As$_{0.07}$Sb$_{0.93}$ barriers. The data points are generated from Figure IV-33.

This set of measurements shows that dilute phosphoric acid etch is slightly better than the more concentrated etch. Furthermore, the surface states can be passivated effectively by treating the surface with ammonium sulfide after etching. Other means of reducing the detrimental effects of a phosphoric etch is by changing the $Al_xGa_{1-x}As_ySb_{1-y}$ barrier composition to contain as much gallium as the device allows. The most straightforward method of obtaining good quality etched surfaces was by using BCl_3 reactive ion etching.

Once the surface current shunting was reduced, reverse I-V-T measurements revealed a generation center at 0.140 eV. While I-V-T measurements don't indicate which band to reference the energy to, the DLTS measurements of bulk $Ga_{0.85}In_{0.15}AsSb$ in an MIS structure yielded an energy level situated 122 meV from the valence band. It should also be noted that the DLTS measurements identified an electron trap at 320 meV below the conduction band, and a hole trap 276 meV above the valence band, both of which may be the same defect center. The 320 meV and 276 meV defect measured by DLTS was believed to be the most probable generation or recombination center, although only the generation characteristics were measured. The energy of 140 meV found by reverse I-V-T is a generation center.

Another goal of the I-V-T measurements besides identifying the dominant generation center was to determine the range of biases that could be used in DLTS and C-V measurements without error from leakage currents. The allowable current during capacitance measurements for DLTS and C-V is limited to ~100 µA by the meter. Any leakage current in excess of this value results in erroneous capacitance measurements and

possibly distorted transients. In the first QW sample structure, this puts a limit of -1 V on the bias used during capacitance measurements up to 300 K. The second sample structure that was treated with $(NH_4)_2S$ for surface passivation, will allow a bias of -5 V up to 350 K. Without $(NH_4)_2S$ surface passivation the allowed reverse bias is only half of what is allowed with $(NH_4)_2S$ passivation. The third structure, which changed the barrier from AlAsSb to $Al_{0.9}Ga_{0.1}AsSb$, exhibits a hard breakdown at >10 V reverse bias. The current is less than 100 μA up to the breakdown voltage, all the way up to a temperature of 400 K.

C-V Profiling of QW Structures

The C-V measurements of each of the three QW structures are given in this section. The features of each will be described, with more detail given for the third QW structure since it entails all of the features that were encountered. The objective is to be able to correlate the biases used in the DLTS measurements with the biases determined to correspond to the well by C-V measurements.

The raw capacitance versus bias voltage data shown in Figure IV-35 are from the C-V measurements for the first QW sample consisting of a 125 Å unintentionally doped p-$Ga_{0.85}In_{0.15}As_{0.12}Sb_{0.88}$ well in unintentionally doped p-$AlAs_{0.07}Sb_{0.93}$. This sample was etched with H_3PO_4, H_2O_2, and H_2O (1 ml:1 ml:10 ml). Each point is an average of 200 sampled points at voltage steps of 5 mV. The leakage current in this sample was fairly high, allowing capacitance measurements only up to 1 V reverse bias at 300 K. The capacitance step results from sweeping the Fermi level through the charge confined in the
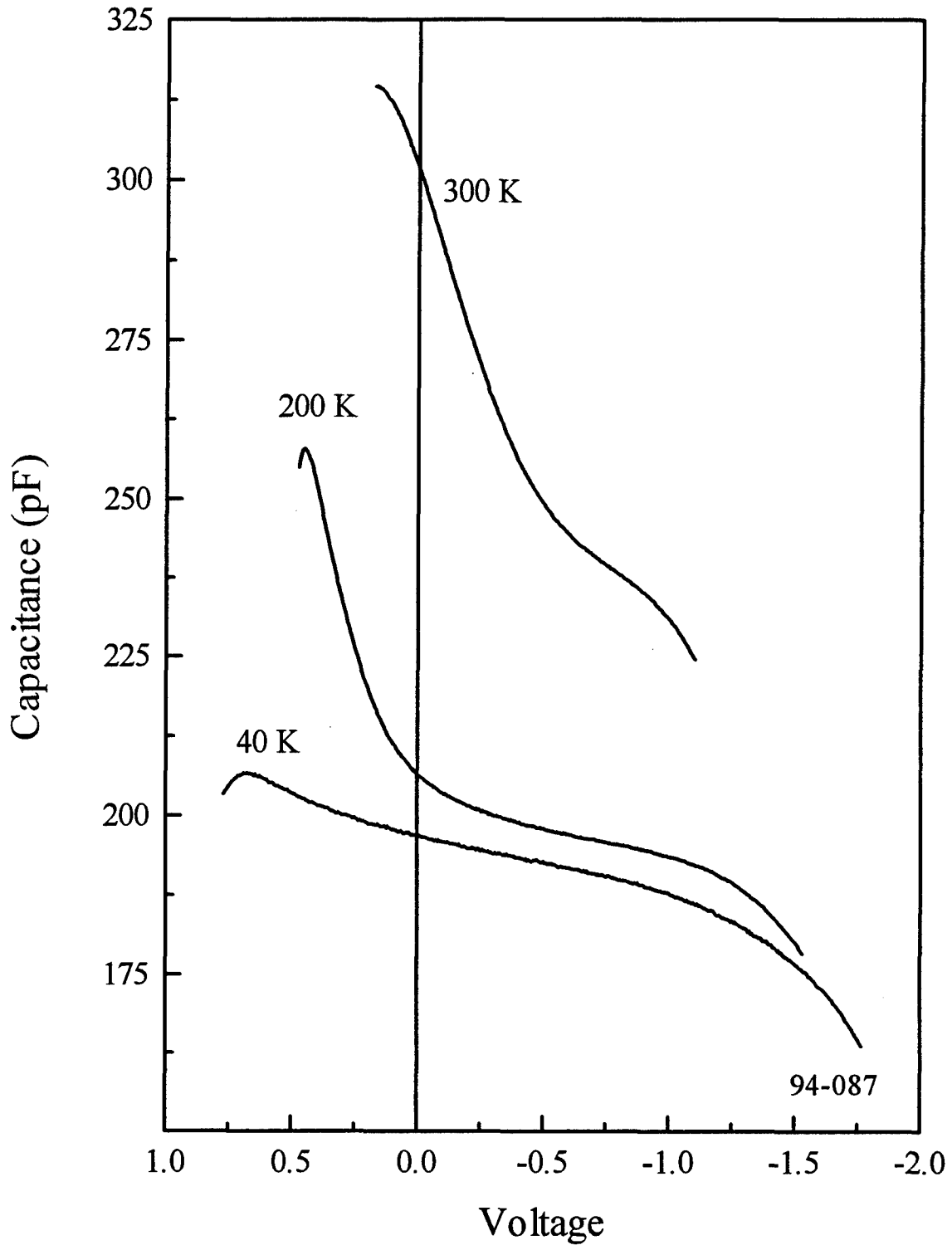
Figure IV-35. Capacitance versus voltage measurements for the quantum well structure consisting of 125 Å $Ga_{0.85}In_{0.15}As_{0.12}Sb_{0.88}$ well in p-$AlAs_{0.07}Sb_{0.93}$ barriers. The well is 500 Å from the n^+-p junction as shown in Figure IV-25.

quantum well. This step broadens and appears at lower capacitance as the temperature decreases. The breadth of the step is related to the density of carriers occupying the states in the well. A higher density of carriers in the well requires a larger change in bias to sweep through it than through the lower dopant density in the bulk barrier material. As the temperature decreases, the delineation between empty and full states becomes sharper, and the occupation probability increases for confined states deeper in the well. Thermionic emission out of the deeper states in the well becomes slower as the temperature decreases. The reduction in thermionic emission rate at low temperature reduces the change in capacitance as the voltage changes.

Charge accumulates in the quantum well as shown by the peaks in the plot of apparent carrier concentration versus apparent depletion width in Figure IV-36. This plot is obtained at temperatures where the holes in the well can respond to the capacitance meter's test frequency of 1 MHz from the previous plot of Figure IV-35 as described in the C-V profiling section for the heterojunction structures. The well is actually located 500 Å from the n^+-p junction rather than the indicated apparent distance of >800 Å. The shift of the peak to a deeper depletion width is a result of carrier freeze-out on the heavily doped n^+ side of the n^+-p junction since the measured depletion width is the sum of the depletion on both sides of the junction. The shift is also due to a decrease in occupation of higher energy states in the quantum well at lower temperature. At low temperature, the Fermi level doesn't start to cross the high density of carriers in the well until a higher reverse bias is reached. The higher accumulation peak at 200 K also reflects the shift in the distribution of carriers deeper in the well.

C-V measurements made at several different temperatures on the second quantum well structure are shown in Figure IV-37. The second sample structure consists of a 100 Å unintentionally doped p-$Ga_{0.81}In_{0.19}As_{0.12}Sb_{0.88}$ well in unintentionally doped p-$AlAs_{0.07}Sb_{0.93}$ barriers, etched with H_3PO_4, H_2O_2, H_2O, and L-tartaric acid (1 ml:1 ml:350 ml:0.4 g). Lower leakage current and higher breakdown voltage in this sample allowed capacitance measurements over a wider range of voltages. For a 1 MHz test signal frequency, the capacitance step begins to appear at 1 V forward bias at low temperature.

Increasing the temperature to 100 K makes the C-V step most prominent. The capacitance step then disappears as the temperature increases farther. At lower temperature the lattice doesn't have enough energy to eject the carriers from the well, so that the holes in the well don't respond to the test frequency. At higher temperature the trapped carriers are distributed more uniformly throughout the well, which includes the states with lower thermal emission energy. It is also notable that the curve with the step has the lowest capacitance over the entire bias range of all of the curves. Higher capacitance indicates that the depletion region is narrower. At low temperature the capacitance is high because the holes trapped in the well do not have enough thermal energy to escape and respond to the 1 MHz test signal, causing the quasi-Fermi level in the well to remain relatively fixed. The capacitance is then defined primarily by the thickness of the barrier layer between the p-n junction and the well. At higher temperature the increase in capacitance is from an increase in ionization of the shallow carriers in the barrier. The shallow carrier ionization energy in a barrier material with high aluminum content is in the 80–150 meV range, requiring a fairly high temperature to ionize a
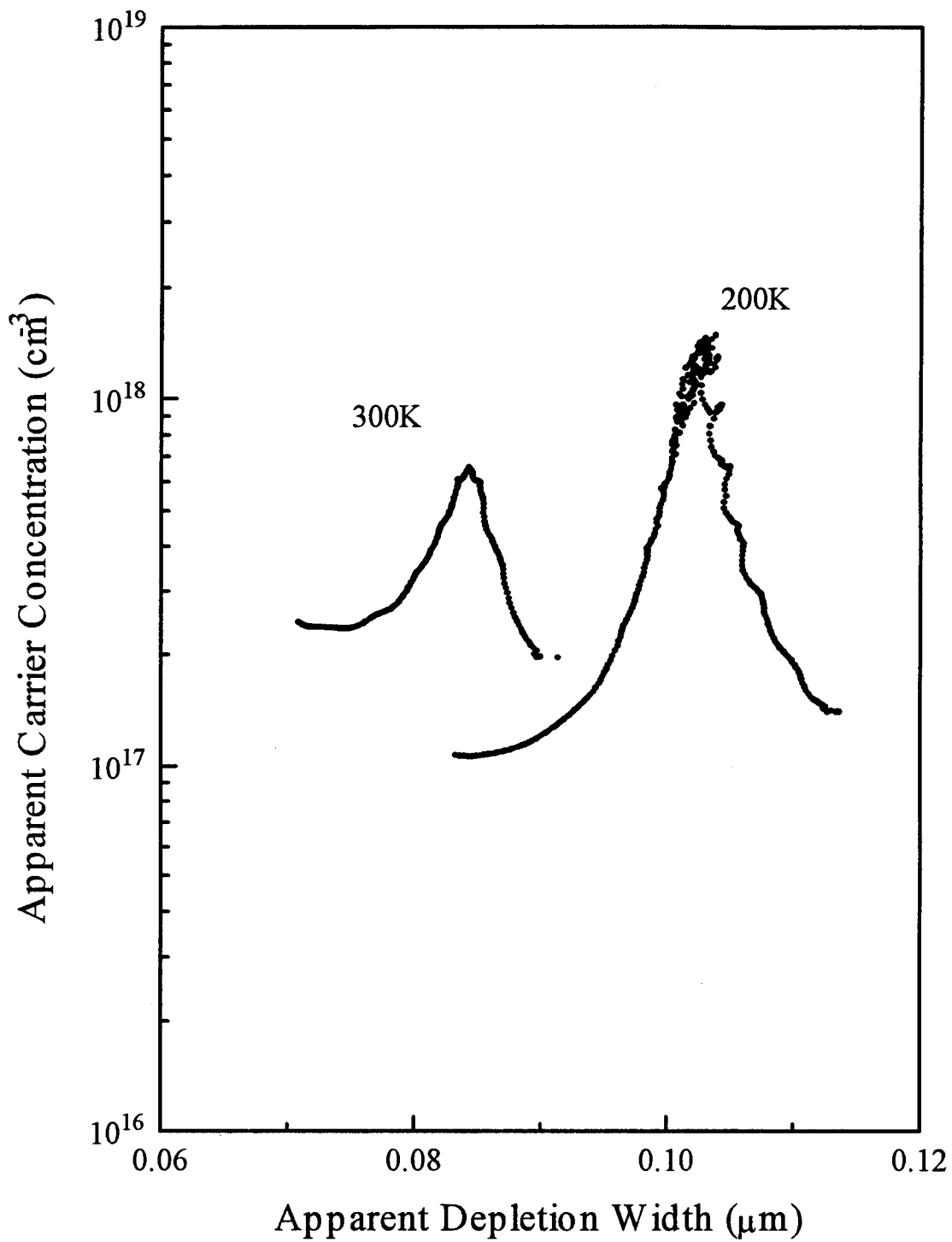
Figure IV-36. Apparent concentration profile determined from the data shown in Figure IV-35 for the quantum well structure consisting of 125 Å $Ga_{0.85}In_{0.15}As_{0.12}Sb_{0.88}$ well in p-$AlAs_{0.07}Sb_{0.93}$ barriers. The peaks at each temperature show the accumulation of charge in the well.
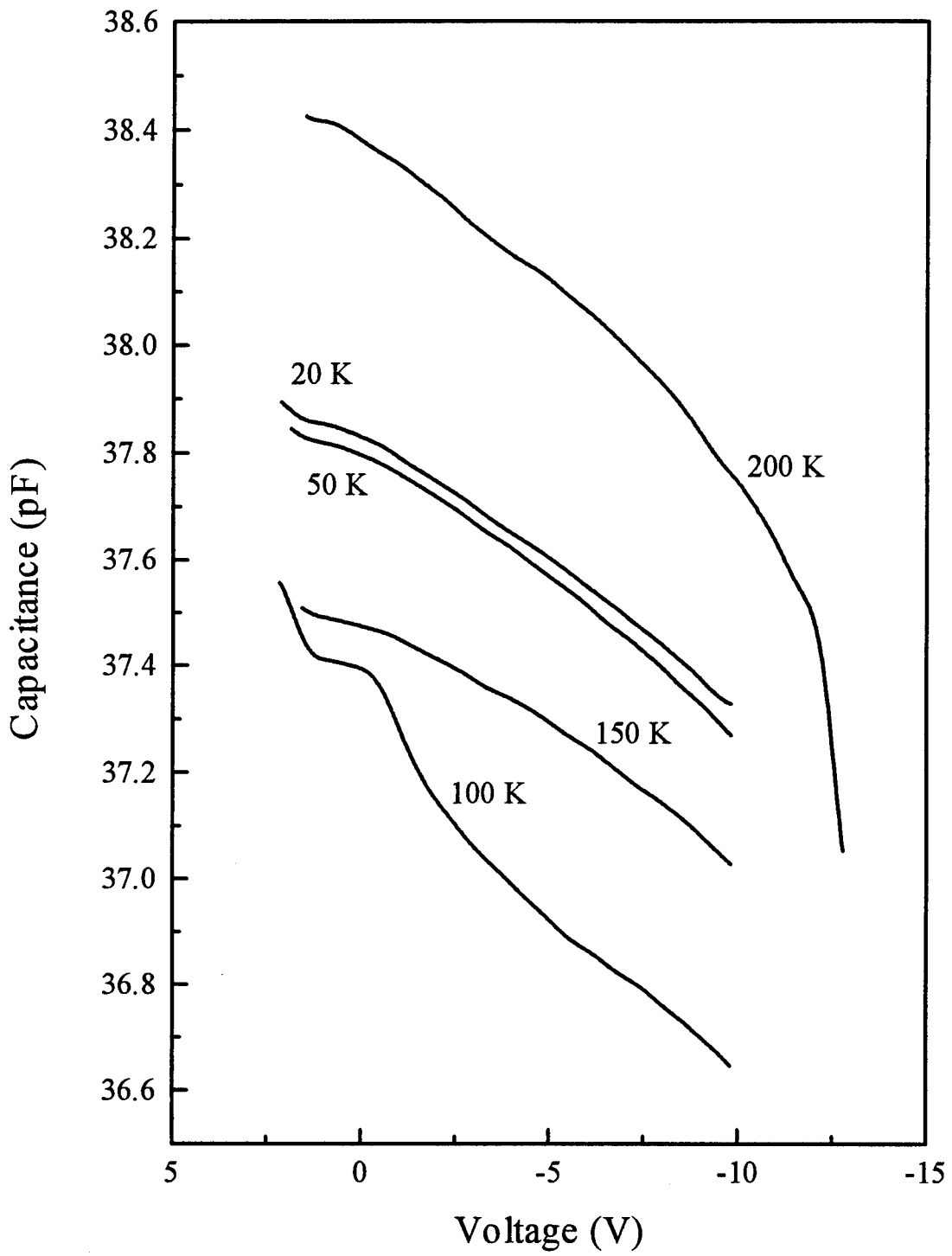
Figure IV-37. Capacitance versus voltage for a 100 Å quantum well of $Ga_{0.85}In_{0.15}As_{0.12}Sb_{0.88}$ in $AlAs_{0.07}Sb_{0.93}$ barriers, 0.1 μm from the n^+-p junction interface.

significant portion of the acceptors (Zhu et al., 1987:127–130). The carriers in the well are also able to follow the test signal frequency. The measurements made at 200 K also show the capacitance dropping off precipitously at a voltage of -13 V. The diodes are near the breakdown voltage at this point, allowing excess current to flow.

The capacitance versus applied bias in Figure IV-38 for the third QW structure is significantly different from the other two, showing more than one step. The third sample structure consists of a 100 Å unintentionally doped p-$Ga_{0.81}In_{0.19}As_{0.12}Sb_{0.88}$ well in unintentionally doped p-$Al_{0.9}Ga_{0.1}As_{0.07}Sb_{0.93}$ barriers. There are two portions of the C-V curve at 0 and 2 V where the capacitance does not change much or even increases slightly with increasing reverse bias. Consequently, the depletion width does not change much, or decreases slightly with increasing reverse bias around these two voltages. This capacitance response corresponds to the point where the Fermi level is passing through an occupied eigenstate of the well. Since capacitance is inversely proportional to the depletion width, $\varepsilon A/W$, and also defined by the change in charge with a change in bias, dQ/dV, the depletion width and the change in charge with bias are nearly constant in the bias range of flat capacitance response. A high carrier concentration serves to hold the quasi-Fermi level at an eigenstate of the well over the range of biases where the capacitance is relatively constant. When the quasi-Fermi level is held relatively constant, the increased reverse bias is applied across the barrier region between the p-n junction and the well. This increases the electric field, similar to the change of the electric field with applied bias in a fixed capacitor. This bias will also deplete the heavily doped side of the p-n junction, but this is not as much of a factor because the n^{+} side of the junction in this
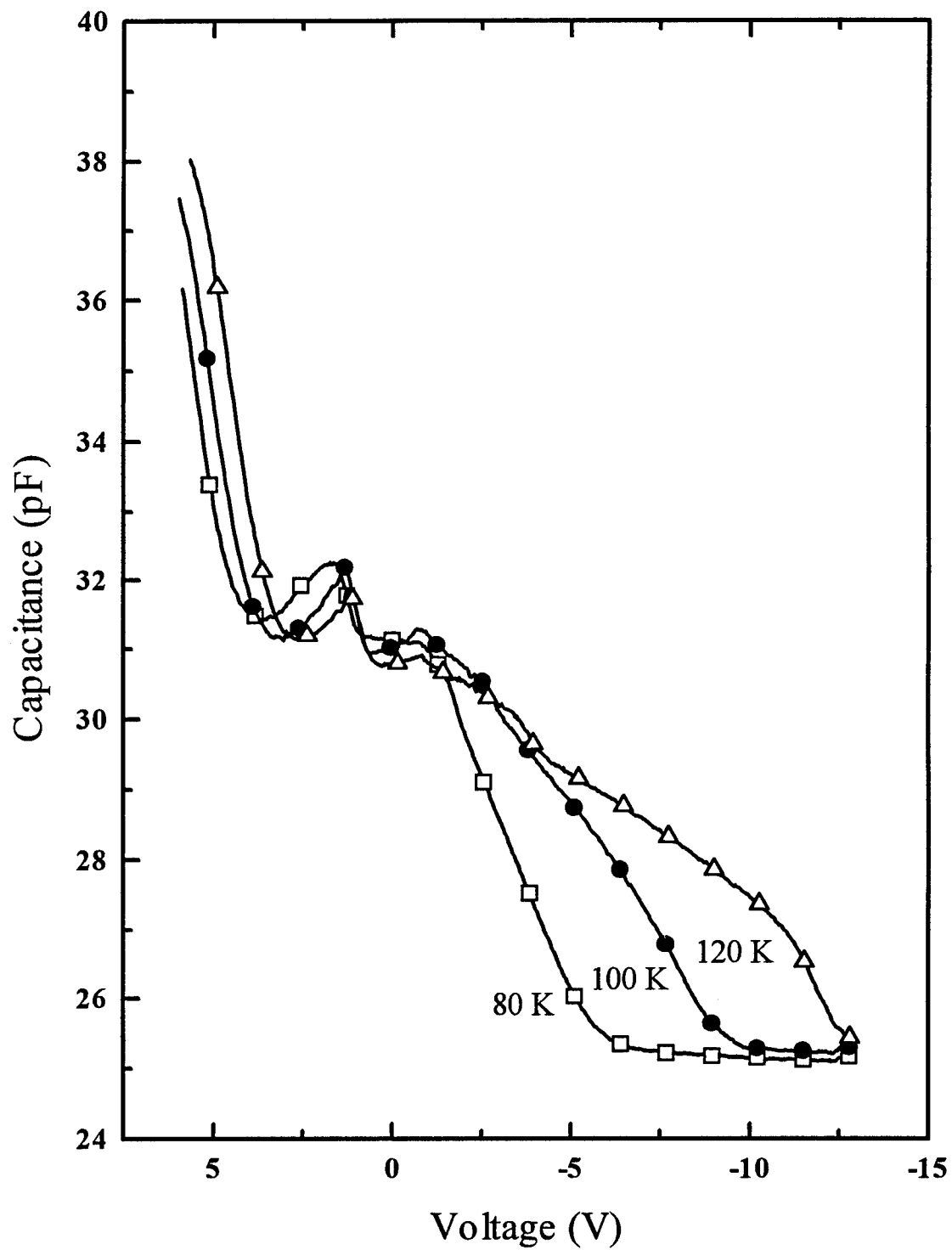
Figure IV-38.   Capacitance versus voltage for a 100 Å quantum well of $Ga_{0.81}In_{0.19}As_{0.12}Sb_{0.88}$ in $Al_{0.9}Ga_{0.1}As_{0.07}Sb_{0.93}$ barriers.   The well is 0.1 μm from the *p-n* junction interface. Several steps show up in this sample structure.

sample was doped heavily compared to the previous two samples. The limited depletion in the n^+ side in this sample is reflected by the absence of any significant horizontal shift in the location of the step features as the temperature changes, in contrast to the previous two samples with more lightly doped n^+ sides.

The product of the density of states and the distribution function in the well is a saw-tooth as shown previously in Figure II-11. There can be several orders of magnitude difference in the concentration between the minimum and maximum of the saw-tooth depending on the temperature. A maximum in the saw-tooth will tend to make the quasi-Fermi level relatively invariant, appearing as a flat portion in the C-V plot. The appearance of more than one step in this case indicates that there are more than one eigenstate that is significantly filled that also has an emission rate greater than 1 MHz. The width of the step along the voltage axis is related to the density of carriers in the eigenstate. The portion of the curve at larger reverse bias, adjacent to the step, has a steeper slope. Here the capacitance can change rapidly with applied bias. The height of the step along the capacitance axis is related to the energy difference between two confined states.

The sequence of biasing conditions shown in Figure IV-39 can be used to point out the origin of the features of the C-V profile in more detail. Starting near zero depletion width (a), depletion takes place in the barrier layer 1 next to the p-n junction until this layer is completely depleted. Then, further depletion of carriers in barrier layer 2 begins (b). Depletion of carriers in this layer continues until the Fermi level reaches the shallowest occupied state of the well (c). At this point, the depletion into barrier layer 2
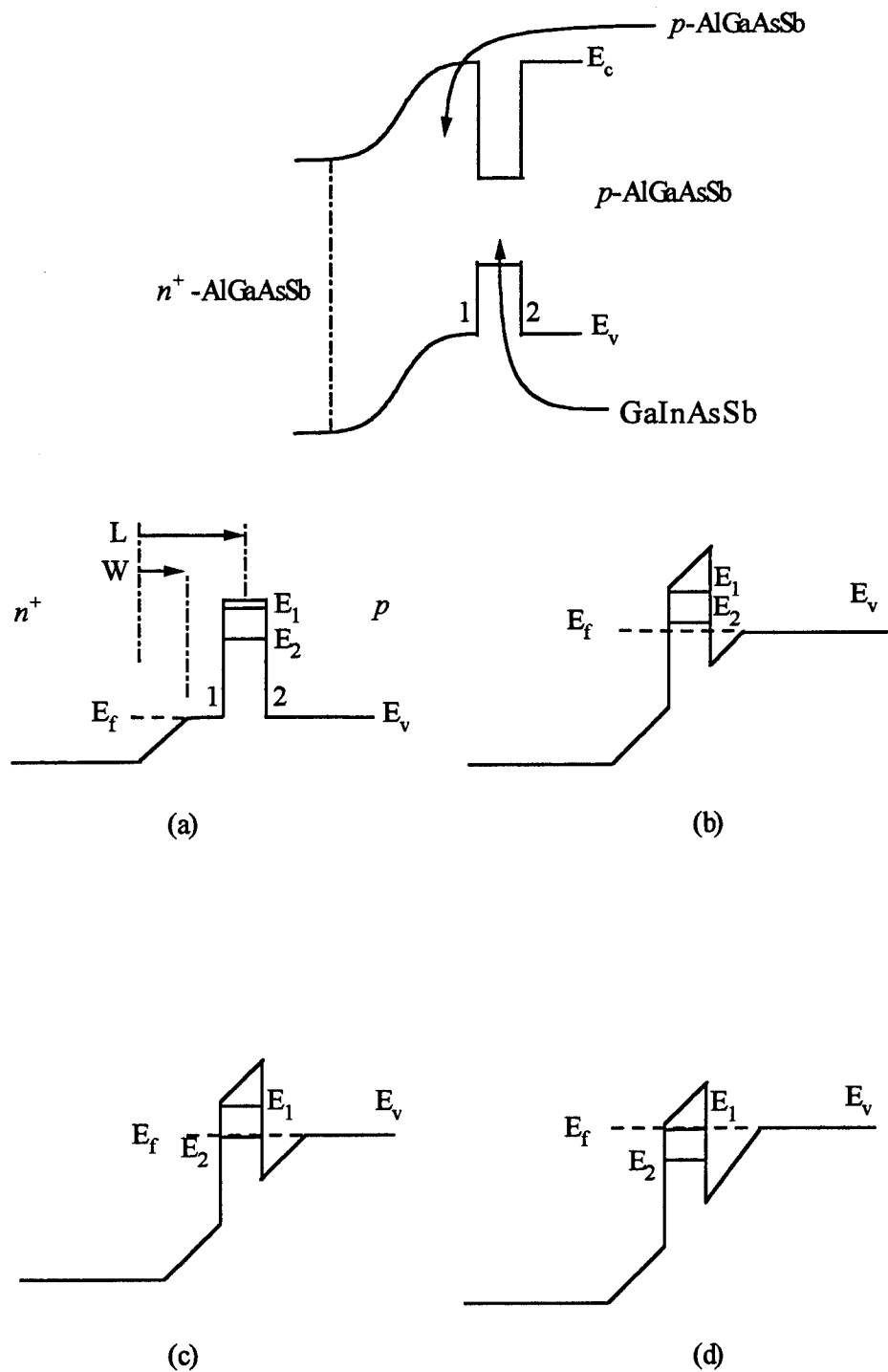
Figure IV-39. A sequence of biasing conditions used to explain the appearance of steps in the C-V characteristics of a quantum well. The full quantum well structure is shown at the top of the figure. (a) Nearly zero depletion in barrier layer 1. (b) Depletion extending into layer 2. (c) The Fermi level reaches confined state E_2. (d) With further depletion in layer 2, the Fermi level reaches confined state E_1.

can be determined by integrating Poisson's equation so that the voltage drop across the second barrier layer is equal to the depth of the highest occupied state, E_n, which is given by

$$E_n = \frac{qN_a}{2\varepsilon}\left(W - (L+a)\right)^2 \ .$$

Once the highest occupied confined state is depleted, further depletion takes place in barrier layer 2 until the next deeper confined state is encountered (d). In principle, the energy difference between two successive energy levels in the well can be determined from the difference in capacitance at the onset of each of the two capacitance steps. The difference in energy between E_n and E_{n-1} is given by

$$E_{n-1} - E_n = \frac{qN_a}{2\varepsilon}\left(W_{n-1}^2 - W_n^2 + 2(L+a)\left(W_n - W_{n-1}\right)\right) \ ,$$

where

$$W_n = \frac{\varepsilon A}{C_n} \ .$$

Ideally, the capacitance steps could be used to determine the energies of the confined states, and then the band offset from the energy of the confined states if they are determined accurately enough. But the capacitance can be shifted during the voltage sweep if the occupation of an energy level in the well is high enough to significantly reduce the total depletion width when the level empties. For example, for a density of carriers in the well of 10^{11} cm^{-2}, the depletion width in the adjacent barrier layer doped to 10^{16} cm^{-3} would be reduced by about 0.1 μm when the carriers in the well are released. In

the relatively flat part of the capacitance response at 2 and 0 V, this is seen by the slight increase in capacitance as the reverse bias increases.

The direction that the voltage is scanned also affects the appearance of the steps. Figure IV-40 is a comparison of a scan from reverse to forward bias, and a scan from forward to reverse bias 140 K. There is approximately 1 pF of hysteresis in the capacitance versus voltage measurements, and the scan from forward to reverse bias shows higher capacitance. Scanning from forward bias to reverse bias starts the measurements with a well that is initially full, whereas scanning from reverse bias to forward bias starts with a well that is initially empty. The resolution of the capacitance measurements is 20 fF.

Some of the diodes processed from the third quantum well structure have a large discontinuity in the C-V measurements at high reverse bias as shown in Figure IV-41. The C-V measurement taken at 150 K shows a large discontinuity at 8 V reverse bias. The DLTS measurements also revealed a very non-exponential component near this temperature. The appearance of this discontinuity, along with the DLTS results, can be shown to be due to tunneling of carriers from the well. There are four possiblities for the tunneling direction as shown in Figure IV-42. The band bending in the figure is drawn arbitrarily so that the tunneling distances are not to scale. Tunneling from the conduction band well to the valence band, indicated by CWV in the diagram, requires both a small tunneling distance and holes available in the valence band. Neither of these factors are satisfied as well as the other tunneling processes since the p-type barrier material is nominally undoped. Also, the band bending is much less on the far side of the well than
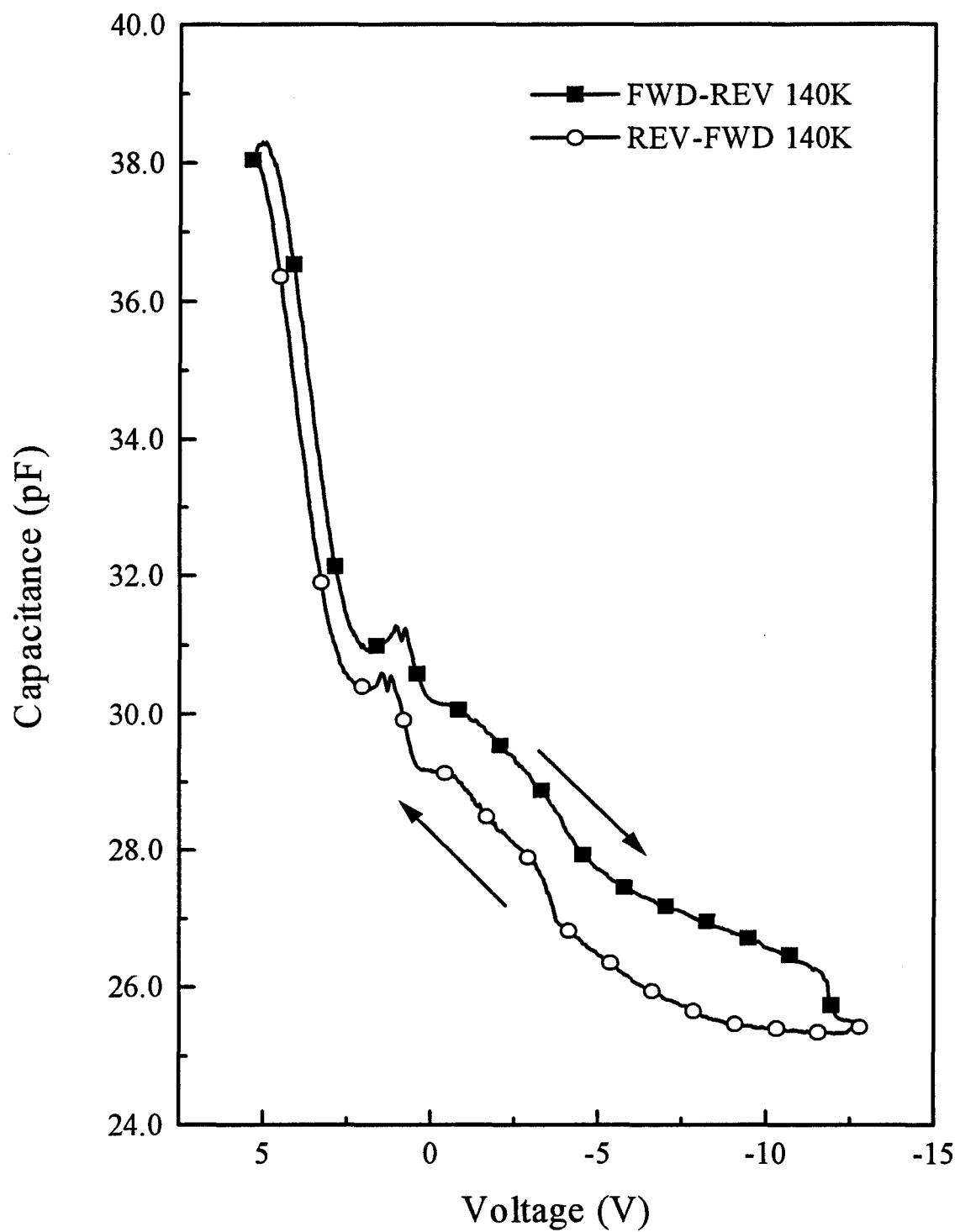
Figure IV-40. The C-V curves scanning from forward to reverse bias and from reverse to forward bias for a 100 Å quantum well of $Ga_{0.81}In_{0.19}As_{0.12}Sb_{0.88}$ in $Al_{0.9}Ga_{0.1}As_{0.07}Sb_{0.93}$ barriers.
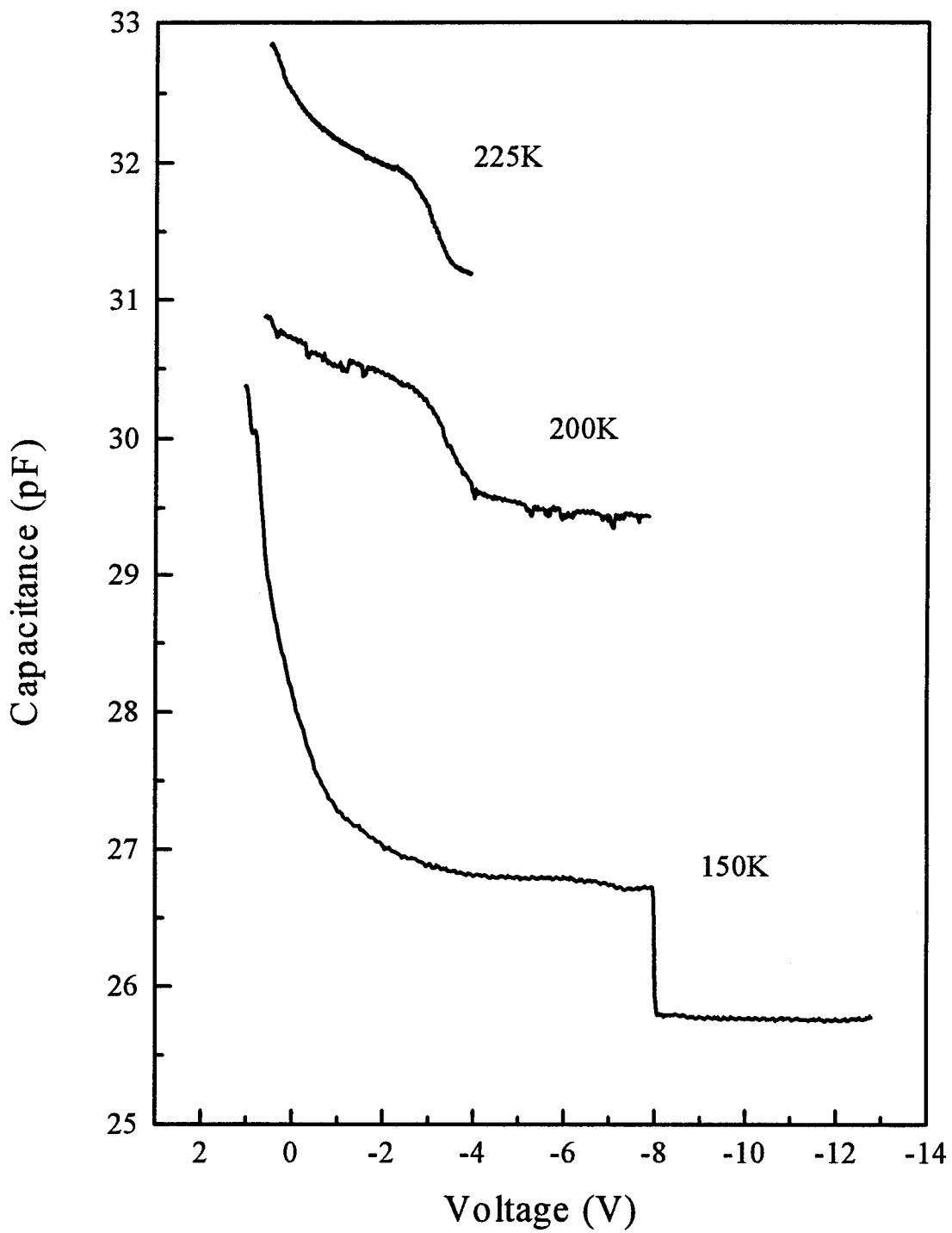
Figure IV-41. Capacitance measurements showing a discontinuity in the measurements made at 150 K for a 100 Å quantum well of $Ga_{0.81}In_{0.19}As_{0.12}Sb_{0.88}$ in $Al_{0.9}Ga_{0.1}As_{0.07}Sb_{0.93}$ barriers.
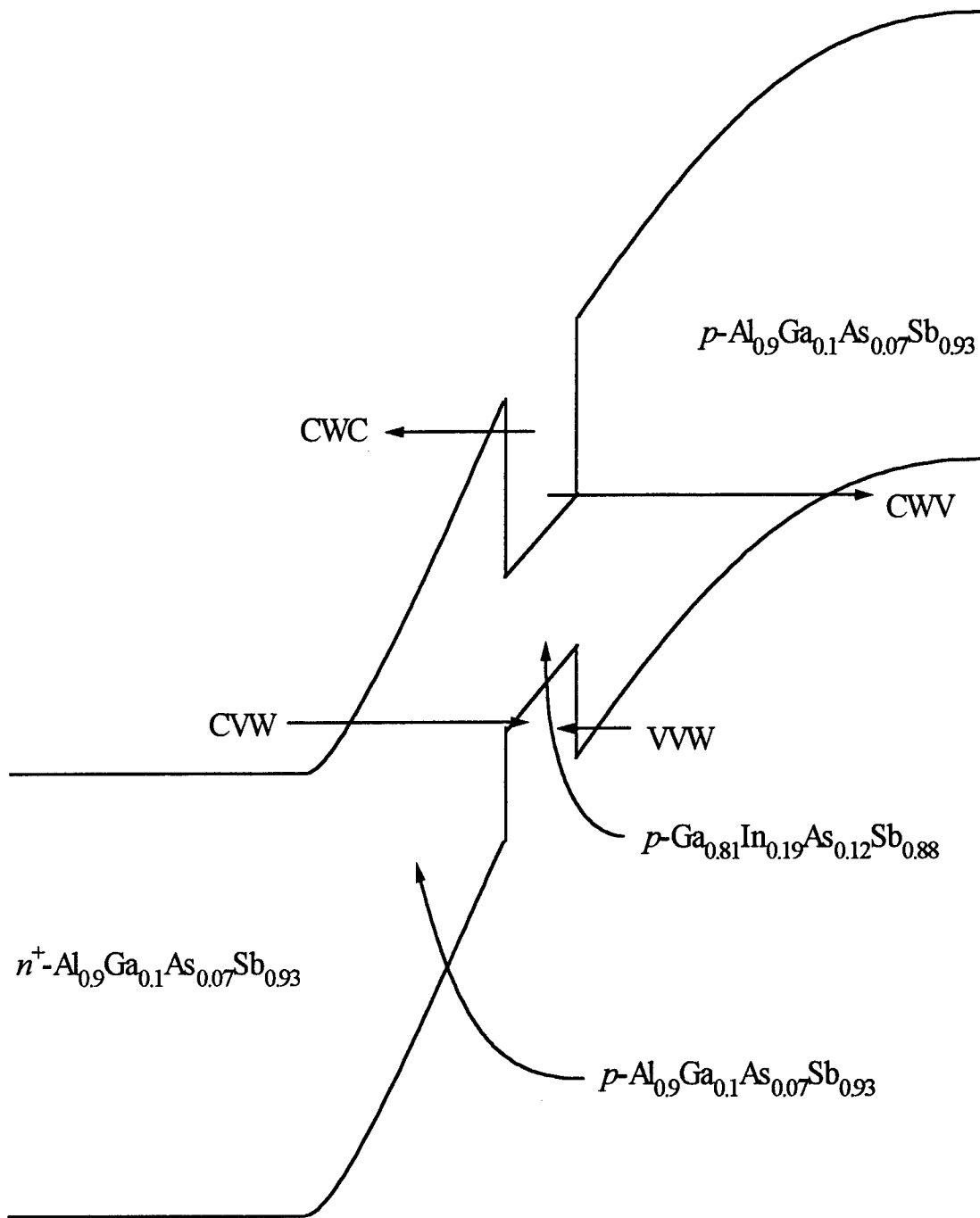
Figure IV-42. n^+-p junction with a $Ga_{0.81}In_{0.19}As_{0.12}Sb_{0.88}$ well showing four possibilities for tunneling involving either well in the p-$Al_{0.9}Ga_{0.1}As_{0.07}Sb_{0.93}$. Tunneling can take place from the conduction band well to the valence band (CWV); from the conduction band well to the conduction band (CWC); from the valence band to the valence band well (VVW); from the conduction band to the valence band well (CVW).

closer to the n^+-p junction. Although there are holes available, tunneling processes are normally associated with high doping.

Tunneling out of the conduction band well into the n^+-$Al_{0.9}Ga_{0.1}As_{0.07}Sb_{0.93}$, labeled CWC, is another possibility. Excited states in the wells have evanescent waves that extend farther into the barrier than the ground state. Also, an electron in the conduction band well has a triangular barrier to tunnel through, the width of which decreases with increasing reverse bias. The extent of the excited evanescent waves, the availability of empty states over a wider range of biases, and decreasing tunneling barrier thickness with increasing reverse bias all favor tunneling out of the conduction band well into the n^+ conduction band. However, this tunneling should be a gradual process, increasing slowly with increasing reverse bias as opposed to the step that is seen in Figure IV-41. The process labeled VVW is also ruled out for the same reason.

Tunneling of an electron from the conduction band of the n^+-$Al_{0.9}Ga_{0.1}As_{0.07}Sb_{0.93}$ to the valence band well, labeled CVW, is the only tunneling process which can explain the abrupt drop in capacitance at -8 V. This process is equivalent to a hole tunneling from the valence band well to the conduction band of the n^+-$Al_{0.9}Ga_{0.1}As_{0.07}Sb_{0.93}$. Abruptly increased tunneling would occur when the states in the valence band well that are occupied by holes line up with the states at the bottom of the conduction band that are occupied by electrons in the n^+ layer. Once tunneling begins, the holes in the ground state of the valence band well are replaced by other holes in the well, which then proceed to tunnel out. The process continues until the valence band well is filled with electrons.

The importance of the capacitance versus voltage measurements is that the gradual steps indicate how many of the energy levels in the well might be expected to appear in the DLTS measurements. It also shows the temperature range where the DLTS peaks should be encountered. The temperature where the step appears in the C-V measurement is a high temperature limit to the temperature range where the DLTS measurements should display a peak, since the C-V measurements are sensitive to emission rates faster than 10^6/sec, whereas the DLTS measurements are limited to emission rates of less than $\sim 10^4$/sec.

DLTS of the AlGaAsSb/GaInAsSb/AlGaAsSb Quantum Well Structures:

The objective of measuring the DLTS spectra of these quantum well structures is to extract the offsets for the conduction band and the valence band from the measured eigenstates of the well. The theoretical aspects of this measurement have been presented in a previous section. Now the problem is to establish experimental conditions that result in measured properties that are valid for determining the band offset.

First, however, there are several factors external to the experimental setup that can influence the measurements. The first thing to consider is the growth of the structures. For the band offset to be predictable, the composition of each material must be known, each interface making up the well must be reasonably free of defects, reproducible, and uniform. The composition of each material must also be known in order to establish the band gap of each material so that, if the band offset of only one band is measured, the band offset in the opposite band can be determined. Prior to growth of a particular

material, a series of calibration runs are made in order to set the reactant fluxes and growth temperature for the desired composition. The band gap is then determined from the band-to-band photoluminescence. But the materials must also be lattice matched. The composition is estimated from the difference in Bragg reflection from the substrate and the epitaxial layer using double crystal X-ray rocking curves. The growth, band gap measurement, and lattice constant measurement is an iterative process for quaternary material since obtaining the correct band gap doesn't guarantee a lattice match. Lattice mismatch can introduce interface states at each of the heterojunctions making up the well. Interface states between the two materials can result in additional band bending at the interface and alter the confined state energies.

After growth, the wafer is processed into diodes. This includes steps that can also have an effect on the diode quality. The section on I-V-T measurements showed that the most critical step is etching the mesas to establish the diode area. The metallization steps can also affect diode quality. Both of these topics were discussed in the section on processing. The resulting problems to watch for in the DLTS measurements are leakage currents through surface states on the perimeter of the mesa from an unintentional selective etch, and diffusion of deposited metal into the p-n junction. Leakage current reduces the sensitivity of capacitance measurements. Surface leakage can also give an alternate path for conduction of charge from the quantum well rather than thermionic emission. Based on the I-V-T measurements, DLTS measurements on the first QW structure may not be as sensitive or accurate as measurements made on the second or third structures due to the larger leakage currents in the first structure.

The general approach to the DLTS measurements is to identify biasing conditions that will separate the signal coming from the valence or conduction band well from other signals. Additionally, the valence band well signal may need to be separated from the conduction band well signal. The valence band well signal will appear as a majority carrier signal and the conduction band well signal will appear as a minority carrier signal since the well is in the p-type material for all three samples. Minority carrier signals can be eliminated by avoiding injection currents during the filling pulse. Emissions from uniformly distributed bulk traps can be reduced by narrowing the spatial emission window using DDLTS.

DLTS spectra for the first QW structure in Figure IV-43 were obtained from two different biasing conditions. The structure is a junction between n^+- and p-AlAs$_{0.07}$Sb$_{0.93}$ with a 125 Å p-Ga$_{0.85}$In$_{0.15}$As$_{0.12}$Sb$_{0.88}$ well, which is 500 Å from the junction. The majority carrier peak (positive signal) is for the DX signal associated with the Te dopant in the n$^+$-AlAsSb. The assignment is based on previously published characterization of the DX-center in Te-doped AlSb grown on GaAs (Nakagawa et al., 1990:1551–1553). The DX trap was discussed in the section on the deep levels in bulk materials. Increasing the reverse bias for measurement widens the depletion region to include emission from the QW, resulting in the minority carrier peak (negative signal). The minority carrier signal corresponds to electron emission from the conduction band well in the p-type AlAsSb. When minority carrier emissions from the well are included, the DX-center signal is completely swamped except for the small depression at 120 K.

Figure IV-43. DLTS spectra of the first QW structure composed of 125 Å well of p-$Ga_{0.85}In_{0.15}As_{0.12}Sb_{0.88}$ in p-$AlAs_{0.07}Sb_{0.93}$ barriers under two different biasing conditions.

A qualitative depth profile was performed to establish that the minority carrier signal corresponds to emission of electrons from the potential well in the conduction bands of the p-type materials. The qualitative profile was also useful as a survey of other signals that needed to be investigated. The profile is from a sample with slightly lower leakage current so that a wider range of biases could be covered. Figure IV-44 shows the trap profile as a series of transients taken at 120 K. Each trace is the difference in capacitance transient response at two measurement biases of V_{m1} and V_{m2} separated by 0.5 V. The top traces are measured after a 1.5 V injection current, making minority carriers available, and the bottom two are without injection. Each pair of measurement biases probes an area incrementally farther from the p-n junction. The emission window is incremented back to the QW where the leakage current under reverse bias starts to interfere. As the emission window is shifted to deeper depletion widths with larger measurement bias voltages, the positive transient from the DX-center is displaced by the larger minority trap signal. The sudden increase in minority carrier signal for the last two biasing conditions [(V_{m1}, V_{m2})=(-1.6 V, -2.1 V) and (-1.7 V, -2.2 V)] that include minority carrier injection show that the minority traps are spatially localized. Since the minority carrier signal is spatially localized, it can be concluded that the minority carrier signal is from the QW. The bottom two transients of Figure IV-44 were obtained without an injection pulse for comparison. The minority carrier signal disappears as expected. However, for the second trace from the bottom [(V_{m1}, V_{m2})=(-1.0 V, -1.5 V)], there is a slower majority carrier emission superimposed on the emission from the DX-center. The slower emission is absent for

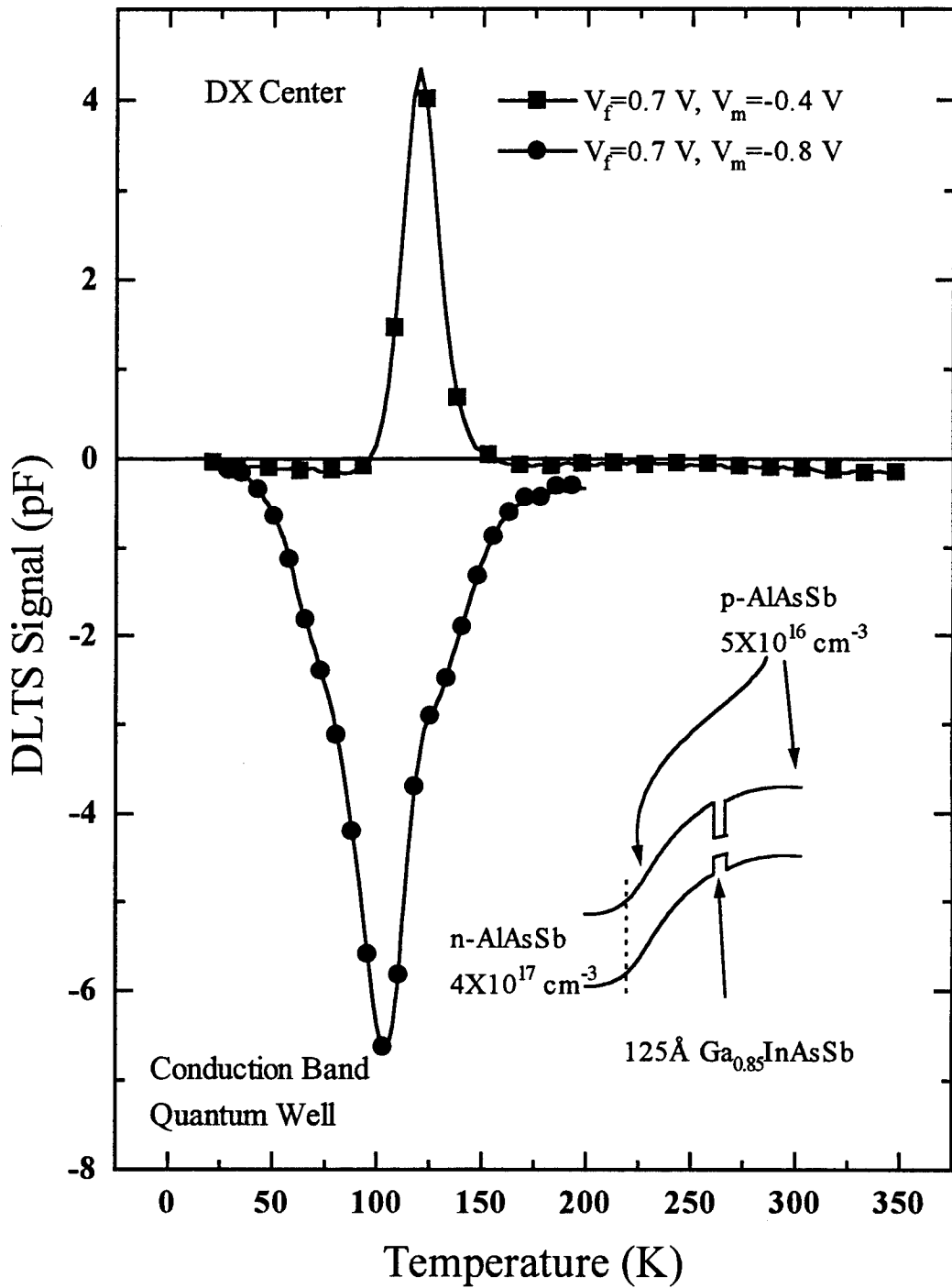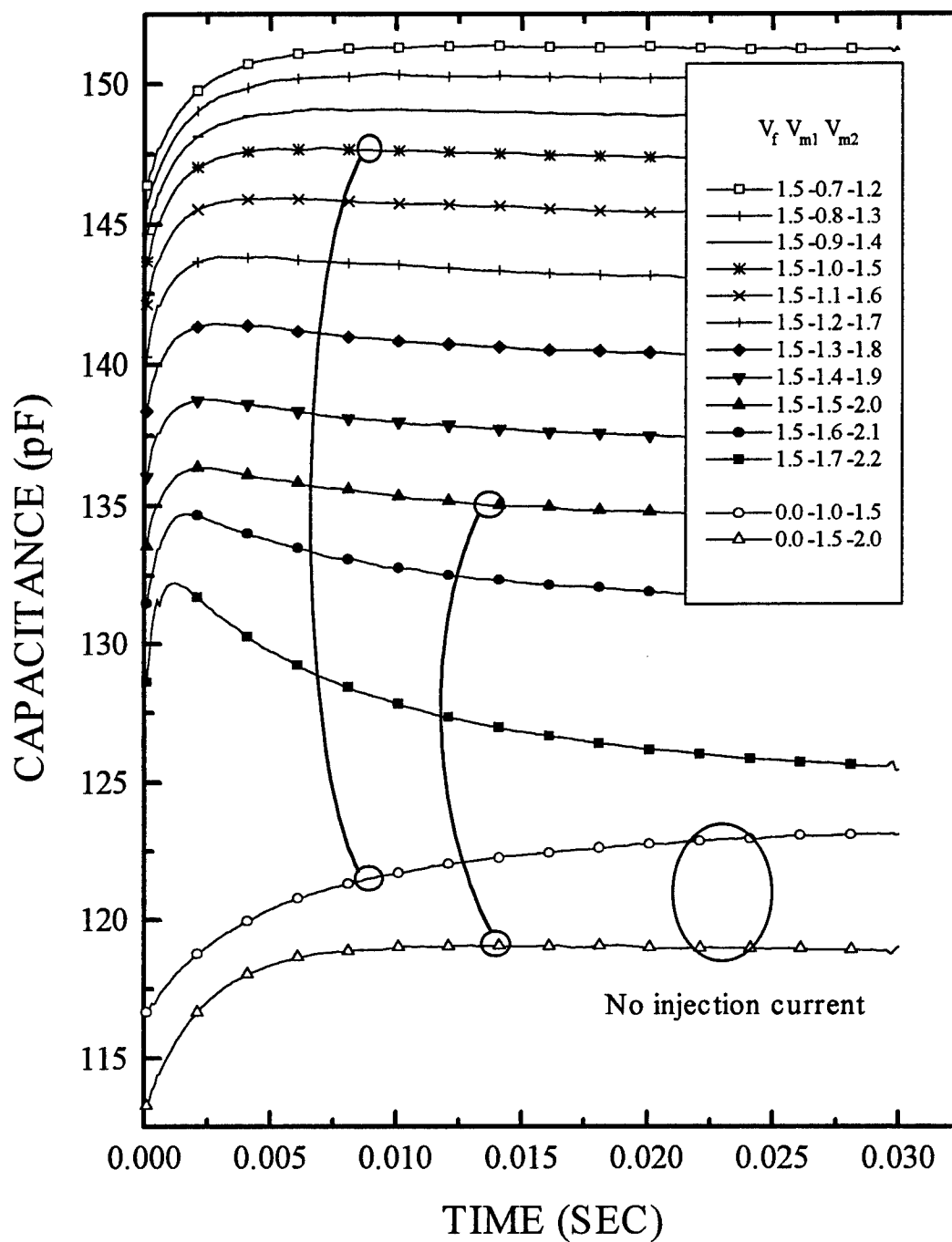Figure IV-44. Capacitance transients from the first QW structure composed of 125 Å well of p-$Ga_{0.85}In_{0.15}As_{0.12}Sb_{0.88}$ in p-$AlAs_{0.07}Sb_{0.93}$ barriers at 120K. The DDLTS mode was used to obtain a qualitative depth profile of the two traps shown in Figure IV-43.

measurement biasing between -1.5 and -2.0 V, indicating that there may be a signal present that can be separated out under the right biasing conditions.

The negative going peak of Figure IV-43 showed up most clearly as a superposition of four traps from the measurements made in the CC-DLTS mode. The rate- window plot is shown in Figure IV-45. Modulating functions fit the transients best for two traps at around 100 K, and two traps at around 140 K. The Arrhenius plot is shown in Figure IV-46, and the results show that there are four minority carrier electron signals from the conduction band well located at 49, 53, 115, and 162 meV deep. Energies that are predicted for the conduction band well place a band of closely spaced energies near the top of the well from the X-band confined states, and more widely separated states in the rest of the well from the Γ-band confined states, as shown previously in Figure IV-23. Emission from the closely spaced X-band states should appear as a broad peak since the separation is on the order of 10 meV. Also, the highest temperature peak should correspond to an energy near the bottom of the well. The deepest X-band states are predicted to be at 115 meV. However, transfer of electrons from X- to Γ-band confined states during capture is expected to be fast enough so that emission from the X-band states may not be seen. Due to the absence of any higher energy traps and the high leakage current in this sample structure, the measured energies could not be used to make an estimate of the band offset from the minority carrier trap signals.

The qualitative depth profile of Figure IV-44 indicated that the large positive peak of Figure IV-43 may be composed of more than one component, one of which was
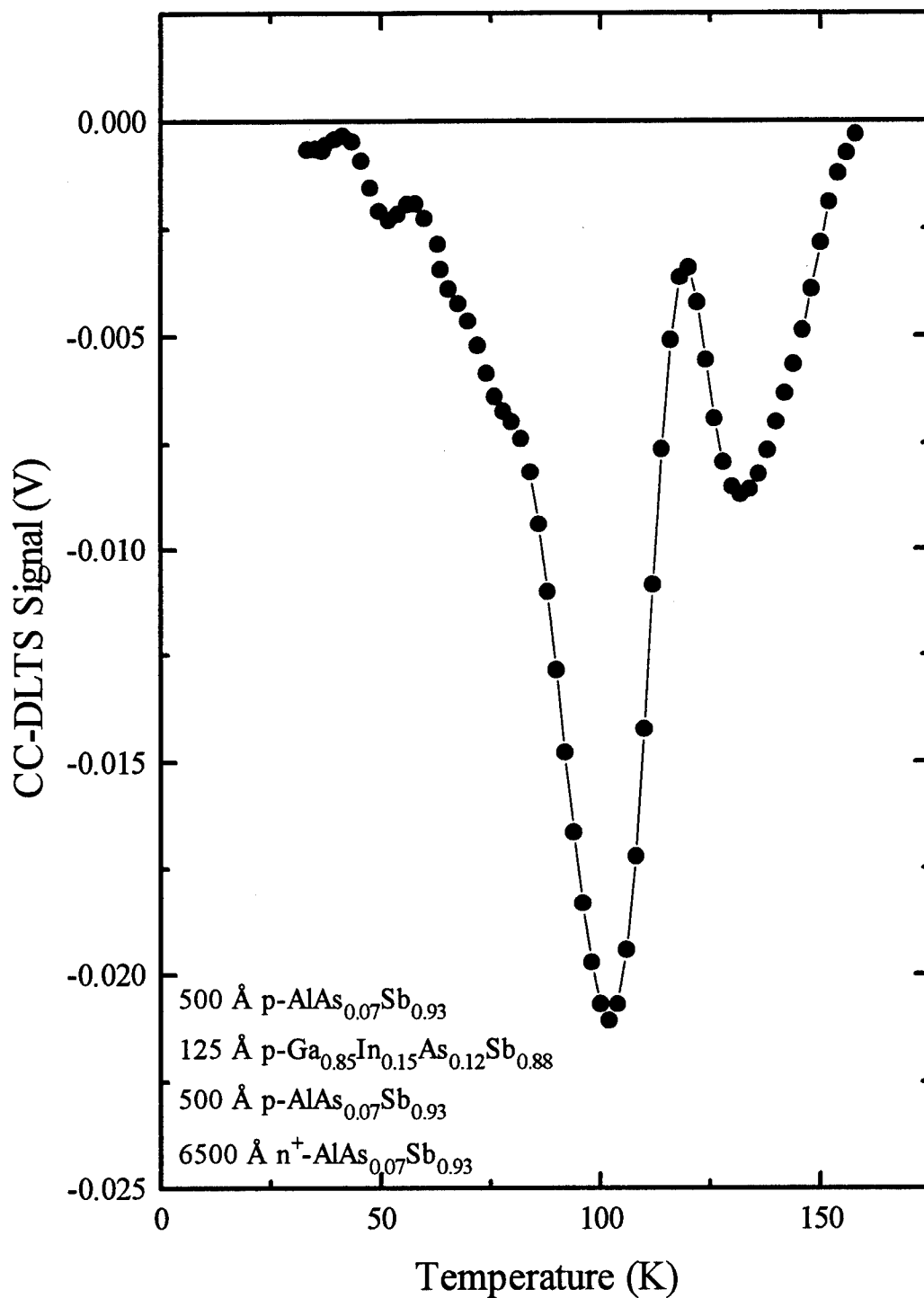
Figure IV-45. CC-DLTS rate-window plot for the minority carrier signal coming from the conduction band well in the first QW structure (125 Å well of p-$Ga_{0.85}In_{0.15}As_{0.12}Sb_{0.88}$ in p-$AlAs_{0.07}Sb_{0.93}$ barriers).

IV-116
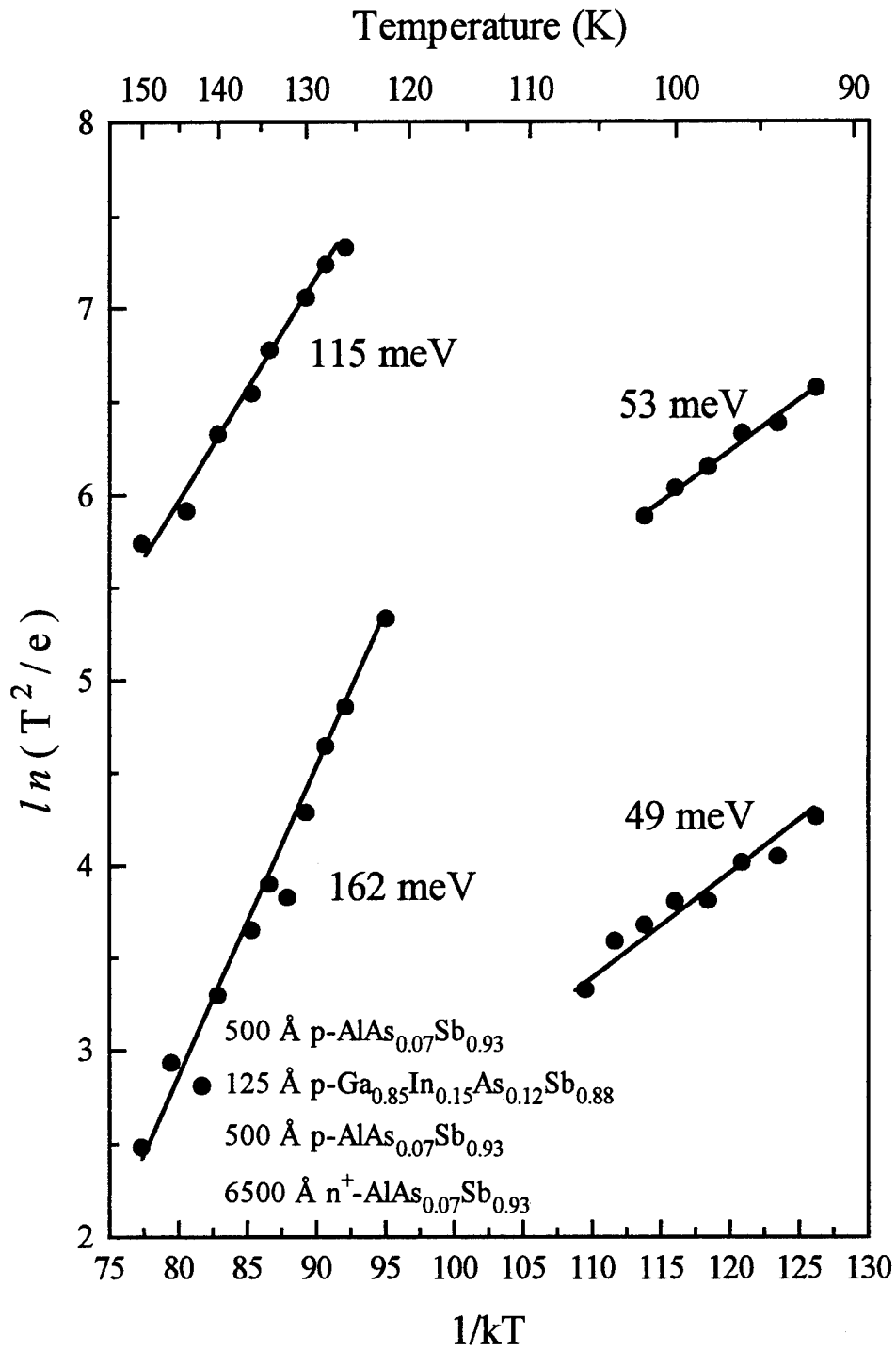
Figure IV-46. Arrhenius plot for the minority carrier (electron) signals from the conduction band well in the first QW sample structure (125 Å well of p-$Ga_{0.85}In_{0.15}As_{0.12}Sb_{0.88}$ in p-$AlAs_{0.07}Sb_{0.93}$ barriers).

spatially localized. The spectra for the large majority carrier signal taken under two different measurement modes are shown in Figure IV-47. The sharper peak of the DX-center was measured using CC-DLTS. The other spectra was measured using standard DLTS. In the CC-DLTS mode, the steady state measurement bias was changed from -2 V to 0 V by the feedback circuit to maintain the capacitance at a constant value over the range of temperatures that were covered. In the standard DLTS mode, the bias used to measure the broader peak was constant at -0.7 V. The constant bias measurements are thereforemore likely to include the well than the CC-DLTS measurements since the reverse bias was larger in the temperature range of the peak. The Arrhenius plot for each of the peaks is shown in Figure IV-48. The broader peak was best fit by a superposition of two traps labeled A and B at low temperature, and one labeled A' at higher temperature, as shown by the solid circles in the Arrhenius plot. Of the two levels that appear between 120 and 140K, the trap with the higher energy of 135 meV makes a transition to a trap with an energy that is similar to the lower energy, lower temperature trap of 85 meV, but now the capture cross section is two orders of magnitude larger. This behavior can be explained by the lower energy level acting as an intermediate emission step for the deeper level as shown by the model in Figure IV-49. The increase in capture cross section of the 85 meV levels from 4.1×10^{-20} to 2.5×10^{-18} cm^2 is a reflection of the additional trap filling route for the 85 meV level through the 135 meV level.

Further insight into the model for emission from the quantum well was obtained from measurements of the occupation of the levels in the well. In Figure IV-50, the concentration of each of the two majority carrier traps measured by DLTS is plotted as a
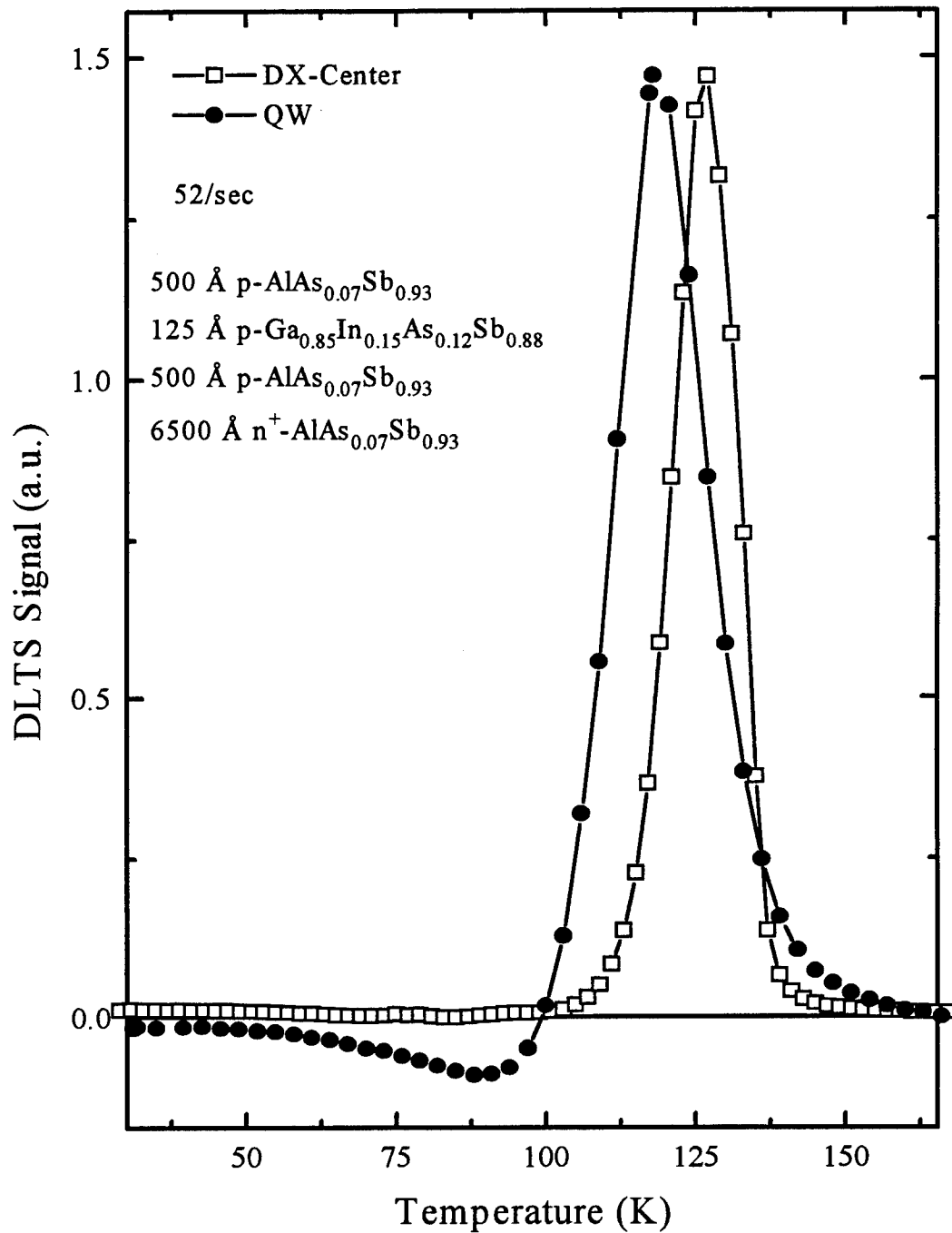
Figure IV-47. A comparison of the majority carrier (hole) signals from the DX-center signature (narrow peak) and a signal from the valence band well (broad peak) measured in the CC-DLTS mode and the DLTS mode, respectively. The sample is the first QW structure composed of 125 Å well of p-$Ga_{0.85}In_{0.15}As_{0.12}Sb_{0.88}$ in p-$AlAs_{0.07}Sb_{0.93}$ barriers.
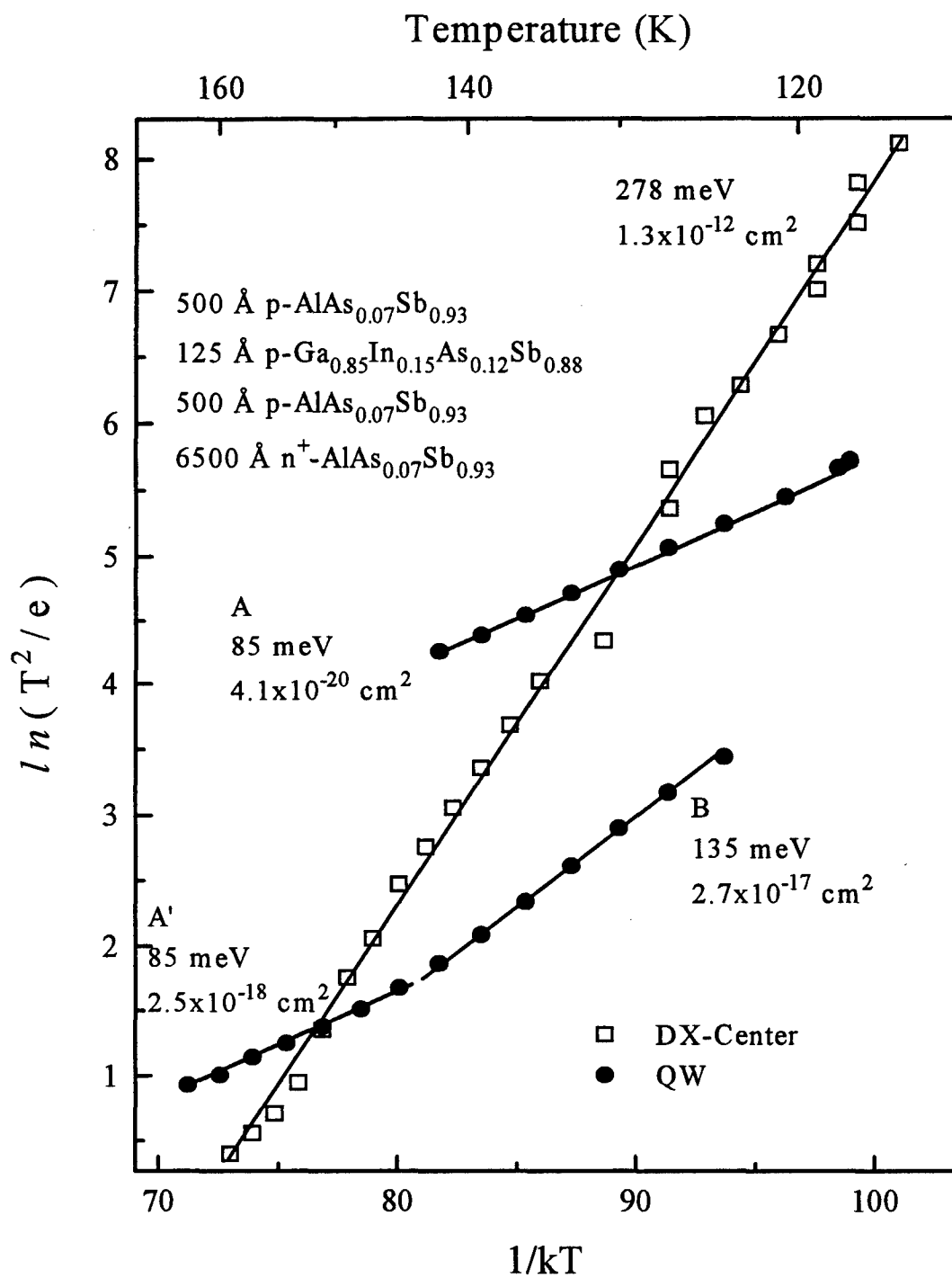
Figure IV-48. A comparison of the Arrhenius plots corresponding to the peaks of the CC-DLTS and DLTS measurements shown in Figure IV-47 for the DX-center and the QW, respectively. The transition of the 135 meV level to 85 meV suggests that the 85 meV level is being refilled by the deeper 135 meV level during emission.
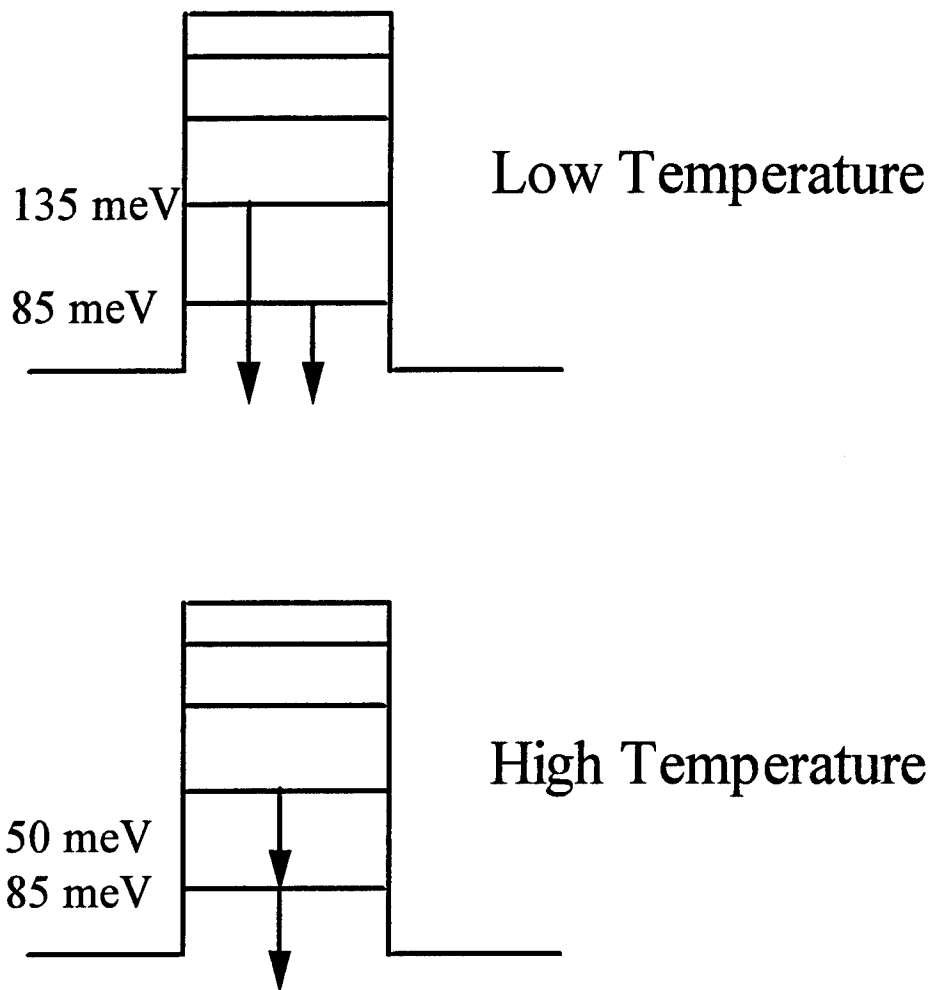
Figure IV-49. Model of emission from two valence band confined states comparing the emission path at low temperature to the emission path at higher temperature resulting in the Arrhenius plot of Figure IV-48.

function of temperature. The plot shows an increase in concentration of one at the expense of the other. Optical measurement of capture processes summarized in a previous section give a time constant on the order of a picosecond. However, the time constants of the capacitance transients during the capture process were on the order of a millisecond. This disparity can be explained by the position of the quasi-Fermi level. If the quasi-Fermi
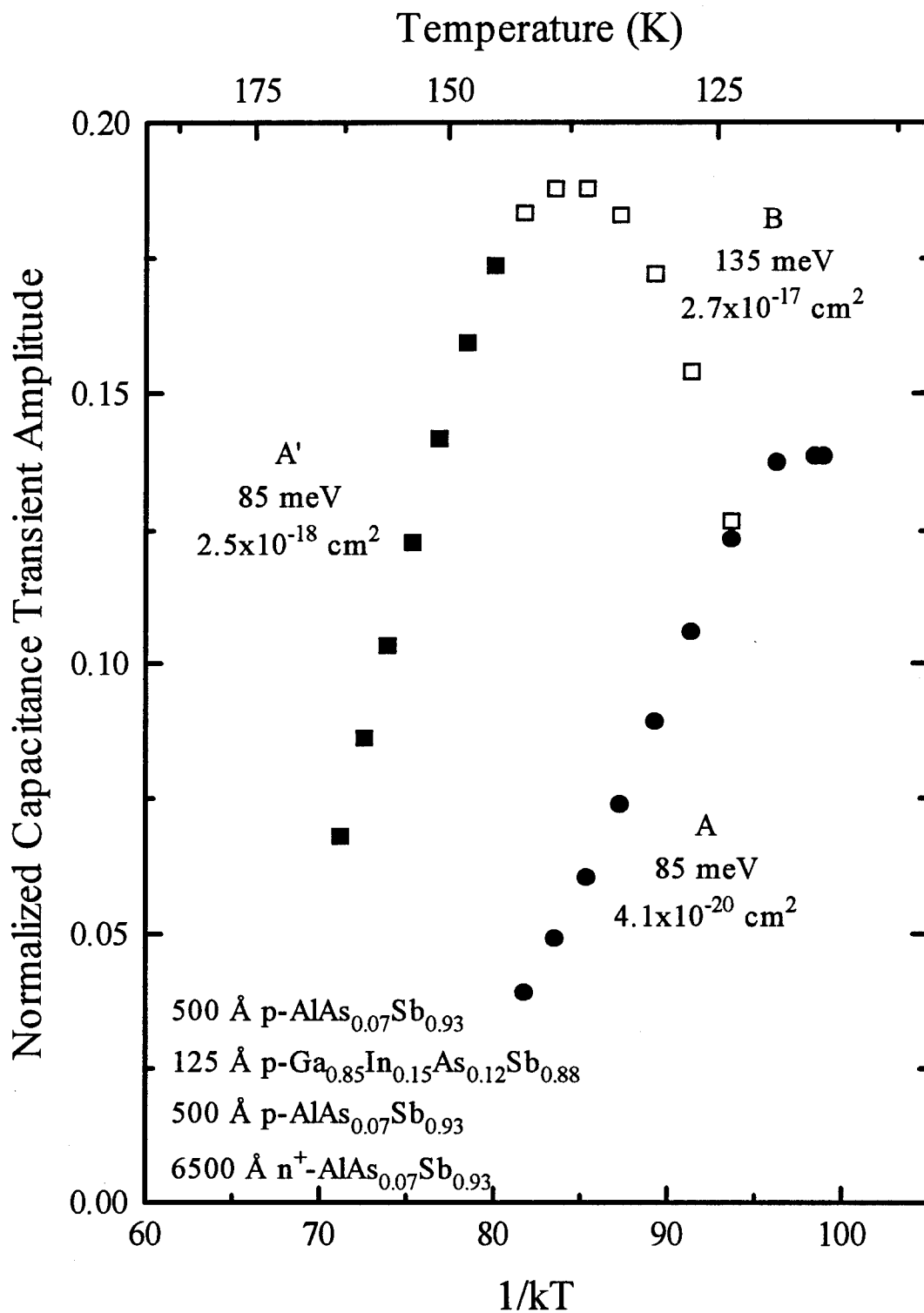
Figure IV-50. The change in concentration of majority carriers trapped on the two energy levels shown by the broad peak in Figure IV-47 as a function of temperature for the first QW sample of 125 Å well of p-Ga$_{0.85}$In$_{0.15}$As$_{0.12}$Sb$_{0.88}$ in p-AlAs$_{0.07}$Sb$_{0.93}$ barriers.

level is making a transition through a confined state, the number of empty positions available will be limited, slowing the capture process. Also, the Arrhenius plot shows that the higher energy trap makes a transition to a lower energy emission path at higher temperatures as drawn schematically in Figure IV-49. At low temperature, both energy levels are substantially filled. As the temperature increases, faster emission from the shallower trap provides available states to allow refilling from the deeper trap. The emission rate is limited by the larger of two energies: either the difference between the two confined state energy levels, 50 meV, or the lower energy trapping level, 85 meV. The 85 meV energy is the rate limiting step in the series emission from the 135 meV energy level via the 85 meV level, so that the 85 meV level was measured at higher temperature. The increase in capture cross section of the shallower 85 meV energy level from 4.1×10^{-20} to 2.5×10^{-18} cm^2 reflects the additional capture path through the deeper confined state. Similar measurements were made in the other sample structures.

There was considerable spread in the measurements from diode to diode of the first sample structure of 125 Å well of p-Ga$_{0.85}$In$_{0.15}$As$_{0.12}$Sb$_{0.88}$ in p-AlAs$_{0.07}$Sb$_{0.93}$ barriers. Of the dozen or so measurements made where there was a broad peak consisting of two trap energies was measured, the energies varied from 70 to 220 meV, and the spacing varied from 4 to 128 meV. This amount of scatter invalidates any attempt to determine the band offset from the first sample structure. The source of the error stems from the leakage current at the surface. The high leakage current prevented a bias from being applied that is large enough to bring the Fermi level below the bottom of the well. The

leakage current only gets worse with increasing temperature, prohibiting measurement of higher energy transitions from the well.

All of the DLTS measurements of both the majority and minority carrier signals made on the first sample structure revealed spatially dependent capacitance transient amplitudes, indicating emission from either the valence band or the conduction band well. However, the measured energies in each case were much lower than expected. If energy measurements from the well in one band are low, energy measurements from the well in the opposite band should be high, and would merely reflect an inaccuracy in the predicted band offset. Since energy measurements from the conduction band well and the valence band well are both low, the conclusion is that the leakage current alters the emission characteristics, invalidating any estimate of the band offset based on measurements of the first sample structure.

The second sample structure was designed with a narrower well, and higher indium content which decreased the effective mass in the well. Both changes have the effect of pushing the levels up in the well, thereby reducing the emission energies. The structure is 100 Å well of $Ga_{0.81}In_{0.19}As_{0.12}Sb_{0.88}$ in $AlAs_{0.07}Sb_{0.93}$ barriers. Decreasing the Ga mole fraction from 85% to 81% also decreases the gap of the $Ga_xIn_{1-x}AsSb$ in the well by 36 meV, most of which is predicted to be accommodated as an increase in the conduction band offset.

Measurements similar to those made on the first sample structure were made on the second sample structure. Two representative DLTS spectra for the second structure are shown in Figure IV-51. The large positive peak, shown reduced by 1/5, was measured
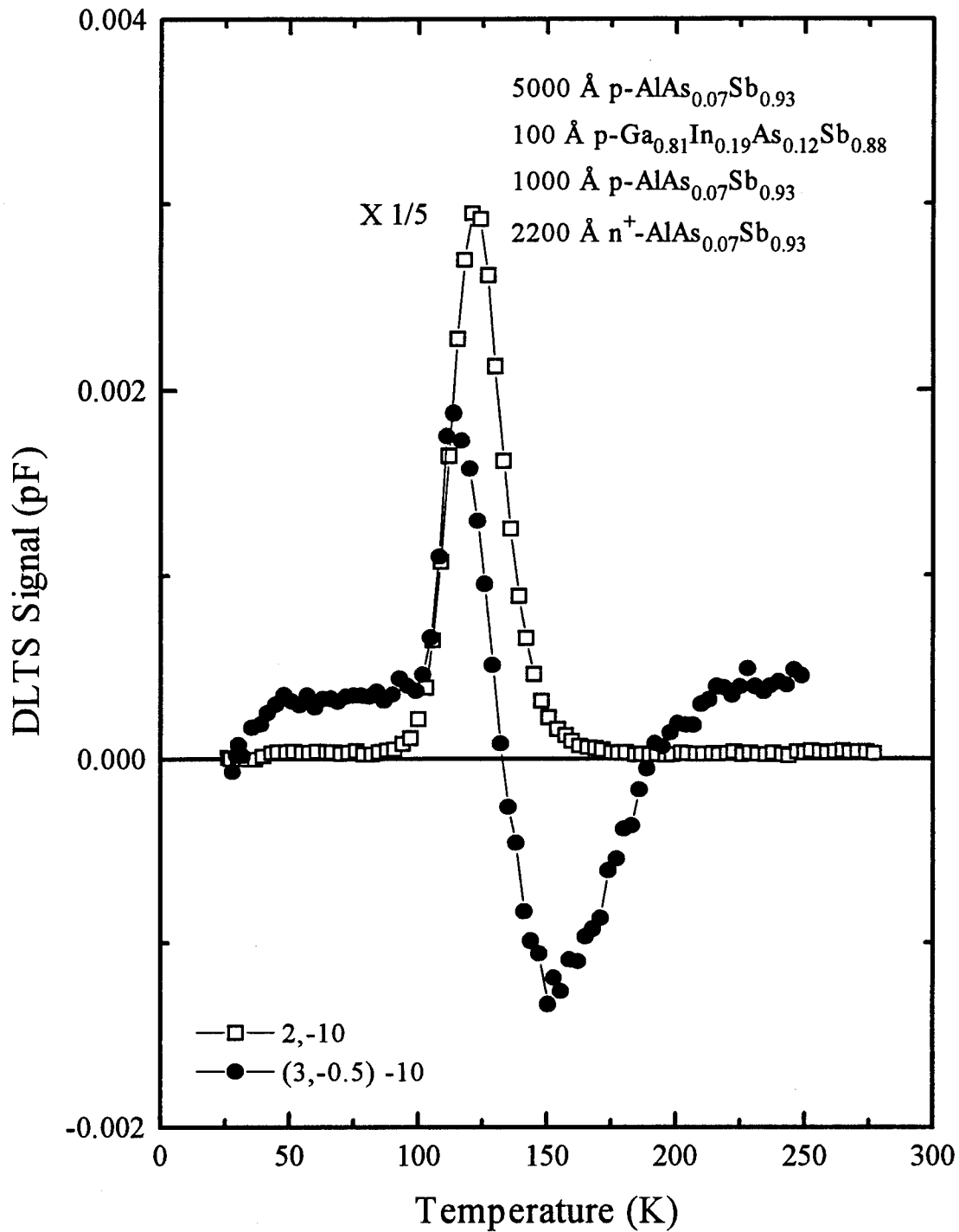
Figure IV-51. DLTS spectra for the second QW structure under two biasing conditions. The solid circles are for measurements made in the DDLTS mode. The second QW structure is 100 Å well of $Ga_{0.81}In_{0.19}As_{0.12}Sb_{0.88}$ in $AlAs_{0.07}Sb_{0.93}$ barriers.

using a single DLTS filling pulse of 2 V and a measurement bias of -10 V. The smaller peak, which includes a minority signal (negative), was measured using DDLTS, where the filling pulses were 3 and -0.5 V, and the measurement bias was -10 V. The 3 V filling pulse probes both majority and minority traps. The -0.5 V filling pulse probes only the majority carrier traps. Subtracting the two signals cancels most of the majority carrier signal. As shown in the figure, DDLTS effectively removed most of the majority carrier signal (reduced by a factor of ~8), revealing the minority carrier peak. The spectra show what signals are available for further measurement and analysis.

In order to show that the signals are from the QW, DDLTS was used to sweep an emission window through the material. Figure IV-52 presents the data in a different form than was used for the first sample structure. In this sample the leakage currents were lower than for any of the first QW sample diodes so that a wider range of biases could be applied. The DDLTS measurements keep the measurement bias constant and takes the difference in the response from filling pulses separated by 1 V. The horizontal axis is proportional to the depletion width, where 0 V is closest to the n^+-p junction. The response peaks as the spatial emission window is swept through the QW. In the first sample structure, only the initial increase was seen before leakage currents interfered. The two traces show that similar response is obtained for the two measurement bias conditions.

Transitions from energy levels in the well in the second structure were similar to what was found in the first sample structure. Measured energies were much lower than what is expected from the bottom of the well. The concentration of the carriers emitted
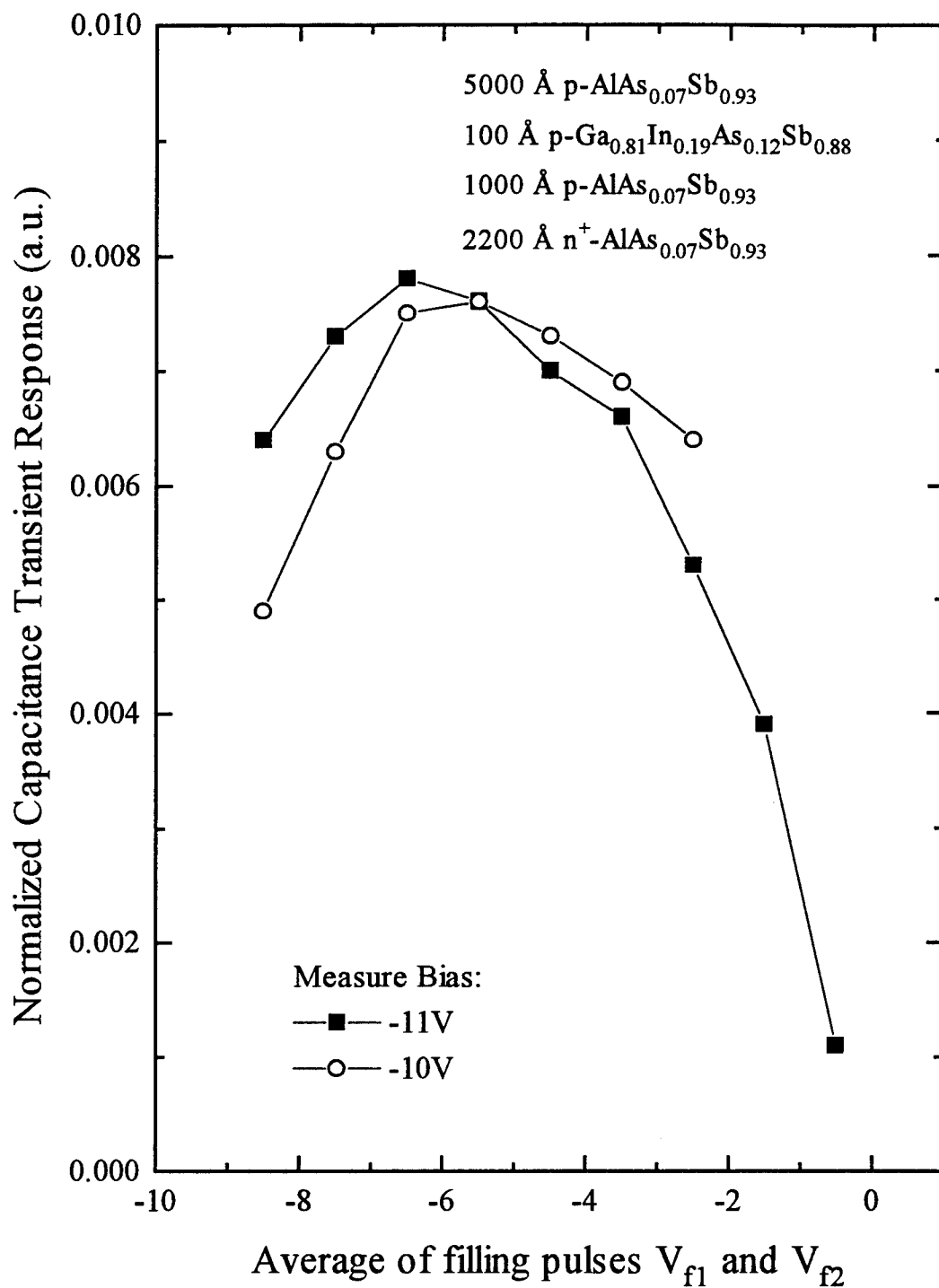
Figure IV-52. Qualitative profile of the second QW sample, which is composed of 100 Å well of $Ga_{0.81}In_{0.19}As_{0.12}Sb_{0.88}$ in $AlAs_{0.07}Sb_{0.93}$ barriers, from the amplitude of the response as the emission window is swept through the QW. Pairs of filling pulses are separated by 1 V from (-9 V, -8 V) to (-1 V, 0 V).

from the levels also changed with temperature in the same manner as the previous sample. The low energies and change in concentration with temperature indicates that the emissions are from the shallower confined states.

In the third structure, the barrier composition was changed from $AlAs_{0.07}Sb_{0.93}$ to $Al_{0.9}Ga_{0.1}As_{0.07}Sb_{0.93}$ resulting in much lower leakage currents. Figure IV-53 shows the DLTS spectra from one sample under various reverse bias conditions. The filling pulse was 100 μsec at 3 V for each. Two rate windows are shown, one at 693/sec and the other at 42/sec. The measurement bias was changed over the values -10, -8, -6, and -4 volts.

The figure shows that the temperature of the peaks increase with increasing measurement bias. This behavior is opposite from what is expected from either field lowering of the barrier or phonon assisted tunneling through the barrier. The increase in the DLTS peak temperature with increasing bias, and thus increasing field, means that the thermal emission energy of the trap is increasing in conjunction with the measurement bias. Recall that at the point on the C-V curve shown earlier in Figure IV-38, where the capacitance is not changing much with bias, the Fermi level remains at an energy level in the well. A series of measurements from small to large reverse bias should show an increase in the peak height initially, and then it should saturate. The saturating behavior is shown best by the rate window plots of 693/sec at 245 K where the peak height for measurement biases of -8 and -10 V are the same. The range of biases where the number of carriers emitted from the well is increasing corresponds to the point where the Fermi level is passing through a confined state energy of the well. The measured energy at this point should be lower than the actual confined state energy depth since carrier recapture is
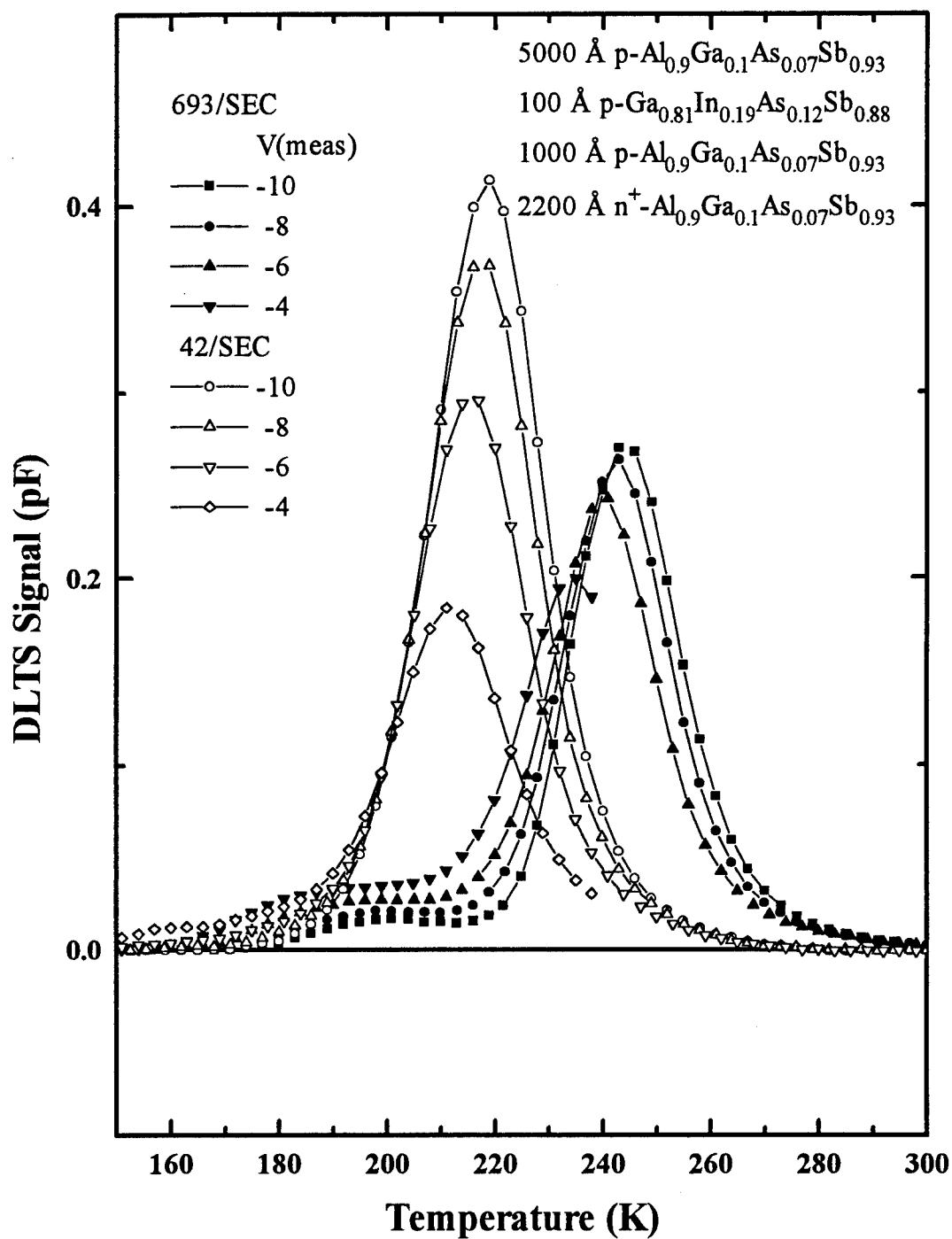
Figure IV-53. DLTS spectra from the third quantum well structure composed of 100 Å of a $Ga_{0.81}In_{0.19}As_{0.12}Sb_{0.88}$ well between $p\text{-}Al_{0.9}Ga_{0.1}As_{0.07}Sb_{0.93}$ barriers for various measurement biases.

a strong competing process. When the number of emitted carriers reaches its maximum, the Fermi level is just below the confined state energy.

Figure IV-54 shows the amplitude of the capacitance transients normalized to the steady state capacitance for each bias condition as the temperature increases. The increase in the response of each with temperature is similar to the response of a bulk deep level with a thermally activated capture barrier, although a very rough fit to the capture model by MPE rules out MPE as the source of the change in transient amplitude with temperature. The change in amplitude is more likely due to the shift of the quasi-Fermi level through the confined state during emission from the well. At high temperature the concentration saturates with increasing reverse bias as expected. To point this out more clearly, there is considerably less difference in normalized capacitance transient amplitude between -8 and -10 V than between -4 and -6 V, at 250 K.

The change in measured activation energy with reverse biasa as shown in Figure IV-55, also indicates that the effect of competing carrier recapture at low reverse bias is a factor to account for. The best fit of the transients using modulating functions show that the capacitance transients are composed of two hole energies labeled A and B in the Arrhenius plot of Figure IV-55. A is the large peak, and B is the low peak shown between 180 and 220 K in Figure IV-53 for the rate widow of 693/sec. Both sets of energy levels show the same trend, increasing in energy with increasing reverse measurement bias. The longest Arrhenius lines, and therefore the most accurate measurements, are for the shallower level, A. The series of measured energies for level A are asymptotic to a value of 0.506 eV as the measurement bias is changed. The energy of 0.506 eV corresponds to
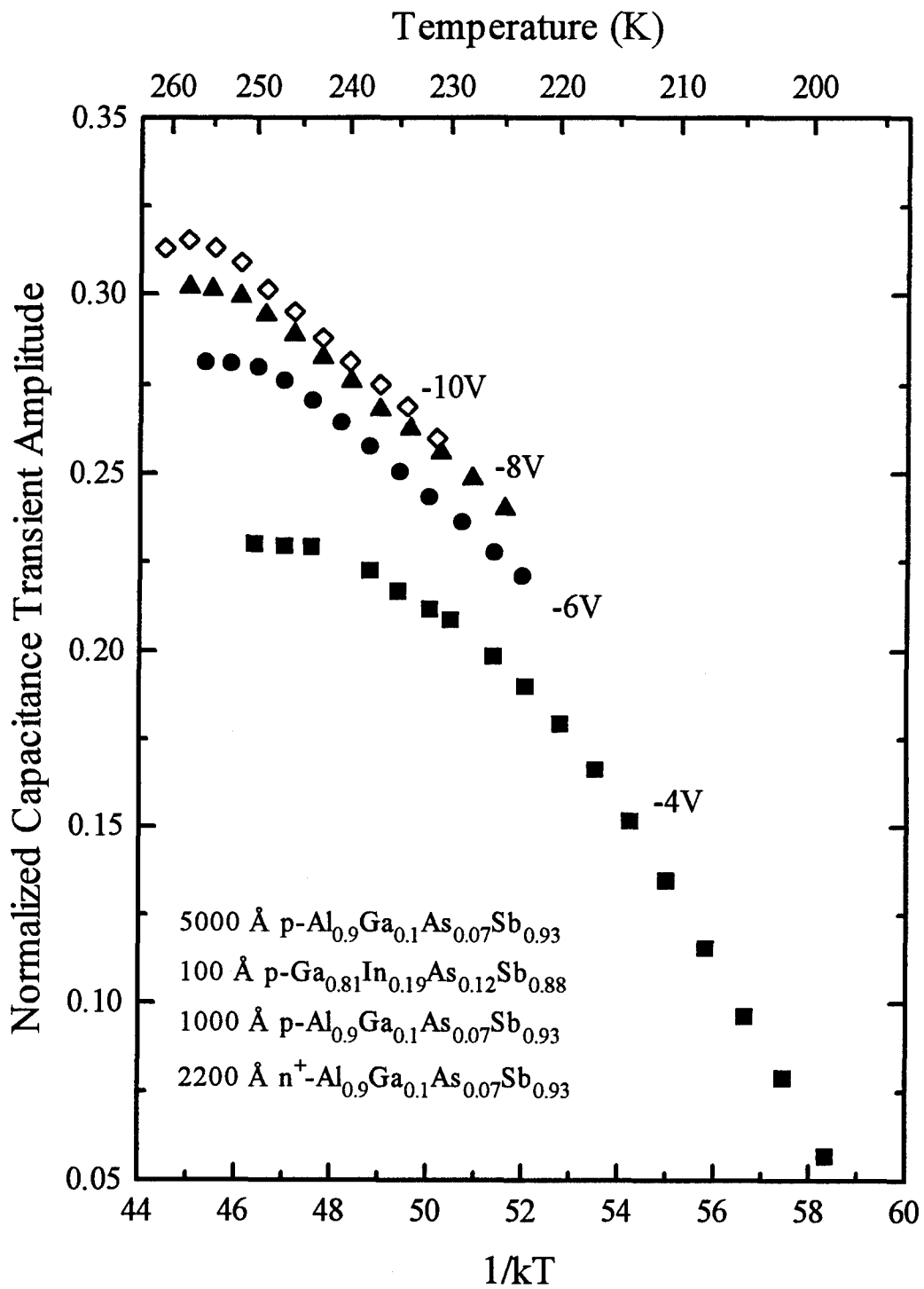
Figure IV-54. Concentration of filled states emitted from the third quantum well structure for several measurement biases.
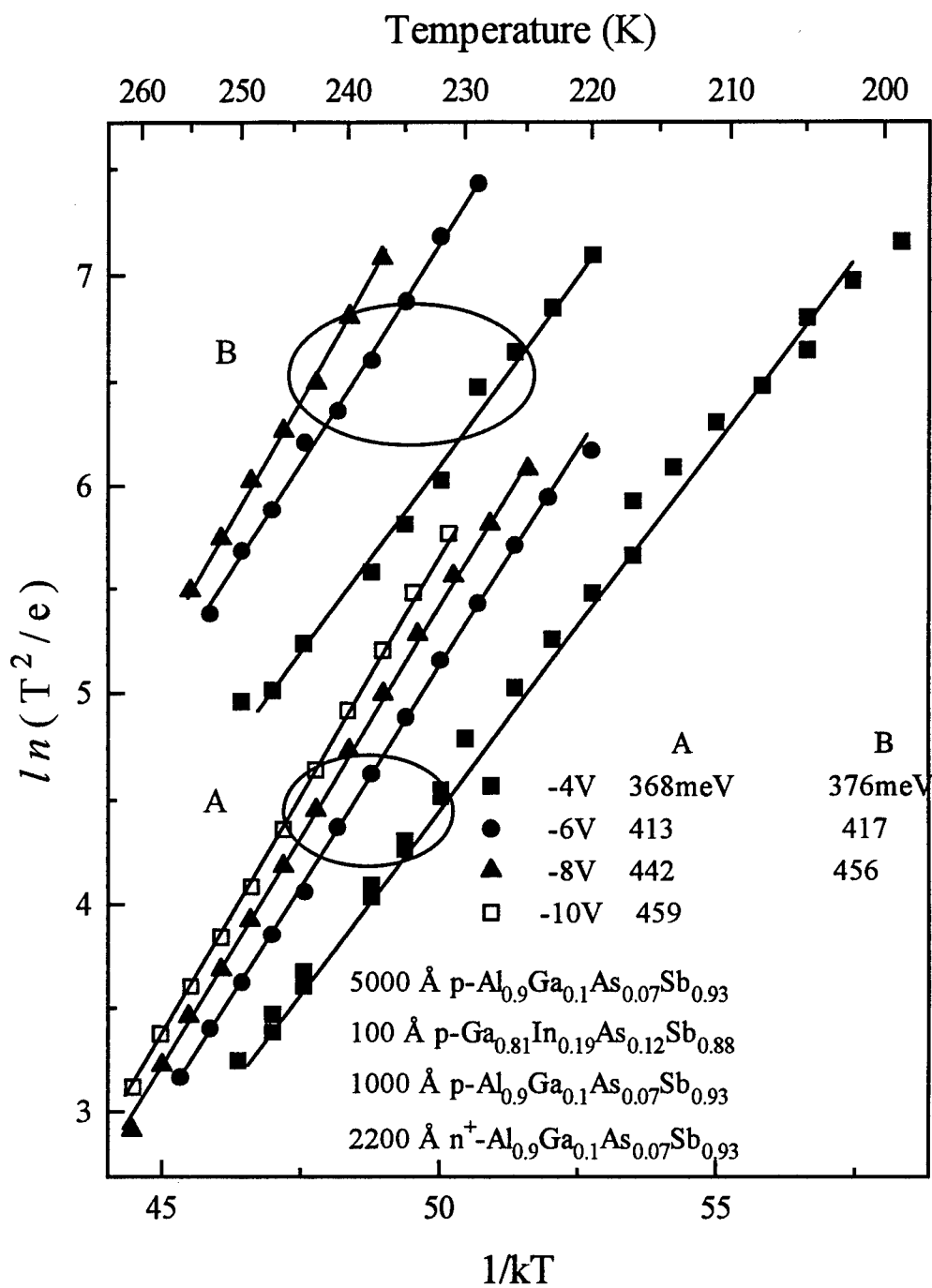
Figure IV-55. Activation energies for the traps seen in the rate window plot of Figure IV-53 for the third QW structure.

reverse measurement biases larger than -10 V where the Fermi level would be farther below level A. Measurement biases larger than -10 V were not used since this is near the breakdown voltage. The calculated energies for confined states at the bottom of the valence band well are 338 meV for the light hole and 367 meV for the heavy hole. However, the measured shallower level was found to have a concentration five times higher than the deeper level, presumably corresponding to the higher density of states of a heavy hole confined state, indicating that the light and heavy hole positions at the bottom of the well are reversed.

The appearance of the heavy hole energy nearer to the top of the well than the light hole energy indicates that the energy levels may have been perturbed due to residual strain, although double crystal X-ray rocking curves (DCXRC) do not indicate any significant strain. However, DCXRC would only reveal differences in lattice constants for relaxed structures. If the QW is narrower than the critical thickness, then it is plausable that there may be unrelaxed strain present. Another explanation for the deeper energy of lower concentration may be that it is an artifact of fitting the transients to an equation that incorporates Boltzmann statistics rather than Fermi-Dirac statistics. The disappearance of level B at higher reverse biases supports this second explanation. Using the difference of 139 meV between the measured value of 0.506 eV and the calculated heavy hole energy of 0.367 eV, the band offset should be 0.52 eV rather than 0.38 eV calculated from an interpolation of the average valence band energy of binary compounds using bowing parameters.

This section effectively demonstrated a method to determine the band offset using a series of DLTS measurements. The DLTS measurements of the three different quantum well structures show the range of results that can be obtained with diodes of various quality, and the caution that should be used in interpreting the data. The leakage current and emission energy of each of the samples show the importance of qualifying the DLTS measurements with I-V measurements. The diodes with high leakage currents tended to have emission energies much lower than expected. Diodes of high quality were obtained from the third sample structure by controlling the surface conduction, most effectively by changing the barrier material to $Al_{0.9}Ga_{0.1}AsSb$ rather than AlAsSb, and using RIE to form the mesas. The C-V measurements also proved useful, establishing a reasonable range of voltages required to drive the quasi-Fermi level below the confined states in the well and observe the resulting emission in the DLTS measurements. Pushing the quasi-Fermi level farther below the confined states in the well improves the accuracy of using Boltzmann statistics. The increase in trap energy with increasing reverse bias measurement conditions reported previously is explained by the inaccuracy of using Boltzmann's approximation rather than Fermi-Dirac statistics at lower reverse bias, where the quasi-Fermi level is close to the confined state energy. Extrapolating the trend in measured energies as the reverse bias is increased bypasses the difficulties of using Fermi-Dirac statistics, which require knowledge of the position of the quasi-Fermi level during emission. Extrapolating the measured energies based on Boltzmann's approximation to a point where the approximation is valid results in a measured valence band offset between $Ga_{0.81}In_{0.19}AsSb$ and $Al_{0.9}Ga_{0.1}AsSb$ lattice matched to GaSb of 0.52 eV.

V. SUMMARY, CONCLUSIONS AND RECOMMENDATIONS

The objectives of this study were to characterize the deep levels in $Al_xGa_{1-x}As_ySb_{1-y}$ and $Ga_xIn_{1-x}As_ySb_{1-y}$ that are used as the wider bandgap and narrower bandgap materials in a quantum well, respectively, for emission in the 2-4 μm wavelength region. The second objective of this effort was to establish methodology to make deep level transient spectroscopy (DLTS) more effective for measuring band offsets between semiconductors of different bandgaps. Each of the objectives were accomplished. Opportunities also arose to expand the scope of routine DLTS measurements to include characterization of the capture mechanism of traps, and recognition of the characteristics of two-level trap kinetics in DLTS measurements. The contributions are separated into improvements in the DLTS measurement and analysis methods, and characterization of material that is technologically important for mid-IR diode lasers. First, the DLTS method was advanced by expanding the scope of characterization of deep levels and developing the methodology for measurement of quantum well (QW) band offsets. Second, the improvements were demonstrated by characterizing the deep levels in $Al_xGa_{1-x}As_ySb_{1-y}$ and $Ga_xIn_{1-x}As_ySb_{1-y}$, and by measuring the band offset between $Ga_{0.81}In_{0.19}As_{0.12}Sb_{0.88}$ and $Al_{0.9}Ga_{0.1}As_{0.07}Sb_{0.93}$. Efforts focused on development of the experimental method of DLTS measurements made on heterojunction and QW structures, since they are becoming increasingly common. The result is that band offsets can be determined accurately, to within 0.01 eV, rather than relying on band offset estimates based on the average valence band energy of the binary constituents, which is considered to be accurate to within 0.1 eV. Also, the measurements identify device performance limitations due to the presence

of deep levels. Detecting the presence and measuring the deep level characteristics are the first step in identifying the origins of the traps reported here. The microscopic composition of each of the traps will require a series of changes in growth parameters such as the III/V ratio, growth temperature, or dopant species and concentration for future studies.

Deep level traps found in $Al_xGa_{1-x}As_ySb_{1-y}$ (x=0, 0.5, 0.6, 1.0) grown by MBE were measured using DLTS. The compositions that were investigated represent materials that can be used as barrier or cladding layers for diode lasers operating in the 2-4 μm range. The Ga_{Sb} double acceptor trap in both $Al_xGa_{1-x}As_ySb_{1-y}$ (x=0, 0.5, 0.6) and $Ga_{0.85}In_{0.15}As_{0.12}Sb_{0.88}$ was identified for the first time by DLTS through a comparison of the DLTS characteristics with theoretical predictions and other experimental measurements for the Ga_{Sb} antisite defect. That is, the energy levels measured by DLTS are close to energies calculated from a tight-binding model and energies measured by other methods. Previously reported values of Ga_{Sb} in GaSb cover a wide range of energies. DLTS suits the measurement of deep levels better than the other methods, which included photoluminescence, optical absorption, and Hall measurements, and should therefore be more accurate. It has been found that the energies for the Ga_{Sb} measured by DLTS in each of the $Al_xGa_{1-x}As_ySb_{1-y}$ (x=0, 0.5, 0.6) compounds decreased as the mole fraction of aluminum decreased, which agrees with the theoretical calculations. The obtained energies are 23 and 76 meV for the Ga_{Sb} defect in GaSb, 32 and 93 meV in $Al_xGa_{1-x}As_ySb_{1-y}$ (x=0.5), and 38 and 102 meV in $Al_xGa_{1-x}As_ySb_{1-y}$ (x=0.6). The Ga_{Sb} defect signal was also expected to be found in AlAsSb (x=1), but the extremely large

signal from the DX center completely dominated the spectra in the temperature regime where the Ga_{Sb} signal should be.

It has been found that the DX center is by far the most commonly occuring trap in any of the compositions of $Al_xGa_{1-x}As_ySb_{1-y}$. Widely varying energies have also been reported for this defect, ranging from 0.25 to 0.315 eV in GaSb, for example. Lack of information about even the presence of the capture barrier or its magnitude contributes to the range of reported values. The presence of a capture barrier can distort the DLTS spectral peaks, and consequently distort the energy level measured by conventional ratewindow DLTS analysis that uses the temperature of the peak rather than the transient analysis method used in this work. Techniques described here extend the state of the art in conventional DLTS measurements to allow easy measurement of capture barriers, and enable testing of the models for the DX center in this material. In AlAsSb, part of the model relies on an accurate measurement of the DX center capture barrier, which is accurately measured at 0.14 eV in this work. The model also depends on the charge state of the defect, which can be determined from the change in emission energy measured by DLTS as the electric field changes. The reduction in emission energy with increasing electric field was found to be less than expected for a center that is neutral after trapping two electrons. This suggests that the model for the DX center as being charged -1q after trapping two electrons is the correct one, assuming a Coulombic defect potential. However, the presence of a capture barrier shows that the defect potential is not purely Coulombic so that the electric field lowering of the emission barrier should not be as large as expected from a pure Coulombic potential.

It has been found that DX centers in AlGaAsSb have fewer trap energy levels than expected. Te (group VI) doped n-AlAsSb should have four possible distinct DX trap energies since there are two species of group V atoms in the three sites that surround an aluminum atom that is pushed to an interstitial site by the substitutional donor. Only one out of four possible configurations was seen in the ternary AlAsSb, and only one was seen in any composition of $Al_xGa_{1-x}As_ySb_{1-y}$ (x=0, 0.5, 0.6). The high concentration and subsequent compensation of the donor by Ga_{Sb} may also be the reason that more peaks related to the donor impurities are not seen. The high concentration of Ga_{Sb} antisite defects may influence the species of atoms that surround the donor-defect complex, giving preference to one configuration over the other possible configurations. Reducing the antisite defect by appropriate growth conditions may cause more peaks with other energies to appear in DLTS measurements, corresponding to different configurations of atoms around the donor related defect.

DLTS measurements revealed one minority electron trap level at 320 meV below the conduction band, and six majority hole trap levels at 24, 76, 108, 122, 224, and 276 meV above the valence band in the $Ga_{0.85}In_{0.15}As_{0.12}Sb_{0.88}$, which is used as the active region in 2 μm lasers. The strong bonding of nitrogen in the insulating layer of Si_3N_4 with Ga in the $Si_3N_4/Ga_{0.85}In_{0.15}As_{0.12}Sb_{0.88}$ MIS structure was used to find that some of the traps were related to excess Ga. Decreasing concentration of the 24, 76, and 108 meV traps as the insulator/semiconductor interface was approached indicates that the traps are related to excess Ga. Furthermore, the two low energy levels (24 and 76 meV) are attributed to the Ga_{Sb} double acceptor, adding $Ga_{0.85}In_{0.15}As_{0.12}Sb_{0.88}$ to the materials

where the Ga_{Sb} anti-site defect is found. Another important trap is a minority trap level at 320 meV and a hole trap level at 276 meV. It is believed that the emission energies to each band originate from a single trap. Since the location of this trap is nearest to midgap, this center may be the most efficient non-radiative recombination center in this material.

For the samples with p-$Ga_{0.85}In_{0.15}As_{0.12}Sb_{0.88}$ well material in p-$AlAs_{0.07}Sb_{0.93}$ barriers, the I-V-T measurements showed that a dilute phosphoric acid etch (H_3PO_4, H_2O_2, H_2O, L-tartaric acid (1 ml:1 ml:350 ml:0.4 g)) produces fewer surface states than a more concentrated etch (1 ml:1 ml:10 ml:0.4 g), reducing the leakage current at -2 V by an order of magnitude at room temperature. Surface states caused the leakage current by providing a low resistance shunt path along the surface of the mesa. Passivating the device with ammonium sulfide after etching reduced the leakage current at -2 V by nearly two orders of magnitude at room temperature after a dilute phosphoric acid etch. Changing the $Al_xGa_{1-x}As_ySb_{1-y}$ barrier composition to contain as much gallium as the device allows also improves the surface etched by phosphoric acid. That is, changing the barrier from $AlAs_{0.07}Sb_{0.93}$ to $Al_{0.9}Ga_{0.1}As_{0.07}Sb_{0.93}$ decreased the leakage current at -2 V by three orders of magnitude compared to a non-passivated surface, both of which were etched with dilute phosphoric acid. The most straightforward method of obtaining a good quality etched surface was by reactive ion etching with BCl_3.

A generation center with an activation energy of 0.140 eV in $Ga_{0.81}In_{0.19}As_{0.12}Sb_{0.88}$ was found from the reverse I-V-T measurements for the samples where the shunt current is not the primary conduction mechanism. I-V-T measurements do not indicate whether to reference the energy to the conduction band or the valence band. However, a similar

deep trap was found from the DLTS measurements in bulk $Ga_{0.85}In_{0.15}As_{0.12}Sb_{0.88}$ in an MIS structure using Si_3N_4 as the insulating layer. The DLTS measurements yielded an energy level situated 0.122 eV from the valence band.

The I-V-T measurements were also used to determine the range of biases permissible in DLTS and C-V measurements without introducing error from leakage currents. The importance of the capacitance versus voltage measurements is that the gradual steps appearing in the C-V plots indicate how many of the energy levels in the well to expect in the DLTS measurements. It also shows the temperature range where the DLTS measurements should encounter peaks, and the biases to be used to modulate the charge in the well. A step in the C-V characteristics appears when the Fermi level crosses a significantly occupied energy level in the well. Previously, when two accumulation peaks appeared in the apparent concentration profile of heterojunctions, one peak was attributed to interface states and the other peak was attributed to the two dimensional electron gas. More than two measured steps in the low leakage current quantum well diodes clearly indicate that the additional peaks are due to confined state energies rather than interface states.

A series of DLTS measurements effectively demonstrated a method to determine the band offset. First, the leakage currents had to be controlled. High leakage current in some of the worst diodes, and the unrealistically low confined state emission energy of the same samples show the importance of qualifying the DLTS measurements with I-V measurements. Diodes with high leakage currents have confined state emission energies much lower than expected from states at the bottom of the well. Controlling the surface

conduction improved the quality in the third sample structure diodes composed of 100 Å of a $Ga_{0.81}In_{0.19}As_{0.12}Sb_{0.88}$ well between p-$Al_{0.9}Ga_{0.1}As_{0.07}Sb_{0.93}$ barriers. Changing the barrier material to $Al_{0.9}Ga_{0.1}As_{0.07}Sb_{0.93}$ rather than $AlAs_{0.07}Sb_{0.93}$, and using reactive ion etching to form the mesas controlled leakage currents most effectively, decreased the surface leakage current at -2 V by three orders of magnitude. Lower leakage currents allowed biases to be applied such that the quasi-Fermi level was pushed successively farther below the confined states in the well, and improved the accuracy of the analysis using Boltzmann statistics. If the quasi-Fermi level is near the confined state in the well Fermi-Dirac statistics should be used. However, Fermi-Dirac statistics would require knowledge of the Fermi level position relative to the confined state, whereas if the quasi-Fermi level is far from the confined state in the well, the Boltzmann approximation can be used. An increase in energy with increasing reverse bias measurement conditions, which has been reported previously and duplicated here, is explained by the inaccuracy of using Boltzmann's approximation rather than Fermi-Dirac statistics at lower reverse bias where the quasi-Fermi level is close to the confined state energy. However, extrapolating a series of quantum well emission energies made using increasing reverse measurement bias to a point where Boltzmann's approximation is valid results in a valence band offset of 0.52 eV between $Ga_{0.81}In_{0.19}AsSb$ and $Al_{0.9}Ga_{0.1}AsSb$ lattice matched to GaSb. This is significantly different from the value of 0.38 eV calculated from the difference in average valence band energy interpolated from the binary constituents using bowing parameters. Comparing the measurement made by DLTS to the predicted value gives a measure of the accuracy of the interpolation method.

During this course of research, new DLTS measurement and analysis methods have been developed which extend the state of the art of conventional DLTS measurements. Recording the entire transient and fitting the transient for multiple emission rates brings out interesting behavior that ordinary ratewindow analysis misses. An Arrhenius plot of emission rates obtained from multi-exponential analysis versus temperature displays the characteristics of multiple level traps and coupled energy levels in a quantum well as distinctively different from single level traps. Multiple level traps show up distinctively as a single line with two slopes. Another aspect of the DLTS analysis using a fit of the entire transient that had not been exploited previously is the use of the amplitude of the capacitance transient emission components as they change with temperature. In the case of coupled quantum well energy levels, the emission amplitudes of the two levels form a pair of parabolas. This characteristic complements the two-slope nature of the Arrhenius plot pointing to a two-level trap. Also the amplitude of the emission transient versus temperature of single-level traps has been extremely useful in identifying traps with capture barriers. In the case of traps with capture barriers due to multi-phonon emission, the additional information provided by the amplitude versus temperature was successfully fit to the model, allowing extraction of the capture barrier energy.

In addition to the need in the future to identify the sources or the microscopic composition of the traps that were found, there are some improvements and additions that can be made to the existing DLTS system. One analytical tool that could be implemented is a pressure cell. A diamond anvil has been used previously with DLTS to determine the

symmetry of a defect as a clue to its origin. The present DLTS system is already developed into a configuration with very unique capabilities. Many DLTS systems cover only liquid nitrogen temperatures and are based on the ratewindow-type analysis. This setup uses a helium refrigerator, extending the range of deep levels that can be characterized to lower energy. In addition, this setup not only uses transient fitting, but also has the CC-DLTS mode of operation, both of which are rarely found in most DLTS equipment due to the added complexity. The capabilities can be extended even further by adding control code to the existing programs to implement current transient spectroscopy that was purchased as an option. This mode would be used for high-resistivity samples or for spectroscopy of FET type devices.

Bibliography

Ababou, S., G. Guillot, A. Regreny. "Electrical Characterization of a GaAs Quantum Well Confined By GaAlAs Layers or by Two Superlattices," J. Appl. Phys., vol. 72, no. 9: 4134-4138 (1 Nov 92).

Adachi, S. "Band Gaps and Refractive Indices of AlGaAsSb, GaInAsSb, and InPAsSb: Key Properties for a Variety of the 2–4 µm Optoelectronic Device Applications," J. Appl. Phys., vol. 61, no. 10: 4869–4876 (15May87).

Alibert, C. et al. "Refractive Indices of AlSb and GaSb-Lattice-Matched $Al_xGa_{1-x}As_ySb_{1-y}$ in the Transparent Wavelength Region," J. Appl. Phys., vol. 69, no. 5: 3206-3211 (1 March 1991).

Anand, S. et al. "DX Centers in AlGaAs and Pressurised GaAs," Mat. Res. Soc. Symp. Proc., vol. 300: 489-494 (1993).

Andre, J. P. et al. International Symposium on GaAs and Related Compounds, Las Vegas (Institute of Physics, Bristol), Paper F6 (1986).

Arnold, C. et al. Appl. Phys. Lett., vol. 45: 1237 (1984).

As, D. J., P. W. Epperlein, and P. M. Mooney. "Deep Electron Traps in GaAs/n-$Al_xGa_{1-x}As$ Single-Quantum Wells," J. Appl. Phys., 64(5): 2408–2414 (1Sept88).

Ashcroft, N. W. and N. D. Mermin. Solid State Physics. Orlando: Holt, Rinehart and Winston, 1976.

Baranov, A. N. "Linewidth Enhancement Factor for GaInSbAs/GaSb Lasers," Appl. Phys. Lett., vol. 59, p. 2360 (1991).

Bastard, G. Phys. Rev. B, vol. 25: 7594 (1982).

Bastard, G. Phys. Rev. B, vol. 24: 5693 (1981).

Beattie, A. R. and P. T. Landsberg. Proc. Roy. Soc., vol. A249: 16 (1958).

Bochkarev, A. E. et al. "Room Temperature Injection Lasers," Sov. J. Quant. Electron., vol. 18: 1362 (1988).

Bonnefoi, A. R. et al. Appl. Phys. Lett., vol.50: 344 (1987).

Bourgoin, J. and M. Lannoo. Point defect in semiconductors II, Springer-Verlag, Berlin, 188–193 (1983).

Bourgoin, J. and M. Lannoo. <u>Point defect in semiconductors II</u>, Springer-Verlag, Berlin, 185–188 (1983).

Buchwald, W. R. and N. M. Johnson. "Revised Role for the Poole-Frenkel Effect in Deep-Level Characterization," <u>J. Appl. Phys., 64(2)</u>: 958-961 (15Jul88).

Butler, J. F. *et al.* <u>Appl. Phys. Lett., vol. 5</u>, p. 75 (1964).

Caneau, C. *et al.* "Reduction of Threshold Current Density of 2.2 μm GaInAsSb/AlGaAsSb Injection Lasers," <u>Electron. Lett., vol. 22</u>, p.992 (1986).

Chadi, D. J. and K. J. Chang. <u>Phys. Rev. B, 39</u>: 10063 (1989).

Chadi, D. J. and K. J. Chang. <u>Phys. Rev. Lett., 61</u>: 873 (1988).

Chen, C.Y., S. N. G. Chu, and A. Y. Cho. <u>Appl. Phys. Lett., vol. 46</u>: 1145 (1985).

Chiu, T. H., J. L. Zyskind and W. T. Tsang. "Molecular Beam Epitaxial Growth of InGaAsSb on (100) GaSb with Emission Wavelength in the 2 to 2.5 μm Range," <u>J. Elec. Matl., Vol. 16, No. 1</u>: 57-61 (1987).

Criado, J. *et al.* "Novel Method to Determine Capture Cross-Section Activation Energies by Deep-Level Transient Spectroscopy Techniques," <u>Appl. Phys. Lett., 52(8)</u>: 660-661 (22Feb88).

DeAlvarez, C. V. *et al.* "Calculated Band Structures, Optical Constants and Electronic Charge Densities for InAs and InSb," <u>J. Phys. Chem. Solids, vol. 34</u>: 337-345 (1973).

Debbar, N. and P. Bhattacharya. "Carrier Dynamics in Quantum Wells Behaving as Giant Traps," <u>J. Appl. Phys., 62(9)</u>: 3845–3847 (1Nov87).

DeJule, R. Y. *et al.* <u>Solid State Electronics, vol. 28, no. 6</u>: 639–641 (1985).

Dhar, S., K. Mallik, and M. Mazamdar. <u>J. Appl. Phys. 77</u>: 1531-1535 (1994).

Dingle, R. <u>Festkorperprobleme/Advances in Solid State Physics, vol. 15</u>, Ed. H. J. Queisser, Vieweg, Braunschweig: 21 (1975).

Doolittle, W. and A. Rohatgi. "A New Figure of Merit and Methodology for Quantitatively Determining Defect Resolution Capabilities in Deep Level Transient Spectroscopy Analysis," <u>J. Appl. Phys., 75(9)</u>: 4570-4575 (1May94).

Dupuis, R. D. *et al.* "Determination of the Indirect Band Edge of GaAs by Quantum-Well Band Filling ($L_z \sim 100$ Å)," <u>Solid State Commun., vol. 27</u>: 531-533 (Aug78).

Dutta, M. D. *et al.* "Delocalized Exciton and Electron Conduction Via the X Valley in GaAs/AlAs Quantum Wells," Physical Review B, vol. 42, no. 2: 14741477 (15Jul90).

Dutta, M. K., K. Choi, and P. G. Newman. "Thermionic Emission and Photoluminescence Studies of the Energy States of GaAs/AlAs Superlattices," Appl. Phys. Lett., vol. 55, no. 23: 24292431 (4Dec89).

Dutta, M. *et al.* "Effect of Electric Field, Both External and Built-In, on GaAs-AlAs Structures," SPIE, vol. 1675: 282286 (1992).

Eglash, S. J., H. K. Choi and G. W. Turner. "MBE Growth of GaInAsSb/AlGaAsSb Double Heterostructures for Infrared Diode Lasers," Journal of Crystal Growth, vol. 111: 669-676 (1991).

Fitzgerald, E. A. *et al.* "Structure and Recombination in InGaAs/GaAs Heterostructures," J. Appl. Phys., vol. 63, no. 3: 693–703 (1 Feb 88).

Fomin, I. A., L. V. Lebedev, and N. M. Annenko. Fiz. Tekh. Poluprov., vol. 18: 734 (1984).

Frensley, W. R. and H. Kroemer. Phys. Rev. B, vol. 16: 2642 (1977).

Goto, G. *et al.* Appl. Phys. Lett., Vol. 23: 150 (1973).

Grimmeiss, H. G. "Deep Level Impurities in Semiconductors," Annual Review of Materials Science, vol. 7: 341-376 (1977).

Guillaume, C. B. and P. Lavallard, Solid State Commun., vol. 1: 148 (1963).

Harrison, W. A. "Theory of Band Line-Ups," J. Vac. Sci. Tech., vol. B3, no. 4: 1231–1238 (Jul/Aug 1985).

Harrison, W. A. J. Vac. Sci. Technol., vol. 14: 1016 (1977).

Hartke, J. L. "The Three-Dimensional Poole-Frenkel Effect," J. Appl. Phys., 39: 4871–4873 (1968).

Hasegawa, H. and T. Sawada. "On the Electrical Properties of Compound Semiconductor Interfaces in Metal/Insulator/Semiconductor Structures and the Possible Origin of Interface States," Thin Solid Films, vol. 103: 119-140 (1983).

Henry, C. H. and D. V. Lang. Phys. Rev. B15: 989 (1977).

Hess, K. *et al.* "Negative Differential Resistance Through Real-space Electron Transfer," Appl. Phys. Lett., 35(6): 469–471 (15Sept79).

Hjalmarson, H. P. *et al.* "Theory of Substitutional Deep Traps in Covalent Semiconductors," <u>Physical Review Letters, vol. 44, no. 12</u>: 810-813 (24 Mar 80).

Holonyak, N. Jr. *et al.* "Phonon-Sideband MOCVD Quantum-Well $Al_xGa_{1-x}As$-GaAs Heterostructure Laser," <u>Appl. Phys. Lett., vol. 34</u>: 502-505 (15Apr79).

Holonyak, N. *et al.* "Quantum-Well Heterostructure Lasers," <u>IEEE Journal of Quantum Electronics, vol. QE-16, no. 2</u>: 170-185 (Feb80).

Horikoshi, Y. <u>Semiconductors and Semimetals, vol. 22, part C</u>, Academic Press, Orlando, Florida: 93-151 (1985).

Hovel, H. J. <u>Semiconductors and Semimetals, vol. 11</u>, Academic Press, New York: (1975).

Huang, J. H., T. Y. Chang and B. Lalevic. "Measurement of the Conduction-Band Discontinuity in Pseudomorphic $In_xGa_{1-x}As/In_{0.52}Al_{0.48}As$ Heterostructures," <u>Appl. Phys. Lett., vol. 60, no. 6</u>: 733-735 (10Feb92).

Huang, Z. C. *et al.* "Energy and Depth Distributions of Interface States and Bulk Traps and Their Electronic Effects in GaInAs/GaAs Heterojunctions," <u>Mat. Res. Soc. Symp. Proc., vol. 240</u>: 633–640 (1992).

Hubik, P. *et al.* "DX-Like Centre in Bulk GaSb:S," <u>Solid State Communications, vol. 86, no. 1</u>: 19-22 (1993).

Ideshita, S. *et al.* <u>Appl. Phys. Lett., 60</u>: 2549 (1992).

Ikossi-Anastasiou, K. *et al.* "Interface States in Regrown GaAs p-n Junctions by Selective Molecular Beam Epitaxy," <u>Appl. Phys. Lett., vol. 61, no. 3</u>: 297-299 (20 Jul 92).

Jeong, J. *et al.* "Study of $n-In_xGa_{1-x}As/n$-GaAs Heterojunction Epilayers," <u>J. Vac. Sci. Technol., B5(3)</u>: 792-795 (May/Jun 1987).

Jiao, K. L. and W. A. Anderson: "Trap Behavior in Nonintentionally Doped AlGaAs/GaAs Single Quantum Well Structures," <u>J. Appl. Phys., vol. 73, no. 1</u>: 271-276 (1 Jan 93).

Johnstone, D. K. *et al.* "Electrical and Optical Characterization of GaSb Based Diode Laser Material for 2-4 μm Applications," (to be published in the International Symposium on Compound Semiconductors Proceedings) (1996).

Kash, J. A., J. C. Tsang, and J. M. Hvam. "Subpicosecond Time-resolved Raman Spectroscopy of LO Phonons in GaAs," Physical Review Letters, 54(19): 2151–2154 (13May85).

Kazmierski, K. *et al.* "C-V Measurement and Modelization of GaInAs/InP Heterointerface With Traps," J. Appl. Phys., vol. 61, no. 5: 1941-1946 (1Mar87).

Kirchner, P. D. *et al.* "The Analysis of Exponential and Nonexponential Transients in Deep-Level Transient Spectroscopy," J. Appl. Phys., 52(11): 6462-6470 (Nov81).

Knox, W. H. *et al.* "Femtosecond Excitation of Nonthermal Carrier Populations in GaAs Quantum Wells," Physical Review Letters, 56(11): 1191–1193 (17Mar86).

Ko, D. Y. K. and J. C. Inkson. Phys. Rev. B., vol. 38: 9945 (1988).

Krijn, M. P. C. M. "Heterojunction Band Offsets and Effective Masses in III–V Quaternary Alloys," Semiconductor Science and Technology, vol. 6, no. 1: 27–31 (Jan91).

Kroemer, H. *et al.* Appl. Phys. Lett., vol. 36: 295 (1980).

Kuramochi, E. *et al.* "Observation of Deep Levels in Undoped GaSb Grown by Molecular Beam Epitaxy," Appl. Phys. Lett., vol. 63, no. 19: 2664-2666 (8Nov93).

Lang, D. V. "Deep-level Transient Spectroscopy: A New Method to Characterize Traps in Semiconductors," J. Appl. Phys., 45(7): 3023–3032 (Jul74).

Lang, D. V. and C. H. Henry. Phys. Rev. Lett., vol.35: 1525 (1975).

Lannoo, M. and J. Bourgoin. Point Defects in Semiconductors I: Theoretical Aspects, Springer-Verlag, New York: 68-112 (1981).

Lax, M. "Cascade Capture of Electrons in Solids", Physical Review, vol. 119, no. 5: 1502–1523 (1Sept60).

Le, H. Q., *et al.* "High-power Diode-laser-pumped InAsSb/GaSb and GaInAsSb/GaSb Lasers Emitting From 3 to 4 μm," Appl. Phys. Lett., 64(2): 152-154 (10Jan94).

Leith, G. A., S. Zukotynski and A. J. SpringThorpe. "Evidence for the Neutral Charge State Model of the DX Center From Low Temperature Hall Mobility Measurements," Appl. Phys. Lett., vol. 60, no. 20: 2517-2519 (18May92).

Letartre, X., D. Stievenard, M. Lannoo. "Admittance Spectroscopy Measurement of Band Offset in GaAs-GaAlAs Multiquantum Well," J. Appl. Phys., vol. 68, no. 1: 116-119 (1 Jul 90).

Letartre, X., D. Stievenard. "Accurate Determination of the Conduction-Band Offset of a Single Quantum Well Using Deep Level Transient Spectroscopy," Appl. Phys. Lett., vol. 58, no. 10: 1047-1049 (11Mar91).

Leu, L. Y. S. R. Forrest. "The Determination of Heterojunction Energy Band Discontinuities in the Presence of Interface States Using Capacitance-Voltage Techniques," J. Appl. Phys., 64(10): 5030-5041 (15Nov88).

Loskutova, E. A. et al. Poverkh. Fiz. Khim. Mekh., vol. 10: 36 (1985).

Luquet, H. et al. "Liquid-phase-epitaxial Growth of $Ga_{0.96}Al_{0.04}Sb$: Electrical and Photoelectrical Characterizations," J. Appl. Phys., 60(10): 3581-3591 (15Nov86).

Martin, P. A. et al. "Transient Capacitance Spectroscopy on Large Quantum Well Heterostructures," J. Appl. Phys., vol. 54: 4689 (1983).

Matthews, J. W., S. Mader, T. B. Light. "Accommodation of Misfit Across the Interface Between Crystals of Semiconducting Elements or Compounds," J. Appl. Phys., vol. 41, no. 9: 3800-3804 (August 1970).

McAfee, S. R., D. V. Lang and W. T. Tsang. "Observation of Deep Levels Associated With the $GaAs/Al_xGa_{1-x}As$ Interface Grown by Molecular Beam Epitaxy," Appl. Phys. Lett., 40(6): 520-522 (15Mar82).

Melngailis, I., Appl. Phys. Lett., vol. 2: 176 (1963).

Mendez, E. E. E. Calleja, and W. I. Wang, Phys. Rev. B, vol. 34, p. 6026 (1986).

Meyer, B. et al. "Optical and Electrical Characterization of $Al_xGa_{1-x}Sb$ Crystals Grown by the Travelling Heater Method," Journal of Crystal Growth, 128: 475-478 (1993).

Milnes, A. G. and A. Y. Polyakov. "Review: Gallium Antimonide Device Related Properties," Solid-State Electronics, Vol. 36, No. 6: 803-818 (1993).

Missous, M., E. H. Rhoderick. "A Simple Method of Modelling the C-V Profiles of High-Low Junctions and Heterojunctions," Solid State Electronics, vol. 28, no. 3: 233-237 (1985).

Mooney, P. "Deep Donor Levels (DX Centers) in III-V Semiconductors," J. Appl. Phys., 67(3): R1-R26 (1Feb90).

Nakagawa, A. et al, "Deep Levels in Te-doped AlSb Grown by Molecular Beam Epitaxy," Appl. Phys. Lett. 57(15): 1551-1553 (8Oct90).

Nakashima, K. "Electrical and Optical Studies in Gallium Antimonide," Jap. J. App. Phys., Vol. 20, No. 6: 1085-1094 (6Jun81).

Nathan, M. I. *et al.* Appl. Phys. Lett., vol. 3, p. 62 (1963).

Nelson, R. J. and N. K. Dutta. Semiconductors and Semimetals, vol. 22, pt. C. 16-25 1985.

Neuberger, M. Handbook of Electronic Material, Vol. 2, III-V Semiconducting Compounds. New York: IFI Plenum, 1971.

Nicholas, D. J. *et al.* "Spectroscopic Studies of Shallow Defects in MBE GaSb," J. Crystal Growth, 81: 298-303 (1987).

Oliveira, J. B. B. *et al.* "Properties of Au-Zn Ohmic Contacts to p-GaSb", J. Appl. Phys., 66(1): 5485-5487 (1Dec89).

Palma, A. *et al.* "Accurate Determination of Majority Thermal-Capture Cross Sections of Deep Impurities in p-n Junctions," J. Appl. Phys., 74(4): 2605-2612 (15Aug93).

Pankove, J. I. Optical Processes in Semiconductors, General Publishing Company, Ltd., Toronto, Ontario: 74-76 (1971).

Pascal-Delannoy, F. *et al.* "InGaSb/GaSb Photodiodes Grown by MOVPE," J. Crystal Growth, Vol. 124: 409-414 (1992).

Phelan, J. *et al.* Appl. Phys. Lett., vol. 3: 143 (1963).

Pickett, N. E., S. G. Louie, and M. L. Cohen. Phys. Rev. B, vol. 17: 815 (1978).

Pinnow, D. A. *et al.* Appl. Phys. Lett., vol. 33: 28 (1978).

Polyakov, A. *et al.* "Electrical Properties of GaSb Schottky Diodes and p-n Junctions," Materials Science and Engineering, B12: 337–343 (1992).

Polyakov, A. *et al.* "High-Resistivity GaSb Grown by Molecular-Beam Epitaxy," J. Appl. Phys., 72(4): 1316-1319 (15Aug92).

Polyakov, A. Y. *et al.* "Schottky Barriers of Various Metals on $Al_{0.5}Ga_{0.5}As_{0.05}Sb_{0.95}$ and the Influence of Hydrogen and Sulfur Treatments on Their Properties," J. Appl. Phys., 71(9): 4411-4414 (1May92).

Poole, I. *et al.*, J. Appl. Phys., 62: 3988 (1987).

Poole, I. *et al.* "Deep Donors in GaSb Grown by Molecular Beam Epitaxy," Appl. Phys. Lett., vol. 57, no. 16: 1645–1647 (15 Oct 90).

Qhang, H. *et al.* Appl. Phys. Lett., vol. 50: 341 (1987).

Ren, S. Y., J. D. Dow, J. Shen. Phys. Rev. B, 38: 10677 (1988).

Rogalski, A. "InAs$_{1-x}$Sb$_x$ Infrared Detectors," Prog. Quant. Electr. Vol. 13: 191-231 (1989).

Rousseau, Y. V., K. L. Wang, and J. N. Schulman, Appl. Phys. Lett., vol. 54, p. 1341 (1989).

Salman, E. G., A. N. Korshunov, and V. N. Vertoprakhov. "A DLTS Study of InAs MIS Structures," Phys. Stat. Sol. A, vol. 117: 509–514 (1990).

Schulz, M., E. Klausmann. Appl. Phys., vol. 18: 169 (1979).

Schulz, M., N. M. Johnson. Solid State Comm., vol. 25: 481 (1978).

Schulz, P. A. and C. E. T. Goncalves da Silva, Phys. Rev. B., vol. 35, p. 8126 (1987).

Shen, J. et al. "Remote n-type Modulation Doping of InAs Quantum Wells by 'Deep Acceptors' in AlSb," J. Appl. Phys., 73(12): 8313-8318 (15Jun93).

Shen, J., S. Y. Ren and J. D. Dow. Phys. Rev. B, 46: 1089 (1992).

Shichijo, H. et al. "Carrier collection in a semiconductor quantum well," Solid State Communications, vol. 27, no. 10: 1029-1032 (1978).

Stirn, R. J. "Proceedings of the 9th IEEE Photovoltaics Specialists Conference, (New York)" IEEE: 72 (1972).

Su, Y. K. et al. "The Effect of Annealing Temperature on Electrical Properties of Pd/n-GaSb Schottky Contacts," J. Appl. Phys., 68(2): 646-648 (15Jul90).

Subramanian, S., S. Anand and B. M. Arora. "Evidence for the Neutral Charge State Model of the DX Center in Aluminium Gallium Arsenide," Solid State Communications, vol. 76, no. 5: 609-612 (1990).

Takeda, Y. et al. "Determination of Al Composition and DLTS Measurements of Al$_x$Ga$_{1-x}$Sb on GaSb Substrate," Jap. J. Appl. Phy., 26 (4): L273-275 (Apr87).

Tang, J. Y. et al. "The Dynamics of Electron-Hole Collection in Quantum Well Heterostructures," J. Appl. Phys., vol. 53, no. 9: 6043-6046 (Sept82).

Tersoff, J., Phys. Rev. B, vol. 30: 4874 (1984).

Tsuchiya M. and H. Sakaki, Appl. Phys. Lett., vol. 50, p. 1503 (1987).

Turner, G. and H. Choi, MIT Lincoln Labs, Lincoln, MA, Personal Communication, 1994.

Turner, G. et al. "Molecular-beam Epitaxy Growth of High-performance Midinfrared Diode Lasers," J. Vac. Sci. Tech., B 12(2): 1266-1268 (Mar/Apr 1994).

Uji, T., T. Suzuki and T. Kamejima. "Deep-level Changes in (Al,Ga)As Double-Heterostructure Lasers Degraded During Accelerated Aging at High Temperatures," Appl. Phys. Lett., 36(8): 655-657 (15Apr80).

Van de Walle, C. G. Phys. Rev. B, vol. 39: 1871 (1989).

van der Ziel, J. P., T. H. Chiu, W. T. Tsang. "Room Temperature Opitcally Pumped Laser Oscillation at 2.07 μm From $Ga_{0.85}In_{0.15}As_{0.13}Sb_{0.87}/Al_{0.4}Ga_{0.6}As_{0.035}Sb_{0.965}$ Double Heterostructures Grown by Molecular Beam Epitaxy on GaSb Substrates," J. Appl. Phys., vol. 60: 4087 (1986).

Vescan, L., R. Apetz, H. Luth. "Determination of the Valence Band Offset of $Si/Si_{0.7}Ge_{0.3}/Si$ Quantum Wells Using Deep Level Transient Spectroscopy," J. Appl. Phys., vol. 73, no. 11: 7427-7430 (1 Jun 93).

Vincent, G., A. Chantra, and D. Bois. "Electric Field Effect on the Thermal Emission of Traps in Semiconductor Junctions," J. Appl. Phys., 50(8): 5484-5487 (Aug79).

Vogl, P. and H. P. Hjalmarson, J. D. Dow. J. Phys. Chem. Solids, 44: 365 (1983).

Waldrop, J. R. et al, J. Vac. Sci. Tech., vol. 19: 573 (1981).

Walters, S. A. and R. H. Williams. "Metals on Cleaved Gallium Antimonide: Schottky Barriers and Interface Reactions," J. Vac. Sci. Technol. B, 6(4): 1421-1426 (Jul/Aug88).

Wang, W. I. and F. Stern. J. Vac. Sci. Technol. B, vol. 3: 1280 (1985).

Willardson, R. K. and A. C. Beer, Semiconductors and Semimetals, Vol. 19: Deep Levels, GaAs, Alloys, Photochemistry, Academic Press, New York (1983).

Wise, F. W., I. A. Walmsley, and C. L. Tang. "Experimental Determination of Hot-Carrier Scattering Processes in $Al_xGa_{1-x}As$," Appl. Phys. Lett., vol. 51, no. 8: 605-607 (24Aug87).

Yamasaki, K., M. Yoshida and T. Sugano. Jap. J. Appl. Phys., vol. 18: 113 (1979).

Zhao, J. H. et al. "Theoretical and Experimental Determination of Deep Trap Profiles in Semiconductors," J. Appl. Phys., vol. 61, no.3: 1063-1067 (1 Feb 87).

Zhu, Y., Y. Takeda, A. Sasaki. "DX Center-Like Traps and Persistent Photoconductivity in Te-doped $Al_xGa_{1-x}Sb$ on GaSb," J. Appl. Phys., vol. 64, no. 4: 1897-1901 (15 Aug 88).

Zhu, Y., Y. Takeda, A. Sasaki. "DX-Center-Like Traps in AlGaSb," <u>Extended Abstracts of the 19th Conf. On Solid State Devices and Matl.</u>: 127-130 (1987).

Vita

Daniel Kevin Johnstone ~~was born on August 20, 1956 in Seattle, Washington~~, to Kenneth and Edna Johnstone. A bachelor of science was earned in Ceramic Engineering in 1981 from the University of Washington. Exposure to electronic ceramics led him to join the Air Force where there was an opportunity to study for a bachelor's degree in Electrical Engineering. After being commissioned, he went to Auburn University in Auburn, Alabama, finishing in 1984. His first assignment was to Electronic Systems Division at Hanscom AFB in Bedford, Massachussetts, where he was a team leader for the ground segments of the Enhanced Joint Tactical Information Distribution System, for secure voice and data communications. After two years, he went to Rome Laboratory, also at Hanscom AFB. There, he made use of his materials and electrical engineering backgrounds growing and characterizing indium phosphide. At Rome Labs he earned an MS degree in Electrical Engineering from the University of Massachussetts (Lowell). After three years he continued working with semiconductors at Wright Laboratory where he was introduced to the characterization method of Deep Level Transient Spectroscopy. Work there resulted in publication of two papers dealing with defects in regrown GaAs, and strain related defects in GaInAs/GaAs interfaces. In 1992 he entered the doctoral program in Engineering Physics at AFIT. He is presently a staff scientist at the Defense Nuclear Agency studying the effects of radiation on semiconductor devices.

~~Permanent Address~~:

~~6549 Kenmare Court~~

~~Woodbridge, VA 22193~~

REPORT DOCUMENTATION PAGE

1. AGENCY USE ONLY (Leave blank)	2. REPORT DATE June 1996	3. REPORT TYPE AND DATES COVERED Doctoral Dissertation

4. TITLE AND SUBTITLE
Electrical Characterization of GaSb-Based Semiconductors for 2-4 μm Diode Laser Applications

5. FUNDING NUMBERS

6. AUTHOR(S)
Daniel K. Johnstone, Major, USAF

7. PERFORMING ORGANIZATION NAME(S) AND ADDRESS(ES)
Air Force Institute of Technology
2950 P Street
Wright Patterson AFB, OH 45433-7765

8. PERFORMING ORGANIZATION REPORT NUMBER
AFIT/DS/ENP/95J-02

9. SPONSORING/MONITORING AGENCY NAME(S) AND ADDRESS(ES)
N. R. Pchelkin
PL/LIDA
Air Force Phillips Laboratory
Kirtland AFB, NM

10. SPONSORING/MONITORING AGENCY REPORT NUMBER

11. SUPPLEMENTARY NOTES

12a. DISTRIBUTION/AVAILABILITY STATEMENT
Approved for public release; distribution unlimited

12b. DISTRIBUTION CODE

13. ABSTRACT (Maximum 200 words)

Deep Level Transient Spectroscopy (DLTS) was used to characterize the band offsets and deep levels in MBE grown GaSb-based semiconductors that are used in 2-4 μm laser diode structures. One of several deep level traps found in $Al_xGa_{1-x}As_ySb_{1-y}$ (x=0, 0.5, 0.6, 1.0) is a Ga_{Sb} double acceptor trap. Progress is also made in establishing the model for the DX center in this material. The degree of compensation of the donor related DX center by Ga_{Sb} affect where donors are situated, giving preference to one configuration over the many other possible configurations. One minority trap 320 meV below the conduction band, and six hole traps 24, 76, 108, 122, 224, and 276 meV above the valence band were found in the $Ga_{0.85}In_{0.15}As_{0.12}Sb_{0.88}$ using DLTS measurements. It is believed that the minority trap level at 320 meV and the hole trap level at 276 meV originate from the same trap, making it the most efficient non-radiative recombination center.

Extrapolating a series of quantum well emission energies measured by DLTS (based on Boltzmann's approximation) to a point where the approximation is valid, results in a valence band offset of 0.52 eV between $Ga_{0.81}In_{0.19}As_{0.12}Sb_{0.88}$ and $Al_{0.9}Ga_{0.1}AsSb$ lattice matched to GaSb.

14. SUBJECT TERMS
DLTS, band offset, GaSb epitaxy, infrared diode laser, gallium antisite defect

15. NUMBER OF PAGES
262

16. PRICE CODE

17. SECURITY CLASSIFICATION OF REPORT Unclassified	18. SECURITY CLASSIFICATION OF THIS PAGE Unclassified	19. SECURITY CLASSIFICATION OF ABSTRACT Unclassified	20. LIMITATION OF ABSTRACT UL